

TECHNISCHE UNIVERSITÄT MÜNCHEN

Physik-Department
Lehrstuhl für Funktionelle Materialien

**QUANTUM DOTS BASED NOVEL
DEVICE ARCHITECTURES**

WEI CHEN

Vollständiger Abdruck der von der Fakultät für Physik der Technischen Universität München zur Erlangung des akademischen Grades eines

Doktors der Naturwissenschaften (Dr. rer. nat.)

genehmigten Dissertation.

Vorsitzender: Prof. Dr. Martin Zacharias

Prüfer der Dissertation: 1. Prof. Dr. Peter Müller-Buschbaum
2. Prof. Jonathan J. Finley, Ph.D.

Die Dissertation wurde am 16.09.2020 bei der Technischen Universität München eingereicht und durch die Fakultät für Physik am 19.10.2020 angenommen.

Abstract

Colloidal PbS quantum dots (QDs) are promising candidate materials in various optoelectronic applications including light-emitting diodes (LEDs), photodetectors (PDs), and photovoltaics (PVs) based on solution-processed thin-film technology. The intrinsic narrow band-gap of the PbS materials and the quantum confinement effect of the QDs enable the PbS QDs to have a broad and customized absorption spectrum, from the visible range to the near-infrared (NIR) range. In this thesis, the stacking behavior of oleic acid (OA) capped QDs is studied in different deposition methods by using grazing-incidence small-angle X-ray scattering (GISAXS). Specifically, the stacking kinetics of OA capped QDs is studied with *in situ* GISAXS during printing. Moreover, the charge carrier dynamics in the ligand exchanged QD solids are also investigated by ultrafast spectroscopy techniques including transient absorption spectroscopy (TAS) and time-resolved photoluminescence (TR-PL). In association with grazing-incidence wide-angle X-ray scattering (GIWAXS) and pump-probe TAS analysis, the exciton hopping rate is correlated with the facet alignment of QDs in spin-coated QD solids which were annealed at different temperatures. Besides, the spray-deposited QD solid demonstrates a better-ordered QD stacking behavior and thus a narrower energy state distribution than the spin-coated QD solid, which are confirmed from the GISAXS and the TR-PL analysis respectively. The related PD device performances are also discussed. Finally, QD-ink is fabricated based on the ligand exchange process in solution and used in PV devices. The overall QD stacking behavior of the layers is studied in an *in operando* PV experiment and static studies are carried out on the specific QD layers. The results suggest that the decreased inter-dot distance of the QDs and the increased spatial disorder of the QD layout in the active layer can be responsible for the device degradation. These findings provide fundamental understanding for further QD based large-scaled device fabrications.

Zusammenfassung

Kolloidale PbS Quantenpunkte (englisch: Quantum dots, QD) sind vielversprechende Materialien, die Anwendung in Licht emittierenden Dioden (LEDs), Photodetektoren (PD) und in lösungsbasierten Dünnschicht-Solarzellen finden. Die intrinsisch kleine Bandlücke der PbS Materialien und der Quanten-Confinement Effekt der QDs ermöglichen ein breites, individuell angepasbares Absorptionsspektrum vom sichtbaren bis in den nahen Infrarot (NIR) Bereich. In dieser Arbeit wird das Anlagerungsverhalten von Oleinsäure-

geschützten QDs für verschiedene Beschichtungsmethoden mit Röntgenkleinwinkelstreuung unter streifendem Einfall (englisch: Grazing-incidence small angle X-Ray scattering, GISAXS) untersucht. Insbesondere die Anlagerungskinetik der OA geschützten QDs wird mittels *in situ* GISAXS während dem Drucken untersucht. Darüber hinaus wird nach einem Ligandenaustausch die Bewegung der Ladungsträger in den QDs mit ultraschnellen spektroskopischen Techniken wie der Transienten-Absorptionsspektroskopie (TAS) und zeitaufgelöster Photoluminescence (englisch: time-resolved transient Photoluminescence, TR-PL) untersucht. Zusammen mit Röntgenweitwinkelstreuung unter streifendem Einfall (englisch: Grazing-incidence wide angle X-Ray scattering, GIWAXS) und Pump-Probe-TAS wird die Exziton-Sprungrate mit der Flächenausrichtung der QDs in QD Festkörpern, die mittels Schleuderbeschichtung hergestellt und bei hohen Temperaturen behandelt wurden, korreliert. Zudem zeigen die gesprühten QD-Festkörper ein geordnetes Anlagerungsverhalten and daher eine engere Verteilung der Energiezustände als die mittels Schleuderbeschichtung hergestellten QD-Festkörper wie mittels GISAXS und TR-PL Analyse bestätigt werden konnte. Die entsprechende Solarzellenleistung wurde ebenfalls diskutiert. Schließlich wird eine QD-Tinte mittels eines Ligandenaustausches in Lösung hergestellt und in Solarzellen verwendet. Das allgemeine QD Anlagerungsverhalten von Schichten wird mittels eines *in operando* Experiments untersucht und statistische Messungen werden mit den entsprechenden QD-basierten Schichten durchgeführt. Die Ergebnisse zeigen, dass der verminderte Abstand zwischen den QDs und die erhöhte räumliche Unordnung der QDs in der aktiven Schicht verantwortlich für die Degradation der Bauelemente sind. Die Ergebnisse liefern ein grundlegendes Verständnis die eine weitere Herstellung von QD-basierten Solarzellen im großen Maßstab.

Contents

List of abbreviations	vii
1 Introduction	1
2 Background	9
2.1 Quantum dot and quantum confinement effect	9
2.2 Colloidal quantum dots and self-organized superlattices	11
2.3 Energy transport in close packed QD solid	14
2.4 The spatial disorder suppresses charge carrier transport	15
2.5 QD based photodetectors and photovoltaics	17
3 Characterization methods	19
3.1 Grazing-incidence X-ray scattering	20
3.1.1 Grazing-incidence small-angle X-ray scattering	21
3.1.2 Grazing-incidence wide-angle X-ray scattering	22
3.2 Transient absorption spectroscopy	23
3.3 Time-resolved photoluminescence spectroscopy	25
3.4 Photodetector characterization	25
3.5 Photovoltaics characterization	27
4 Sample preparation	31
4.1 Synthesis of PbS QDs	31
4.2 Deposition of QDs via layer-by-layer method	33
4.3 QD ink preparation and deposition	34
4.4 Fabrication of photodetector device	36
4.5 Fabrication of solar cell device	37
5 Structure and charge carrier dynamics in QD solids	39
5.1 Motivations and main discoveries	39
5.2 Introduction	39
5.3 Experimental details	42
5.4 Solid-state ligand exchange induced phase transition	43

5.5	Structure landscape of strongly-coupled QD solid	45
5.6	Energetic landscape of strongly-coupled QD solid	51
5.7	Conclusions	54
6	Stacking kinetics of QDs during printing deposition	57
6.1	Motivations and main discoveries	57
6.2	Introduction of printing colloidal QDs	58
6.3	Experimental details	59
6.4	Material synthesis and characterization	62
6.5	Thin-film deposition via slot-die printing	64
6.6	GISAXS line-cuts evolution	66
6.7	Superlattice orientation evolution	71
6.8	Superlattice calculation	72
6.9	Conclusions	75
7	Spray-deposited QD solid for near-infrared photodetector	77
7.1	Motivations and main discoveries	77
7.2	Introduction of QD photodetector	78
7.3	Experimental details	79
7.4	Structural analysis by GIXS	82
7.5	Charge carrier dynamics analysis by TR-PL	91
7.6	Device performance	95
7.7	Conclusions	98
8	Structural degradation of QD solid in solar cell	101
8.1	Motivations and main discoveries	101
8.2	Introduction of in operando experiment	102
8.3	Experimental details	103
8.4	In operando experiment design	105
8.5	Device performance degradation	108
8.6	Structral degradation analysis	112
8.7	Degradation discussion	120
8.8	Conclusions	121
9	Conclusion and outlook	123
	Bibliography	127
	List of publications	139

Acknowledgements

143

List of abbreviations

AA	ammonium acetate, $C_2H_7NO_2$
AFM	atomic force microscopy
AM	air mass
BCC	body-centered cubic
BTA	n-butylamine
CQD	colloidal quantum dots
DESY	Deutsches Elektronen-Synchrotron
DMF	N,N-dimethylformamide, C_3H_7NO
DWBA	distorted wave Born approximation
EDT	1,2-ethanedithiol, $C_2H_6S_2$
ET	energy transfer
ETL	electron transport layer
FCC	face-centered cubic
FF	fill factor
FRET	fluorescent resonance energy transfer, also known as Förster transfer
FTIR	fourier-transform infrared spectroscopy
FWHM	full width at half maximum
GISAXS	grazing-incidence small-angle x-ray scattering
GIWAXS	grazing-incidence wide-angle x-ray scattering

GIXS	grazing-incidence X-ray scattering
GSB	ground state bleaching
HR	high resolution
HTL	hole transport layer
ITO	indium doped tin oxide
LBL	layer-by-layer
LED	light-emitting diode
LMA	local monodisperse approximation
MA	malonic acid, $C_3H_4O_4$
M-A	Miller-Abrahams
MEG	multiple exciton generation
NC	nanocrystal
NIR	near infrared
OA	Oleic acid, $C_{18}H_{34}O_2$
ODE	octadecene, $C_{18}H_{36}$
P03	The Micro- and Nanofocus X-ray Scattering Beamline at PE-TRA III, DESY
PCE	power conversion efficiency
PD	photodetector
PL	photoluminescence
PV	photovoltaic
QD	quantum dot
SAXS	small-angle x-ray scattering
SDD	sample to detector distance
SEM	scanning electron microscopy

SL	superlattice
SLD	scattering length density
TA	transient absorption
TAS	transient absorption spectroscopy
TBAI	tetrabutylammonium iodide, C ₁₆ H ₃₆ IN
TCSPC	time-correlated single photon counting
TEM	transmission electron microscopy
TIR	total internal reflection
TR-PL	time-resolved photoluminescence
WAXS	wide-angle x-ray scattering
XRD	x-ray diffraction

1 Introduction

Quantum dots (QDs) are semiconductor nanocrystals made of hundreds or thousands of atoms. The materials were found and initially studied in the 1980s by Alexei Ekimov and Louis Brus respectively. They observed interesting optical properties in comparison with bulk semiconductors. [1, 2] The size (effective diameter) of QDs is typically in the range of 2-10 nm, which is smaller than the Bohr radius of the generated excitons. Thus, the excitons in the QDs suffer quantum confinement effects from three dimensions and therefore QDs are known as a “zero-dimensional” material. The main feature of QDs is the spectral response, including the absorption and the emission, which are tunable based on different compositions and different sizes of the QDs. Thus, when decreasing the size of the QDs, the corresponding bandgap of the QDs is increasing simultaneously, [3] which is known as the “QD size effect”. The effect provides a feasible and convenient way to design the semiconductor material with a desired bandgap. This makes QDs attractive in many optoelectronic applications, such as light-emitting diodes (LEDs), [4–6] photodetectors (PDs) [7–9] and photovoltaics (PVs). [10–13]

For QDs based on the II-VI group, lead chalcogenides (PbS, PbSe) intrinsically have a larger permittivity than cadmium chalcogenides (CdS, CdSe, CdTe). This means Pb based QDs can better screen the Coulomb interaction of hole and electron in the photon generated excitons than Cd based QDs. [14]. Thus, the exciton binding energy in Pb based QDs is smaller than in Cd based QDs and the excitons in Pb based QDs are easier to dissociate into free charge carriers compared with those in Cd based QDs. Therefore, in practical applications, the Pb based QDs are suitable for being used in devices driven by charge transport and extraction, such as PVs and PDs, while the Cd based QDs are normally used for light-emitting devices, for instance, LEDs. Moreover, II-VI group QDs belong to the group of direct semiconductors, which demonstrate a much higher absorption coefficient than the indirect semiconductor QDs, such as Si QDs. [15] This makes QDs promising for the third generation of thin-film photovoltaic devices. Due to the narrow bandgap, Pb based QDs usually have a broad absorption range covering the entire visible range till short-wave infrared (SWIR). Therefore, Pb based QDs can be used for collecting the solar energy in long wavelength-regime beyond the limits of Si-solar cells

and perovskite solar cells. [16] In this thesis, PbS QDs are mainly used and discussed, and the term "QDs" in the following text refers to PbS based QDs unless stated.

Conventionally, size-monodisperse QDs are synthesized in a solution phase condition, known as colloidal QDs. Long-chain organic ligands play an important role for the precise control of the size growth of QDs and to limit their size dispersity by preventing particle aggregations. These ligands enable QDs to disperse in many organic solvents, which endows QDs compatible with many large-scalable solution-processed fabrication methods, such as roll-to-roll printing and spray deposition. However, the barrier potential induced by the long-chain ligands can decrease the electronic coupling and lead to a low efficient energy transport between neighboring QDs. [17, 18] Therefore, to enhance the electronic coupling of the QD solid, long-chain ligands are replaced by short-chain ligands, *e.g.* small molecules, or halide ions via a ligand exchange process. The exchange process is performed automatically when QDs are immersed in the precursor solvent, which is attributed to the different binding energies of different ligands to the surface of the QDs. [19] After the ligand exchange treatment, the inter-dot distance for all neighboring QDs in the solid is decreased, which results in an enhanced electronic coupling property to the ensemble of the QDs (strongly-coupled QD solid). This process is known as the functionalization process of the QD solid.

Two main strategies for the ligand exchange are described, namely solid-state ligand exchange and solution-phase ligand exchange. To assure a thorough solid-state ligand exchange, the process is normally integrated into a layer-by-layer (LBL) process. The product from a solution-phase ligand exchange is known as QD ink, which is deposited in a single-step. Notably, due to the small size, QDs possess a large surface area to volume ratio, which makes the semiconductor properties of QDs sensitive to different surface modifications. For instance, the QD solid reveals *n*-type semiconductor properties when they are treated by halides in an inert atmosphere. Moreover, the QD solid can also show *p*-type behavior when it is treated by thiol in ambient conditions. [20, 21] Thus, the work function of the QD solid is customizable by performing different ligand exchange treatments. This feature makes the pure QD junction device architecture becoming possible, for instance, solar cells [22, 23] as well as photodetectors, [24] with promising device performances.

The mechanism for the ligand exchange process as well as the electronic coupling configurations can be easily understood from a model of two-neighboring QDs. Without the ligand exchange, two neighboring QDs are separated by the organic ligands and demonstrate weak electronic coupling for the energy transfer. After the ligand exchange, QDs exhibit strong electronic coupling, which is beneficial for energy transport. In reality, the situation is much more complicated since the electronic properties of the QD solid are

determined based on all neighboring QDs in the QD solid. Therefore, many factors can cause inhomogeneity of the energy state distribution, such as, the size distribution of the QDs, the homogeneity of the QD inter-dot distances, and the facet alignment of the QDs in local regions, [25] or even dimerizations. [26, 27] Early studies suggest that the carrier mobility is influenced by the energy state disorders from the size distributions. [28, 29] Moreover, the charge carrier dynamics are also influenced by the facet alignment for all QDs in the QD solid. [30, 31]. Besides the size distribution and the surface treatment, the stacking behavior of QDs can also dominate the energy state disorder (by inhomogeneous coupling). This is because QDs are not ideal spheres, [32] and as result, many factors can influence the stacking behavior during the self-organization process, such as the shape or the size of the QDs, the ratio of the ligand thickness to the QD radius, [33, 34] different deposition types, and different ligand exchange treatments. [31] Moreover, the stacking behavior of the ligand exchanged QDs is mainly driven by the maximizing the entropy of the ensemble considering the shape factor of the QDs. [35] However, the stacking phase transitions are generally rapid in real situations, for instance, the QDs suffer a fast self-organizations from a colloidal state to a close-packed state during a solid-state ligand exchange process. [36] In case of the QD ensemble, QDs shift from a long-range order to a non-ideally short-range order. The fast transition can also lead to a spatial disorder due to a non-ideal stacking configuration. As a result, the disorder stacked QDs are responsible for broadly distributed inter-dot distance and a disordered effective energy state distribution.

To statistically evaluate the distribution of the inter-dot distances of the QDs inside of the QD solids, the conventional characterization techniques, such as transmission electron microscopy (TEM) and scanning electron microscopy (SEM), are quite limited due to the resolution and the electron beam penetration depth. More importantly, the electronic properties of the QD solids are more correlated to their inner structure (such as the inter-dot distance of the neighboring QDs and the distance distribution) rather than their surface topography. However, cross-sectional characterizations are normally influenced by the sampling treatment with inevitable damages. These challenges bring difficulties to associate the electronic properties of the QD solid with their inner structure. As mentioned above, different surface treatments and different depositions can all influence the stacking configuration of the final QD solid. Therefore, based on conventional methods, it is a tough challenge to elucidate the real mechanisms and correlated them with the inner structure.

Early studies introduced small-angle X-ray scattering (SAXS) to evaluate the stacking behavior of QD superlattice structures. For instance, Kagan *et al.* investigated the electronic energy transfer in CdSe QD array with SAXS to obtain the inter-dot dis-

tance. [37, 38] Bian *et al.* used SAXS to study the structural stability of PbS QD superlattices. However, in SAXS, the transmitted intensity is measured, thus, a thick film, proving a sufficient imprint length ($> 1 \mu\text{m}$), is necessary for a good signal. Therefore, in most thin-film ($\sim 300\text{nm}$) based fabrications, SAXS is not a preferable measurement technique.

Grazing-incidence X-ray scattering (GIXS) provides a non-destructive method that can statistically and reliably probe the inner structure of the QD solid, from the Angström scale to sub-micrometer scale, due to a long footprint and a large scattering volume (X-ray-sample interaction region). Specifically, the crystal lattice or facet orientation of QDs can be analyzed by grazing incidence wide-angle X-ray scattering (GIWAXS). [31, 39] Moreover, the stacking configurations, inter-dot distances and QD aggregates can be studied by grazing-incidence small-angle X-ray scattering (GISAXS). [8, 40] Additionally, the main features of well-ordered QD arrays, known as the QD superlattices, also can be investigated by the GISAXS technique. [12, 41–43] Notably, most strongly-coupled QD solids demonstrate much less superlattice features due to their inevitable spatial disorder. Their inter-dot distance and the distance distribution (spatial disorder) are still observed in the GISAXS measurement. In fact, nowadays, GISAXS becomes an effective tool to evaluate the inner structure of QD solids. For instance, Carey *et al.* used GISAXS to probe the inter-dot distance of the QDs in the QD solids. [44] After that, the GISAXS measurement has been frequently used to evaluate the inter-dot distance of neighboring QDs of the QD solid, in which different surface treatments of the QDs [10, 45–48] and different depositions of the QDs [49] are involved in the discussions. However, the realistic connections between the inner structure of the QD solid and the electronic properties cannot simply be represented by the inter-dot distance. [25] The spatial disorder of the QDs can result in the inhomogeneity of the couplings and thus broaden the energy state distribution of the QD solid, which has been rarely mentioned in most GISAXS data analysis of strongly-coupled QD solids.

Moreover, as mentioned above, in GISAXS measurement, Choi *et al.* found different inner structure configurations of the QD solids made by different depositions were found by GISAXS measurement. His work compared the inter-dot distance of the neighboring QDs and the electronic properties of the spin-coated and spray-deposited QD solids. The results provide two indications: One is that even if the same surface treatment of the QD is applied, the structural configuration of the QD solid can be still influenced by different deposition processes. Another indication is that different stacking configurations of the QDs can lead to different electronic properties. Practical fabrications prefer to use up-scalable deposition techniques, such as spray-deposition and roll-to-roll printing. The as-obtained QD solids are supposed to have different inner structures compared with lab-

scale spin-coating. This can be attributed to different self-organization processes of the QDs under different deposition conditions and GIXS provides a practical way to compare and study these deposition induced structural differences. In this thesis, the main focus is on the stacking kinetics of QDs deposited *via* different methods including the lab-scale spin-coating, and large-scale slot-die printing and spray deposition.

To evaluate the quality of QD solids, besides the structural landscape studies based on GIXS techniques, the energy state distribution and the charge carrier dynamics in the QD solids are mainly studied by the ultrafast spectroscopy techniques. In this thesis, transient absorption spectroscopy (TAS) and time-resolved photoluminescence spectroscopy (TR-PL) are mainly used. The time-resolved spectral tracking focuses on the first exciton absorption peak and the emission peak of the QD solid for the TAS study and the TR-PL study, respectively. [29, 50, 51] After excitation, the charge carriers spontaneously shift from a higher energy level to the minimum level. The relaxation process is obtained from the time-resolved spectral peak tracking during their diffusion process. Consequently, the energy state disorder can be described by the energetic peak shift evolution. From the fabrication aspect, different depositions can lead to different structural configurations of the QDs, consequently with different energy state landscapes due to different self-organization processes. Very importantly, the charge carrier dynamics in “a pumped state” QD solid fundamentally reflects the charge carrier mobility of the QD solid in “a steady-state” (operational state). [29, 52]

Figure 1.1 overviews the main research methods in the thesis related projects. The fabrications involve the synthesis of the QDs, the QD surface modifications, the solid thin-film depositions, and the optoelectronic device assembly. By combining GIXS and ultrafast spectroscopies, the main research target is to investigate the connections between the structural landscape and the energetic landscape of the QD solids. Based on these connections, the material characters as well as the device performances are elucidated, which paves the way to develop more advanced devices.

In the Chapter 2, fundamental knowledge about QDs, including the quantum confinement effect, the self-organization process, the energy transport, the ligand exchange treatments, and the related device operation principles are introduced, respectively.

The main characterization methods are introduced in chapter 3. The basic principles for the GISAXS/ GIWAXS, and ultrafast spectroscopies, including TAS and TR-PL, are presented. The device characterization methods for PDs and PVs are also explained.

In the sample preparation chapter (Chapter 4), the basic route for the synthesis of high quality PbS QDs and corresponding spectral characterization methods are introduced. The ligand exchange processes including the solid-state ligand exchange and the solution-

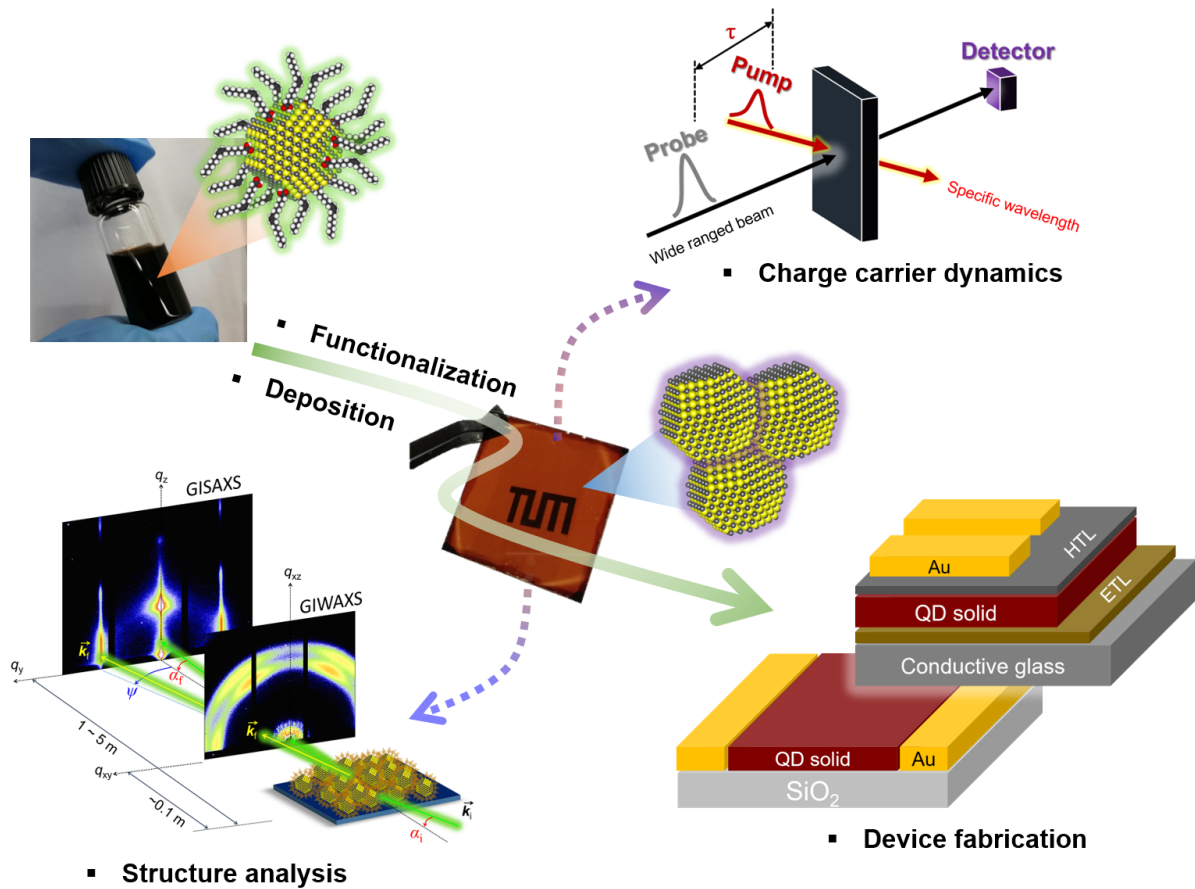


Figure 1.1: Overview are related research topics which including the QD material synthesis, surface modifications, thin-film deposition, and device fabrications. The structural disorder and the correlated energetic state disorder of the QD solids are investigated via GIXS and ultrafast spectroscopies.

phased ligand exchange are presented, respectively. In addition, the device architecture and the fabrication protocol of the PDs and PVs are also introduced.

The connections between the inner structure and the charge carrier dynamics are studied in Chapter 5. The solid-state QD ligand exchange induced phase transition is studied in both crystal lattice scale and superlattice scale via GIXS analysis. Moreover, the thermal annealing at different temperatures is used to treat the final strongly-coupled QD solids. The orientation distributions for both, nanocrystal facet and QD superlattice of the QD solids are studied. The charge carrier dynamics of the QD solids are studied by TAS. The connections between the overall energetically shifting rate and the lattice alignment are discussed.

Without doubt, the ideal deposition for solution-processed thin-films is based on roll-

to-roll printing. As mentioned above, the electronic properties of the as-obtained QD solids are influenced by specific depositions. In Chapter 6, the stacking kinetics of small-sized QDs is studied by in-situ GISAXS observations. The QDs are deposited by slot-die printing and, simultaneously, GISAXS continuously probes the inner structure of the as printed QD solid during the drying process. The superlattice formation and the distortion are studied by the line-cut evolution and GISAXS analysis. The mechanism of the self-organization process is well elucidated, which provides the origin of the structural disorder in the potential strongly-coupled QD solid.

In chapter 7, another large-scalable deposition, spray deposition, is also examined by using large-sized QDs towards photodetector applications in a long-wavelength spectral range. Notably, large-sized QDs, made by hot-injection method, principally exhibit a prominent shape feature and small ratios of ligand thickness over the QD radius. As a result, a different stacking behavior in the self-organization process is proposed. In the discussion, the inner structures of spin-coated QD solid and spray-deposited QD solids are compared, before and after the ligand exchange treatment, based on GIXS analysis. The energetic landscapes of the strongly-coupled QD solids are mainly investigated by TR-PL with spectral mapping. Associating with lithography based inner digital electrodes (IDEs) techniques, the related photodetectors based on spray-deposition and spin-coating are fabricated and compared.

Since the electronic properties of the QD solid are correlated with the inner structure, the collapse of the structure can be responsible for the degradation of the device performance. In Chapter 8, the solution-phase ligand exchanged QD ink is used in solar cell fabrication. The structural degradation of the devices is investigated by intermittent GIXS measurements when the devices are in operation mode and the device performances are tracked simultaneously. The measuring set-up is well designed which can rule out the influences from ambient conditions. Independent structural degradation, as well as spectral analysis for different QD functional layers before and after the degradation, are carried out to reveal the true origin of the device degradation.

The overall conclusion and outlook are given in Chapter 9.

2 Background

2.1 Quantum dot and quantum confinement effect

Different from most bulk semiconductor materials, QD material exhibits quantized energy levels and the tunable bandgap behavior as indicated by Figure 2.1. The smaller size of the QDs, the higher energy of the electron inside of the QDs will be. This is because the electron is squeezed in the tiny space of the QD with the size smaller than the electron Bohr-radius. The phenomenon is well explained as "quantum confinement effect" or "size effect", which can be elucidated mathematically by solving the Schrödinger equation with setting boundary conditions. These features make QDs desirable to obtain different bandgaps according to Brus equation [53] as follows,

$$E_g^{QD} = E_g^{bulk} + \frac{h^2}{8m_0r^2} \left(\frac{1}{m_e^*} + \frac{1}{m_h^*} \right) - \frac{1.8e^2}{4\pi\epsilon\epsilon_0r} \quad (2.1)$$

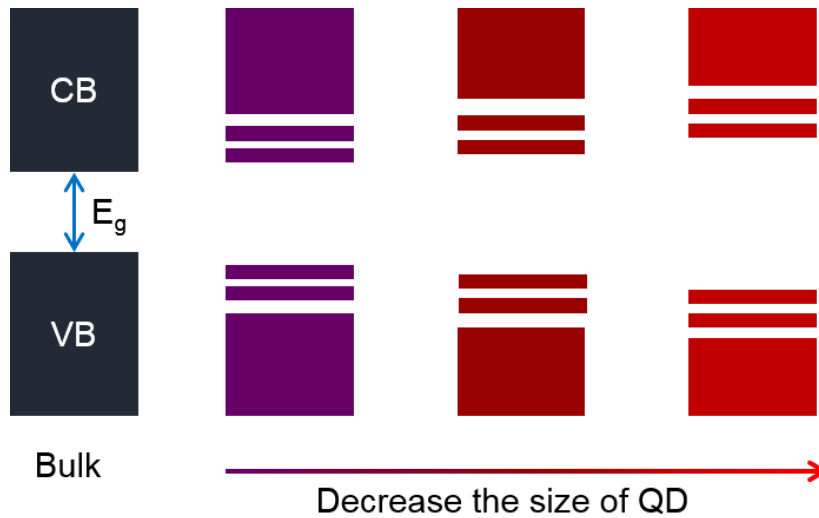


Figure 2.1: Increased bandgap of the QD with decreasing the size, in which a quantized energy states of the QD can be seen.

On the right side of the equation, the first term, E_g^{bulk} is the bandgap of the bulk material. The second term describes the quantum confinement effect in which r stands for the effective radius of the QD, h is the Planck constant and m_0m^* indicates the effective mass of electron or hole. The third term infers the Coulomb attraction between electron and hole which is influenced by the dielectric screen. Therefore, QD material establishes a practical method by which the bandgap of the QDs is tunable continuously by controlling the size or selecting different elemental component of the QDs.

Moreover, due to the charge carriers travel as waves inside of the QDs, the motion of the charge carrier is described by the probability density distribution. In the case of a simplified 1-D model, the probability density distribution of the charge carrier, at the first energy state, exhibits a sinusoidal-related distribution as seen in Figure 2.3 The

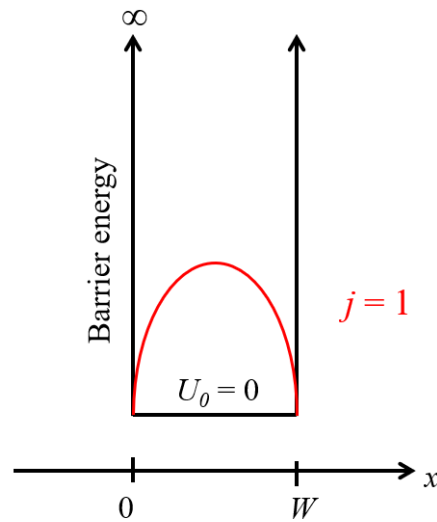


Figure 2.2: Probability density distribution of the charge carrier in their first energy state in an infinite potential quantum well.

distribution indicates that the charge carrier probability is not uniformly distributed inside of the QDs. The wavefunction of the charge carrier decreases to zero at the surface of an isolated QD in an infinite barrier condition. [54] When two QDs are close enough, the infinite barriers collapse leading to the penetration of the wavefunction as indicated by the 2.3 QDs with overlapped wavefunctions are defined as strongly-coupled QDs, and energy transfer among strongly-coupled QDs are possible. In strongly-coupled QD solid, the charge carriers are mostly confined in the finite barriers as seen in Schematic 2.3. The main features, such as bandgap, of the QDs, still remain with slight change consequently. Since the neighboring QDs are close enough (small edge-to-edge distance), the charge carrier

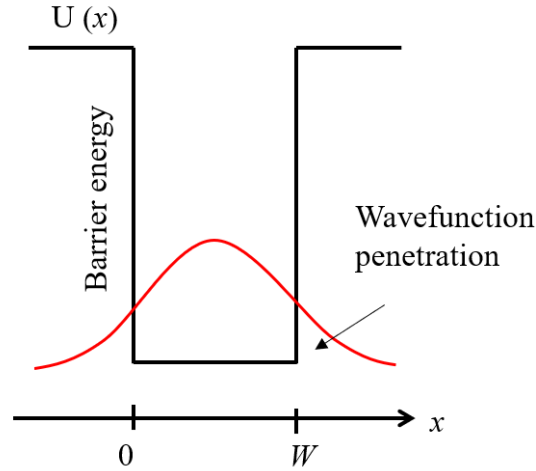


Figure 2.3: Probability density distribution of the charge carrier in their first energy state in a finite potential quantum well.

can potentially transfer energy from a QD site to another. The quantum confinement effect decreases in strongly-coupled QD solid compared with the situation when QDs are fully isolated with an infinite-high boundary condition. This has been used to explain the "exciton leakage behavior" in type-I core-shell structured QDs, [55], or the "energy transfer" in strongly-coupled QDs. [17, 56] Consequently, a steady-state spectral red-shift is usually observed in type-1 core-shell structured QDs or strongly coupled QD arrays, as a sign of the weakened infinite boundary condition of the QDs. [25] Notably, the energy transfer mechanism and corresponding efficiency are mainly influenced by the surface-to-surface distance of the neighboring QDs, even in a strongly-coupled mode, [56] which will be discussed in the following sections.

2.2 Colloidal quantum dots and self-organized superlattices

As mentioned in Chapter 1, PbS QDs are attractive for various optoelectronic applications due to the wide spectral response. Specifically, besides the application for a long-wavelength photodetector, the QDs are intensively investigated in the multi-exciton generation (MEG) PV devices [14] due to the potential to overstep the Shockley–Queisser limit of the conventional solar cells. [57] As the main metrics of the QD quality, the monodisperse QDs (with monodispersity $< 5\%$) are conventionally synthesized in a so-

lution condition. Under this condition, the as-produced QDs are wrapped by long-chain organic ligands, such as oleic acid (OA). Generally, QDs *via* this solution phased synthesis are also known as colloidal QDs with a typical structure as seen in Figure 2.4. These ligands are coordinated on the surface sites of QDs and make QDs soluble in various solvents and better solution-processable. The long-chain ligands can be replaced by other ligands with high kinetic energy, [19] by which the QDs can be functionalized for different purposes. The strong-coupled QD solids are realized based on QDs with short ligands, in which the ligand exchange process is mainly performed on the solid-state films or in the solvent. In the synthesis process, the size and the monodispersity of QDs can be pre-

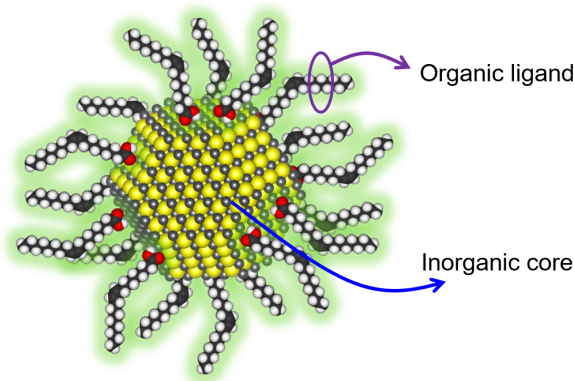


Figure 2.4: Schematic of inorganic PbS QD capped by organic oleic acid ligands

cisely controlled by the adjusting the ratio of the precursors, the amount of the ligands in combination with the reaction temperature. [58] For the storage of QDs, the ligands play an important role in maintaining the good solubility of QDs. This makes QDs quite compatible with a variety of large-scalable deposition facilities, such as roll-to-roll printing or spray deposition.

As a balance between the surface energy and intrinsic crystal growth behavior, QDs are not ideally spherical but demonstrate a polyhedron character in different sizes as seen in Figure 2.5. In the QD formation process, the initial crystal clusters are the results of the QD crystal nucleation with strong surface energy, which is also known as magic particles with the shape close to octahedron in size (diameter) of 1 - 3 nm. Small-sized QDs in a range of 3 - 4 nm exhibit the shapes of an octahedron with pure $\{111\}$ facets or truncated octahedron with both $\{100\}$ and $\{111\}$ facets on the surface. Large-sized QDs with size over 4 nm demonstrate a more cubic character with more distinguished $\{100\}$ facets, such as cuboctahedron or cubic. [32, 59, 60] Recent research indicates that the shape of PbS QDs can be well controlled by the cation-exchange synthesis method, [13] and shape distinguished octahedral PbS QDs with an effective size of around 3 nm can be

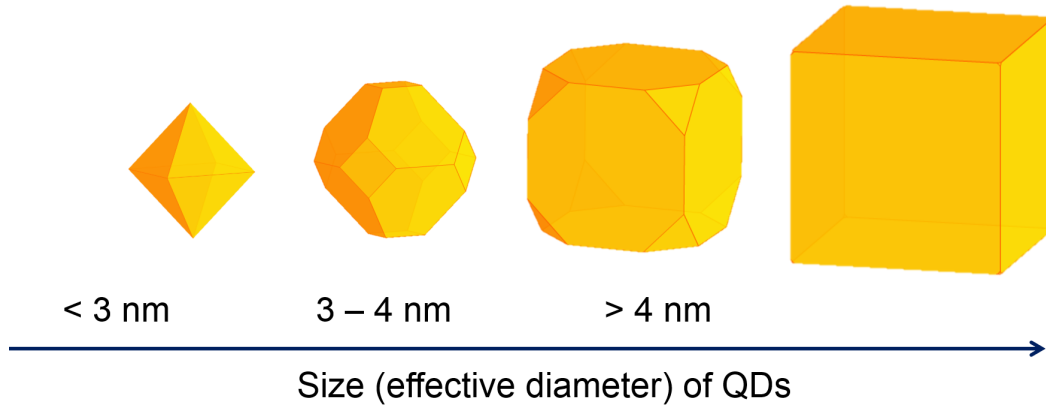


Figure 2.5: Shape sketches of PbS QD with different size

obtained. [12] In most optoelectronic applications, QDs are working in a strongly-coupled configuration. Regardless of different depositions, the strong-coupled configuration of the QDs is realized in a self-organization process, which is eventually driven by minimizing the total area to maximize the entropy of the ensemble. [35] However, the stacking behavior will inevitably be influenced by several factors, such as the size and the shape of QDs according to the Wigner-Seitz constructions, [31, 61, 62] the ratio of ligand thickness to QD radius, [33, 34, 63] and also specific deposition methods. [41, 42, 64]

The ligands of QDs are stretched when QDs are dispersed in a compatible solvent while the ligands may shrink at an incompatible solvent or in a solid-state. The ligands provide uniform spacers for QDs' isolating from each other, which results in the superlattice formation after the deposition. [65] Soft ligand wrapped small-sized QDs prefer to stack into a face-centered cubic (FCC) superlattice due to a high ratio of ligand thickness over the radius. When the ratio decreases, QDs turn to form a superlattice close to a body center cubic (BCC) configuration. [33, 41] According to the Wigner-Seitz close-packed construction, [42, 66] octahedral (or truncated octahedron) QDs prefer to stack in a BCC configuration towards a higher space-filling ratio than spheres' stacking can achieve. The self-organizations of QDs in most depositions are driven by maximizing the system entropy by reducing the total surface. Different stacking behaviors lead to different spatial disorders of the QD solids. Consequently, the energetic disorder in the QD solids is eventually influenced by the different inter-dot distances and distance distributions. [64] Notably, as a side-effect of the spatial disorder, a short-range order, such as aggregations or dimerizations of the QDs, will inevitably lead to inhomogeneity of the electronic coupling to the ensemble of the QD solid, [25–27] which hinders the overall charge carrier transport capability of the QD solid.

2.3 Energy transport in close packed QD solid

The energy transport between the neighboring QDs depends on the inter-dot distance (containing the information of the surface-to-surface (or edge-to-edge) distance of the QDs) as seen in Figure 2.6. When the edge-to-edge distance of the QDs is over 2 nm,

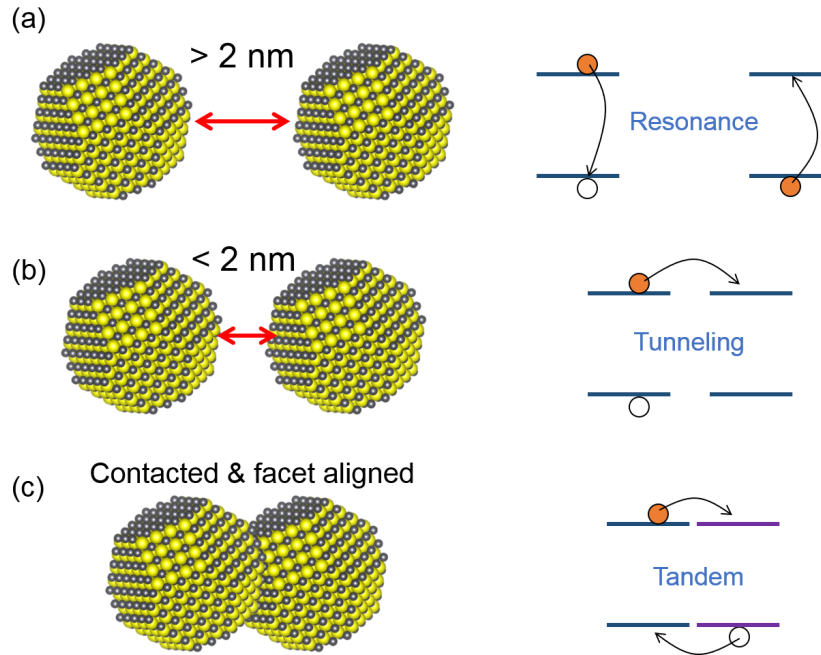


Figure 2.6: Schematic for inter-distance dependent energy transport between neighboring QDs

the QDs are in a weak electronic coupling configuration. In this configuration, the energy transport can be implemented by the dipole-dipole resonance effect also known as Förster resonance energy transfer (FRET). During the energy transfer process, the excited electron returns to the valence band of the QD, simultaneously, an electron in a neighboring QD has been excited to the conduction band via the resonance process. Notably, in the FRET process, the carriers are mostly excitons rather than charge carriers such as electrons or holes. Moreover, when the edge-to-edge distance in the range of 0 - 2 nm, the energy transfer can be performed via a tunneling process of the charge carriers. The small edge-to-edge distance provides a suitable condition that leads to a partial overlap of the wavefunction of the charge carriers. In this condition, the charge carrier can hop directly from the conduction band of one QD to the counterpart of a neighboring QD. The tunneling process dominates the energy transfer process in most strongly-coupled QD solids. [18] According to a recent study, a tandem effect has been hypothesized when two QDs touched each other with shared facets based on the second-order perturbation theory. [54] Consequently, to the two-QDs system or an ideally homogeneous QD ensem-

ble, a smaller inter-dot distance benefits the ET process. However, in reality, the energy transfer process is influenced by both spatial disorder and energetic disorder.

For energy transport in an energetic disordered QD solid, the spontaneous carrier hopping is considered as random when the disorder of energy is smaller than $k_B T$. The k_B stands for the Boltzmann constant and T is the temperature. Then the hopping rate is described by Equation 2.2 known as the Miller-Abrahams (M-A) equation.

$$k_{i \rightarrow j} = \begin{cases} k' \exp\left(-\frac{(\varepsilon_j - \varepsilon_i)/2}{k_B T}\right) & \varepsilon_j > \varepsilon_i \\ k' & \varepsilon_j < \varepsilon_i \end{cases} \quad (2.2)$$

in which $k_{i \rightarrow j}$ indicates the hopping rate from site i to site j , ε represents the bandgap of the QD site. The k' in the equation is presented by the Equation 2.3

$$k' = k_0 \exp(-\beta r_{ij}) \quad (2.3)$$

In the equation, r_{ij} denotes the edge-to-edge distance and β stands for the attenuation constant which is correlated with the dielectric constant of the ligand matrix. The energy disorder in the QD solid is not only introduced by the broad size distribution of the QDs, the hybrid QD mixtures but also related to a broadly distributed inter-dot distance. As a consequence, in strongly coupled QD solids, the energetic disorders are more originated from the non-uniform stacking behavior of the QDs inside, which usually caused by different fabrication process. On one hand, the closer-distanced QDs in a small region, such as in the aggregates or fused facet effect (dimerization), exhibit localized stronger electronic coupling behavior. These configurations relax the quantum confinement effect of the QDs locally and increase the overall energetic disorder to the whole QD solid by broadening the energy state distribution. [25–27] On the other hand, the non-uniform edge-to-edge distances, known as the spatial disorder, of the QDs suppress the overall carrier transport according to the hopping theory. In the following section, the energetic disorder is discussed in association with the spatial disorder of the QDs in the solid film.

2.4 The spatial disorder suppresses charge carrier transport

The spatial disorder in strongly-coupled QDs is mainly originated from the non-ideal treatments in the ligand exchange process and the QD stacking phase transitions during the depositions. In the case of a solid-state ligand exchange process, QDs transfer from a colloidal state superlattice configuration to a close-packed state QD solid during the ligand exchange treatment. The arrangement of QDs also transfers from a long-range

order to a short-range order with decreased inter-dot distances which inevitably leads to an inhomogeneous arrangement of the QDs. Since the energy transfer rate attenuates exponentially with the increase of the edge-to-edge distance of the neighboring QDs. [25], a broad inter-dot distance distribution in the final QD solid leads to inhomogeneous electronic coupling and broadens energy state distribution. Moreover, potential facet aligned QDs, such as aggregations, or dimerizations, can further relax the quantum confinement effect locally, which increases the energetic disorder and broadens the energy state distribution as mentioned in the last section. [25–27] As a result, the effective hopping rate is suppressed as indicated by Figure 2.7 according to the M-A equation 2.2. Notably, the suppression is much more complicated, since the charge carrier dynamics is related to not only the energy state distribution but also the overall electronic coupling of the QD solid. Moreover, the surface trap states also limit the efficient charge carrier transferring. In addition, the influence of the microscopic morphology also can not be ignored to the charge carrier transport.

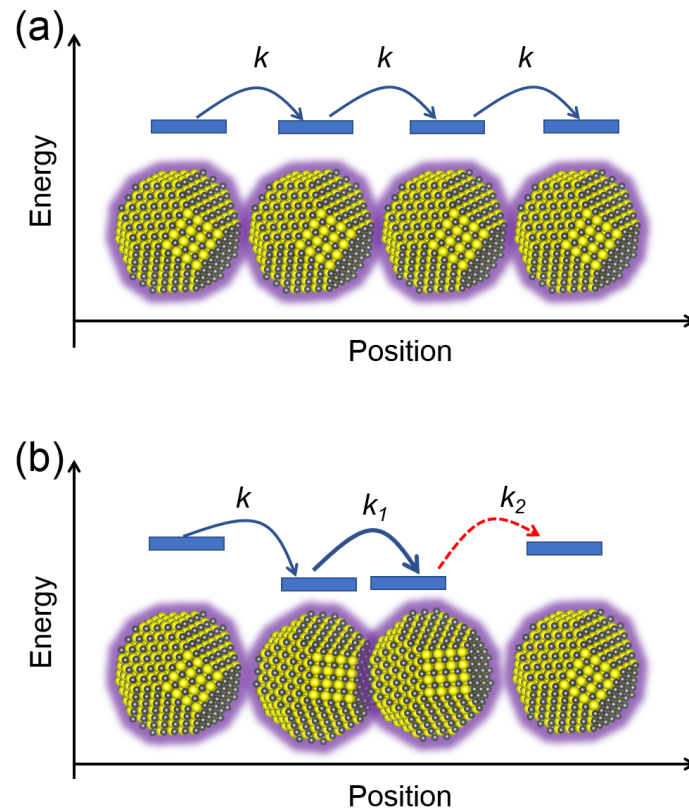


Figure 2.7: Schematics of the suppressed charge carrier transport by spatial disorder.

2.5 QD based photodetectors and photovoltaics

QD solids mostly act as the active layers in a variety of optoelectronic device architectures. Figure 2.8 illustrates the schematics for photodetectors, in which the left one (a) is the device architecture of photodiodes and the right one (b) is the photoconductor. The photodiode is also known as the vertical-structured photodetector, while the photoconductor is the lateral-structured photodetector. The photodiodes exhibit a sandwiched device ar-

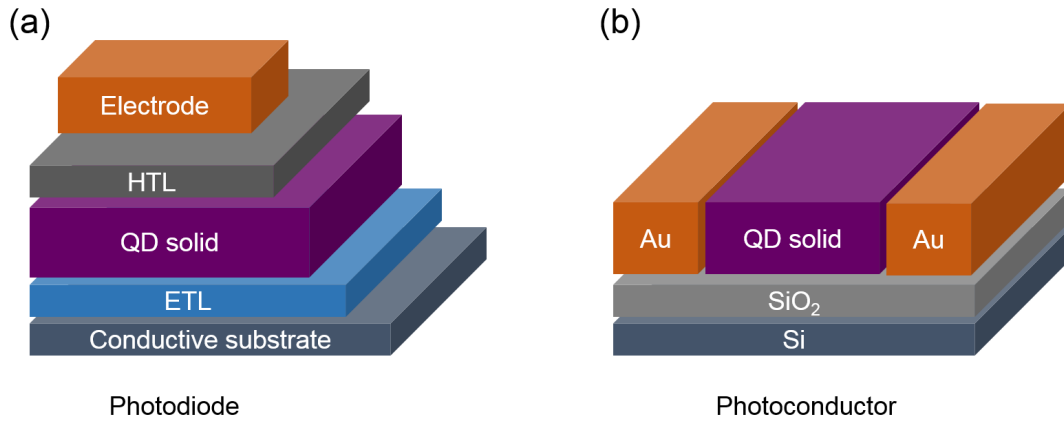


Figure 2.8: Schematics for photodetector device architectures: (a) photodiode, (b) photoconductor

chitecture in which the QD solid layer is fabricated between the electron transport layer (ETL) and the hole transport layer (HTL). The device configuration is in similarity with the device structures of LEDs and PVs. The working principle of the LEDs is known as charge injection and carrier recombination in the active layer. A reversed behavior of the charge carriers happens in PVs and photodiodes, in which charge carriers are generated in the active layer (exciton generation and dissociation) and then extracted by the ETL or HTL becoming current signals. Most photodiodes are designed for purposes of highly efficient photon response at a specific wavelength region. The PV solar cells can be regarded as refined photodiodes with excellent solar spectral utilization and high charge extraction efficiency. Notably, in this thesis, planar structured QD solar cell architecture is mainly involved, in which the quantum junction is regarded as the device working principle as seen in Figure 2.9(a). [22, 67, 68]

In this device architecture, the optimal thickness of the active layer (QD solid) for the solar cell is determined by the tradeoff between the utilization of the solar light and the charge carrier diffusion length (L_d). L_d is related to diffusion coefficient (D) and charge carrier lifetime (τ) as equation 2.4

$$L_d = \sqrt{D\tau} \quad (2.4)$$

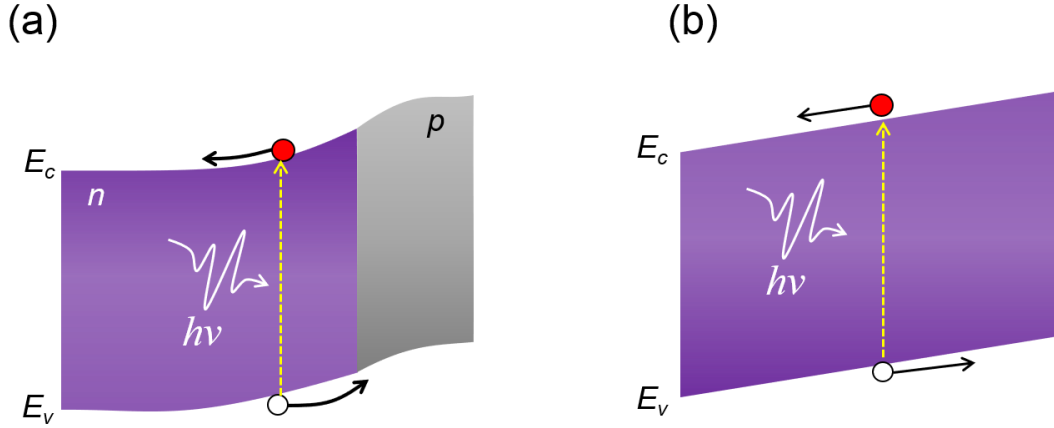


Figure 2.9: Energy band diagram and charge carrier extraction for QD solid in (a) photodiode and (b) photoconductor device architecture, respectively.

In the equation, D is determined by temperature (T) and charge carrier mobility (μ) according to the Einstein relation 2.5

$$D = \frac{kT\mu}{q} \quad (2.5)$$

in which the q is the elemental charge. The charge carrier lifetime is correlated with the trap state density. An ideal interface between hetero-junction layers can also improve the charge extraction by reducing the carrier recombination at the interface.

The device architecture for photoconductors is much more simplified than that for photodiodes. In a typical photoconductor device architecture, the QD solid is located between two lateral electrodes. The photon generated charge carriers drift in the QD solid under the applied bias acting as the photocurrent in the circuit. The photon current density J_{ph} is expressed by 2.6

$$J_{ph} = n_{ph}q\mu\varepsilon \quad (2.6)$$

in which n_{ph} denotes photon generated carrier concentration, ε stands for the applied electric field between the two electrodes in the device geometry. The current under the bias without light shining on the QD solid is known as the dark current which is contributed by the thermal-stimulated carriers from those shallow traps close to the band edges.

3 Characterization methods

The morphology and the size monodispersity of QDs are normally characterized by real-space imaging techniques, such as transmission electron microscopy (TEM), high resolution (HR) TEM, and HR-scanning electron microscope (SEM). These methods can obtain direct morphology information of the thin-film samples. The QD crystal lattice information can be directly seen by HR-TEM and thus, the crystal lattice distance can be estimated from the image for crystallinity analysis. The size distribution of colloidal state QDs (long-chain ligand capped) can be obtained from TEM or SEM measurements with corresponding data treatment, such as fast Fourier transformation. Notably, some specific software for TEM and SEM, such as imageJ or Nano-Measurement, and some specific data treatment functions such as converting morphology information of the sample in real space into reciprocal space towards an overall statistical analysis. Moreover, QD superlattice films formed from the self-organization processes can be also observed by TEM or SEM measurement, by which the inter-dot distance of neighboring QDs as a key factor from geometry can be directly distinguished. In addition, the surface morphology of QD solid films including roughness, pin-holes, and aggregate information, of QD functional solids rely on SEM or atomic force microscopy (AFM) for the characterization. However, these tools mainly focus on the surface of the samples. The inner structure of thin-films is usually probed with the cross-sectional SEM measurement, which inevitably brings in unexpected structure damages due to the necessary treatment process. The cross-sectional imaging data can partially reveal the inner structure of the thin-film, however the obtained information is limited for an overall evaluation of the total inner structure information of the samples. More importantly, in the QD solids, after ligand exchange treatment towards strongly-coupled QD solids, configuration, QDs are tightly packed without a clear contrast for SEM or TEM to distinguish their boundaries. Grazing-incidence X-ray scattering (GIXS) is a powerful tool to achieve the inner structure distribution for thin-film samples without destroying samples. GIXS measurements are nowadays widely used to study the inner structure of many solution-processed QD thin-film solids. The schematic of the measurement is seen in Figure 3.1

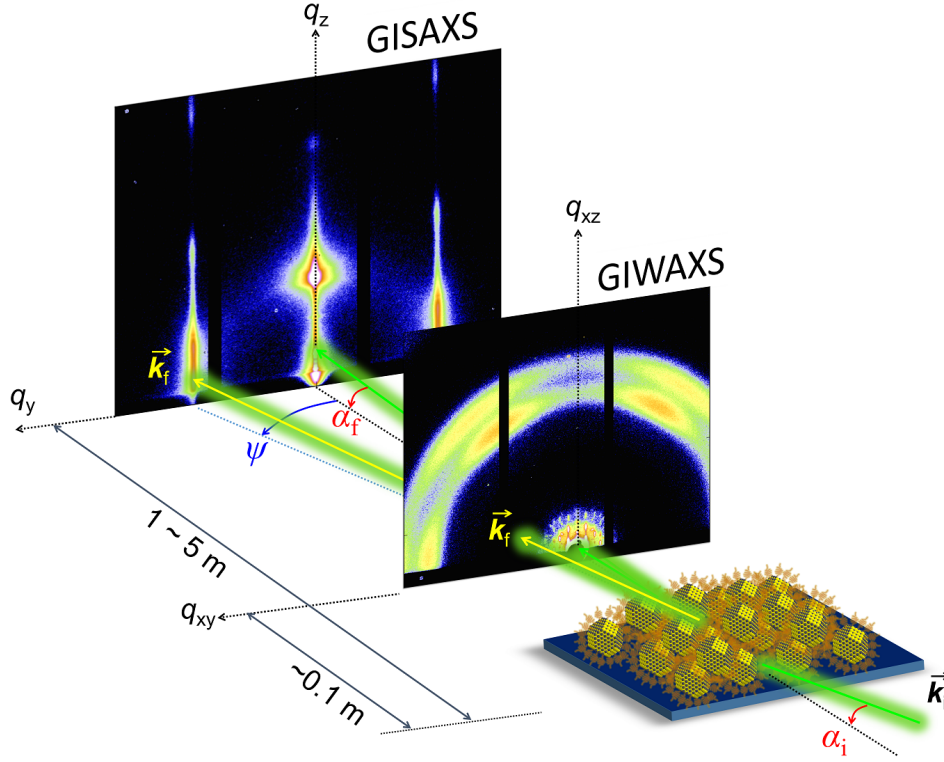


Figure 3.1: Schematic of grazing-incidence X-ray scattering (GIXS) measurements.

3.1 Grazing-incidence X-ray scattering

The schematic for GIXS measurements is shown in Figure 3.1. During the GIXS measurement, the X-ray beam, the sample, and the detector are set and aligned in a vertical plane. In the plane, the X-ray beam imprints on the center of the sample surface with momentum \vec{k}_i under a shallow incident angle α_i ($\alpha_i < 1^\circ$). In most inner structure studies of QD solids, α_i is normally selected higher than the critical angle α_c of the sample to obtain more structure information from the inner structure rather than that from the near sample surface. [40] With the configuration of a small incidence-angle, the X-ray beam penetrates the sample generating scattering signals in a long footprint. The measurement configuration endows a high signal-to-noise ratio of the inner structure information on the detector. The exit X-ray wave vector \vec{k}_f is described by the combination of the in-plane angle α_f and out of plane angle ψ . The Equation 3.1 is used to describes the scattering vector with the X-ray wavelength λ as follows

$$\vec{q} = \vec{k}_f - \vec{k}_i = \frac{2\pi}{\lambda} \begin{pmatrix} \cos\alpha_f \cos\psi - \cos\alpha_i \\ \cos\alpha_f \sin\psi \\ \sin\alpha_i + \sin\alpha_f \end{pmatrix} \quad (3.1)$$

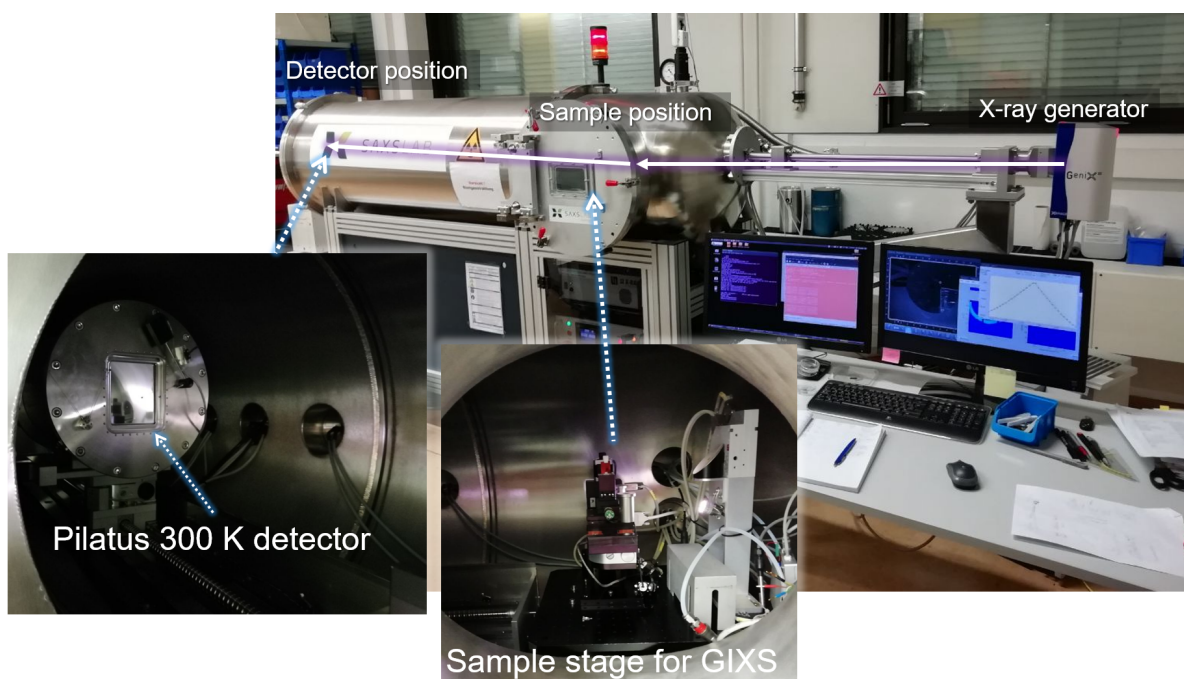


Figure 3.2: Photograph of the Ganesha SAXSLab 300XL with the sample stage component and the Pilatus 300K detector.

In the measurement, the resolution depends on several factors including the X-ray photon energy (or X-ray wavelength λ), the sample to detector distance (SDD), beam size, and the detector pixel size. The X-ray photon energy is ~ 8 keV for in house GIXS with in-house Ganesha 300XL SAXS-WAXS instrument and in a range of (12 ± 1) keV for most measurements at the synchrotron (*e.g.* P03 beamline, DESY, Hamburg). Under the same X-ray photon energy, a larger SDD enables the detector to capture scattering signals in a small scattering angle range, which reflects the information from larger structures. In a small SDD configuration, the detector can collect signals in a wide scattering angle, which can be used to analyzed small structures. The crystal lattice distance and the orientation information can be obtained when the SDD is extremely small. Figure 3.2 shows the Ganesha SAXSLab 300XL setup and specific components.

3.1.1 Grazing-incidence small-angle X-ray scattering

Grazing-incidence small-angle X-ray scattering (GISAXS) is performed with a long sample-detector distance (SDD) (> 1 m) configuration. In the case of a thin-film GISAXS data analysis, the inner structure sizes, inter-structure distances, and their distributions are estimated based on horizontal line-cuts and corresponding modeling. The modeling is es-

established based on the distorted wave Born approximation (DWBA) framework and the local monodisperse approximation (LMA) describes the structure size distribution. [69] Consequently, the effective lateral structure features are contained in the total internal reflection (TIR) plane propagating along with X-ray direction and having a "cross-line" with the detector. In the vertical plane, the "cross-line" position is known as the Yoneda peak position. The TIR angle respecting to the substrate horizon can be calculated based on scattering length density (SLD). The horizontal line cut derived scattering intensity can be expressed as Equation 3.2.

$$I(q) = P(q)S(q) \quad (3.2)$$

in which the $P(q)$ and $S(q)$ indicate the form factor and structure factor, respectively. The form factor is related to the shape of the domains and the structure factor stands for the inter-domain distances. According to the scattering intensity contribution, the inner structures are derived by reproducing the intensity- q curve based on setting models with different configurations.

The scattering signal contribution originates from the variation in the refractive index (Equation 3.3).

$$n = 1 - \delta(\lambda) + i\beta(\lambda) \quad (3.3)$$

in which $\delta(\lambda)$ and $\beta(\lambda)$ denote the dispersion and the absorption of wave-material interaction, respectively. Moreover, the real part of the refractive index is directly related to the electron density and a known δ infers to the critical angle (α_c) of the material, which is expressed by relation 3.4. [40, 69]

$$\alpha_c = \sqrt{2\delta} \quad (3.4)$$

In practical data analysis, the Yoneda peak position is obtained normally from the vertical line cut when the solid thin-film is homogeneous and has a good surface quality. The thin-film density or the porosity can be also estimated according to the SLD calculation. Notably, an inhomogeneous solid or rough surface condition can result in the peak feature being smeared out.

3.1.2 Grazing-incidence wide-angle X-ray scattering

Grazing-incidence wide-angle X-ray scattering (GIWAXS) is the GIXS measurement with a short SDD configuration towards probing the atomic-scale structure, specifically for the crystallinity, the lattice distances, and the lattice orientation distributions. In the case of those single-crystal-like materials, distinguished bright scattering spots can be found on their specific locations on the detector, which can be indexed by Miller indices to

investigate the lattice constants and the orientation information accordingly. In the case of a polycrystalline sample with a preferred lattice orientation, smeared Bragg peak signals behave as broadened intensity spots at specific locations. Thus, the distribution of the orientation can be estimated statistically, which is due to the large probed region on the sample in GIXS configuration. In the case of when the polycrystals are isotropically distributed, the Bragg peaks translate into specific rings (χ direction). Moreover, the detector place in GIWAXS mode is close to the scattering center known as the center of the Ewald sphere. Thus, the \vec{k}_f contains strong contributions from both the q_x and q_y directions. As a consequence, in GIWAXS, a reshaping correction is necessary, from which a reshaped 2D map is obtained (described by the q_r and q_z). The q_r^2 is

$$q_r^2 = q_x^2 + q_y^2 \quad (3.5)$$

After reshaping correction, the orientation distribution of the Bragg peaks can be directly extracted from the 2D patterns by a “tube-cut”. The normal direction to the substrate is defined as $\chi = 0^\circ$.

For the QD superlattice structure analysis, a similar method (diffraction) is used for GISAXS data analysis. The superlattice distortion can be also investigated by the scattering peaks distributions. Notably, in the long SDD configuration, the contribution in q_x direction to \vec{k}_f can be ignored.

3.2 Transient absorption spectroscopy

The transient absorption spectroscopy (TAS), also known as a pump-probe method, is nowadays frequently used to study the relaxation process of the charge carriers from an excited state to an equilibrium state. In the thesis related project, the TAS set-up mainly includes a *fs*-laser system, a collinear optical parametric amplifier (TOPAS), an optical module as illustrated in Figure 3.4, in which the optical paths for the probe pulse and pump pulse are labeled. The schematic of the measurement principle of TAS is described in Figure 3.3. In the measurement, the photon energy (E_{ph}) of the pump pulse is selected usually slightly higher than the bandgap of the QD solid to study to $1S_e$ - $1S_h$ state-related charge carrier dynamics. Much higher photon energy ($E_{ph} > 2 E_g$) is used to learn the hot carrier relaxation process in literature. [14]. The excitation process of the QD solid is described as the ground states bleaching (GSB) process, in which the input power density of the pump pulse is much higher than that of probe pulses. The probe pulses with a specific time interval are quasi-continuously imprinting, transmitting the sample, and carrying the information of charge carrier relaxation process probed by the detector. The

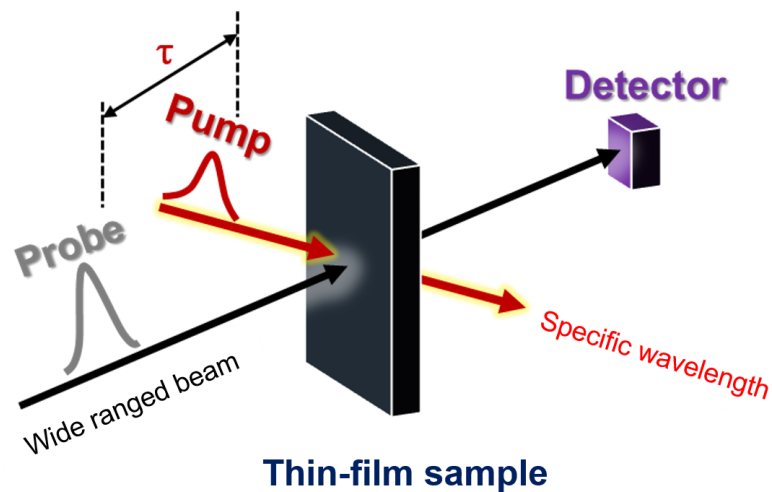


Figure 3.3: Schematic of transient absorption spectroscopy (TAS) measurement.

obtained signals contain both temporal and spectral information and they well describe the state of charge carriers.

Recently advances indicate that the TAS becomes a powerful tool to study the energetic disorder in QD solid. By tracking the bleaching peak from the spectra, the "funneling effect" which indicates charge carriers flowing to band-tails can be recognized and compared. Thus, the effective charge carrier transport capabilities of the QD solids are accordingly evaluated. Moreover, the time-resolved energetic shift behavior of the peak

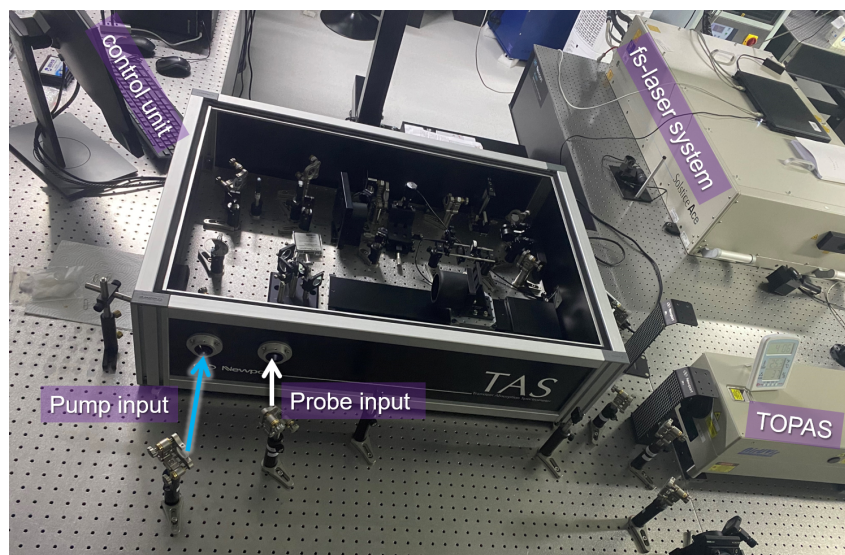


Figure 3.4: Photograph of the TAS setup with labeled main components.

position also reflects not only the energetic disorder but also the charge carrier mobility in the QD solid. Many recent works used TAS to evaluate the charge carrier mobility of the QD solids, such as Gilmore *et al.* derived the hopping prefactor of charge carriers from the temporal peak shifting. *Via* Kinetic Monte Carlo simulation, and the relative charge carrier mobility was calculated accordingly. [29, 52] Moreover, Proppe *et al.* developed TAS to monitor the charge transfer rates in a donor-acceptor mixed QD system and thus evaluate the charge carrier mobility of the QD solids. [70]

3.3 Time-resolved photoluminescence spectroscopy

Time-resolved photoluminescence (TR-PL) spectroscopy is another time-resolved tool to study charge carrier dynamics, especially for those charge carriers relaxation through radiative recombination. The used TR-PL setup is illustrated as seen in Figure 3.5 in which a laser source is used for excitation. A time-correlated single-photon counting (TCSPC) unit system is integrated and responsible for measuring the time-dependent photon numbers captured by the single-photon sensitive detector. used relying on high frequent excitation pulses. A photomultiplier is used to detect the emitted photons from the sample with a time delay information. The photon-counting events are repeated many times with different time delays, which statistically generates the lifetime information of the fluorescence. The final statistic photon-counting generates the final photon lifetime information. By carrying out the TCSPC measurement in a wavelength range (spectral mapping), TR-PL can not only obtain the charge carrier lifetime but also obtain the information of the charge carrier transfer by monitoring the shifting of the recombination center as a function of time delay. As seen in Figure 3.5, the excited carriers (such as excitons) recombine simultaneously with charge carrier transfer moving towards relatively lower states. By which the energetic disorder of the sample can be obtained. The schematic is shown in Figure 3.6.

3.4 Photodetector characterization

The lateral photodetectors (refer to photoconductors) are mainly evaluated by a probe station (SOFN 7-SCF06A/ B) system as illustrated in Figure 3.7. The fabricated photodetector device is settled on the probe station for the optoelectrical measurements. Source Meter (Keithley 4200) is used to apply and test the electrical signal on the photodetector device. The source meter provides a broad range of bias voltage from 0 to 200 V and tests a tiny current signal is possible until the level of $\sim fA$. Combined with the light source (Zolix, TLS2-T250-DZL) and monochromator, the setup is used for the characterizations

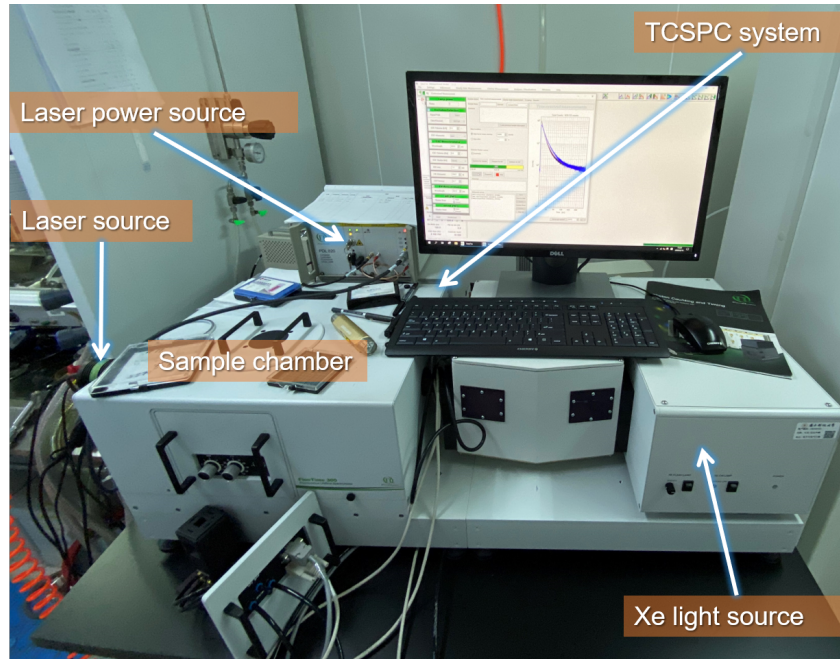


Figure 3.5: Photograph of TR-PL setup with labeled main components.

of IV relation and responsivity of the photodetectors. The responsivity of the device is referred to the ability to transfer light into the current signal and it is calculated *via* Equation 3.6:

$$R = \frac{I_{light} - I_{dark}}{P_{input}} \quad (3.6)$$

in which I_{light} stands for the light current, I_{dark} stands for the dark current and P_{input} refers to the input light power density. Combined with an oscilloscope and a light chopper, the on/off-response of the photodetector could be obtained. To calculate another important metric, detectivity, the noise analysis is performed by a lock-in amplifier SR 570 and SR 830. The detectivity D^* is calculated according to Equation 3.7 [71]

$$D^* = \frac{\sqrt{A}}{NEP} = R \sqrt{\frac{A \Delta f}{\bar{I}_n}} \quad (3.7)$$

which is based on the noise to signal ratio (SNR) of the detector with the active area ($A = 1 \text{ cm}^2$) under the input power (1W) at 1Hz electrical bandwidth (Δf). NEP refers to the noise equivalent power and the \bar{I}_n denotes the means noise current. A detailed case for the device performance analysis can be found in Chapter 7 or ref [72].

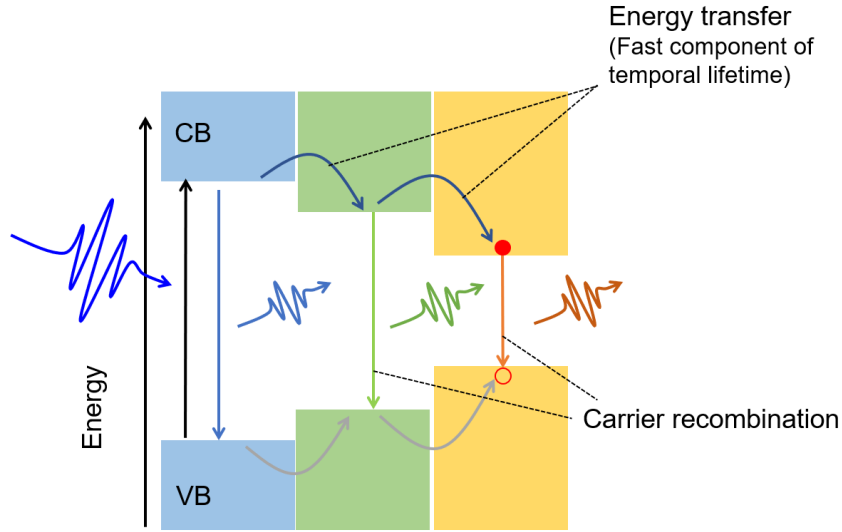


Figure 3.6: Main information obtained from the TR-PL integrated with the spectral mapping.

3.5 Photovoltaics characterization

The photovoltaic device performance is evaluated by a self-established system, as shown in Figure 3.8, which includes an AM 1.5 solar simulator, an *IV* analyzer by Keithley Source Meter (2611B), a reference solar cell for the calibration of the light power density illuminated on the tested device. A computer terminal for the characterization operation and data acquisition. In a practical measurement configuration, a shadow mask with 6 open pixels is employed to determine the working area of the solar cell. The solar cell is measured with a 4 wire system to get rid of the influences from the wires and connections. The diode behavior of the solar cell is measured by an *IV* scanning in a dark condition. When the solar simulator is providing a stabilized solar beam with a calibrated illumination power density (100 mW/cm^2), an *IV* curve is obtained by tracking the current signal as a function of applied voltage, as indicated in Figure 3.9.

The physics principle for the *IV* curve is the co-effect of the diode behavior and photon generated current respecting to the bias. According to the *IV* curve, as shown in Figure 3.9, the open-circuit voltage V_{oc} is defined as the maximum voltage and the short circuit current I_{sc} as the maximum current from the cell can be obtained as marked by the crosses respectively. The fill factor (FF) is defined as the ratio of the potential maximum power to the product of V_{oc} and I_{sc} , thus, FF can be expressed as Equation 3.8.

$$FF = \frac{P_{mp}}{V_{oc}I_{sc}} = \frac{V_{mp}I_{mp}}{V_{oc}I_{sc}} \quad (3.8)$$

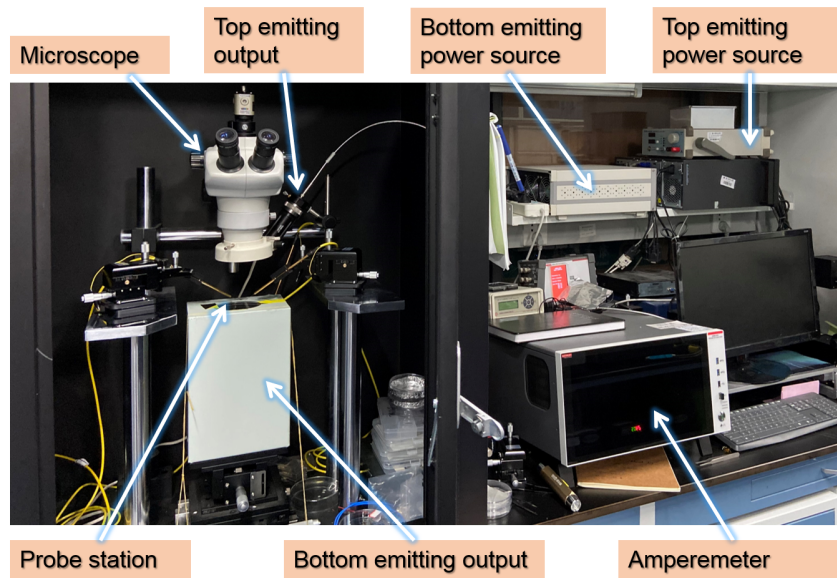


Figure 3.7: Photograph of the probe system with labeled main components for photodetector characterizations.

The I_{mp} and the V_{mp} are the coordinates of the maximum power point from the solar cell. Thus, the power conversion efficiency (PCE) is calculated according to Equation 3.9.

$$PCE = \frac{V_{oc} I_{sc} FF}{P_{in}} \quad (3.9)$$

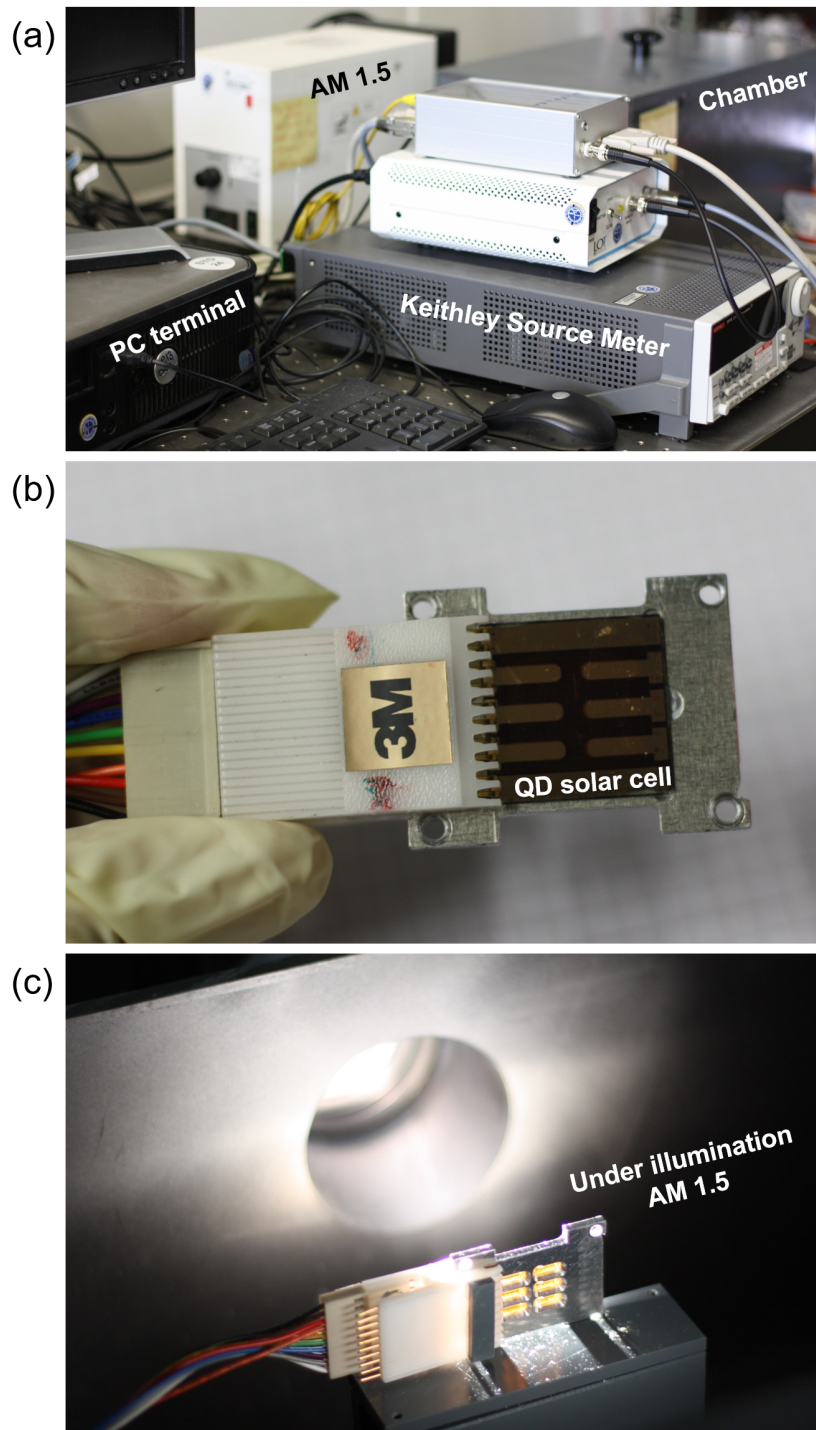


Figure 3.8: (a) Self-established system for the measurement of solar cell. As fabricated QD solar cell is (b) on a 4-wire clip board and (c) measured under AM 1.5 illumination.

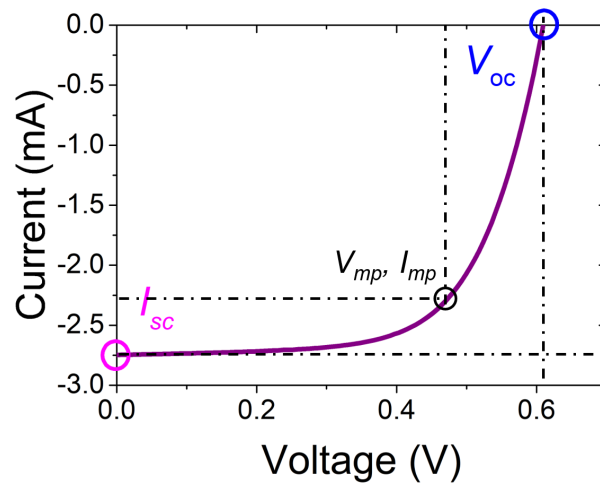


Figure 3.9: A typical I V curve of the solar cell under AM1.5 condition with circles labeling the I_{sc} and V_{oc} and the maximum power point $V_{mp}I_{mp}$.

4 Sample preparation

4.1 Synthesis of PbS QDs

According to the previous literature, the PbS QDs are synthesized by a typical "hot-injection method" with certain different modifications, in order to obtain the different-size QD particles. [73] The formation of the QDs is described by two stages, a nucleation stage, and a further growth stage. In the nucleation stage, the monomers rapidly aggregate to form highly energetic crystal seeds with a fast growth rate, which consuming many precursor monomers around in the solution. Further growth is relatively slower than the nucleation stage, which is mainly due to more energy required for the epitaxial growth on the size increased nanocrystals. Three main parameters, the ratio of precursors (Pb/S), the ligand (oleic acid)/Pb component ratio and the reaction temperature, dominate the fabrication process of the QDs, by which the size of the QDs are customized precisely.

The fabrication protocol is described as Figure 4.1, in which the lead precursor is initially prepared by adding PbO powders in the mixture of oleic acid and octadecene (ODE) in a three-neck-flask. The temperature is increased to around 100 °C and simultaneously a degassing process is performed by long time evacuation to remove the low boiling point solvent for the purification of the precursor. The sulfur precursor is prepared by completely mixing bis(trimethylsilyl)sulfide, [(TMS)₂S], in ODE. After the purification process by evacuation, inert gas, such as argon, is filled with the flask and keep a mild positive pressure. The temperature is increased to 150 °C to fully dissolve the PbO by fast magnetic stirring and obtain transparent Pb(OA)₂-ODE as the final Pb precursor. The (TMS)₂S mixture is then fully injected into the lead precursor to trigger the nucleation and fast growth of PbS QDs. The growth of QDs is monitored by measure the absorption of the sampling reaction solvent. When the absorption peak of the sampling QDs reaches the target wavelength, the growth of the QDs is terminated immediately by an ice-water bath. Once the precursors are prepared, the injection temperature and the growth time are adjusted to obtain different sizes of the QDs in specific requirements.

The initial purification of QDs is implemented by solvent extraction, by which the excess precursor and solvent can be removed via a phased separation process. The refined purification is realized by adding slight-poor solvents, such as methanol and butanol, into

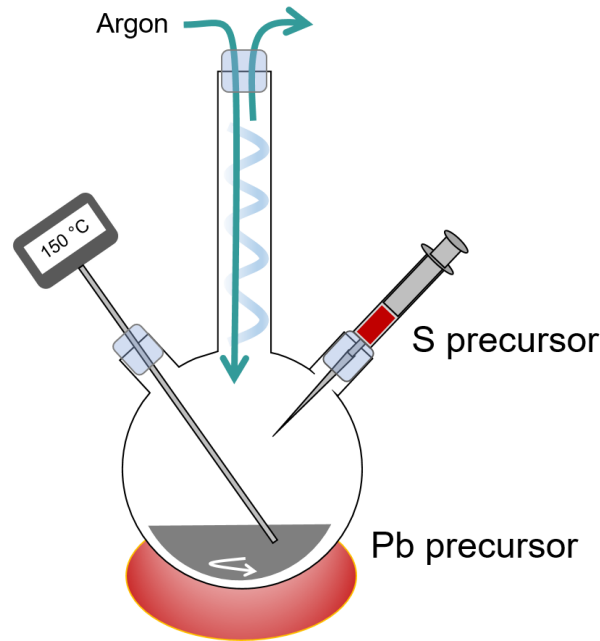


Figure 4.1: Sketch of the synthesis of PbS QDs with injection temperature of 150 °C

QDs' solution. The purified QD is precipitated via the high-speed centrifugation. The final QDs are weighted and re-dispersed in the desired solvent, such as octane, with a certain concentration for further uses.

Recent advances reveal some drawbacks of the "hot-injection" method, such as the rapid speed of the nucleation and the initial growth at a relatively high temperature. These make it hard to precisely control the size of the QDs, especially for those QDs fabricated with a small-sized requirement. Moreover, due to the high temperature, QDs prefer to exhibit a polyhedron feature in shape with more $\{100\}$ facets which lead to an unsatisfactory solubility in a solution-phase ligand exchange process towards QD ink. [48, 74] Zhang *et al.* has developed the synthesis of PbS QDs based on a cation exchange method which can produce high-quality PbS QDs at a quite low temperature. Under a kinetic growth condition, the as-fabricated QDs demonstrated a more octahedral shape feature with less $\{100\}$ facets comparing with the conventional higher temperature synthesized QDs. The GISAXS measurements on QD self-organized arrays reveal the differences in shape features of the QDs, the truncated octahedral QDs via high temperature, Figure 4.2(a), and octahedral QDs via low temperature, Figure 4.2(b). The method provides an essential way to improve the solubility of QD ink but also leads to better electronic coupling configuration and less surface trap states of the as-formed QD solid which are beneficial for the related device performances.

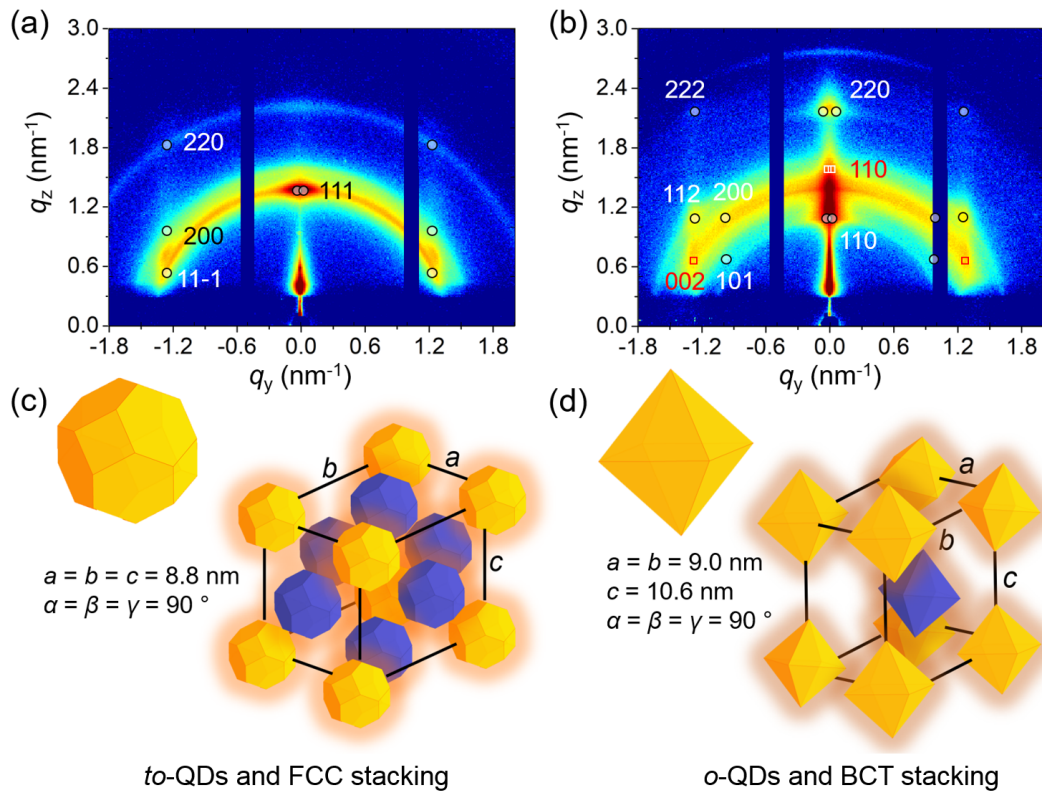


Figure 4.2: Effect of particle shape on the packing behavior in ≈ 3 nm PbS QD assemblies. 2D GISAXS data of the superlattice formed by a) truncated octahedral QDs and b) octahedral QDs. The white dots in the GISAXS data are calculated scattering peaks based on standard superlattice models. Diagrams for c) FCC and d) BCT superlattices with different lattice parameters. Reused with permission from ref [12]. Copyright (2020) John Wiley & Sons Inc.

4.2 Deposition of QDs via layer-by-layer method

The deposition of QDs via a layer-by-layer (LBL) method is described as an integrated post-ligand exchange method. One cycling deposition of the LBL is based on the deposition of oleic acid capped QDs on a selected substrate by lab-scaled spin-coating or upscalable spray deposition and printing as indicated in Figure 4.3. The as-deposited QD film was then soaked in a ligand-replacer solution condition, in which the oleic acid is substituted by desired short-chain ligands, such as (EDT (1,2-ethanedithiol), MA (malonic acid), or ions (such as I^-) [22, 47, 75]. The ligand exchanged process could take place automatically due to the different kinetic energies of the ligands coordinated to the surface of the QDs. After the exchange process, the residual components are removed by several times of the rinsing process. A single-layered QD solid is obtained and the QDs inside of the solid are close-packed and strongly electronic coupled as seen in as Figure 4.4.

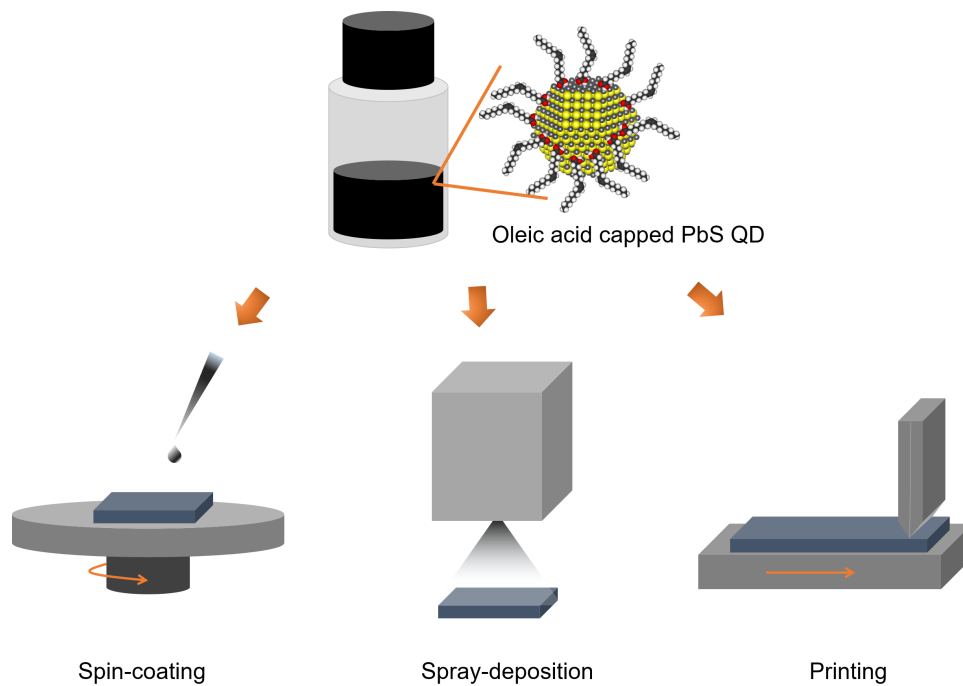


Figure 4.3: Oleic acid capped QDs are suitable for various depositions, including lab-scale spin-coating, or upscalable spray deposition and printing

The thickness can be precisely controlled by repeating the LBL cycling. The macroscopic structural defects, such as cracks, can be refilled and modified during the LBL.

4.3 QD ink preparation and deposition

The ink fabrication is known as the pre-ligand exchange process, or the solution-phase ligand exchanging, by which the long-chain oleic acid ligands can be substituted by lead halide (PbX_2 , $X = \text{I}$ or Br) or perovskite components in a solution-phase condition. The as-treated QDs are extracted by a phase separation process, as seen in Figure 4.5.

The treated QDs are transferred from an octane phase into a *N,N*-dimethylformamide (DMF) phase after mixing and phase separation. More octane is introduced to fully extract oleic acid from the DMF, which is repeated several times until a clear phase boundary can be seen in the QD solution. By removing the top octane layer, a 1:1 volume ratio of toluene is added to precipitate the QDs through a centrifugation process. QDs become pellets after vacuum drying treatment. The ink is fabricated by dissolving the QD pellets with a certain amount of DMF or *n*-butylamine (BTA). The concentration is normally controlled at a high value ($\sim 200\text{mg/mL}$) to obtain the desired thickness of the QD solid in a single-step deposition as shown in Figure 4.6. A higher thickness of the

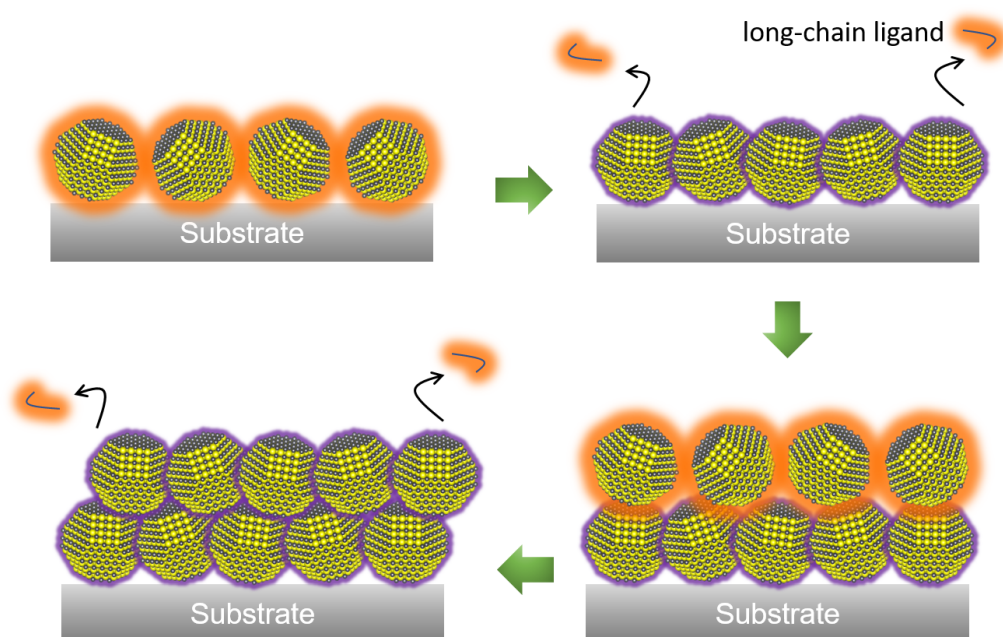


Figure 4.4: Solid-state ligand exchange treatment for a single layer of the LBL process.

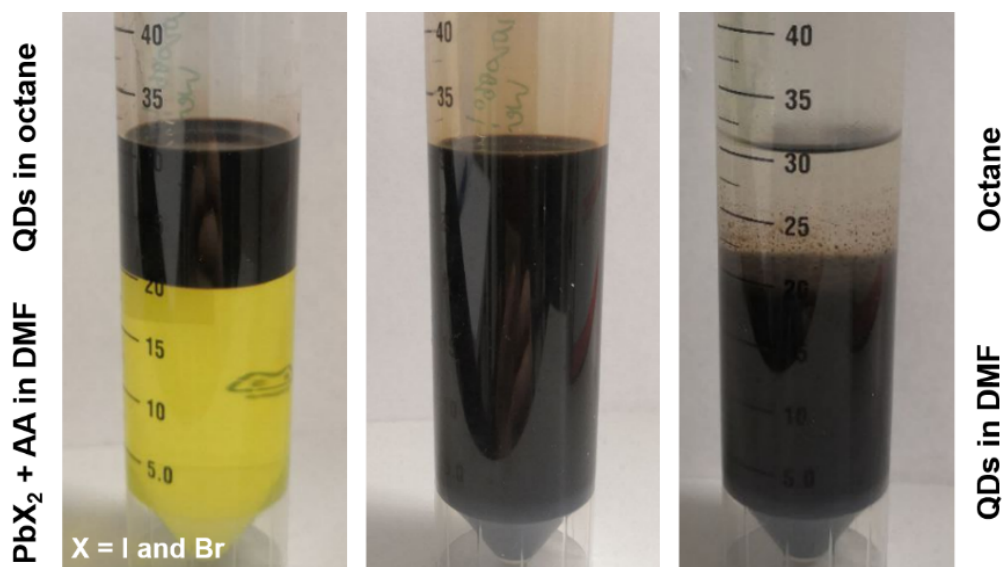


Figure 4.5: Photographs of solution-phase ligand exchanging process with a clear phase separation process.

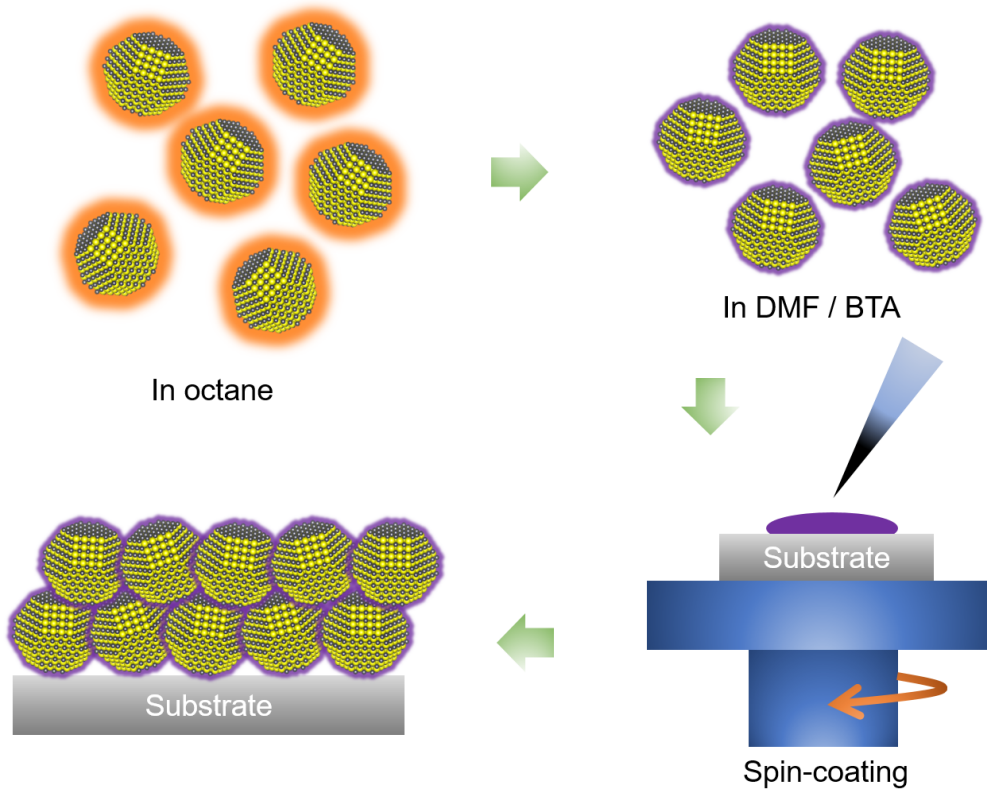


Figure 4.6: QD ink fabrication (solution-phase ligand exchange) and single-step deposition *via* spin-coating.

QD solid is obtained by increasing the ink concentration and slowing down the spin-speed of spin-coating. However, the surface morphology of the QD solid gets worse when the spin speed dropped.

4.4 Fabrication of photodetector device

The photodetector in the following mainly refers to the photoconductor which is known as the "lateral structured" device. Two main substrate types are investigated in the thesis related projects. The one is the laser patterned ITO glass with a gap width of $100 \mu\text{m}$ between two electrodes. The PD is accomplished by deposited QDs into the gap via spin-coating with a solid-state ligand exchange treatment afterward. The LBL strategy is used to increase the solid thickness. The substrates were mainly used in the project with PD devices based on a two-step ligand exchanged QD solids. [8]. The project found that the QDs, with a pre-ligand exchange treatment, exhibit improved electronic coupling

behavior in the final QD solid and thus improves the device performances. The other type of substrate is based on silicon wafers. A lithography method is used to obtain patterned gold electrodes, known as inter-digital electrodes (IDE), with a much narrower gap ($\sim 5 \mu\text{m}$) configuration comparing with laser-treated ITO electrodes. The substrates are mainly used in the project with PD device fabrications based on spray deposited QD solids. More detailed fabrication processes are illustrated in Chapter 7.

4.5 Fabrication of solar cell device

As the main component of the QD solar cell, two main strategies can be used for the active layer fabrication. One is a solid-state ligand exchange method. [22, 23] The surface morphology, as well as the thickness of the active layer, are controlled by the LBL procedure. The other strategy is based on QD ink and the single-step deposition. [19, 76] The solution-phase ligand exchange strategy provides various opportunities for the surface modifications of QD particles in the ink solution, such as the ion-based surface engineering, [77, 78] specifically the ion-based engineering on facets of the QDs, [48, 74], and the surface engineering by some perovskite components [46, 79].

Figure 8.5 describes a basic protocol of solar cell fabrication. A clean ITO glass is selected as the bottom electrode. In the thesis related projects, ZnO or SnO₂ ink is used for fabricating the ETL *via* spin-coating and annealing. The QD active layer is then deposited on the ETL *via* the LBL process or the ink deposition. For the HTL fabrication, the thiol (such as EDT) is used to perform solid-state ligand exchange of OA capped PbS QDs *via* the LBL process. Notably, besides the ligand exchange treatment, a conjugated polymer [80] or polymer-based bulk heterojunction layer [81] can be also used for efficient hole extraction in QD solar cell devices. In a conventional device architecture, the top gold electrode is deposited by thermal evaporation and the conventional solar cell fabrication process can be found in Chapter 8.

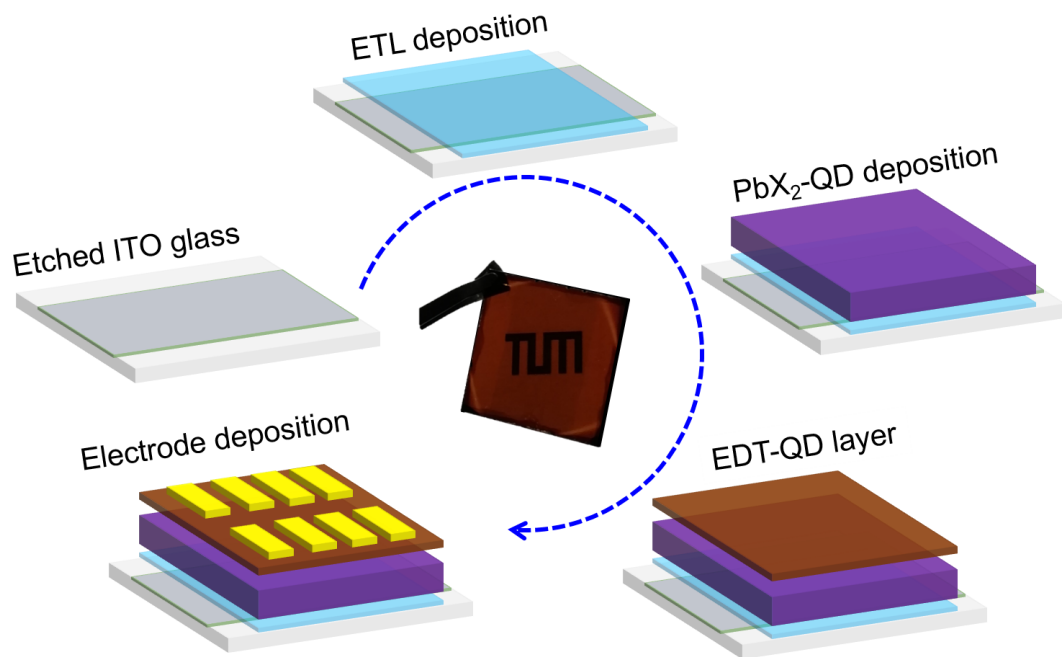


Figure 4.7: Fabrication protocol of the conventional planar-structured QD solar cell, including etching the ITO glass, ETL deposition, QD ink (PbX₂-QD) deposition, HTL deposition, and electrode deposition.

5 Structure and charge carrier dynamics in QD solids

Parts of this chapter were prepared in collaborations with Southern University of Science and Technology (SUSTech) and Shenzhen University, Shenzhen, China, and are published in: "Structure and Charge Carrier Dynamics in Colloidal PbS Quantum Dot Solids" (Chen, W.; *et al.*, J. Phys. Chem. Lett. 2019, 10, 9, 2058–2065, DOI: 10.1021/acs.jpcclett.9b00869). Reproduced with permission from ref [31] Copyright (2019) American Chemical Society.

5.1 Motivations and main discoveries

The ligand exchange process is a key step in the fabrication of quantum dot (QD) optoelectronic devices. In this work, on the basis of grazing incidence X-ray scattering techniques, it is found that the ligand exchange process with halide ions changes the PbS QD superlattice from face-centered-cubic to body-centered-cubic stacking, while the QD crystal lattice orientation also changes from preferentially "edge-up" to "corner-up". Thus, the QDs' shape is supposed to be the main factor for the alignment of QDs in close packed solids. Moreover, by tailoring the alignment of the close packed solids by thermal treatments, the inner charge carrier dynamics of the QD solids are further investigated by pump-probe transient absorption experiments. An overall better structure alignment optimizes the charge carrier hopping rate, as confirmed by the time dependence of the photon bleaching peak shift. The QD solid treated at 100 ° shows the best inner structure alignment with the best charge carrier hopping rate.

5.2 Introduction

In recent years, colloidal PbS quantum dots (QDs) have been intensively investigated in many areas such as photodetectors, [9, 24, 82] light-emitting diodes, [6, 83, 84] transistors [85–87] and photovoltaics, [23, 50, 77, 88–91] due to their outstanding semiconductor

properties, such as high absorption coefficients, tunable band-gap, and high charge carrier mobility. Moreover, QDs can be easily processed in solution and are compatible with scalable deposition techniques such as printing and spray-coating. [36,68,92] Normally, rather monodisperse colloidal QDs are synthesized via a “hot-ions injection” method at high temperatures. They are intrinsically stable against oxygen and moistures, so that they could be directly used in ambient conditions without the need of an inert gas atmosphere. [22] Therefore, in general, QD materials are promising candidates for solution-processed thin-film optoelectronic devices.

Colloidal QDs are made of an inner inorganic nanocrystal core and surrounded by an organic ligand layer shell, which acts as a surfactant to prevent QD aggregation. QD solids with a superlattice structure can form directly after deposition, because of the narrow size distribution of the QDs and due to a constant gap introduced by the ligand molecules. [42, 65, 93–95] However, a large average inter-dot distance would result in a weak electronic coupling of the QDs and thus frustrate the charge carrier transport in the QD solids. [18,96–98] Thus, QD solids with shorter inter-dot distance are preferred. They could be realized by the removal of the organic ligands. Such QD solids have a better electronic coupling and thereby enable the efficient tunneling of charge carriers between QDs. [29,54,70,99] However, in practical applications, ligand exchange processes with short-chain ligands or ions are performed to remove of the long-chain ligands and decrease the inter-dot distances. [22,23,50]

The colloidal state QD solid is obtained by a direct deposition of colloidal QDs on a substrate. Next, the ligand exchange process is induced by dropping an ionic (or short ligand) solvent on the colloidal state QD solid. [19] Afterwards, several iterations of a rinsing process are necessary to completely remove the long-chain ligands out of the QD layer. The desired film thickness can be tuned by repeating the cycles of deposition and ligand exchange several times. The resulting close packed QD solids can be directly used for example as the active layers in related QD devices.

In this work, the inner structure of the colloidal state QD solid made of long ligand capped colloidal QDs and that of close packed QD solids made of ligand exchanged QDs are investigated with grazing-incidence small-angle X-ray scattering (GISAXS) and grazing-incidence wide-angle X-ray scattering (GIWAXS). Thus, the ligand exchange induced differences in the QD crystal lattice and the QD superlattice are studied with grazing incidence X-ray scattering (GIXS) measurements in terms of distances and orientations of the lattices. [39,40,65,95,100] Therefore, the ligand exchange process and its effect on QD crystal orientation can be better understood, which is beneficial for further investigation of the rearrangement of QDs from a colloidal state QD solid to a close packed QD solid. [35] Additionally, thermal treatments with different temperatures are

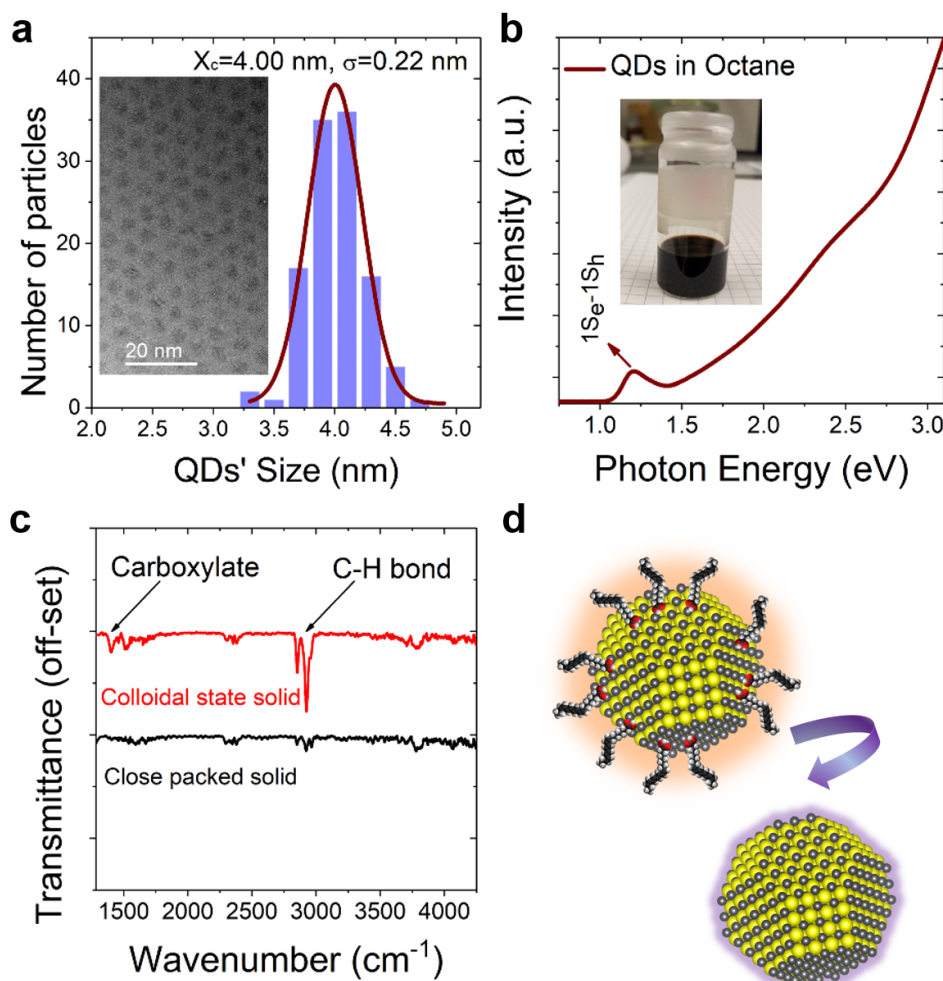


Figure 5.1: (a) Example of TEM image of as-synthesized colloidal PbS QDs with the statistical size distribution fitted by a Gaussian function. (b) Colloidal QDs' absorption spectrum with the 1Se-1Sh peak; inset: QDs in solution under daylight. (c) FTIR spectra of the colloidal state QD solid (red line) and ligand-exchanged close packed QD solid (black line), respectively. (d) Sketch of ligand exchange treatment. Reproduced with permission from ref [31] Copyright (2019) American Chemical Society.

introduced for close packed QD solids to tailor their inner structure and thereby their photophysics. With femtosecond pump-probe transient absorption (fs-TA) spectroscopy, the corresponding charge carrier dynamics of the QD solids are studied. Based on structure information obtained from GIXS, the energetic disorders and charge carrier hopping rate inside of the QD solids are discussed.

5.3 Experimental details

Synthesis of PbS QDs: The lead precursor was prepared by mixing 2.7 g PbO, 9 ml OA and 20 ml ODE in a 100 ml three-neck flask. The temperature of the mixture was slowly (step-by-step) increased to 100 °C. During the temperature increase, the atmosphere in the flask was changed to Ar atmosphere and vacuum status alternatively and eventually vacuum was applied for about 6 hours to completely remove oxygen and moisture. After the degassing process, the flask was refilled with Ar. The temperature of the solvent was increased to 150 °C. The sulfur precursor was prepared by completely dissolving 900 μL bis(trimethylsilyl)sulfide, $[(\text{TMS})_2\text{S}]$, in 10 ml ODE. When the temperature of the Pb precursor solvent reached 150 °C, the S precursor was immediately injected into the flask. The solution changed from yellowish to black immediately. The reaction was maintained for 30 s and was terminated by an ice-water bath. For the purification of PbS CQDs.

Purification of PbS CQDs: The as-prepared PbS CQDs were purified by adding a mixture of methanol and butanol, followed by high-speed centrifugation (2000 rpm). The extracted QDs were then dissolved in hexane and then precipitated twice with a mixture of ethanol and acetone. The nanoparticles were dried in a vacuum condition at room temperature and obtain the weight value by a balance. The particles were then finally re-dispersed in octane (50 mg/ml).

QD solid fabrication: The silicon wafers were cleaned by an acid solution (diluting H_2SO_4 (198 mL, 95 98%) in H_2O_2 (84 mL, 30%) and H_2O (54 mL)) at 80 °C. DI water was used to rinse them several times afterward. 40 μL CQDs with the concentration of 50 mg/mL were dropped on the cleaned silicon wafer and deposited by spin-coating with 2500 rpm for 10 s (and 2 s for the acceleration) to obtained colloidal state QD solids by repeating the spin-coating for 5 times. For close packed QD solids, the ligand-exchanged was carried out after one single layer colloidal QDs deposition as following: 200 μL TBAI-methanol (10 mg/ml TBAI in methanol) was applied completely covering films for approximately 30-45 s and spin-coated off afterward. 300 μL methanol was used to rinse the excess ligands twice. The whole depositing process was repeated for 5 times to obtain one close packed QD solid sample for characterization.

GIXS characterization: The GIXS measurements were carried out with an in-house Ganesha 300XL SAXS-WAXS instrument with an 8 keV Cu-K α X-ray source. The sample detector distances were 1056.2 mm for GISAXS and 106.2 mm for GIWAXS, respectively. The incident angle was set to 0.40°.

TA Measurement: The pump photon energy was 1.72 eV (corresponding wavelength= 720 nm) with pumping duration of 100 fs in spot size of 0.15 mm (diameter). The pump fluence power was set as 0.4 mW (2 $\mu\text{J}/\text{cm}^2$). The hot-excitons dynamics were probed

with the continuum in the range of 1.46 eV to 0.88 eV (850 nm to 1400 nm) with a resolution of 150 fs.

5.4 Solid-state ligand exchange induced phase transition

Lead chalcogenide (PbS) QDs are selected due to their weaker exciton binding energy as a result of their smaller effective electron mass and higher dielectric constant as compared with cadmium chalcogenide QDs. [101] Therefore, PbS QD solids show excellent performance for charge carrier transport and charge extraction, which appears suitable for photovoltaic applications. The colloidal PbS QDs used in this work are synthesized via the conventional hot-ions injection method as described in previous studies, [101,102] and further details of the synthesis can be found in the detailed experimental section. Figure 5.1 (a) shows a transmission electron microscopy (TEM) image indicating rather monodisperse QDs. According to the Gaussian fitting of the particle histogram, the average diameter of the QDs is 4.00 nm with a polydispersity of $\sigma = 0.22$ nm according to the standard deviation. In the absorption spectrum of the colloidal QDs (Figure 5.1(b)) the first absorption peak at 1.21 eV (peak wavelength=1024.6 nm) corresponds to the 1Se-1Sh exciton energy state, [14] which is in the best band-gap range for single p-n junction solar cells according to Shockley's theory. [57] Several layers of oleic acid (OA) capped colloidal QDs dissolved in octane (50 mg/mL) were spin-coated on silicon wafers to obtain the colloidal state QD solid. The ligand exchange processes were carried out by a layer-by-layer method in ambient conditions as described in the experimental section. The close packed QD solid was obtained with a thickness of about 300 nm. The successful ligand exchange has been confirmed by Fourier-transform infrared spectroscopy (FTIR). The corresponding spectra are given in Figure 5.1c. After ligand exchange, the peaks corresponding to the carboxylate bond (-COOH) and C-H bonds (-CH₂ and -CH₃) almost vanish, indicating the removal of the oleic acid ligands. [76]

Figure 5.4(a) displays the schematic setup of the GIXS measurements with a GISAXS and GIWAXS detector position as well as the applied azimuthal integration performed in the analysis of the 2D GIWAXS data. From this integration, a tube cut is obtained along the χ direction, which averages the intensity in a narrow q range. From the intensity distribution along χ , the lattice orientation distribution is determined from the corresponding q value the respective lattice distance. Figure 5.4b shows 2D GISAXS and 2D GIWAXS data of the colloidal state QD solid and the related TEM image. For the close packed QD solid this information is displayed in Figure 5.4c, respectively. From the GISAXS data analysis in terms of fitting the horizontal line cuts (with a sphere model) [103] a decreased inter-dot distance from 5.4 nm in colloidal state QD solid to 3.6

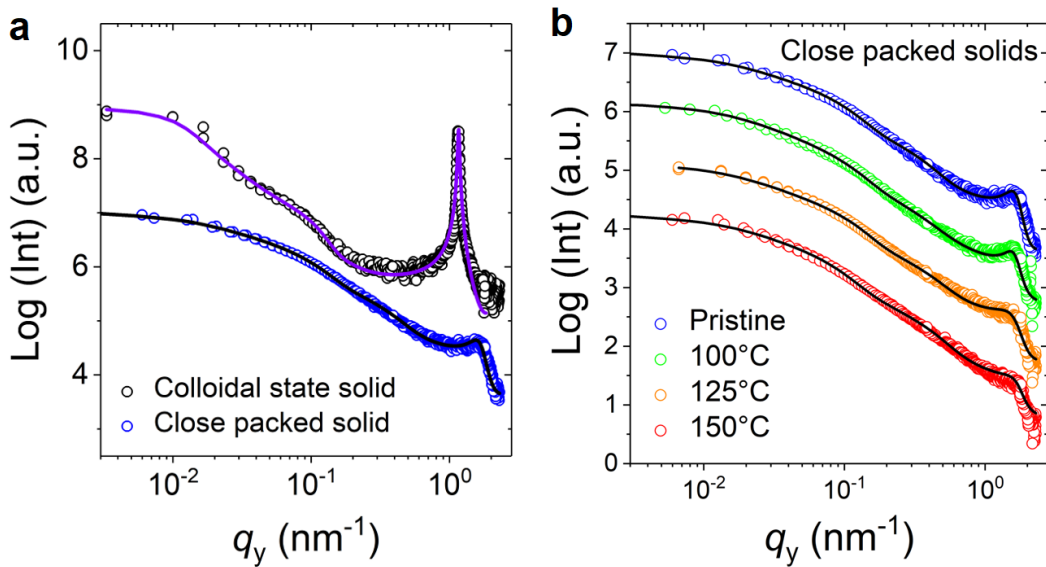


Figure 5.2: (a) Horizontal line cuts of the 2D GISAXS data fitted with a model approach based on spherical form factors for colloidal state QD solid (black) and ligand-exchanged solid-state QD solid (blue). (b) Horizontal line cuts of the 2D GISAXS data for thermally treated solids with different temperatures as indicated. The solid lines are fits to the data using the same model approach. The curves are shifted along the y axis for clarity of the presentation. Reproduced with permission from ref [31] Copyright (2019) American Chemical Society.

nm in close packed QD solid is extracted (see Figure 5.2a), which is also verified from the TEM images (Figure 5.4). Thus, the colloidal state QD solid shows an almost perfect particle alignment. After ligand exchange, the QD solid packed more densely as a result of the collapse of the organic structure. The decreased inter-dot distance significantly improves the electronic coupling properties in the QD array by expanding the exciton wave functions to the boundaries, [54, 104] which also well explains the absorption peak shifting from 1.21 eV (in solution) to 1.15 eV (in the close packed QD solid) as seen in Figure 5.3(a). Notably, in the close packed QD solid, the inter-dot distance is even smaller than the average QD size (4.0 nm) obtained from the statistical analysis of the TEM data. This deviation results from QDs being not standard spherical particles. As a trade-off between the crystal growth behavior and the high surface energy (by a high surface per volume ratio), a truncated octahedron model is more appropriate to describe the QD shape accurately, especially when discussing their crystal facet orientations in close packed solids. [32, 66, 105] Moreover, it is found the shape of QDs affects their stacking behavior during the ligand exchange process. In the following, the subscript “SL” is used

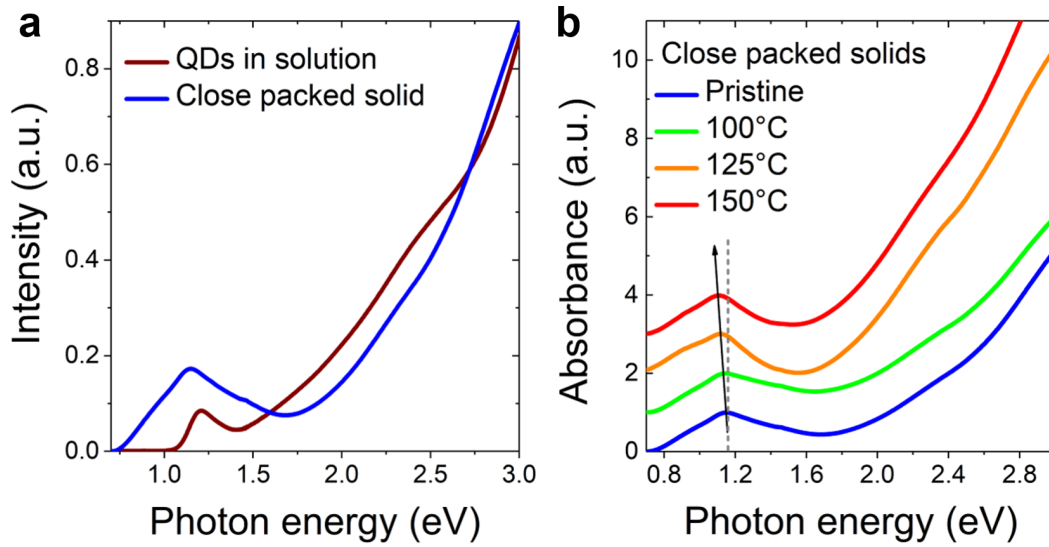


Figure 5.3: (a) Absorption spectra of colloidal QDs in solution (red) and of close packed QD solids (blue). (b) Absorbance of close packed QD solids treated at different temperatures as indicated. Curves are shifted along the y axis for clarity of the presentation and a change in the peak position is indicated by the solid arrow. Reproduced with permission from ref [31] Copyright (2019) American Chemical Society.

to mark the QD superlattice (SL) information in order to distinguish it from the actual QD crystal lattice denoted with the subscript “NC”.

5.5 Structure landscape of strongly-coupled QD solid

The face-centered cubic (FCC) superlattice structure of the colloidal state QD solid and the body-centered cubic (BCC) superlattice structure of the close packed QD solids are confirmed by the azimuthal integration of the GISAXS data in a χ range from -90° to 90° and the derived peak positions as shown in Figure 5.4(c). [33,34,95,106] Resulting tube cuts are shown in Figure 5.5 for the colloidal state QD solid displaying the $(111)_{SL}$ SL peak ($1.0 \text{ nm}^{-1} < q < 1.3 \text{ nm}^{-1}$) and $(200)_{SL}$ SL peak ($1.3 \text{ nm}^{-1} < q < 1.5 \text{ nm}^{-1}$). The $(111)_{SL}$ SL peak originates from a parallel alignment of the QD superlattice with respect to the substrate, which is in agreement with the TEM image in Figure 5.4(b). The plane orientation at $\chi = 67.0^\circ$ (Figure 5.9) results from a tetrahedron structure induced by particle stacking, which is also the basic unit in the FCC structure. The orientation at $\chi = 56.0^\circ$ seen in the tube cut of $(200)_{SL}$ SL peak matches the intersection angle of 54.7° between $(111)_{SL}$ and $(200)_{SL}$ SL peaks. Due to the presence of organic ligands

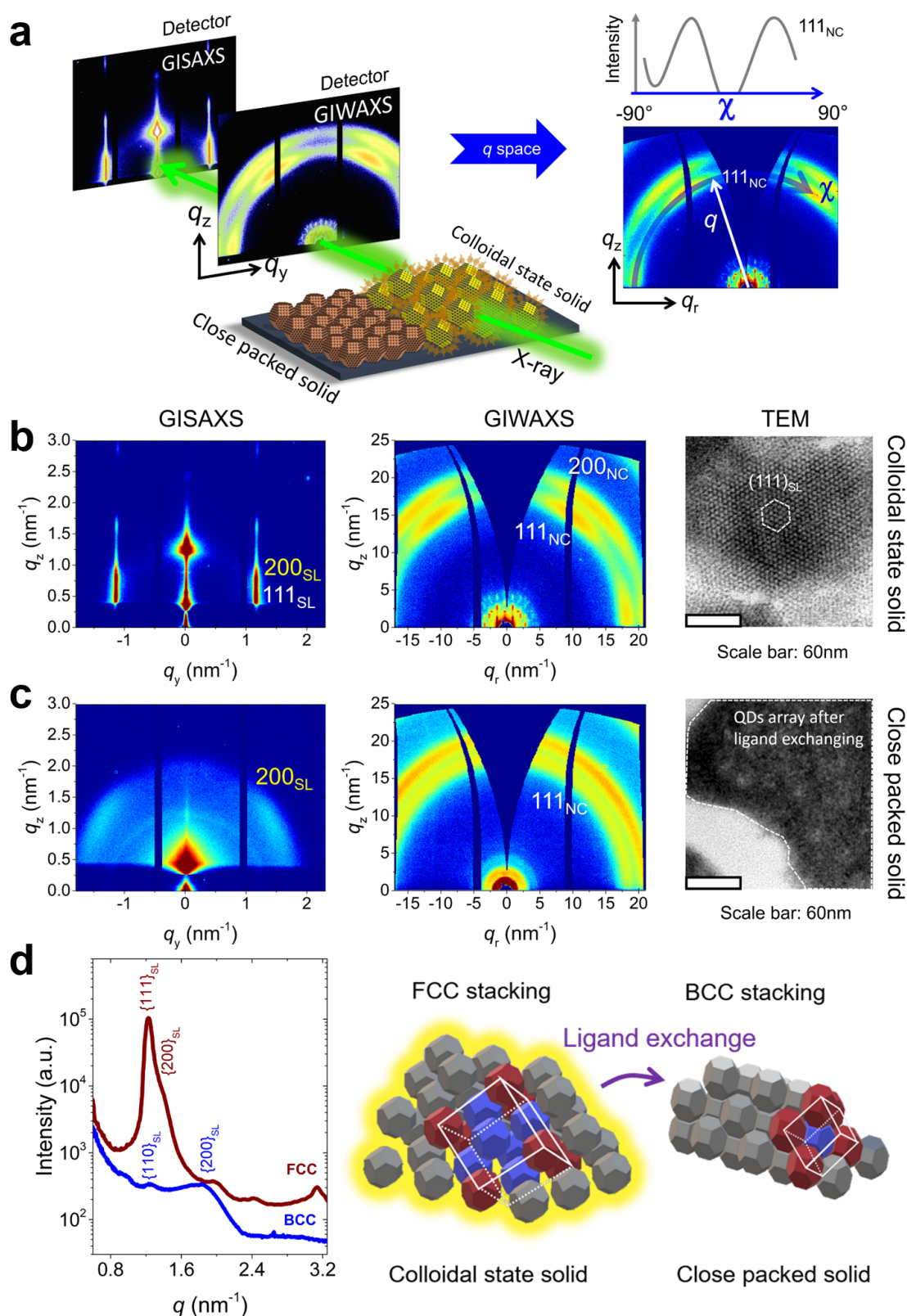


Figure 5.4: (a) Sketch of GIXS set-up and GIXS data analysis. GIXS data and TEM images for (b) colloidal state QD solids and (c) close packed QD solids after ligand exchange. (d) Azimuthal integrals of GISAXS data of QD arrays in colloidal state solid (red) and ligand exchanged close packed solids (blue). The face-centered cubic (FCC) stacking of colloidal state QD solid changes to a body-centered cubic (BCC) stacking of the close packed QD solid after ligand exchange. Reproduced with permission from ref [31] Copyright (2019) American Chemical Society.

and the selected QD concentration in the liquid used for deposition, QDs have been able to form a periodic structure during spin-coating, which exhibits distinct scattering peaks (Bragg peaks from the QD array) in the GISAXS measurements (Figure 5.4(b)). After the ligand exchange, in the close packed QD solid the $(200)_{SL}$ SL peak ($1.7 \text{ nm}^{-1} < q < 1.9 \text{ nm}^{-1}$) reveals a changed preferential orientation located at around $\chi = 48.0^\circ$ with a broad orientation distribution of $\sigma = 11.2^\circ$. Furthermore, a sharp peak at $\chi = 0$ with a small orientation distribution ($\sigma < 1^\circ$) also occurs in the tube cut of $(110)_{SL}$ SL peak ($1.2 \text{ nm}^{-1} < q < 1.3 \text{ nm}^{-1}$) as seen in Figure 5.7. It originates the truncation rod of (000) Bragg reflection from the direct beam rather than an indication of orientations. Therefore, the $(111)_{SL}$ plane of the BCC structure is also confirmed to be parallel to the substrate.

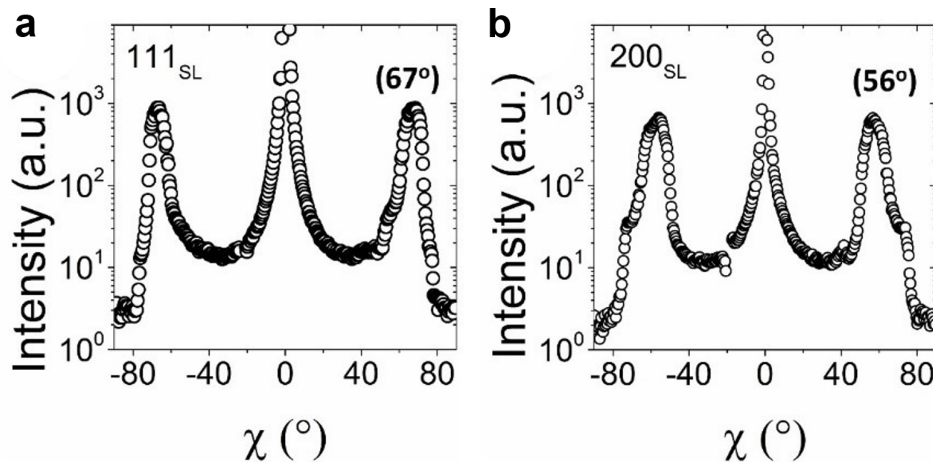


Figure 5.5: Tube cuts of the (a) $(111)_{SL}$ SL peak and (b) $(200)_{SL}$ SL peak in the GISAXS data of the colloidal state QD solid. Reproduced with permission from ref [31] Copyright (2019) American Chemical Society.

Figure 5.6 provides the orientation distributions of the QD lattices derived from tube cuts of the $(111)_{NC}$ and $(200)_{NC}$ Bragg peaks in the GIWAXS patterns. The $(111)_{NC}$ and $(200)_{NC}$ Bragg peaks and their orientations of the colloidal state QD solid are easily recognized from the GIWAXS patterns in Figure 5.6(b). The tube cuts suggest that the preferential orientation of $(111)_{NC}$ peak is at $\chi = 36.4^\circ$ shown in Figure 5.6(a), while the angle for the $(200)_{NC}$ Bragg peak is at $\chi = 40.8^\circ$ (Figure 5.6(b)). Therefore, the $(110)_{NC}$ plane is supposed to be “preferential parallel” to the substrate, marked as “edge-up” in Figure 5.6(c), by calculating their intersection plane angles in a cubic model. Moreover, after ligand exchange, QD crystal plane orientation distributions of the $(111)_{NC}$ and $(200)_{NC}$ planes are observed to broaden. The QD crystal lattice orientation distribution can be still extracted from the GIWAXS data using Gaussian fitting as seen in Figure

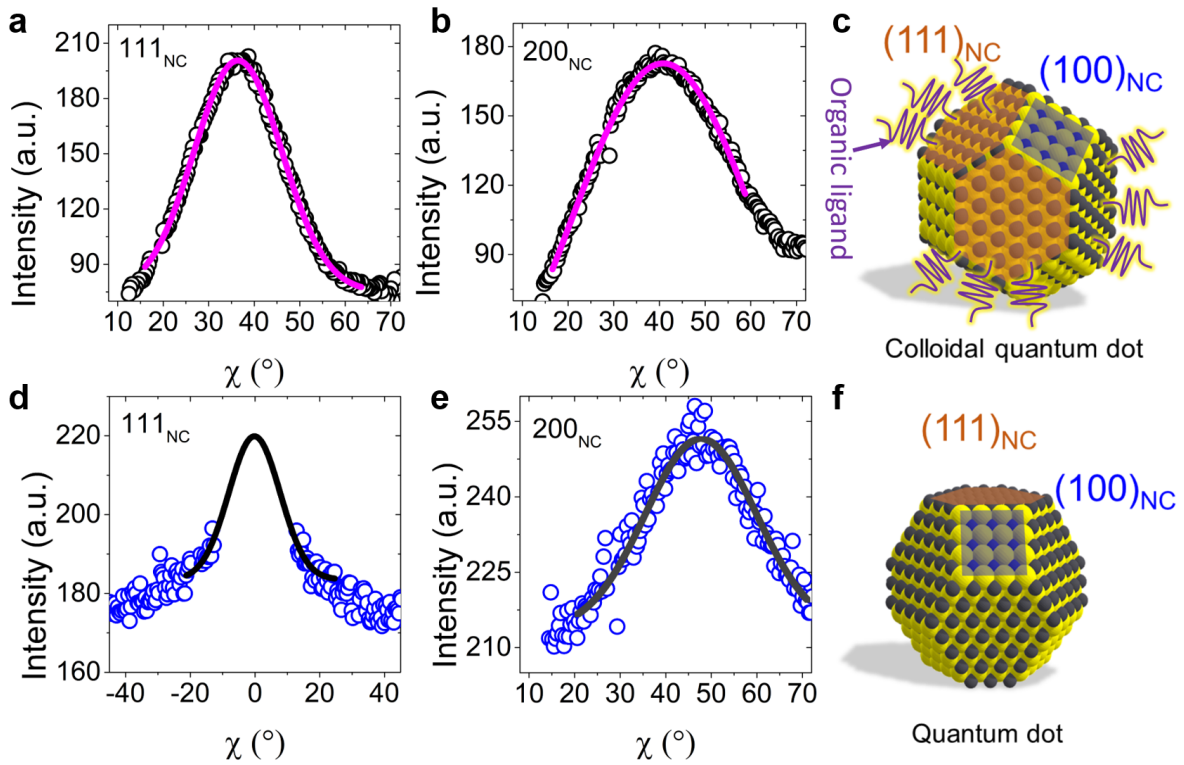


Figure 5.6: Preferential nanocrystal (NC) orientation of QDs in the (a-c). colloidal state QD solid and (d-f). ligand-exchanged close packed QD solid as derived from tube cuts of the 2D GIWAXS data at the (a), (d) $(111)_{NC}$ and (b), (e) $(200)_{NC}$ Bragg peak positions. Sketches of the corresponding orientations of (c) colloidal QD with ligands and (f) QD without ligands, respectively. Reproduced with permission from ref [31] Copyright (2019) American Chemical Society.

5.6(d) and Figure 5.6(e). The $(111)_{NC}$ Bragg peak moves to $\chi = 0$ ($\sigma = 7.9^\circ$) as seen in Figure 5.6(d), while the $(200)_{NC}$ peak moves to 47.5° ($\sigma = 10.7^\circ$) as seen in Figure 5.6(e). These rotations suggest that the $(111)_{NC}$ plane of the QD crystals is parallel to the substrate (marked as “corner-up”) in the close packed solid as shown in Figure 5.6(f).

When QDs are in a colloidal state solid, they are wrapped by soft ligands and have a certain inter-dot distance with their neighbors. According to the analysis above, they are considered as spherical particles in an approximation that form an FCC stacking in order to fully fill space. However, the real and non-spherical shape of the QDs needs to be considered when the soft ligands are removed. Since the size of the PbS QDs used in this work is smaller than 5 nm, the QDs are considered as truncated octahedrons rather than as spheres. The QD particles still reveal their tendency to completely fill space in order to minimize the total surface area and increase the system entropy. [35] Thus, the truncated

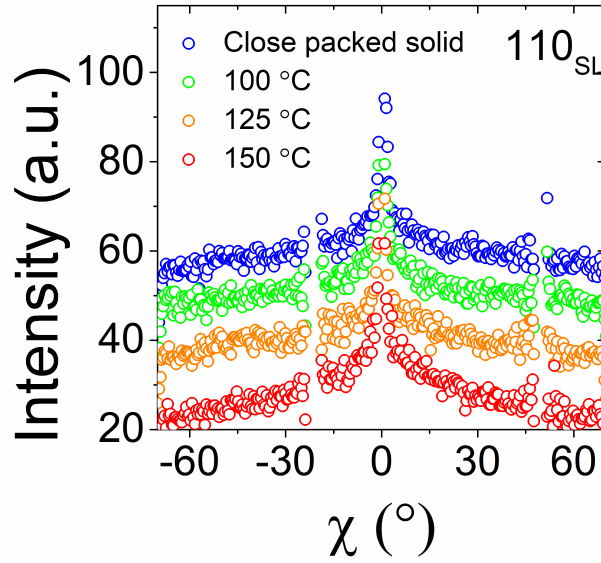


Figure 5.7: Tube cuts of the $(110)_{SL}$ SL peak in the GISAXS data of the close packed QD solid (after ligand exchange) for different temperatures as indicated. Reproduced with permission from ref [31] Copyright (2019) American Chemical Society.

octahedron QD particles finally form a “BCC-like” stacked solid meeting the Wigner-Seitz close packed construction with a minimized area for the surface energy and a maximized system’s entropy. [33–35, 106] The broad orientation distributions in our observations are induced by many factors, including a non-perfect QDs size distribution, the non-ideal ligand exchange conditions as well as the applied rinsing afterwards. Consequently, the lattice alignments of the QDs inside the close packed QD solid could be still modified during the fabrication processes and further treatments. Since GIXS provides statistical scattering information derived from a long footprint of the X-ray path on the sample, it can be assumed that the observed better defined QD crystal lattice and superlattice alignments (short-range order) induced by the shape of the QDs will be representative.

The effect of thermal treatment on the inner structures is further investigated by studying thermal-treated close packed QD solids at 100 °C, 125 °C and 150 °C (10 minutes at each temperature). The GIXS patterns of thermal-treated close packed QD solids are found in Figure 5.9. Figure 5.8(a) shows the inter-dot spacing values derived from line cut fittings. A treatment at 100 °C results in the largest distance between neighboring QDs (3.75 nm), which is even slightly larger than in the case of the pristine QD solid (3.60 nm). The inter-dot distance decreases to 3.50 nm (125 °C) and 3.30 nm (150 °C) when higher temperatures have been applied. The $(200)_{SL}$ SL peaks in the GISAXS data is also analyzed as shown in Figure 5.8(b) and Figure 5.8(c). The QD solids treated at 100 °C and 125 °C have a much better-aligned superlattice structure with a lower orientation

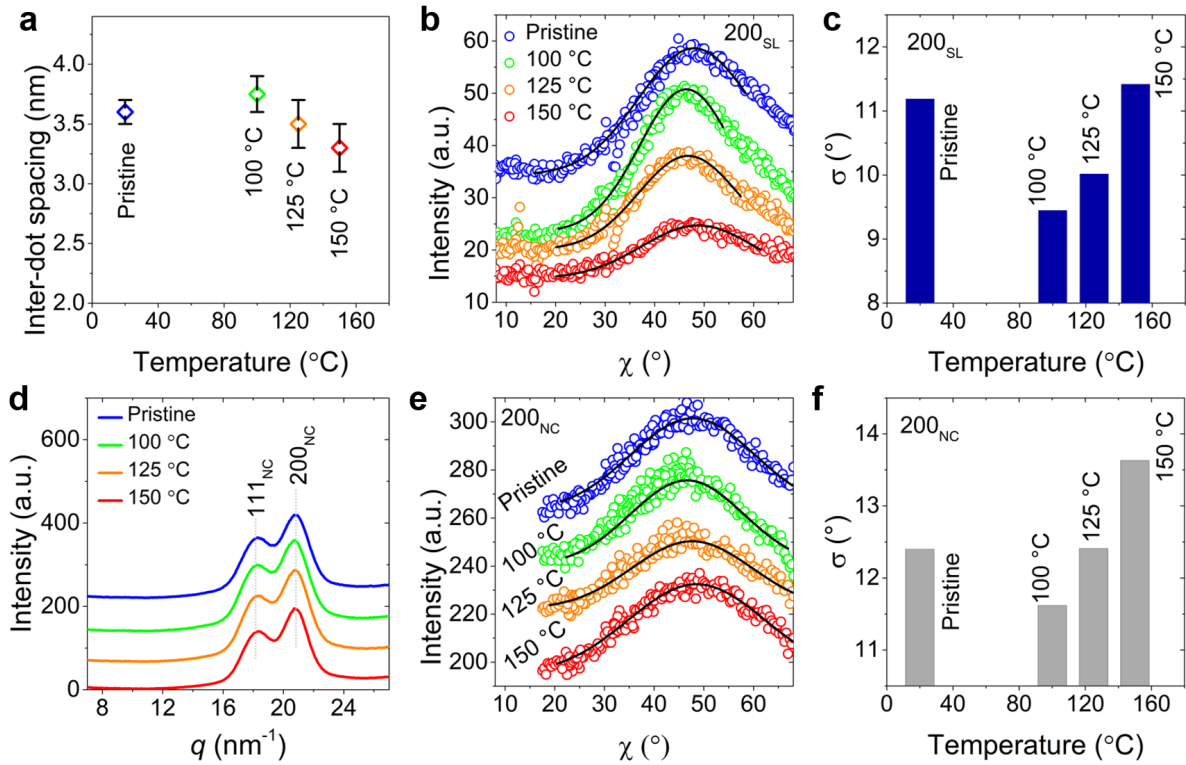


Figure 5.8: Close packed QD solids treated at different temperatures as indicated: (a) Inter-dot spacing values derived from line cut fittings. (b) Tube cuts of (200)_{SL} SL peaks (circles) fitted with Gaussian functions (solid lines). (c) Orientation distribution σ for the (200)_{SL} SL peaks as a function of temperature. (d) Azimuthal integrals from the 2D GIWAXS data for all QD solids. (e) Tube cuts of (200)_{NC} Bragg peaks (circles) fitted with Gaussian functions (solid lines). (f) The orientation distribution for (200)_{NC} Bragg peaks as a function of temperature. Reproduced with permission from ref [31] Copyright (2019) American Chemical Society.

distribution σ as derived from the Gaussian fitting as compared to the pristine QD solid and QD solid treated at 150 °C (Figure 5.8(c)). Figure 5.8(d) shows the azimuthal integral in q direction derived from the GIWAXS data, which indicates that the QD lattice in all close packed QD solids possesses a rather high crystallinity and excellent stability against thermal treatments since the peaks are not changing during the applied thermal treatments. The crystal plane orientation distributions of the (200)_{NC} Bragg peaks of the QDs in thermal-treated solids are analyzed by tube cuts as plotted in Figure 5.8(e) and Figure 5.8(f). The solids treated at 100 °C and 125 °C reveal a better orientation alignment in both, the QD crystal lattice and stacked QD superlattice. Thus, the orientations of crystal lattices are coherent with the orientations of their superlattices. From these observations, it is suggested that a temperature of 100 °C or 125 °C can provide proper thermal energy to increase the system entropy by releasing the stress from the

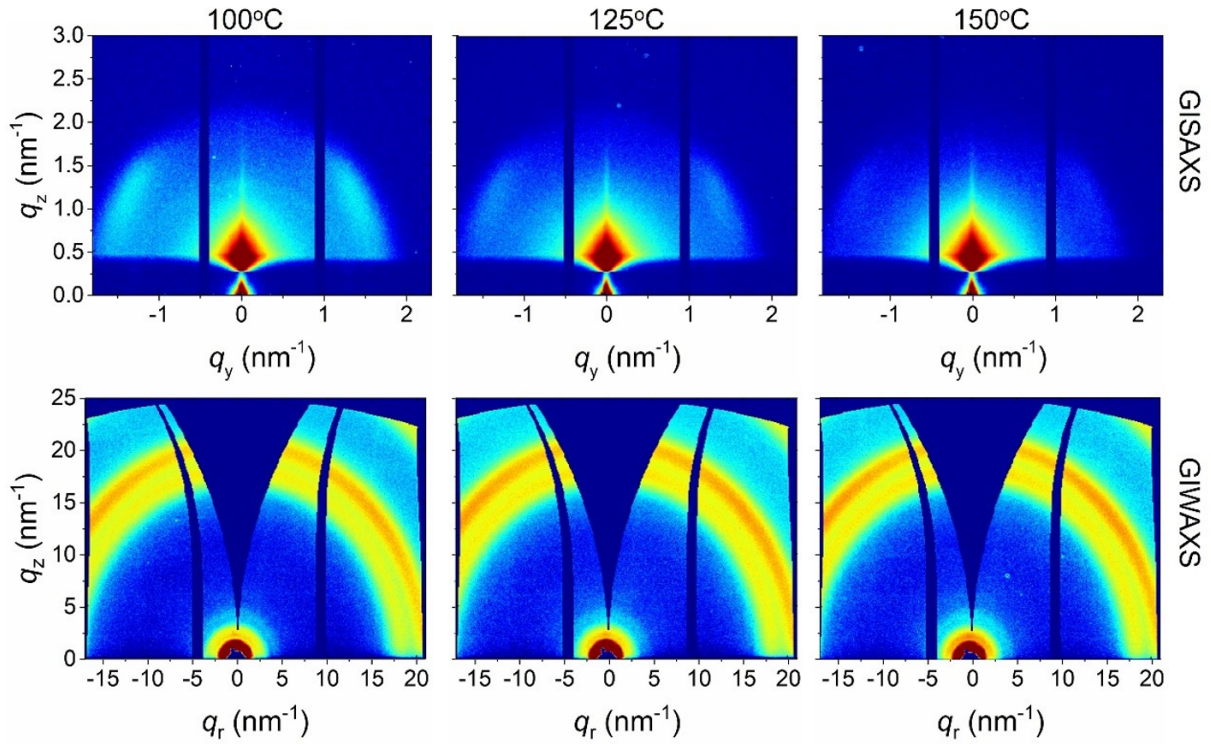


Figure 5.9: (top row) 2D GISAXS and (bottom row) 2D GIWAXS data of ligand exchanged close packed QD solids treated at (left) 100 °C, (middle) 125 °C and (right) 150 °C. Reproduced with permission from ref [31] Copyright (2019) American Chemical Society.

spin-coated films and the afterwards applied ligand exchange process. Therefore, the QD particles can adjust their lattice orientation to suit a better stacking alignment, in comparison to the pristine QD solid. However, when a higher temperature (150 °C) has been applied, the QD solid becomes denser than before. It is assumed that this densification is due to part of QDs having sufficient thermal energy for crystal fusion at facets.^{31, 48} This morphology transformation has been also inferred from both, the gradually fading scattering intensity of the $(200)_{SL}$ peaks in the GISAXS patterns (Figure 5.9), and the gradual weakening of the peak intensities in the line cuts (Figure 5.2(b)).

5.6 Energetic landscape of strongly-coupled QD solid

In order to investigate the effects of the thermal treatment on the carrier dynamics of close packed QD solids, fs-TA spectroscopy is used. Figure 5.11(a) shows the TA spectra of the pristine QD solid as function of time measured under $2 \mu\text{Jcm}^{-2}$ (0.4 mW) pump fluence. Figure 5.11(b) illustrates the corresponding spectra at selected delay times. The TA spectra of the QD solids prepared under other conditions can be found in Figure 5.10.

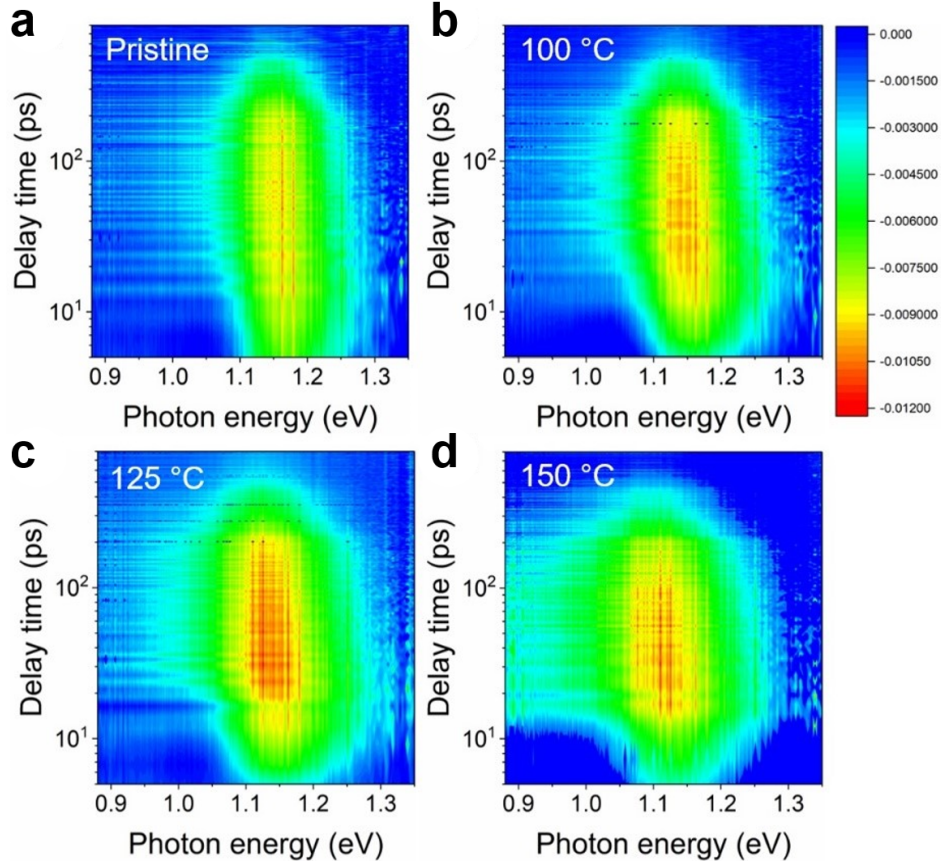


Figure 5.10: Spectro-temporal transient absorption maps for (a) pristine QD solids and QD solids after thermal treatment at (b) 100 °C, (c) 125 °C and (d) 150 °C. The data are measured under a fluence power density of $2 \mu\text{J}/\text{cm}^2$. Reproduced with permission from ref [31] Copyright (2019) American Chemical Society.

The TA spectra are analyzed with Gaussian functions. The exciton energy “funneling effect”, indicated by ΔE in Figure 5.11(a), is demonstrated by the bleaching peak position evolution seen in Figure 5.11(c). The temporal evolutions are well fitted with an exponential decay function adapted from previous literature as following, [51]

$$E(t) = E(0) + \Delta E \exp(-k_{\Delta E} t) \quad (5.1)$$

where $E(t)$ denotes the real-time bleaching peak position and E_0 is determined from the TA spectra by the energy peak position in the equilibrium state, ΔE is the saturated hopping energy and $k_{\Delta E}$ is correlated with charge carrier’s hopping rate, which will be discussed later. Figure 5.11(d) shows the TA spectra of all differently treated QDs solids when photon bleaching has reached a maximum depth, respectively. These curves are fitted with Gaussian functions in which σE is used to describe the solids’ inner energetic

distribution. Figure 5.11(e) shows the derived σE values and indicates that σE increases when higher temperature treatment is applied. Considering that the size distribution of the QDs is constant for all QD solids' fabrication in this work, the energetic inhomogeneous broadenings of QD solids' increased band-gaps are explained by [29]

$$\sigma_E^2 = \sigma_{QD}^2 + \sigma_{ECR}^2 \quad (5.2)$$

in which σ_{QD} is derived from QDs intrinsic energetic distribution approximately treated as a constant indicating the term of the homogeneously broadening, while σ_{ECR} is assumed to be generated from the energetic distribution of strong electronic coupled regions (ECRs), which are mainly contributed by QDs' shape induced and regionalized structure better alignments. This term represents the energetic inhomogeneous broadening in equation 1. Consequently, the ΔE is supposed to have a proportional relation with the term as follows,

$$\Delta E \propto -\frac{\sigma_{ECR}^2}{k_B T} \quad (5.3)$$

in which k_{BT} is the Boltzmann constant times temperature, which matches well with our data as seen in Figure 5.11(e). The charge carrier hopping rate for all QD solids is estimated by equation 1 and the results are plotted in Figure 5.11(f). Paring the inter-dot distances in solids from the GISAXS data in Figure 5.8(a), the hopping rate tendency seems in contradiction to an expected tunneling rate as follows [52]

$$k(T) \propto \exp(-\beta l) \quad (5.4)$$

where the $k(T)$ is temperature-dependent tunneling rate, while β stands for tunneling barrier and l indicates the tunneling distance. It can be assumed that in a halide-ions treated close packed solid, which is treated as a quasi-solid, the carrier hopping rate is not only correlated with their inter-dot distance but also related to their structure alignment, especially when comparing the hopping rate tendency with structure orientation distribution in the GIXS data as seen Figure 5.8(c) and Figure 5.8(f). The QD solid treated at 100 °C, having the best structure alignment, also reveals the highest expected carrier hopping rate. In comparison, the QD solid treated at 125 °C shows a lower rate for charge carriers' hopping and the QD solid treated at 150 °C has the worst performance in our study. The overall better-aligned lattice in the QD crystal as well the better-defined superlattice can generate a broader facet-to-facet area, which is supposed to be beneficial for the tunneling and thereby dramatically decrease the tunneling barrier β and thus increase the hopping rate.

Sample	X_c (eV)	Sigma (meV)	Area
Pristine	1.163	62	1.67
100 °C	1.150	64	2.08
125 °C	1.142	72	2.34
150 °C	1.113	84	2.52

Table 5.1: Fitting data of TA spectra with Gaussian functions at samples' correspondent maximum bleaching depth. Reproduced with permission from ref [31] Copyright (2019) American Chemical Society.

Moreover, it is found that thermal-treated QD solids can generate more hot-excitons than pristine QD solids by comparing their maximum bleaching area (Table 5.1), which is proportional to the charge carrier density. This is probably because the thermal treatment can passivate the QDs' surface and thus reduce the surface defects and active more excitable energy states. A similar effect has been explained by the better structure alignment induced by the increasing the facet-to-facet touching area of neighboring QDs.

5.7 Conclusions

In summary, GIXS techniques have been used to analyze the inner structure of QD crystal lattices as well as the stacked superlattices in colloidal state QD solids and close packed QD solids, respectively. By performing the ligand exchange process, the QD crystals lattice changes from "edge-up" to "corner-up" as seen in the GIWAXS data analysis, while the superlattice phase transition from a face-centered cubic (FCC) to body-centered cubic (BCC) lattice has been revealed by the GISAXS studies. The QDs' shape is the main factor for the structural realignment in the close packed QD solids. The transition is explained by a Wigner-Seitz close packed construction with a minimized total area for surface energy and a maximized system entropy as the driving forces for the self-organization. Moreover, the charge carrier dynamics in QD solids have been investigated by transient absorption and the temporal photon bleaching spectra are used to investigate the charge carrier dynamics. The strong electronic coupled regions are assumed to contribute to the inhomogeneous broadening of the QD solids' band-gaps and result in the large peak energy shifts in the temporal spectra. Moreover, it is also found that an overall better-aligned structure, including QD crystal lattice as well as the stacked QD superlattice, is beneficial for the charge carrier hopping conditions. The close packed QD

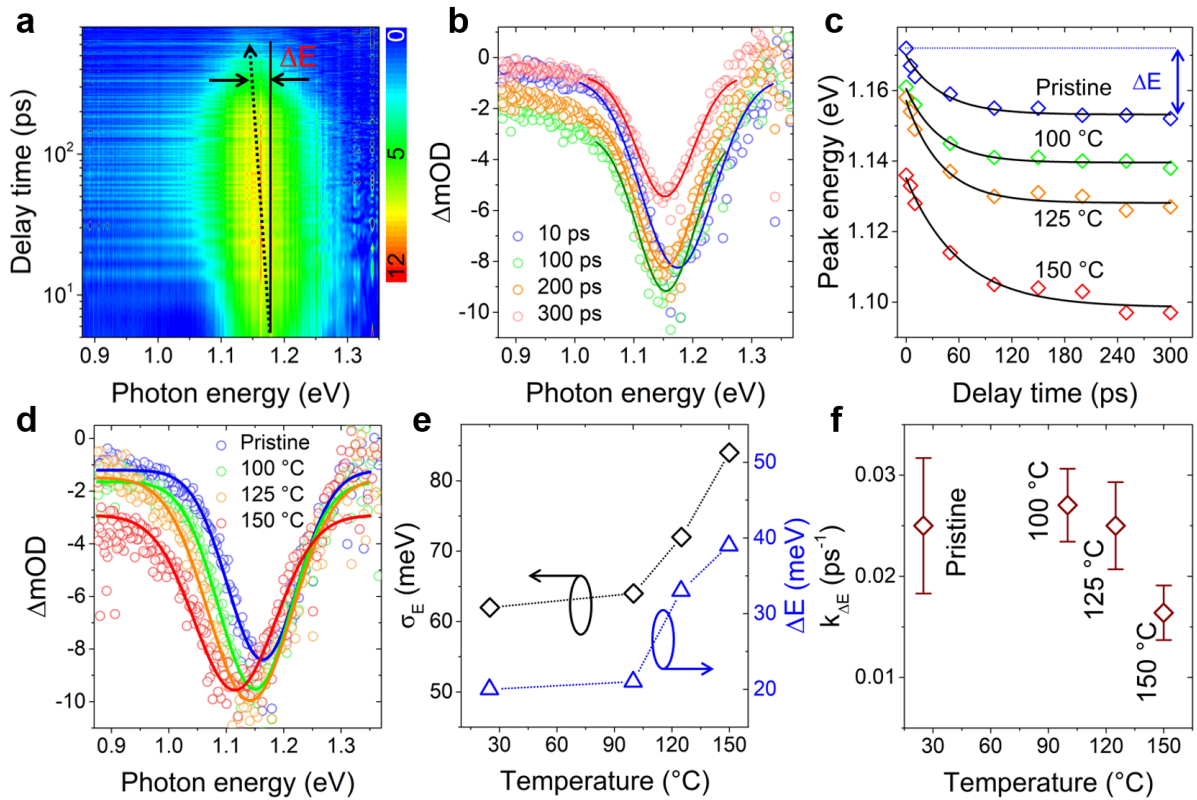


Figure 5.11: (a). Spectro-temporal transient absorption map for pristine QD solid measured under $2 \mu J/cm^2$ pump fluence with ΔE indicated. (b). TA spectra of the pristine QD solid at selected times (circles) fitted with Gaussian functions (solid lines). (c). Photon energy peak positions' as functions of delay time (open symbols) fitted by equation 1 (solid lines). (d). Corresponding TA spectra of QD solids at their maximum bleaching depth (symbols) fitted with Gaussian functions (solid lines). (e). Derived standard deviation σE (black symbols) representing energetic dispersity and the peak energy shift ΔE (blue symbols) as a function of temperature. (f). Resulting fitted carrier hopping rate $k_{\Delta E}$ as a function of temperature. Reproduced with permission from ref [31] Copyright (2019) American Chemical Society.

solid treated at 100 °C exhibits the best structure alignment together with the best charge carrier hopping rate.

6 Stacking kinetics of QDs during printing deposition

Parts of this chapter were prepared in collaborations with Deutsches Elektronen-Synchrotron (DESY), Hamburg, Germany and Southern University of Science and Technology (SUSTech), Shenzhen, China, and are published in "Colloidal PbS quantum dot stacking kinetics during deposition via printing" (Chen, W.; *et al.*, *Nanoscale Horiz.*, 2020, 5, 880-885, DOI: 10.1039/D0NH00008F). Reproduced from Ref [41] with permission from the Royal Society of Chemistry.

6.1 Motivations and main discoveries

Colloidal PbS quantum dots (QDs) are attractive for solution-processed thin-film optoelectronic applications. In particular, directly achieving QD thin-films by printing is a very promising method for low-cost and large-scale fabrication. The kinetics of QD particles during the deposition process play an important role in the QD film quality and their respective optoelectronic performance. In this work, the particle self-organization behavior of small-sized QDs with an average diameter of 2.88 ± 0.36 nm is investigated for the first time in situ during printing by grazing-incidence small-angle X-ray scattering (GISAXS). The time-dependent changes in peak intensities suggest that the structure formation and phase transition of QD films happen within 30 seconds. The stacking of QDs is initialized by a templating effect, and a face-centered cubic (FCC) film forms in which a superlattice distortion is also found. A body-centered cubic nested FCC stacking is the final QD assembly layout. The small size of the inorganic QDs and the ligand collapse during the solvent evaporation can well explain this stacking behavior. These results provide important fundamental understanding of structure formation of small-sized QD based films prepared *via* large-scale deposition with printing with a slot die coater.

6.2 Introduction of printing colloidal QDs

Colloidal PbS quantum dots (QD) are attractive for being used in various optoelectronic applications due to their tunable band-gap with a large absorption wavelength range from the visible to the near-infrared region. [107, 108] Moreover, due to the high intrinsic permittivity, the exciton binding energy of PbS is smaller than in cadmium chalcogenide QDs and polymer materials, which is beneficial for devices driven by charge carrier generation and transport, e.g. photovoltaics and photodetectors. [6, 13, 14, 92, 109, 110] Colloidal QDs are commonly synthesized via hot-injection methods, [73, 111] in which the organic ligands in the precursor play an important role in controlling the size and shape of the QDs during the synthesis process and also for maintaining the suspension of QDs in the solvent without aggregations. [32] Therefore, colloidal QDs reveal a good solubility in many solvents, which indicates their compatibility with various large-scale solution-processing thin-film deposition techniques, [112, 113] including spray-deposition and printing. [49, 64, 114] Moreover, due to these ligands, QDs are treated as semi-soft particles with a hard-core/soft-shell configuration. The stacking behavior of QDs in a self-organization process determines the quality of as-deposited film.¹⁶ Related studies also provide the fundamental insights on the self-organization process of colloidal particles. [65, 93] The kinetics of PbS QDs in a slow evaporation process (over 30 min) was reported previously, in which the as-formed superlattice based on large-sized QDs (over 5 nm in diameter) and the corresponding phase transitions were well described and explained. [42, 94] Considering that the organic shell layer thickness of the QDs is determined by the ligand thickness, which can be treated as a static value in specific solvent conditions, the semi-soft material properties are influenced by the solvent conditions as well as by the ratio of the ligand thickness (L) over the radius of the QDs (R). Thus, the stacking behavior of the QDs is determined by their overall size as seen in Figure 6.1. Small-sized QDs, with a less pronounced shape contribution from their inorganic core, due to the large ratio of ligand-layer-thickness over the QD radius, [35] exhibit a more sphere-like behavior during the drying process than large-sized QDs. Such differences suggest different particle kinetics during their self-assembly in a wet chemical deposition process such as printing. Moreover, from the aspect of potential applications, PbS QDs with a small average diameter demonstrate better photovoltaic performances in a planar heterojunction architecture, [22, 23, 50, 110, 115, 116] in which a large-scaled QD's deposition would also be highly desired. Although the recently developed QD-ink technologies create a simplified way for the deposition and the functionalization in a single step, these ink techniques still face many challenges. For example, ligand exchanged QDs in a solvent significantly rely on the use of costly lead halides (PbI_2 or PbBr_2) in combination with metal ion coordinating solvents, like butylamine, to maintain their solubility, thereby making it less compatible with current deposition meth-

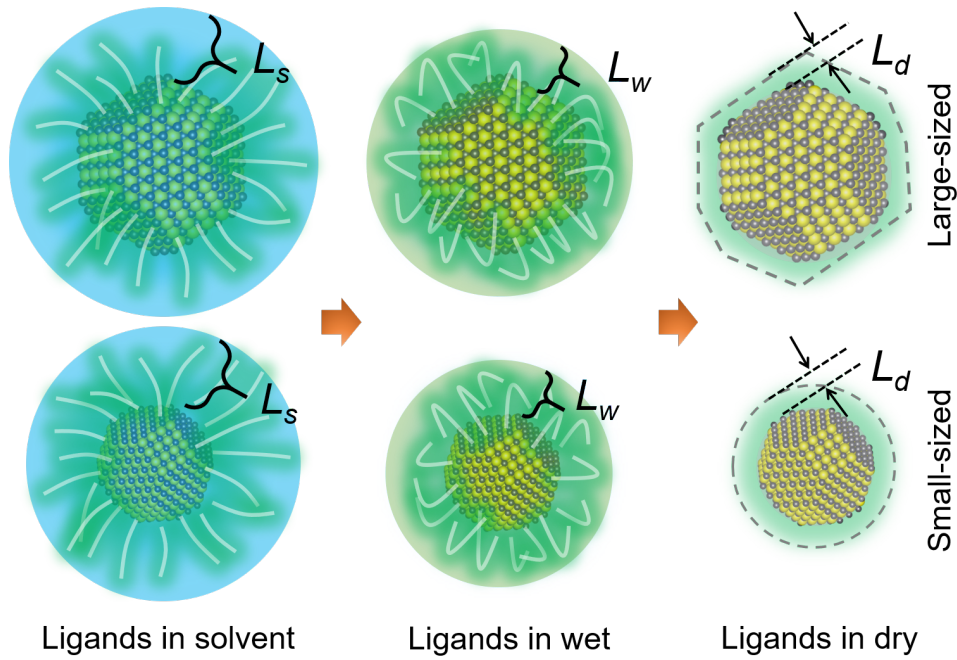


Figure 6.1: Ligand thickness L variation of QDs in different conditions during the drying process, in which $L_s > L_w > L_d$, corresponding to the ligand thickness for QDs in the solvent state L_s , in wet (no apparent solvent state but not fully dry) L_w and dry conditions L_d , respectively. Larger sized QDs with an apparent final shape factor are shown in the upper row and smaller sized QDs with a non-apparent shape factor in the lower row. Reproduced from Ref [41] with permission from the Royal Society of Chemistry.

ods. [50, 74, 76, 117–121] Therefore, the deposition of conventional ligand capped QDs is still promising for a low-cost large-scale device fabrication in the near future, in which the as deposited QD solids are functionalized by a post-ligand-exchange treatment as reported in previous works. [22, 122] Thus, the kinetics of small-sized QDs during particle stacking into a close packed configuration in a large-scale deposition process will provide a significant fundamental understanding. For example, QDs with different superlattice stacking will result in a different neighboring inter-dot distance distribution, which induces different inter-dot couplings and leads to the inner energy state disorder of QD film. [123]

6.3 Experimental details

Synthesis of colloidal PbS quantum dots: the synthesis method was following previous literature with slight modifications, briefly described as follows: 1.1 g PbO powder

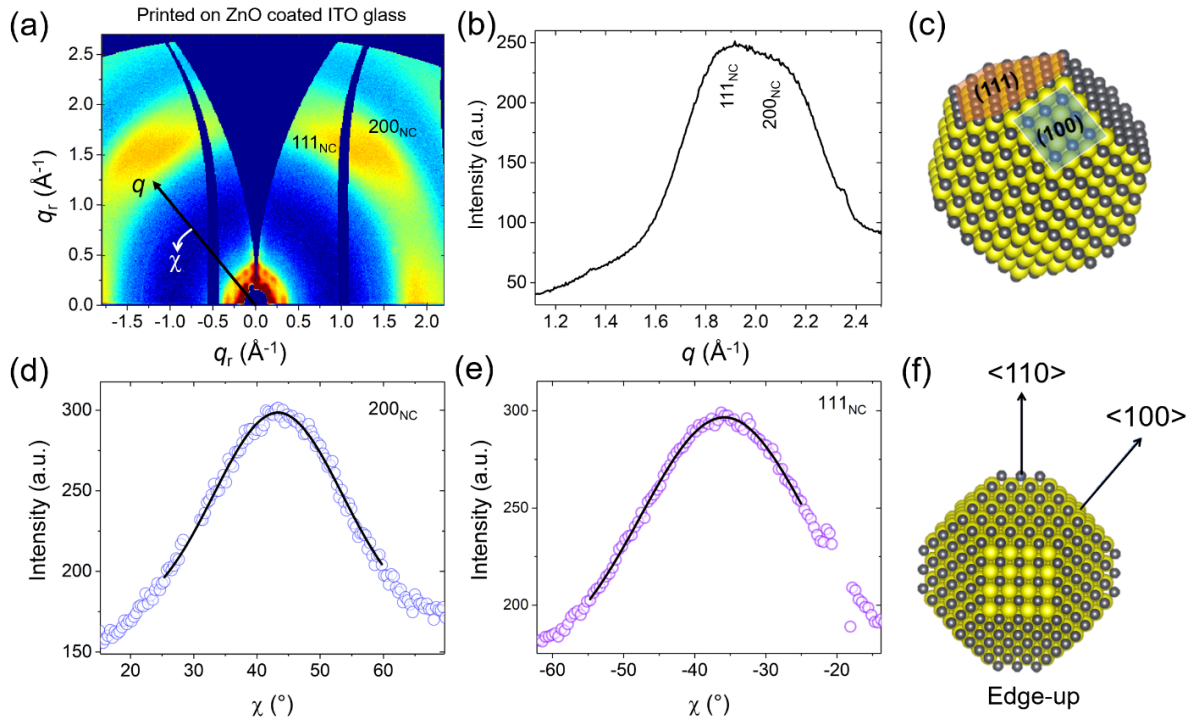


Figure 6.2: (a) 2D GIWAXS data of printed PbS QD superlattice solids on ZnO coated glass. (b) Azimuthal integration of the 2D GIWAXS data along q showing the 200_{NC} and 111_{NC} Bragg peak contributions and (c) schematic of corresponding facets on a PbS QD with $(200)_{NC}$ plane and $(111)_{NC}$ plane. Orientation distribution of (d) 200_{NC} and (e) 111_{NC} Bragg peaks. (f) Sketch of the final facet orientations of PbS QDs in the final array, which is described as edge-up. Reproduced from Ref [41] with permission from the Royal Society of Chemistry.

was loaded into a three-necked flask mixing with 7 mL oleic acid ($C_{18}H_{34}O_2$, OA) and 20 mL octadecene ($C_{18}H_{36}$, ODE). The mixture was degassed three times, with alternatively injecting pure argon (Ar), then heated up to 150 °C to obtain a transparent $Pb(OA)_2$. The temperature of the mixture was decreased back to 100 °C and a degassing process for 6 hours was performed to completely remove the inner moisture and the organic solvent with a low-boiling point. Ar was injected with stop degassing simultaneously and the temperature was decreased to 80 °C. 530 μL $(TMS)_2S$, was injected in $Pb(OA)_2$ solvent to initiate the nucleation and growth of PbS QDs. The reaction was last for 90 s and the flask was cooled down immediately by an ice-bath, simultaneously, 10 mL octane was injected into the flask to terminate to the reaction. The acetone was used to purify the QDs by high-speed centrifugation. QDs were then re-dispersed in octane with a concentration of 50 mg/mL for the printing deposition.

Printing of QDs: The printing of QDs was performed with a home-made slot-die

coater, which had a fixed printer head with a 25 mm wide solvent-flow-guider, a microfluidic syringe pump, a substrate holder and a computer control. To initialize the deposition, the injection rate of QDs was set at 100 $\mu\text{L}/\text{min}$ and the height of the flow-guider measured from the substrate was set to 0.5 mm. When the solvent flew out along the flow-guider, the substrate holder was moving with the rate of 3 mm/s along the printing direction simultaneously. The deposition was terminated when the sample holder reached a preset position and the injection was stopped simultaneously with the print-head rising for 0.5 mm to avoid reflux of residual solution. A QDs film was achieved when the solvent was fully dried. Notably, QDs were directly printed on the ZnO layer in the following steps. The film homogeneity and flatness were checked by GISAXS scanning along the printing direction before printing and the in-situ observation as seen in Figure 6.7(c). and Figure 6.7(d). The ZnO coated ITO/Glass was also used for the deposition of QDs as a reference sample. The corresponding GISAXS data of QDs on ZnO/ITO/Glass is shown in Figure 6.3. It shows similar scattering features as the GISAXS data of QDs/ZnO/Glass sample.

In situ GISAXS measurement: The printer was installed in the beamline P03 of the Deutsches Elektronen-Synchrotron (DESY) in Hamburg. The complete printing setup was fixed on a hexapod that was responsible for the alignment and scans. The X-ray photon energy was 12.9 keV corresponding to the wavelength of 0.96 Å. The Pilatus 1M was used as GISAXS detector with a sample-detector distance of 2591 nm, which was further calibrated by AgBeh. The incident angle was set to 0.4 ° which was higher than the theoretical critical angles of Si/SiO_x, ZnO and bulk PbS materials based on scattering length density calculations. The alignment of the substrate was performed before the in-situ experiment and an X-ray scan was performed to localize a uniformed and smooth region (with a length of 3 mm, which is divided into 15 points) on the substrate for the in-situ observation afterward. The in-situ monitoring started immediately after the sample holder stopped moving. The first single GISAXS measurement on the as-deposited QD film was close to the printer head and close to the fresh deposition region. The duration of the single GISAXS measurements was set to 0.1 s and realized by the fast-shutter. The setup then moved to the next point in another 1.9 s for the next single GISAXS measurement. The evaporation of the solvent and the film drying were quite fast (30 s), as confirmed by the time-resolved 2D GISAXS data.

The simulations and calculations: The 2D GISAXS data simulations were performed with the software BornAgain (version 1.61). [124] The scattering functions of simulated materials were all based on their scattering length density. The QDs with a uniformed diameter of 2.88 nm were modeled by a hard sphere with selected inter-distance. The layout of the assembly of QDs was described by a hexagonal 2D lattice.

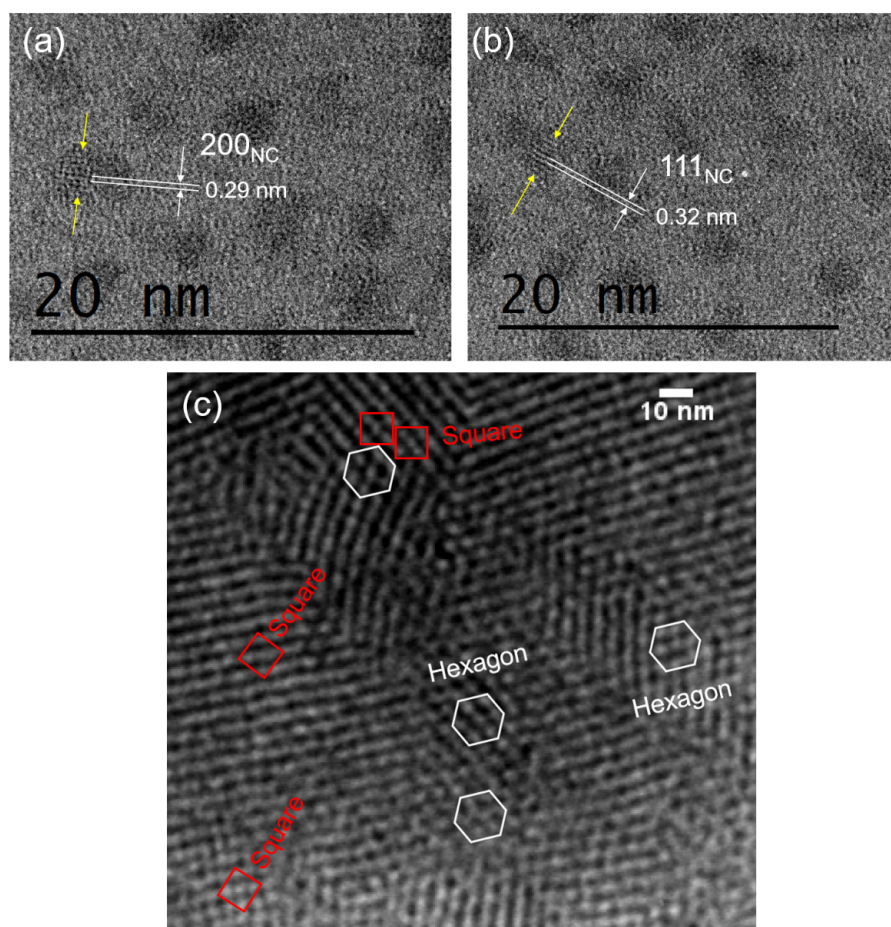


Figure 6.3: High-resolution TEM images showing the (a) $(200)_{NC}$ plane and (b) $(111)_{NC}$ plane of the used PbS QDs. The corresponding lattice distances are 0.29 ± 0.01 nm and 0.32 ± 0.01 nm, respectively, as measured over 5 lattice fringes. (c) TEM image of printed QD film on a carbon film (on a copper grid). The red squares indicate the $(110)_{SL}$ plane in the BCC superlattice and the white hexagons indicate the $(111)_{SL}$ plane in the FCC superlattice. Reproduced from Ref [41] with permission from the Royal Society of Chemistry.

The superlattice-diffraction calculations were based on the GIXSGUI package (version 1.7.1) on the MATLAB platform. [125]

6.4 Material synthesis and characterization

In this work, the stacking behavior of small-sized PbS QDs is investigated during deposition via printing. Printing with an in situ characterization are combined based on grazing-incidence small-angle X-ray scattering (GISAXS) at a synchrotron (P03, DESY). [126] The QDs were prepared according to the literature with some modifications as seen in the

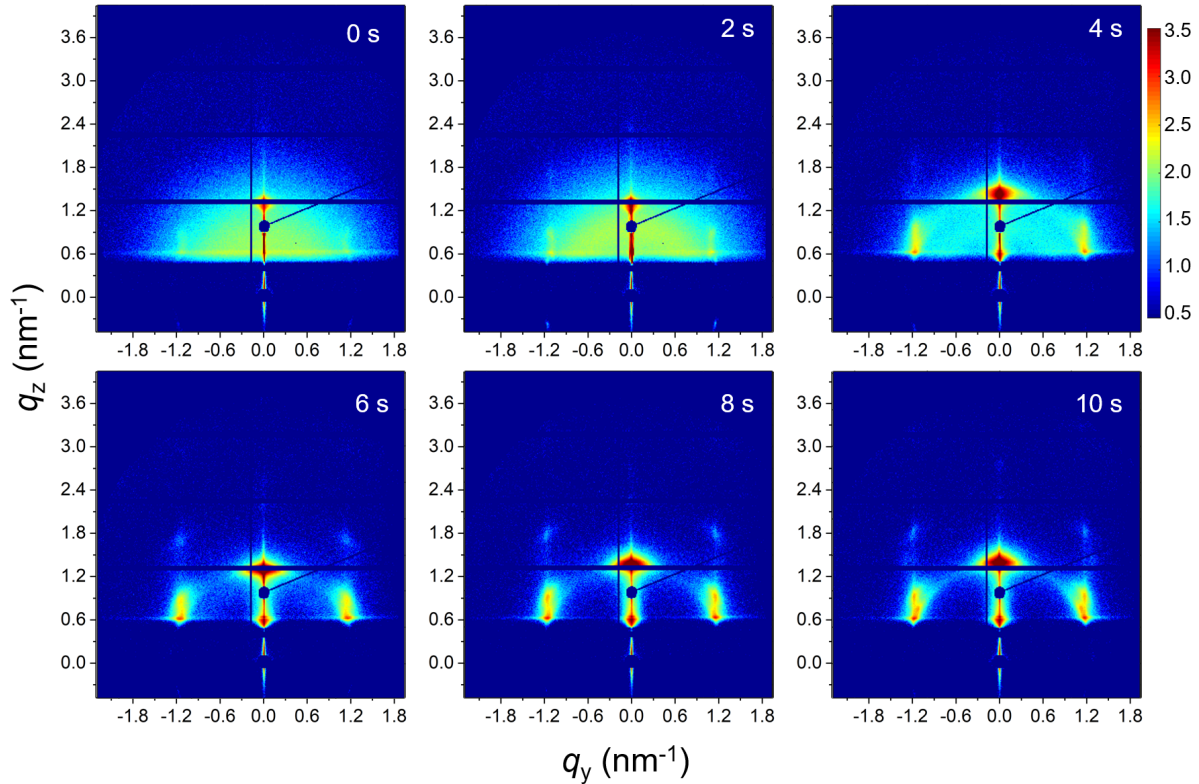


Figure 6.4: 2D GISAXS data of QDs film deposited on a different substrate (ZnO/ITO/glass) by printing with the same protocol as used for the printing on ZnO/glass substrate at times as indicated. Times are not exactly compatible with the printing experiment described in the main manuscript due to additional alignment before the measurement. The observed superlattice structure evolution indicates similar QD stacking kinetics. Reproduced from Ref [41] with permission from the Royal Society of Chemistry.

experimental section.10 The final QDs with an average diameter of 2.88 ± 0.36 nm reveal the first exciton absorption peak at 935 nm as seen in Figure 6.5. Figure 6.5(a) illustrates the QDs under room-light conditions, revealing a full absorption of the visible light by the QDs. Transmission electron microscopy (TEM) images (Figure 6.5(b)) indicate a good dispersion of the QDs without aggregation, due to the capping with oleic acid as surface ligands, as sketched in Figure 6.5(c). The histogram data in Figure 6.5(d) derived from the TEM image analysis shows the narrow size distribution of the QDs. The bandgap of the QDs (Figure 6.5(e)) is well meeting with the requirements for high-performance photovoltaic applications. [31, 57]

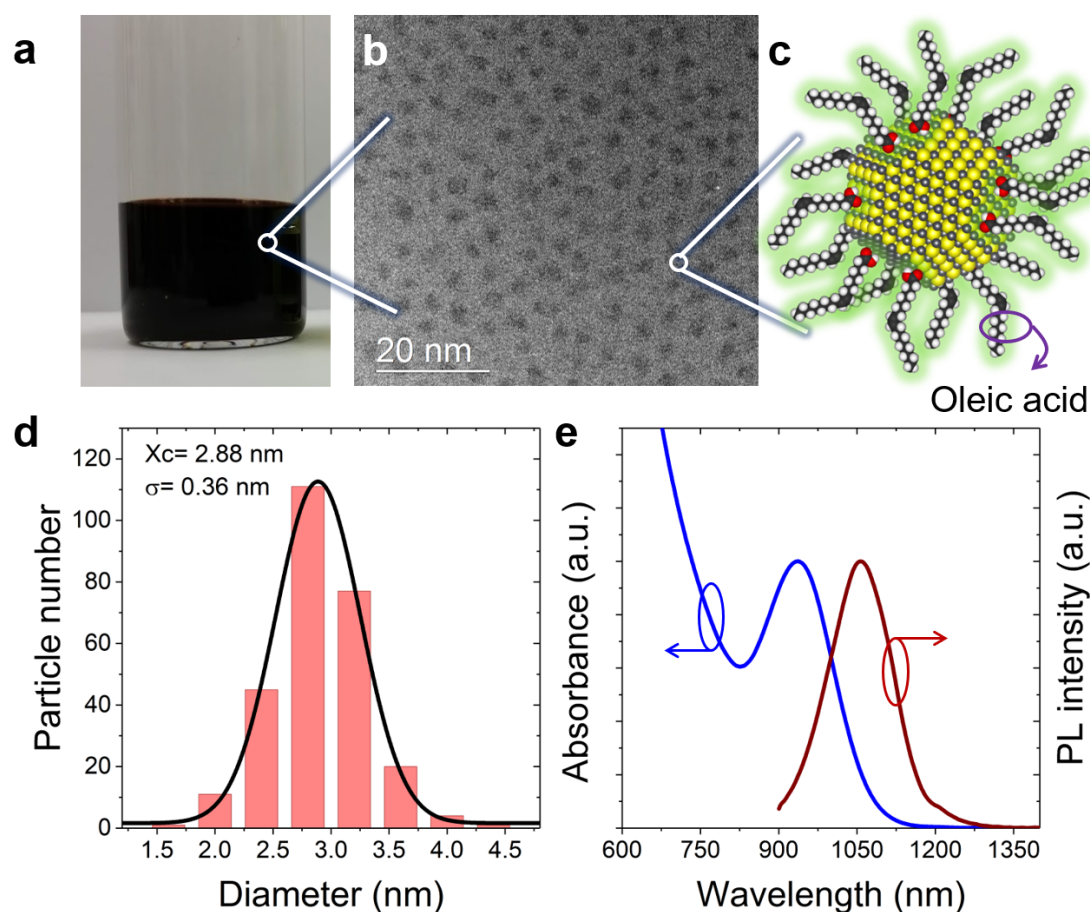


Figure 6.5: (a) Photograph of QDs in octane solvent (room light conditions). (b) TEM image of QDs. (c) Structure sketch of a QD with PbS core and an oleic acid acting as the organic ligand shell. (d) Size histogram from the TEM image analysis indicating the average diameter is $2.88 \pm 0.36 \text{ nm}$. (e) Absorption spectrum of QDs in octane and corresponding PL emission spectrum. Reproduced from Ref [41] with permission from the Royal Society of Chemistry.

6.5 Thin-film deposition via slot-die printing

The wet-chemical deposition via printing is performed with a home-made slot-die coater, which is installed in the beamline for the time-resolved in situ GISAXS study. [127] The printer head is fixed inside the printer chamber. Thus, the deposition is driven by the solvent injection and simultaneously moving of the substrate holder when the solvent flows out along the flow-guider. Notably, the morphology of printed QD films can be influenced by using different solvents and by tuning the printing parameters. Parameters are selected to ensure homogeneous films after printing. After the deposition of QDs, the

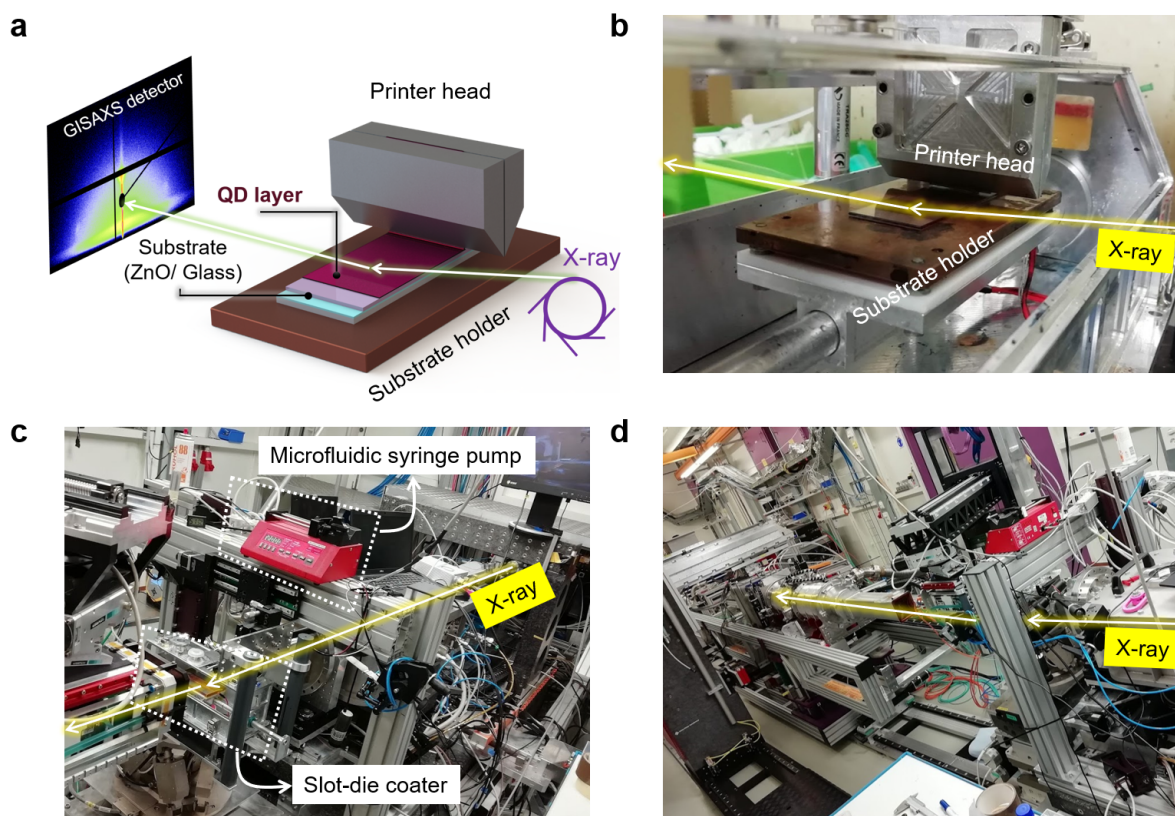


Figure 6.6: Schematic (a) of the in-situ set-up used for printing and (b) the corresponding photograph with print head and substrate holder as indicated (X-ray beam is sketched for clarity). (c), (d) Photographs of the integration of the slot-die coater in the experimental station P03. Reproduced from Ref [41] with permission from the Royal Society of Chemistry.

whole printing set-up moves back by the motors to the preset position of X-ray spot and the GISAXS monitoring is started immediately. This moment is defined as $t = 0$ s for measuring the stacking kinetics of the deposited QDs. More details about the printing process are described in the experimental section. The related photographs of the set-up are seen in Figure 6.6. The X-ray photon energy is 12.9 keV with a focused beam size of $25 \mu\text{m} \times 20 \mu\text{m}$. The sample-detector distance is set to 2591 mm to ensure that the scattering signal of the QDs is well recorded. The incident angle is 0.4° . The monitoring region on the substrate is pre-selected as a small homogenous region (in 3 mm width), which is confirmed by the GISAXS scanning as seen in Figure 6.7, in which a line cut mapping is shown. For in situ measurements, the region is divided into 15 points with intervals of 0.2 mm width. 0.1 s X-ray exposure is selected for each point to avoid beam damage. More detailed parameters for the in situ GISAXS experiment are provided in

the experimental section. As acquired time-resolved 2D GISAXS data are seen in Figure 6.9.

6.6 GISAXS line-cuts evolution

Figure 6.8 shows the 2D mapping presentation (by software DPDAK [128]) of a. vertical line cuts at $q_y = 0 \text{ nm}^{-1}$ and b. horizontal line cuts at $\alpha_f = 0.2^\circ$, which is corresponding to the Yoneda peak position of the final QD film. [129] The corresponding time-resolved scattering curves are seen in Figure 6.8(c). and 6.8(d)., respectively. In the initial stage of the QD deposition, the QD film has a disordered particle density distribution. A well-pronounced Yoneda peak of the QDs is found at $\alpha_f = 0.2^\circ$ (marked with blue arrow in Fig 2.(c)) at $t = 20 \text{ s}$. Thus, the solvent has almost fully evaporated and the QDs are in a close packed configuration. [69] Moreover, intensity peaks emerge at larger scattering angles due to an ordered QD layer formation (blue arrows in Figure 6.8(c).). [130] The scattering peak at $\alpha_f = 0.75^\circ$ originates mainly from the vertical layer-to-layer stacking in the as formed QD superlattice. Its position matches with a face-centered cubic (FCC) stacking with a superlattice distance d_{111SL} (real space sketch of crystal structure as indicated in Figure 6.8(e)). In the horizontal line cuts Bragg peaks emerge at larger q_y values due to the formation of a well-defined inter-dot distance of neighboring QDs. [131] At $t = 18 \text{ s}$, double Bragg peaks are showing up at 1.08 nm^{-1} and 1.13 nm^{-1} (see inset in Figure 6.8(d)) indicating the formation of an initial close-packed configuration in the QD assembly with two characteristic length scales. During drying, the Bragg peak at a smaller q_y position is vanishing, whereas the one at a larger q_y position is increasing in its scattering intensity. Such templating effect is confirmed by the corresponding simulations with the software BornAgain. [124] As seen in Figure 6.11, the hexagonal layout of QDs on the substrate plane with different inter-dot distance fits well the observed scattering peaks. Thus, the templating effect is considered to be initialized by the hexagonal arrangement of the QDs, in which the QD layout on the substrate plane corresponds to the $(111)_{SL}$ plane of the FCC superlattice. This hexagonal arrangement of QDs with fully stretched ligands maximizes the ensemble entropy in combination with a high degree of space filling. Moreover, the interlayer distance in the vertical direction decreases from 6.0 nm to 5.5 nm due to having a close to fully evaporated solvent. The QDs are in an ambient-condition-transition from “in solvent” to “in wet”. Upon evaporation, a further ligand collapse is continuously observed from the shift of the q_y position of the Bragg peak. The final Bragg peak position of $q_y = 1.16 \text{ nm}^{-1}$ corresponds to a final inter-QD distance $d_{\text{inter-dot}} = 5.41 \text{ nm}$, based on spherical models. [8] A homogeneous stacking of the QDs in a large region is observed.

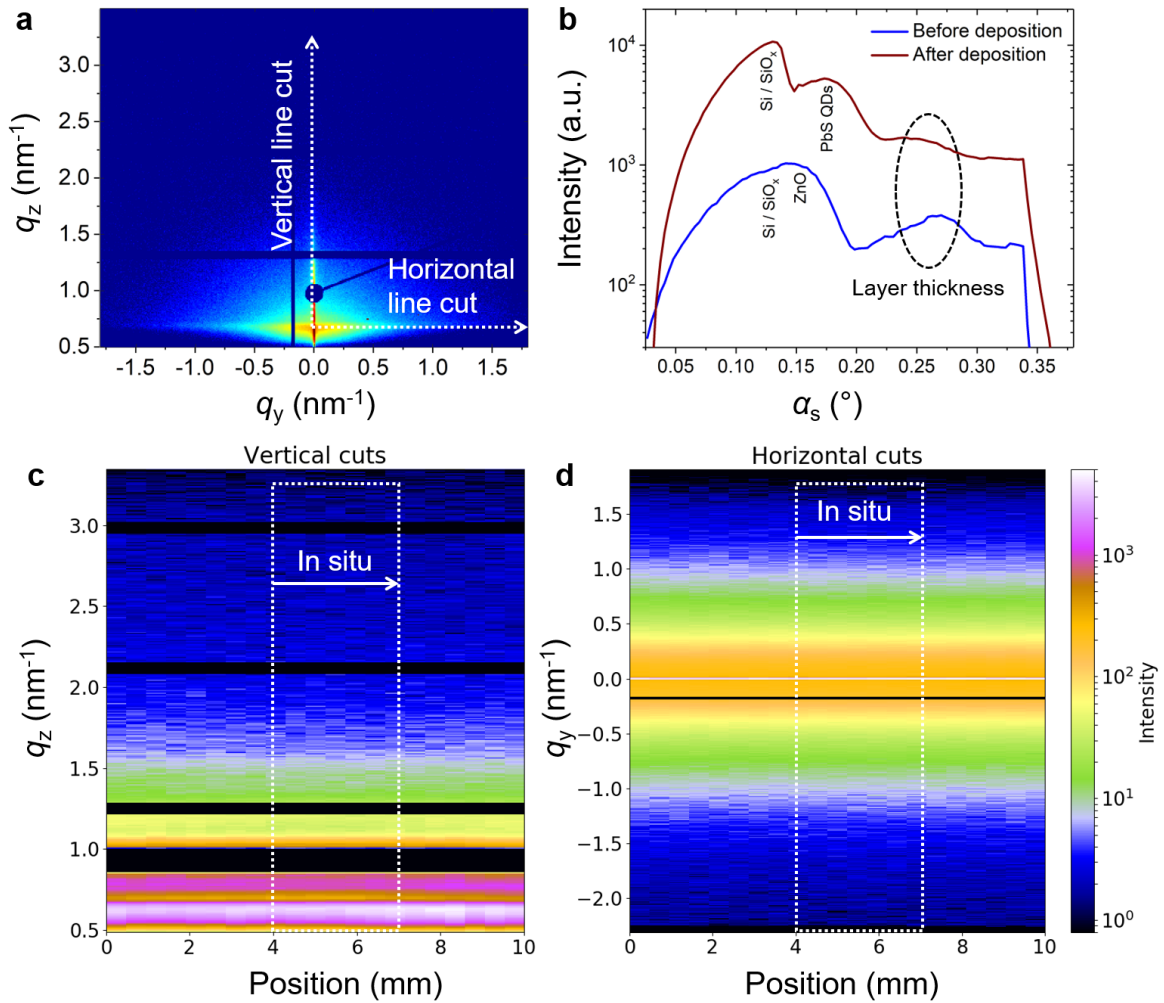


Figure 6.7: (a) 2D GISAXS pattern of ZnO coated glass substrate with the schematics for the vertical and horizontal line cuts. (b) Vertical line cuts of 2D GISAXS data before (blue) and after (red) deposition of the QDs as function of the scattering angle α_f with Yoneda peak positions of the involved materials as calculated from the corresponding scattering length density values. The intensity modulation in the angular range $0.25^\circ < \alpha_f < 0.3^\circ$ resembles the ZnO (blue) and PbS (red) layer thickness. Mapping of (c) vertical and (d) horizontal line cuts of the 2D GISAXS data of the ZnO coated glass substrate. The range selected for the in situ experiment is highlighted in dashed box. Reproduced from Ref [41] with permission from the Royal Society of Chemistry.

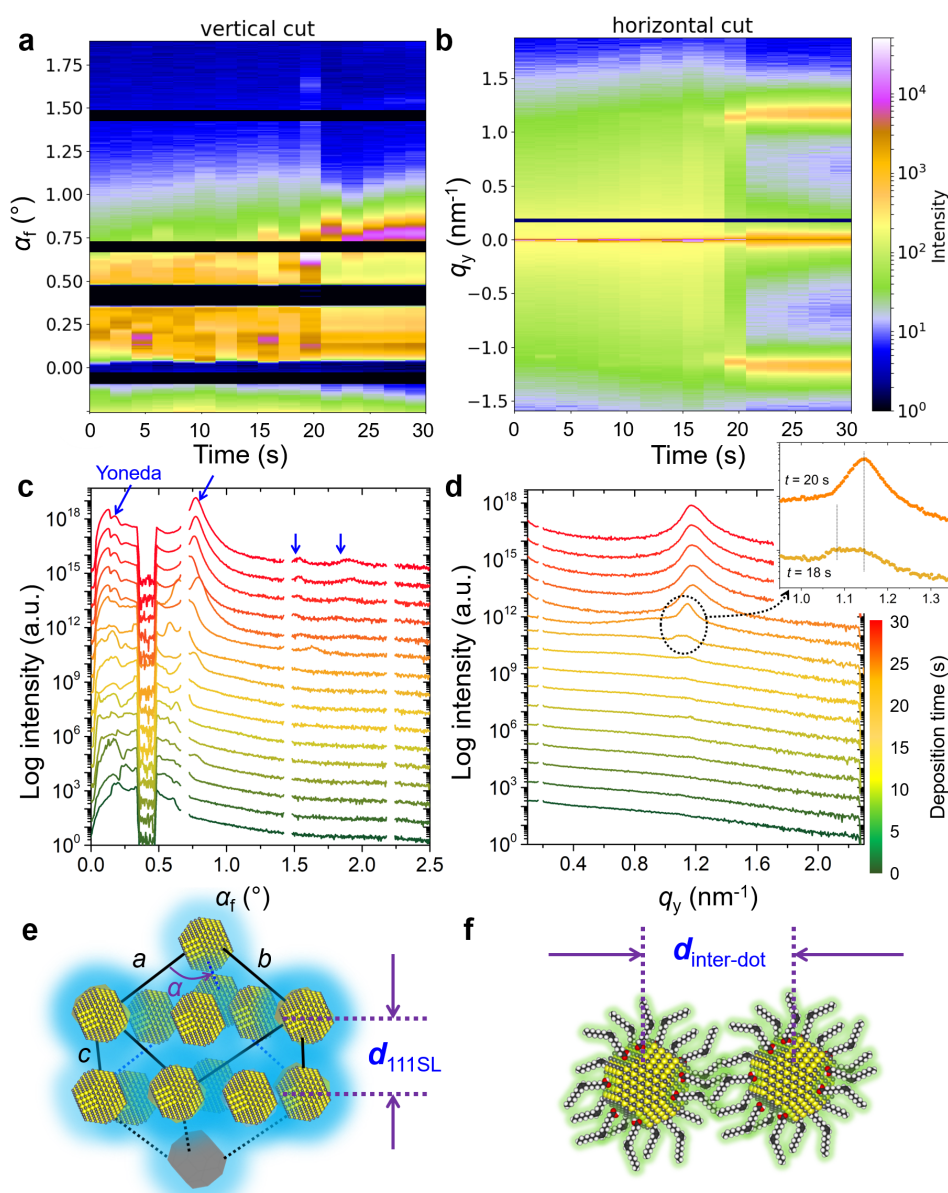


Figure 6.8: 2D mapping presentation of (a) vertical line cuts and (b) horizontal line cuts of the 2D GISAXS data. In the corresponding curves in (c) vertical direction the specular beam is shielded and in (d) horizontal direction the resolution limit is not shown. Arrows mark scattering features in vertical (blue) and horizontal direction (black) as described in the text. Schematics for the (e) inter-lattice distance in vertical direction, in which for example d_{111SL} from an FCC configuration causes a scattering peak at $\alpha_f = 0.75^\circ$ and for the (f) inter-dot distance in horizontal direction corresponding to the in-plane Bragg peak at around $q_y = 1.2 \text{ nm}^{-1}$. Reproduced from Ref [41] with permission from the Royal Society of Chemistry.

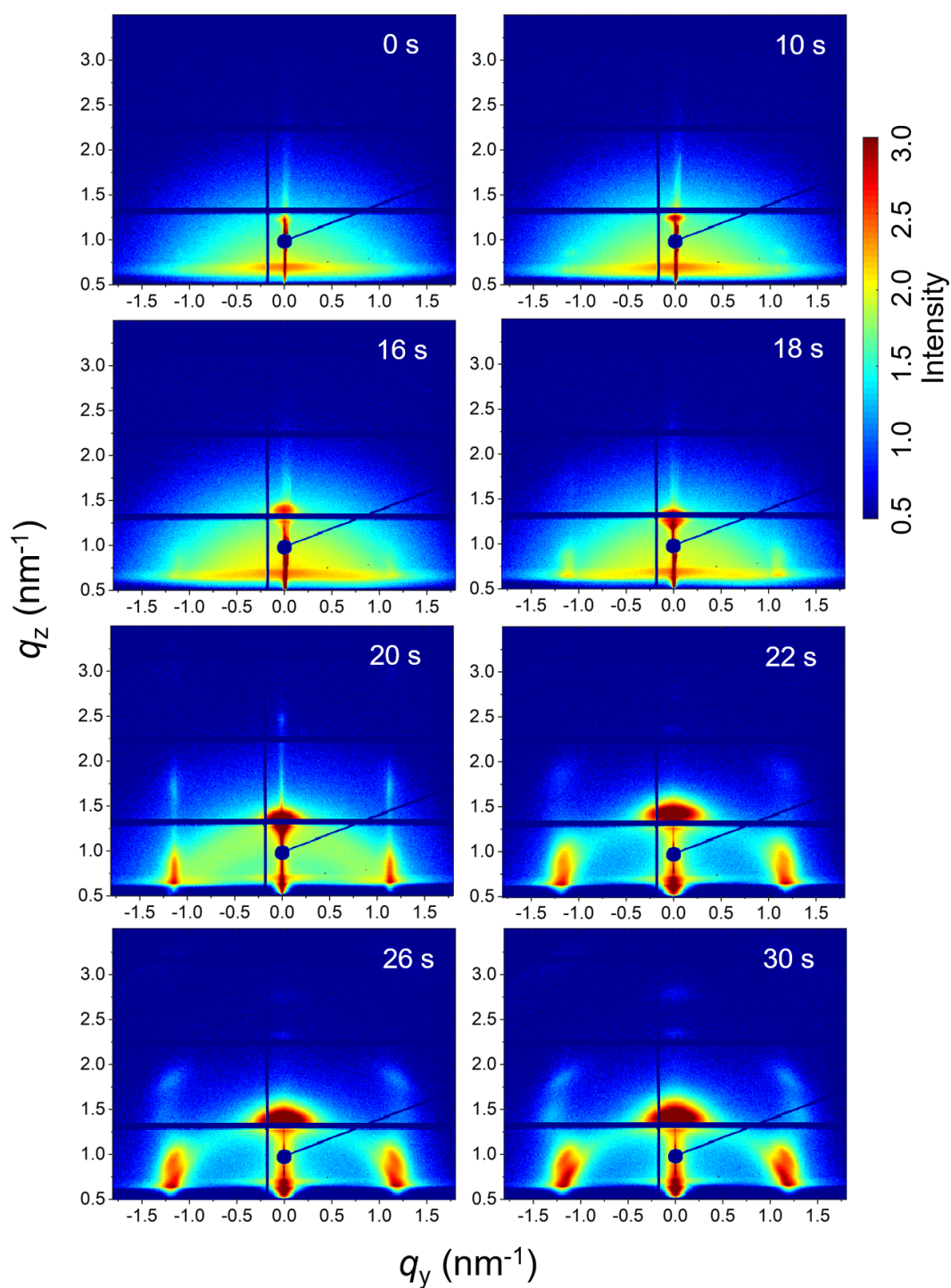


Figure 6.9: Selected 2D GISAXS data at different times after deposition as indicated. Reproduced from Ref [41] with permission from the Royal Society of Chemistry.

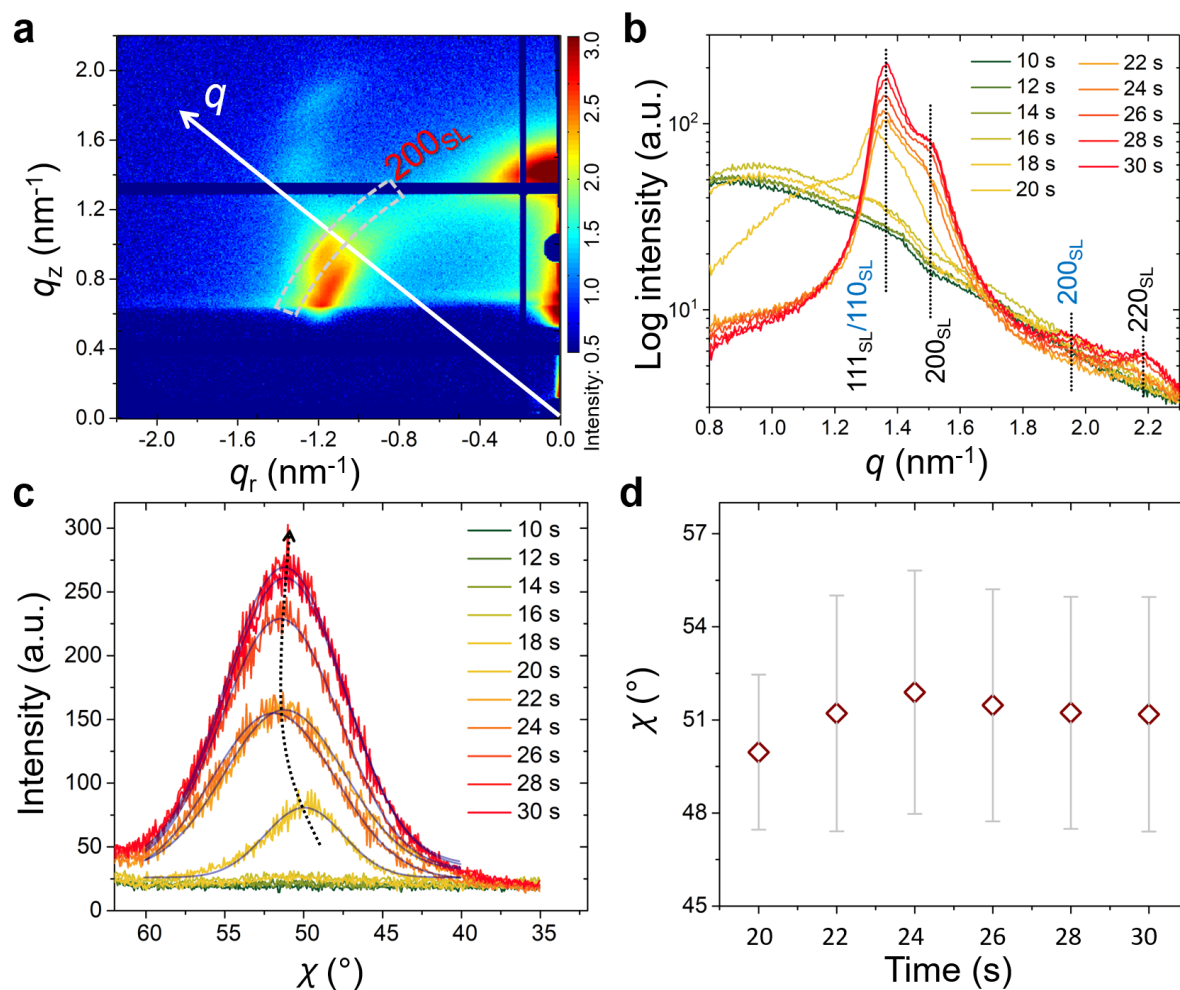


Figure 6.10: Diagram for the superlattice orientation analysis in the (a) 2D GISAXS data indicated by the q direction and χ direction along the 200_{SL} superlattice peak (dashed box). (b) Sector integration in a range of $-70^\circ < \chi < -20^\circ$ with dashed lines marking expected Bragg peaks from the superlattice. The FCC superlattice is indexed in black and the BCC superlattice in blue. (c) Orientation distribution of the 200_{SL} peak from the FCC superlattice fitted by Gaussian function. (d) Corresponding peak positions from the fits with the dispersity represented by sigma from the corresponding Gaussian function shown by the bar. The experimental error is shown by the symbol size. Reproduced from Ref [41] with permission from the Royal Society of Chemistry.

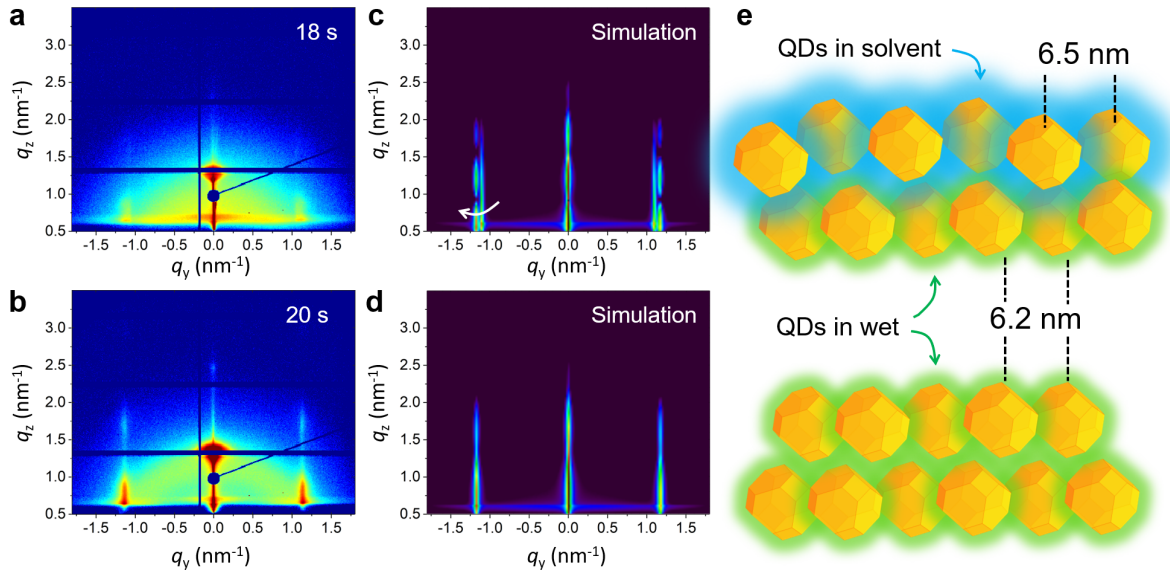


Figure 6.11: (a), (b) 2D GISAXS data and (c), (d) respective simulated 2D images with BornAgain at (a), (c) $t = 18$ s and (b), (d). $t = 20$ s describing a templated stacking behavior of QDs. In the BornAgain simulation, a lattice length of 6.5 nm and 6.2 nm in a hexagonal layout is used to describe the scattering peaks at small and larger q_y values, respectively. (e) The corresponding schematics for describing the changes of inter-dot distances at $t = 18$ s (top) and $t = 20$ s (bottom). Reproduced from Ref [41] with permission from the Royal Society of Chemistry.

6.7 Superlattice orientation evolution

To better understand the stacking process of QDs, the superlattice based specific lattice orientation is further analyzed from the sector integration of the 2D GISAXS data and the corresponding tube cuts as indicated in Figure 6.10(a). During the drying process of the as-deposited film, the QD superlattice is gradually forming, as seen by the development of the Bragg peaks in the integrated data (Figure 6.10(b)). The QD film transforms from a disordered state to an ordered state (superlattice state) at $t = 18$ s by the driving forces of an increased QD concentration in the deposited film. The uniform structure factor originates from the size mono-dispersity of the QDs and from the surface ligand shell with a defined thickness. The peaks are indexed with the QD superlattice (SL), in which the 200_{SL} peak from the FCC stacking demonstrates a full scattering peak signal, without hidden information on the detector, with an intensity, which is used for a further orientation distribution analysis. Thus, the tube cuts are performed along the χ direction in a range of $1.45 \text{ nm}^{-1} < q < 1.55 \text{ nm}^{-1}$ to cover the time-resolved 200_{SL} peak evolution (Figure 6.10(c)). A Gaussian function is used to fit the 200_{SL} peak in the tube-cuts and

the results are shown in Figure 6.10(d). The 200_{SL} peak starts to show up at $t = 20$ s resembling an orientation peak at $\chi = 49.5^\circ$. Afterwards, the peak moves to higher scattering angles. It reaches $\chi = 52^\circ$ at $t = 24$ s. Notably, this value is approaching the theoretical value of 54.7° , which is the intersection angle between $(200)_{SL}$ and $(111)_{SL}$ planes in a standard cubic model, in which the $(111)_{SL}$ plane is parallel to the substrate. That the theoretical value cannot be fully reached in the grazing-incidence configuration, even though the superlattice is perfectly aligned, is attributed to refraction effects. [132] During the further drying process, the 200_{SL} peak moves to a decreased χ value in the time range of $26 < t < 30$ s, which indicates a superlattice distortion. The ligand collapse is supposed to be the reason for this distortion. [33] Instead of the original spherical shape introduced by the ligand capping, a truncated octahedron shape from the inorganic core of the QDs is dominating in dry conditions. Thus, the stacking behavior of QDs undergoes a transition from FCC (for spheres) to a BCC (for truncated octahedrons) packing according to their specific close packed configurations during drying, respectively. [31] Consequently, the particle self-organized system intrinsically reveals a decreased total surface area and thus an increased entropy. [35]

6.8 Superlattice calculation

To rule out the beam radiation induced influence on the stacking structure of the QDs, beam damage tests after *in situ* experiment at the probed positions and results are seen in Figure 6.13.

To describe the particle kinetics in more detail and accuracy, model lattice calculations based on standard superlattice models are performed with the software GIXSGUI,⁵¹ to compare with the measured GISAXS patterns. Selected GISAXS data with calculated positions of Bragg peaks are seen in Figure 6.12(a-c). Apparently, before $t = 18$ s the QDs have a disordered packing as seen by the absence of structure factor contributions in the GISAXS data. At $t = 18$ s, initial Bragg peaks show up at $q_y = 1.1 \text{ nm}^{-1}$ with a weak intensity as seen in Figure 6.12(a). At this stage, the solvent evaporation increased the QD concentration reaching a transition between the “solution phase” and the “wet phase”. QDs with stretched ligands are in an isotropically close-packed configuration, giving rise to a uniform structure factor. Moreover, due to the ligand stretching in the residual solvent, the QDs still behave like spheres as indicated in Schematic 1. Thus, the QDs are supposed to stack in an FCC packing due to the increased entropy. Sphere models prefer to better occupy space in order to decrease the total surface energy. Therefore, an FCC superlattice model with lattice parameters $a = b = c = 9.40 \text{ nm}$ and $\alpha = \beta = \gamma = 90^\circ$ is used in the calculation of the scattering peaks (Figure 6.12(a), red circles for transmission, white

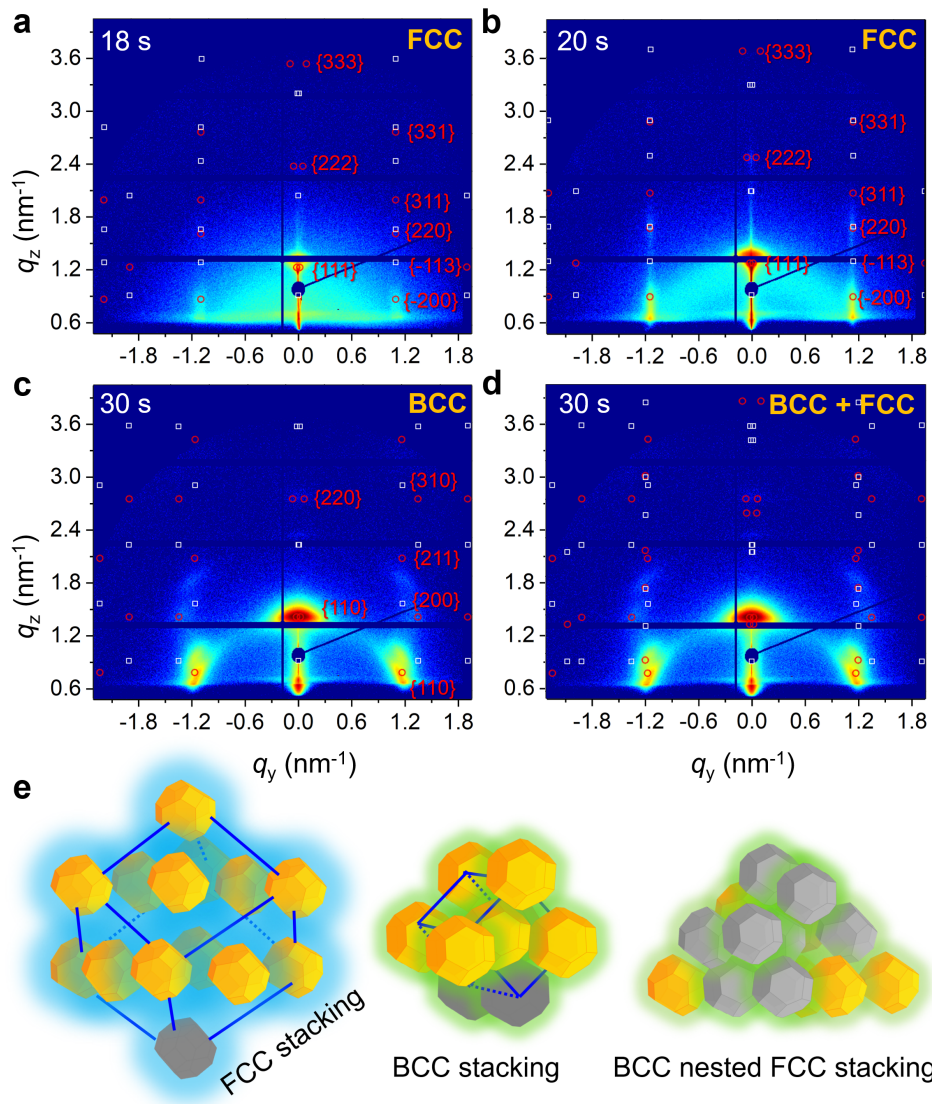


Figure 6.12: 2D GISAXS data at (a). $t = 18$ s and (b). $t = 20$ s with calculated scattering peaks based on an FCC superlattice. 2D GISAXS data of $t = 30$ s with (a) (c). BCC and (d). BCC nested FCC superlattice Bragg peaks (red dots: transmitted scattering peaks; white dots: reflected scattering peaks). Schematics for the FCC superlattice with $(111)_{SL}$ plane parallel to the substrate, BCC superlattice with $(110)_{SL}$ plane parallel to the substrate and BCC nested superlattice with $(111)_{SL}$ plane of FCC lattice parallel to the substrate and $(110)_{SL}$ plane of BCC lattice parallel to the substrate. Reproduced from Ref [41] with permission from the Royal Society of Chemistry.

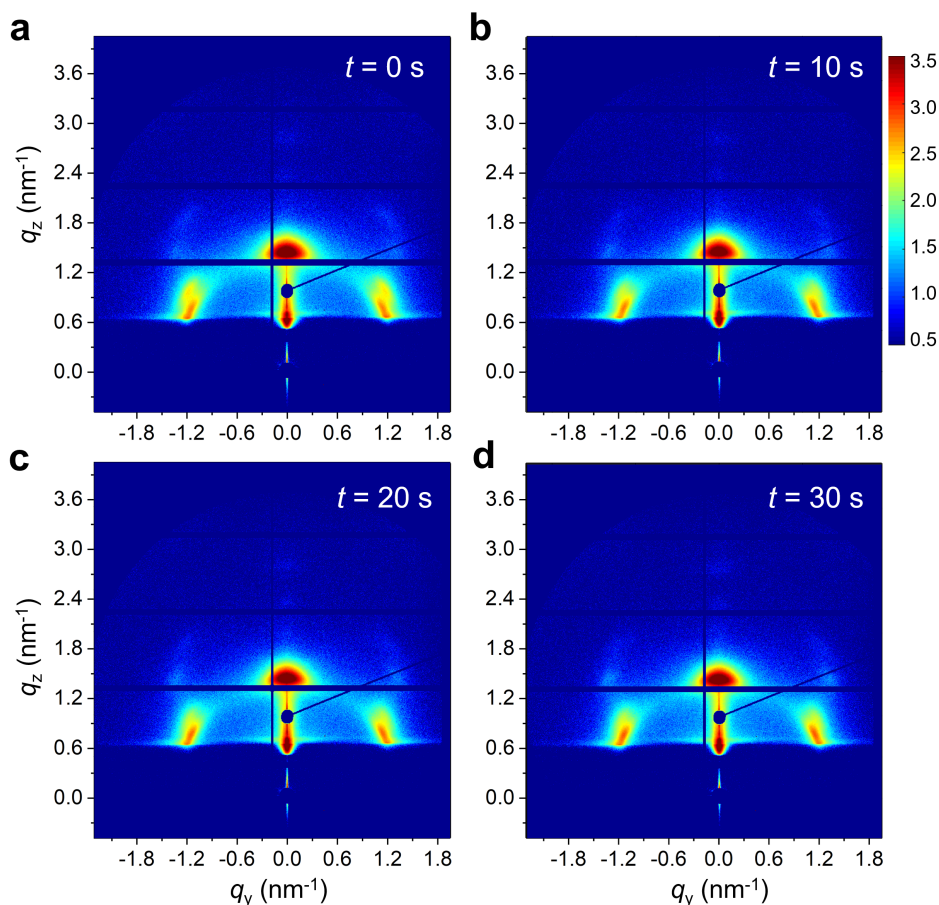


Figure 6.13: 2D GISAXS data from the beam damage check performed after the X-ray measurement. The GISAXS data are taken at exactly the same positions corresponding to the GISAXS in situ measurements during the printing at times as indicated. Reproduced from Ref [41] with permission from the Royal Society of Chemistry.

circles for reflection). A good agreement with the detected scattering peaks is observed, in which the $(111)_{SL}$ plane is oriented parallel to the substrate. The phase transition happens rapidly in the following 2 s. The FCC lattice decreases slightly from 9.40 ± 0.10 nm to 9.00 ± 0.10 nm (see calculations in Figure 6.12(b)). Moreover, the scattering from the FCC superlattice is dominating the 2D GISAXS intensity distribution, meaning that all QDs are aligned in superlattice structures. The calculation indicates that the stacking of the QDs is getting denser. The obtained superlattice distance of $(220)_{SL}$ is 6.36 nm, which can infer that the ligand thickness of the QDs is around 1.74 nm considering the average diameter of the QDs from the TEM image analysis. The superlattice undergoes a further collapse during the next 2 s with a lattice spacing of 8.60 nm, meaning that the thickness of the ligand shell decreases to 1.60 nm (Figure 6.14). Further variations of

the superlattice parameters are also found to give rise to additional Bragg peaks showing up as seen in Figure 6.12(c). A body-centered cubic (BCC) superlattice model with lattice parameters of $a = b = c = 6.60$ nm and $\alpha = \beta = \gamma = 90^\circ$ is found to match these additional scattering peaks very well, especially for the 200_{SL} peak in the BCC superlattice, in which the $(110)_{SL}$ plane is parallel to the substrate. The agreement indicates that the final QDs have nested superlattice structures with both FCC and BCC packing as indicated in Figure 6.12(e). Moreover, the effective ligand thickness of the QDs in the BCC structure is further decreased to 1.42 nm, which is calculated based on the superlattice distance of $(111)_{SL}$ in the BCC superlattice. Notably, these results differ slightly from the in-plane line cut analysis of the GISAXS data due to the used superlattice approximation. QDs are treated as spherical particles in the superlattice stacking as a simplification in the ligand thickness calculation. The crystal lattice orientation analysis (Figure 6.2) indicates that QDs reveal a specific orientation of the facets, which is in good agreement with previous research. [31, 42] This BCC packing originates from the shape of the QDs in dry conditions. Since the ligands are collapsed and the QDs reveal more a behavior like truncated octahedrons, a BCC stacking tendency is found. However, the QDs superlattice in the final dry film still mainly remains an FCC stacking character. This means that the QDs still mainly have a sphere-like stacking behavior due to the large ratio of ligand thickness over the average radius of the QDs.

A quite similar stacking behavior of the QDs is found when the printing is done on a different substrate using the same printing parameters as seen in Figure 6.4.

6.9 Conclusions

In conclusion, in situ monitoring of the kinetics of the QD assembly during printing with in situ GISAXS allows to derive the nanoscale structure formation including a superlattice analysis. The QDs undergo a fast superlattice formation on the second time-scale and a phase transition process during the deposition and solvent evaporation. The stacking behavior of the QDs is initialized by a hexagonal templating effect and their subsequent FCC stacking behavior originates from the large ratio of the ligand thickness over the radius of the QDs due to their small size. With ongoing solvent evaporation, the ligand shell exhibits a further collapse, which impacts on the shape of the QDs. The effective shape of the QDs is considered to play an important role in the finally formed superlattice. With further decreased inter-QD distance and distorted orientation distribution, a BCC nested FCC superlattice finally forms. These results provide important fundamental understandings of the structure formation of thin QD films via the large-scale deposition method printing, based on small-sized QDs. Moreover, the ligand-dependent kinetics of

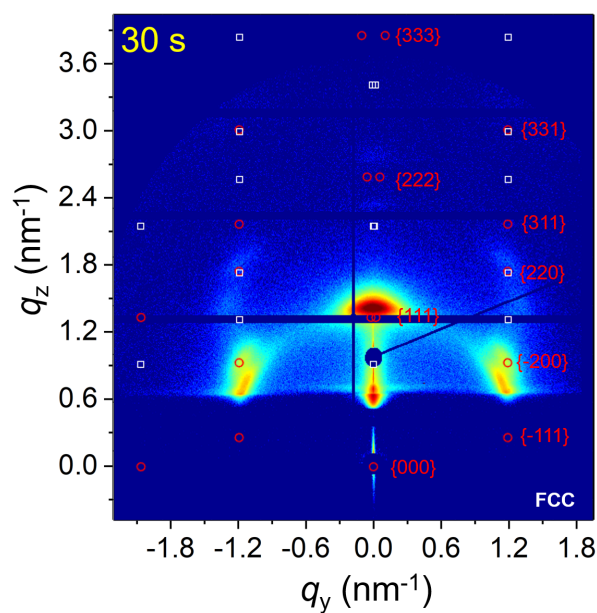


Figure 6.14: 2D GISAXS image of printed film at $t = 30$ s with predicted Bragg peak positions as indicated with white (reflected) and red (diffracted) points based on the FCC superlattice calculation with lattice parameters $a = b = c = 8.6$ nm and $\alpha = \beta = \gamma = 90^\circ$. Reproduced from Ref [41] with permission from the Royal Society of Chemistry.

the QDs also infers that a control of the stacking behavior of QDs via a ligand engineering will also be possible.

7 Spray-deposited QD solid for near-infrared photodetector

Parts of this chapter were prepared in collaborations with Southern University of Science and Technology (SUSTech), Shenzhen, University of Macau, Macau, China, University of Birmingham, UK, and are published in: "Spray-deposited PbS Colloidal Quantum Dot Solid for Near-Infrared Photodetectors" (Chen, W.; *et al.*, Nano Energy, 2020, 105254, DOI: 10.1016/j.nanoen.2020.105254). Reprinted (adapted) with permission from ref [72]. Copyright (2020) Elsevier Ltd.

7.1 Motivations and main discoveries

Colloidal PbS quantum dots (QDs) are promising candidates for various optoelectronic applications based on solution-processed thin-film techniques. In this work, a versatile layer-by-layer (LBL) spray deposition of the QDs is introduced aiming for a future large-scale fabrication process of optoelectronic devices. As compared to spin-coated QD solids, a smaller inter-dot distance and a better-ordered superlattice stacking behavior of the QDs is found in the spray-deposited QD solids as confirmed by grazing-incidence small-angle X-ray scattering (GISAXS). The spectral mapping combined time-resolved photoluminescence analysis indicates a longer carrier lifetime and better order energy state distribution of the spray-deposited QD solid comparing with the spin-coated solid. Thus, photodetectors based on spray deposition of QD solids demonstrate an excellent device performance, with the responsivity achieving 365.1 A/W and the detectivity reaching up to 1.4×10^{12} Jones under an illumination power of $63.5 \mu\text{W}/\text{cm}^2$ at a wavelength of 1250 nm. The spray-deposited device performances indicate a great potential of spray deposition of large sized QDs in large-scale fabrications for optoelectronics using longer wavelengths.

7.2 Introduction of QD photodetector

Colloidal quantum dots (QDs) have demonstrated great potential in solution-processed thin-film optoelectronics, including light-emitting diodes, [6, 83] photodetectors, [8, 9, 120, 133] transistors, [85–87, 134] and photovoltaic devices, [12, 13, 74, 79] mainly due to their tunable bandgap, which covers an extremely large range from visible to near-infrared (NIR). [107, 108] Moreover, their solution processability makes them compatible with various thin-film deposition methods, such as, spin coating, printing, and spray deposition, in which the surface ligands of the QDs and the ligand exchange mechanisms play a crucial role in the films' deposition and its designable functionalization. [17, 41, 49] Intrinsic colloidal state QDs are capped by long-chain organic ligands, which helps to obtain size monodisperse QDs during the synthesis and also to maintain the solubility of the QDs in different solvents. [135] These ligands give the QDs a semi-soft material character and induce the formation of a superlattice in QD self-organized assemblies, which is driven by the uniform distance between neighboring QDs and the system entropy. [35] However, the existence of long-chain ligands also results in a weak electronic-coupling configuration in the films out of ligand capped QD assemblies. [136] The long-chain ligands inevitably form high barrier potentials which significantly decreases the overlap of the wave-functions between neighboring QDs by their spatial separations, thereby depressing their energy transport. [96, 137] The ligand exchange engineering is performed normally for the purpose of decreasing the inter-distance of neighboring QDs, which is the key step to functionalize the QD solid to reach an improved electronic-coupling behavior and thus a better energy transport configuration. [70, 99, 138, 139]

In the literature, two main strategies for ligand exchange of QDs are intensively studied. The one strategy is based on performing the ligand-exchange treatment in the solution of the QDs with a specific phase separation process, in which the QDs will be transferred from a long-chain-ligand capped state to an ion capped state. [48, 76, 119, 140] The as-formed QD ink can be deposited in a single step, and directly forms a functionalized active layer with excellent optoelectronic properties. Another strategy is making use of a post-ligand-exchange treatment on the as-deposited solid-state films. [22] To completely exchange all organic ligands out of the QDs, the multi-deposition process is typically described as a layer-by-layer (LBL) method combining the ligand exchange treatment and rinsing processes afterwards on each single layer, which is considered as an effective strategy in various deposition processes, including spin coating as well as spray deposition. Besides, also the hybrid strategy, based on solution ligand-exchanged QDs being deposited in an LBL process, also demonstrated good device performances. [23, 36] To fully exploit the potential of large-scale deposition methods, like printing and spray deposition, the QD inks are still facing many challenges. Specifically, the perovskite modified inks significantly rely

on large amounts and costly high-quality dehydrate PbX_2 ($X = \text{I}$ or Br). Moreover, the solution ligand-exchanged QD particles (ion capped QDs) are easily aggregated becoming sediments and their metallic affinity results in pipe blockages in the deposition facilities (specifically in print head or spray nozzle). Therefore, the deposition of organic ligand capped QDs, specifically by spray deposition, is still much easier and very well compatible with future large-scale deposition fabrication, [41, 64, 141] which is believed to be highly promising for future thin-film optoelectronic applications based on QDs.

In this work, spray deposition of oleic acid capped PbS QDs is introduced as a facile and potentially large-scale deposition method for high-performance photodetectors. Specifically, the structural disorder, as well as energetic state disorder, of the QD solids are investigated via grazing incidence X-ray scattering technique and time-resolved photoluminescence (TR-PL) spectroscopy respectively. After the spray deposition of a single QD layer, a post ligand exchange treatment by tetrabutylammonium iodide (TBAI) in methanol is performed on this layer to achieve an electronic coupled QD solid single layer. [8, 19, 23, 24, 31, 76] Then a rinsing treatment is carried out on the film surface to terminate a single deposition step. The final thickness of the whole QD layer is determined by the number of deposition steps in the LBL process. For reference, the spin coating based LBL deposition of the QDs is also performed to obtain QD solids and the related QD devices. The inner structures including the inter-dot distance of neighboring QDs and the structure, in the deposited QD solids, are studied by grazing-incidence small-angle X-ray scattering (GISAXS). Also, the facet orientation of the QDs in the solids are characterized by grazing-incidence wide-angle X-ray scattering (GIWAXS). Moreover, the structure induced different charge carrier dynamics and the energy states distribution are studied by spectral mapping combined TR-PL spectroscopy. In addition, photodetectors are fabricated based on spin-coated and spray-deposited QD solids and the respective device performances are compared and discussed. It turns out that the spray-deposited QD solid devices exhibit a better photodetector performance with apparent lower cost than spin-coated one.

7.3 Experimental details

Synthesis of colloidal PbS quantum dots: The synthesis of the QDs was carried out following the previous literature with slight modifications, [73] which is briefly described as follows: 0.446 g PbO was loaded into a three-neck-flask mixing with 3.8 mL oleic acid (OA) and 50 mL octadecene (ODE). The atmosphere inside of the flask was changed to inert gas by alternatively evacuation filling argon for several times. The mixture was then heated up to 150 °C and the solution was transformed into a transparent liquid as the lead

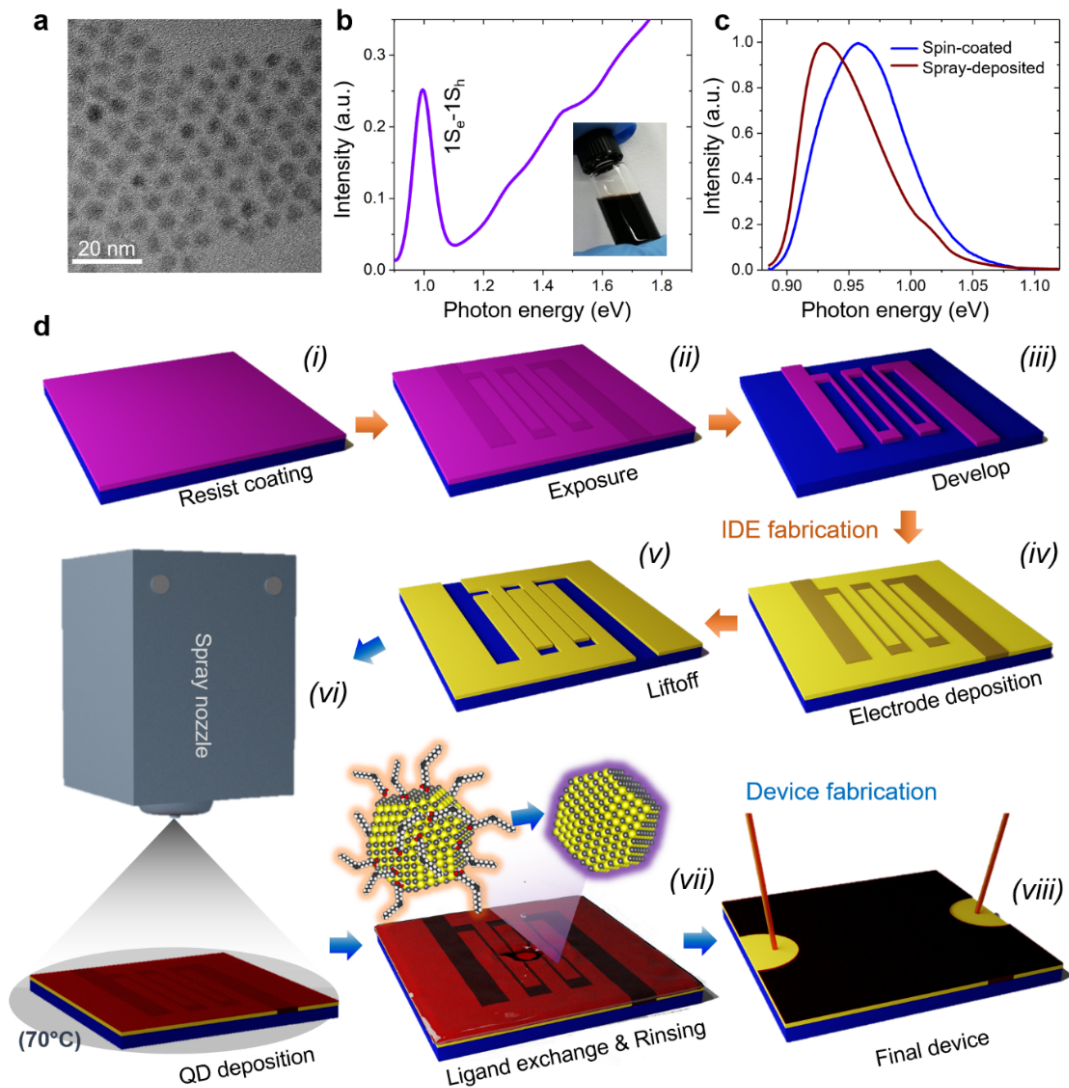


Figure 7.1: (a) Representative TEM image of as-prepared PbS QDs. (b) Absorption spectrum of the QDs in octane with a concentration of 25 mg/mL (inset: photograph under room light illumination). (c) PL spectra of as-deposited close-packed QD solids via spin coating (blue) and spray deposition (red), respectively. (d) Schematic for the photodetector device fabrication processes, including the inter-digital electrode (IDE) substrate by a lithography process (i-v), QDs' deposition process via spray deposition (vi) and the ligand exchange treatment process (vii) and final device (viii). Reprinted (adapted) with permission from ref [72]. Copyright (2020) Elsevier Ltd.

precursor. The temperature was decreased to 100 °C for a 6-hours degassing process in the evacuated state, in which the moisture inside of the solvent was completely removed. The sulfur precursor was prepared by dissolving (TMS)₂S into ODE. After degassing, the argon was filled into the flask again and the sulfur precursor of 90 μL (TMS)₂S in 3 mL ODE was quickly injected into the lead precursor. The solvent transformed into dark immediately due to the nucleation and growth of the QDs. The reaction lasted for 8 min and another amount of sulfuric precursor (25 μL (TMS)₂S in 3 mL ODE) was continuously injected into the flask to perform the second-step growth of QDs, and the growth also lasted for 8 min. Then the last 25 μL (TMS)₂S in 3 mL ODE was injected and 8 min further growth was terminated by quenching in an ice-bath and injection of 10 mL hexane simultaneously. The QDs were then purified by acetone and dried by evacuation. QDs were then dispersed into octane with a concentration of 50 mg/mL for the further deposition.

IDE Fabrication Protocol: A 4-inch silicon wafer, with a 300 nm thick thermal oxide layer (SiO_x), was used as the substrate for the IDE fabrication. For the photolithography process, double layer resists were deposited respectively with parameters as follows. Firstly, the LOR7A (MicroChem, USA) layer was spin-coated on the substrate with the speed of 5000 rpm for 30 s, which was then baked at 170 °C for 8min. Afterwards, the RZJ-304 (Suzhou Ruihong, China) as the second layer was deposited with the spin-rate of 4000 rpm for 30 s, then the substrate was baked at 100 °C for 90 s. The exposure process was carried out with the light dose of 40 mJ/cm². The substrate was developed with RZX-3038 (Suzhou Ruihong, China) for 80 s, rinsed with deionized water then baked at 100 °C for 5 min. A descum process was performed by 20 s inductively-coupled plasma (ICP) O₂ etch treatment. The deposition rate for Cr was set at 0.67 Å/s to achieve a 5 nm thickness metal layer and followed with the deposition of gold, with a rate of 1.67 Å/s, to achieve a 100 nm thick layer. The Liftoff process was performed by immersing the substrate in hot Dimethyl sulfoxide (DMSO) (at 80 °C) for more than one hour then rinsing with DI water.

Spray set-up and fabrication of sprayed samples: The spray deposition was performed by 1 MPa N₂ pulses with an air atomizing nozzle. The distance between the nozzle and substrate was set to 20 cm. The duration of each pulse was at 0.2 s with 2.8 s second waiting time afterwards before the next pulse. The used QDs had been diluted into 25 mg/mL. To accelerate the films' drying process, the substrate was placed on a heating plate with a constant temperature of 70 °C during the spray deposition. Two continuous pulses were applied during the deposition as one layer before the ligand exchange treatment by tetrabutylammonium iodide (TBAI) in methanol (10 mg/mL) for 30 s. A rinsing process was then performed to remove the residuals for the second

layer spray deposition. In total, 5 QD layers were performed, accomplishing the whole deposition. The thicknesses of the spray-deposited QD solids were 479 ± 35 nm, which were significantly smaller than the channel width of the IDE ($5 \mu\text{m}$).

Fabrication of spin-coated sample: The spin coating process of the QDs was performed by a conventional method with a QD concentration of 50 mg/mL and the spin-rate of 3000 rpm for 10 s. The ligand exchange treatment afterwards was performed by solution casting of TBAI-methanol solvent on the QD layer for 45 s. The residuals were then removed by the rinsing process twice with pure methanol. The process had been repeated 4 times to reach the final solid thickness via an LBL method. The spin-coated QD solids were annealed at 70°C for 300 s after the LBL process. The thicknesses for the spin-coated QD solids were 144 ± 4 nm.

X-ray measurements: The static GISAXS and GIWAXS measurements for ligand exchange QD solids were performed by an in house SAXS machine Ganesha SAXS300L with the X-ray photon energy of 8.05 keV (the corresponding wavelength = 1.54 \AA). The sample-detector distances (SDDs) for GISAXS and GIWAXS were 1045 mm and 95.7 mm respectively and a Pilatus 300 K was used as the detector for both GISAXS and GIWAXS measuring, having a pixel size of $172 \mu\text{m} \times 172 \mu\text{m}$. The incident angle was set to 0.35° . TR-PL mapping measurements: The TR-PL measurements, with a spectral mapping range of 1100 nm to 1400 nm, were performed by a FluoTime300 fluorescence lifetime spectrometer (PicoQuant). The wavelength for excitation was 405 nm. The substrates for the TR-PL measurements were SiO_x/Si wafers with a SiO_x layer thickness of 300 nm.

Photodetector characterization: The fabricated photodetectors were characterized using a SOFN7-SCF06A/B probe station connected with a Keithley 4200. The Samples were illuminated by a halogen light source Zolix TLS2-T250-DZL and the light intensity was acquired by Thorlabs PM100D with relevant sensors.

7.4 Structural analysis by GIXS

The QDs have been synthesized according to previous work with modifications as seen in the experimental section. [73] The size distribution of the QDs is characterized by transmission electron microscopy (TEM) as seen in Figure 7.1(a). The average size is estimated as 5.07 ± 0.44 nm, which is derived from the statistical data analysis by fitting a Gaussian function as seen in 7.2. Figure 7.1(b) shows the absorption spectrum of the QDs in octane with the first exciton (1Se-1Sh) peak energy at 0.99 eV (corresponding to a wavelength of 1250 nm at the peak position), which means photons with a rather large photon energy are all able to be probed in our device architecture. In addition, a narrow spectral peak feature reveals that the QD particles exhibit a narrow-distributed

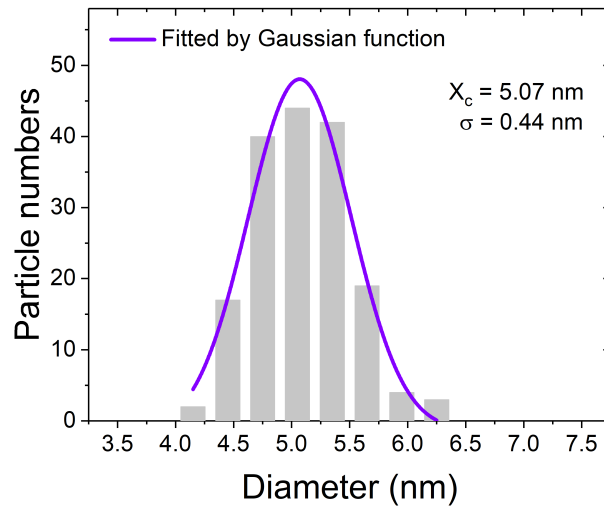


Figure 7.2: Histogram data derived from the TEM image analysis of PbS QDs which is fitted by a Gaussian function. According to the fitting results, the average diameter of the QDs is 5.07 nm and the standard deviation is 0.44 nm. Reprinted (adapted) with permission from ref [72]. Copyright (2020) Elsevier Ltd.

bandgap of the 1Se-1Sh transition. A photograph of the QDs in octane in room light demonstrates the excellent absorption behavior for photons in the visible range. 7.1c shows the photoluminescence (PL) spectra of the QDs solids prepared by spin-coating and spray deposition, respectively. The spray-deposited QD solid reveals a lower photon energy of the radiative recombination center (peak) than the spin-coated solid, which is due to the better energy transfer configuration. [31] Moreover, the spin-coated QD solid demonstrates a broader emission line-width than that of the spray-deposited QD solid, which is due to an inhomogeneous broadening effect. [29] Detailed physics insights of the spectra will be discussed in association with the structure study and energy state analysis in the following parts. 7.1d illustrates the final QD solid or the device fabrication process, in which the inter-digital electrode (IDE) of gold on a Si wafer with a gap-width of $5 \mu\text{m}$ is realized by a lithography process (i-v) as seen in the experimental section. The spray deposition (vi) is driven by high-pressure N_2 pulses with a constant gas pressure of 1 MPa. The spray pulse duration is set to 0.2 s and a waiting time of 2.8 s is selected afterwards for film drying to operate in the dry spray regime. The spray cone angle is approximately 10° which is calculated from the height between the nozzle and the substrate (~ 20 cm) and the effective spray region (diameter ~ 7 cm). The substrate holder is heated to a constant temperature of 70°C during the spray deposition to accelerate the evaporation of the solvent. Notably, a lower temperature of the substrate would result in the initial film being ruined by the following spray flow in the current setup configuration. During

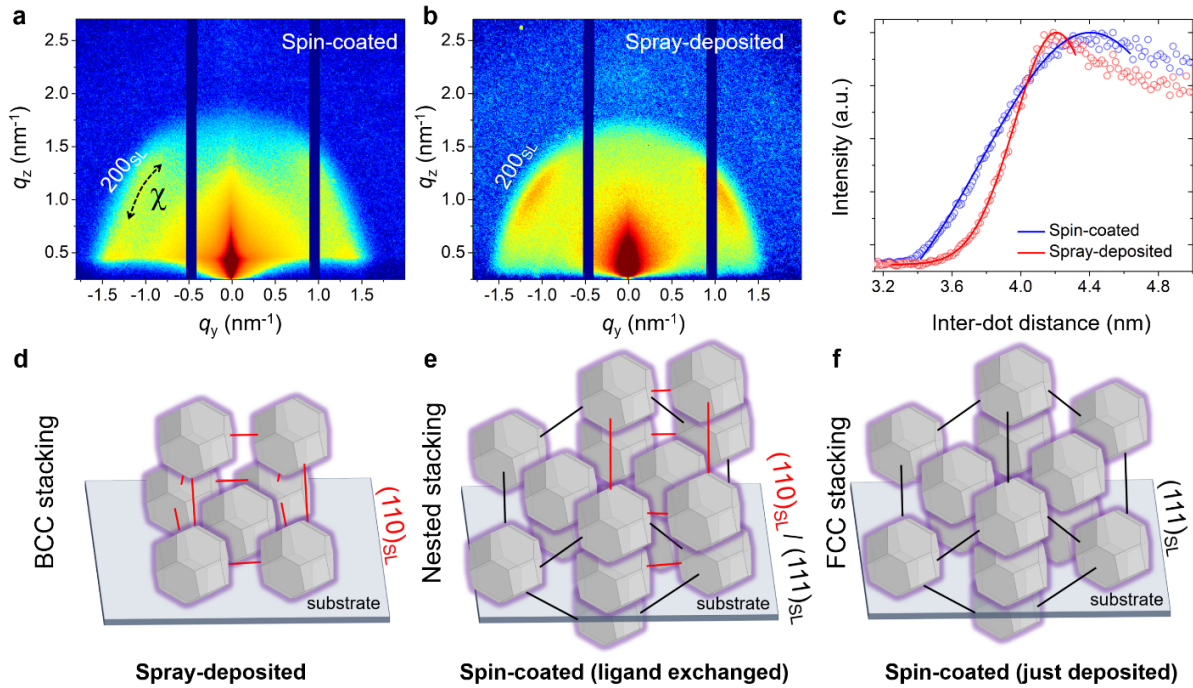


Figure 7.3: 2D GISAXS data of a) spin-coated solid b) spray-deposited QD solid. c) Inter-dot distance evaluation of the QDs derived from the azimuthal integration. Superlattice schematics for d) BCC stacking (red frame), (e) BCC nested FCC stacking and (f) FCC stacking (black frame). Reprinted (adapted) with permission from ref [72]. Copyright (2020) Elsevier Ltd.

the deposition process, the ligand exchange treatment (vii) is integrated into the LBL method. Details are described in the experimental section, in which also the preparation of the LBL spin-coated reference QD solid as well as of the photodetector devices are described. To make both device types (spray-deposited and spin-coated QD solids based) comparable, the spin-coated QD solid was also annealed at 70 °C for 300 s after the LBL process.

The inner structure of the ligand-exchanged QD solids prepared by spin-coating and spray deposition is studied with GISAXS. 7.3a and 7.3b illustrate the 2D GISAXS data of the final spin-coated and the spray-deposited QD solids, respectively. The overall inter-dot distance of the QDs is studied by azimuthal integrations as seen in Figure 7.3(c). The QDs inside of the spray-deposited solid exhibit a smaller inter-dot distance of 4.2 ± 0.2 nm than that of the QDs in the spin-coated solid (4.4 ± 0.6 nm). Since the QDs have the same size distribution, a smaller inter-dot distance of the QDs provides the spray-deposited QD solid with a stronger electronic-coupling property, which results in hybridized band-edge orbitals and corresponding relaxed quantum confinement effects,[23] and also explains the red-shift in the emission spectra in Figure 7.1(c). Notably, the spray-

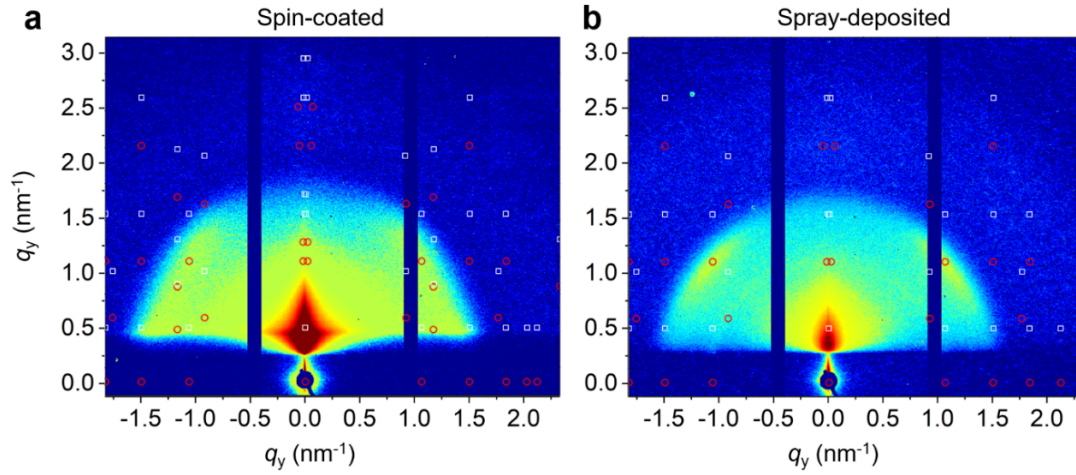


Figure 7.4: 2D GISAXS data of (a) the spin-coated QD solid with BCC nested FCC stacking; and (b) the spray-deposited QD solid with BCC stacking, in which the scattering dots are based on standard lattice parameters of $a = b = c = 8.8$ nm, $\alpha = \beta = \gamma = 90^\circ$ for FCC stacking and $a = b = c = 8.4$ nm, $\alpha = \beta = \gamma = 90^\circ$ for the BCC stacking, and. The white spots are from the reflection and red spots are based on transmission. Reprinted (adapted) with permission from ref [72]. Copyright (2020) Elsevier Ltd.

deposited QD solid also reveals a narrower distribution of the inter-dot distances, which indicates more uniform electronic coupling behavior. Moreover, the broader distribution of the inter-dot distance in the spin-coated QD solid leads to the inner inhomogeneous energy state distribution. The stacking behavior of the QDs in solids prepared by the different deposition methods are analyzed by diffraction peak calculations, which are based on standard superlattice models as seen in Figure 7.4. A superlattice distortion is suspected in the spin-coated QD solid. While, a clear body-centered cubic (BCC) stacking of the QDs, with the $(110)_{SL}$ plane parallel to the substrate, is observed in the spray-deposited QD solid, which can be described by Figure 7.3(d), in which the subscript “SL” denotes superlattice. The distorted superlattice in the spin-coated QD solid has been explained by the “BCC nested face-centered cubic (FCC)” stacking behavior as described by Figure 7.3(e), in which the $(110)_{SL}$ plane of the BCC and $(111)_{SL}$ plane of the FCC are equal and both are parallel to the substrate. A full FCC model, with the $(111)_{SL}$ plane parallel to the substrate, is also provided in Figure 7.3f for further discussion. The orientation distribution of the superlattice is measured by tube cuts in the range of $1.4 \text{ nm}^{-1} < q < 1.6 \text{ nm}^{-1}$. The ligand exchanged QD solids demonstrate a distinguished feature of the BCC stacking property with the 200_{SL} peak orientation at $\chi_{200_{SL}} = 45.7^\circ$ in the spray-deposited QD solid and $\chi_{200_{SL}} = 45.1^\circ$ for the spin-coated QD solid as seen in Figure 7.5, which is in good agreement with the intersection angle between the

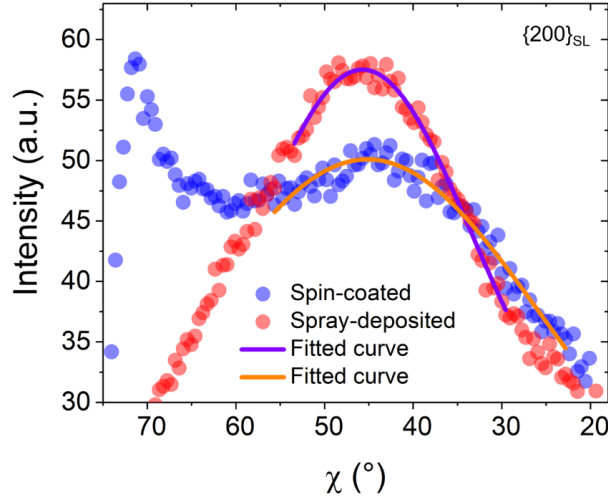


Figure 7.5: Tube-cuts of the 2D GISAXS data for the spin-coated (blue) and spray-deposited (red) QD solids with respective Gaussian fit functions (solid lines) to derive the orientation distributions. Reprinted (adapted) with permission from ref [72]. Copyright (2020) Elsevier Ltd.

$(200)_{SL}$ plane and $(110)_{SL}$ plane in a BCC model when the $(110)_{SL}$ plane is parallel to the substrate (Figure 7.3(d)).

The distribution is described by the standard deviation from the Gaussian function and it amounts to $\sigma_{spray200SL} = 12.3^\circ$ for the spray-deposited QD solid, which is significantly smaller than $\sigma_{spin200SL} = 27.4^\circ$ for the spin-coated QD solid. These results suggest that the QDs have a better aligned stacking behavior in the spray-deposited QD solid, this is due to the spin-coating is a “fast-freezing” deposition with a very short time for the particle self-organization compared with the spray-deposition. Notably, similar comparison is shown in literature, [64] the difference of the spray-deposited solid in this work shows a distinguished BCC superlattice feature, which is contributed by the larger-sized QDs with a higher radius over ligand ratio. [34, 41]

Moreover, our previous research indicates, that the spin-coated QDs exhibit an FCC stacking behavior, and it changes to a BCC stacking to minimize the surface area during the ligand exchange treatment. [31, 41] Interestingly, the additional GISAXS experiments, based on the one-layered QD films via different deposition methods and without ligand-exchange treatments, suggest that the initial deposition process significantly influences the final QD stacking as seen in Figure 7.6.

According to the superlattice analysis, the FCC stacking of the QDs is formed by the spin-coating process, and a direct BCC stacking behavior is formed during the spray deposition due to long-time self-organization which matches well with the self-organization process described in the literature, [42] Moreover, the better-aligned stacking of ligand

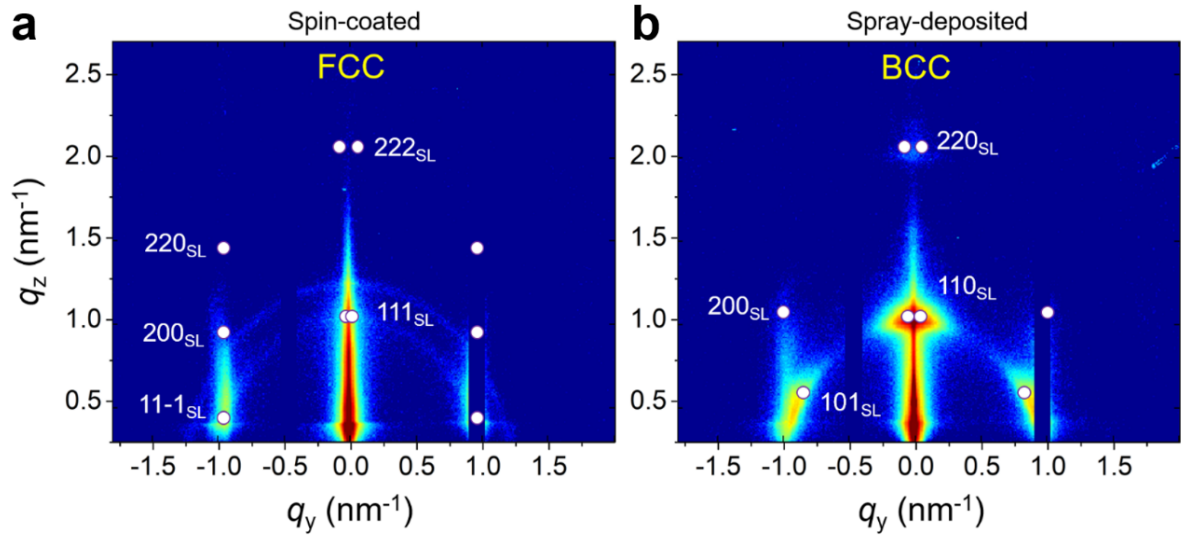


Figure 7.6: 2D GISAXS data of one-layered QD films prepared via different deposition methods spin-coating (a) and spray deposition (b) and without ligand exchange treatment. The white spots are the calculated superlattice scattering peaks with superlattice parameters of $a = b = c = 10.5$ nm, $\alpha = \beta = \gamma = 90^\circ$ for the FCC stacked QDs in spin-coated film ($(111)_{SL}$ is parallel to the substrate), and $a = b = c = 8.8$ nm, $\alpha = \beta = \gamma = 90^\circ$ for BCC stacked QDs in spray-deposited film ($(110)_{SL}$ is parallel to the substrate). Reprinted (adapted) with permission from ref [72]. Copyright (2020) Elsevier Ltd.

capped QDs can also result in a better stacking behavior of ligand exchanged QDs in the close-packed QD solid. During the ligand exchange treatment, the long-chain ligands are removed and bare inorganic QDs with truncated octahedral shape always prefer to form a BCC structure according to the Wigner-Seitz close packed constriction, which is driven by the entropy increase of the QD ensemble. [29,35] Therefore, an incomplete phase transition in the ligand exchange treatment is considered to lead to the nested stacking behavior seen before in the spin-coated solid. [31,64]

To further confirm the stacking disorder, sector-integrations are performed at selected orientation ranges. To large-sized QDs induced better-ordered configuration, the scattering from the superlattice can contribute the featured peak significantly, such as $\{200\}_{SL}$ in a BCC layout and $\{200\}_{SL}$ and $\{220\}_{SL}$ in an FCC superlattice layout. Therefore, the sector-integrations are performed separately in ranges of $40^\circ < \chi_{200SL} < 50^\circ$ for the BCC lattice (the theoretical peak orientation is at 45.0°) and $50^\circ < \chi_{200SL} < 60^\circ$ for the FCC lattice (the theoretical peak orientation is at 54.7°) in order to find out the inter-superlattice distances from different potential stacking behaviors. The spray-deposited QD solid apparently reveals a smaller inter-superlattice distance of $\{200\}_{SL}$

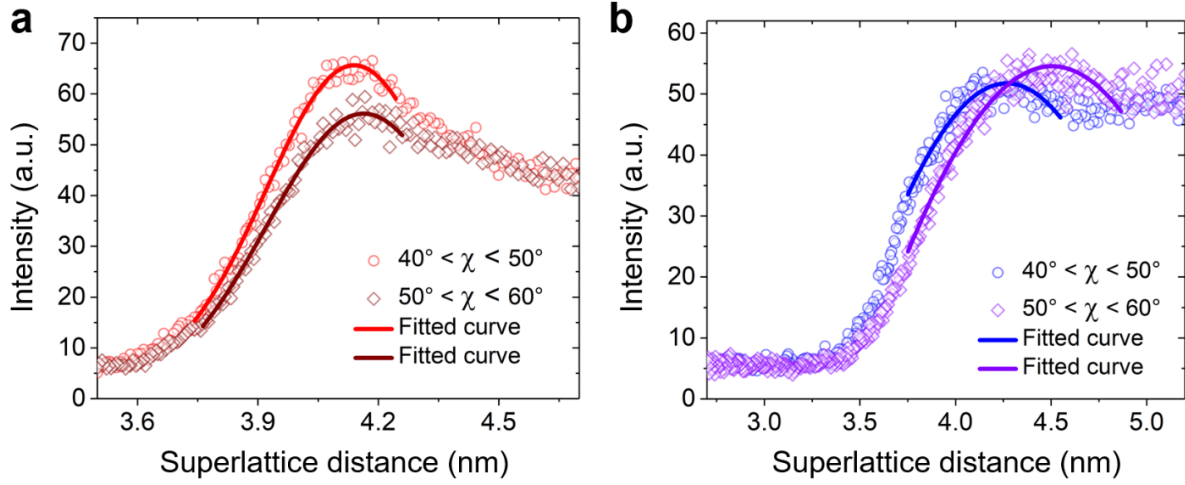


Figure 7.7: Superlattice distances derived from the sector integrations of 2D GISAXS data for (a) the spray-deposited QD solid and (b) the spin-coated QD solid. Reprinted (adapted) with permission from ref [72]. Copyright (2020) Elsevier Ltd.

with a narrower distribution than that of the spin-coated QD solid, which matches well with the azimuthal integration data shown in Figure 7.3(c). This finding indicates an excellent short-range order layout of the QDs in the spray-deposited solid, resulting in an expected strong electronic coupling effect. In Figure 7.7(a), for the spray-deposited QD solid, the scattering intensity of the 200_{SL} peak decreases significantly when changing the integration angle range from BCC to FCC, which means that the BCC layout of the QDs dominates the QD stacking in the spray-deposited solid. The dominant BCC layout explains the closer and narrower distributed inter-dot distance of the QDs in the spray-deposited QD solid as compared to the spin-coated QD solid, which is also due to the shape of the individual QDs. [31, 34] As seen in Figure 7.7(b), for the spin-coated QD solid, the scattering intensity of the 200_{SL} peak in the FCC layout exhibit similar intensity with the 200_{SL} peak in the BCC layout. Thus, to QDs in the spin-coated solid, the BCC and the FCC stacking are highly mixed resulting in a broader distribution of final inter-dot distance and orientation in Figure 7.5, resulting in a more inhomogeneous energy state.

The inner lateral structures of the QD solids prepared by the different depositions are determined from modelling the horizontal line-cuts of the 2D GISAXS data taken at the Yoneda peak positions. In the vertical line-cuts of the 2D GISAXS data (7.9a) the Yoneda peak appears at $\alpha_f = 0.18^\circ$ for the spray-deposited QD solid and at $\alpha_f = 0.23^\circ$ for the spin-coated QD solid. Notably, the specular reflection peak is completely smeared-out due to the rough surface of the spray-deposited QD solid, which also results

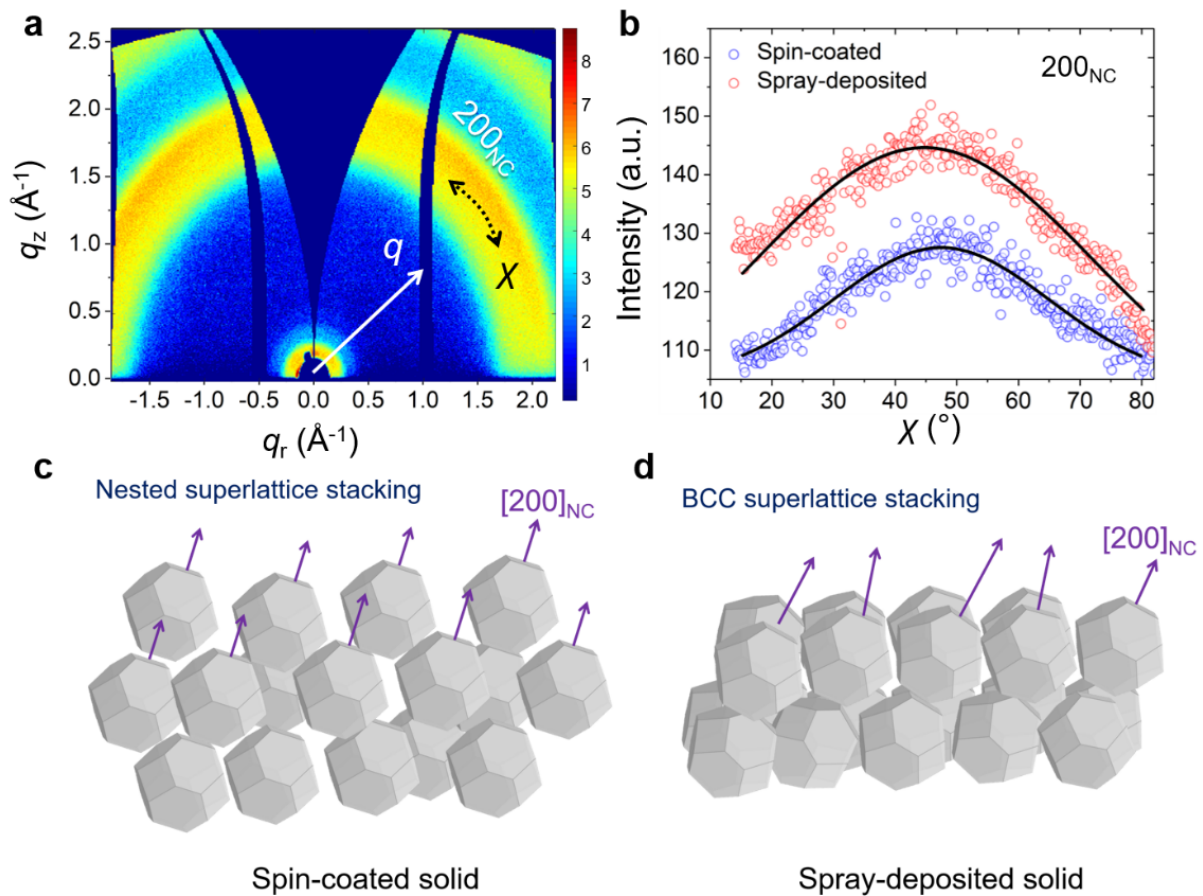


Figure 7.8: (a) 2D GIWAXS data of spray-deposited QD solid. (b) Orientation distribution data presented by the tube cuts ($1.97 \text{ \AA} < q < 2.17 \text{ \AA}$) of QD solids prepared via spin-coating (blue) and spray deposition (red). Schematics of orientation of individual QDs causing the 200_{NC} Bragg peak orientation distributions in (c) the spin-coated QD solid and (d) the spray-deposited QD solid (purple arrows indicate the $[200]_{\text{NC}}$ facet directions of individual QDs). Reprinted (adapted) with permission from ref [72]. Copyright (2020) Elsevier Ltd.

in the lower effective film density at the scale of the X-ray illuminated area causing the lower angle Yoneda peak position. [69] The respective horizontal line cuts are shown in Figure 7.9(b). For modelling, cylinders with large radii and spheres with small radii are used to describe large QD aggregates and all single QDs, respectively. [142] The model parameters are listed in Table 7.1. Besides a scattering signal from the individual QDs, in case of the spray-deposited QD solid a scattering signal from QD aggregates with a radius of $22.6 \pm 9.9 \text{ nm}$ and in case of the spin-coated QD solid one from a large structure with a radius of $220.3 \pm 79.2 \text{ nm}$ can be seen in Figure 7.9(b). The smaller-sized structure formed by QD aggregation in the spray-deposited QD solid is also confirmed by scanning

Sample	$R_L(nm)$	$D_L(nm)$	$R_M(nm)$	$D_M(nm)$	$R_{QD}(nm)$	$D_{QD}(nm)$
Spin	220.3 ± 79.2	520 ± 161.2	22.6 ± 9.9	57.0 ± 24.5	2.1 ± 0.2	4.2 ± 0.4
Spray	18.0 ± 6.5	480 ± 148.8	4.2 ± 1.0	29.0 ± 12.5	2.1 ± 0.2	4.0 ± 0.6

Table 7.1: Modeling results of horizontal line-cuts based on a cylinder model for large structures with radius R_L and medium structures with radius R_M and a spherical model for the individual QDs with a radius R_{QD} , their inter-distances are denoted by D_L , D_M and D_{QD} , respectively. Reprinted (adapted) with permission from ref [72]. Copyright (2020) Elsevier Ltd.

electron microscopy (SEM) as seen in Figure 7.9(c). In the spin-coated QD solid the large structures are separated by apparent crack boundaries as seen by SEM in Figure 7.9(d). Moreover, the size-distributions of the QDs are different from those determined from the azimuthal integration due to the improved superstructure assembly in the spray-deposited QD solid, which causes the scattering signal to appear in the out-of-plane instead of the in-plane direction.

The orientation distribution of the individual QDs in the QD solids is studied with GIWAXS as seen in Figure 7.8(a) and Figure 7.10(a) for the spray-deposited and the spin-coated QD solids, respectively. An azimuthal integration of the 2D GIWAXS data (Figure 7.10(b) shows the same crystal structure of the individual QDs irrespective of the applied deposition method. The tube cuts containing the 200NC Bragg peak in a range of $1.97 \text{ \AA}^{-1} < q < 2.17 \text{ \AA}^{-1}$ are shown in Figure 7.8(b), in which the subscript “NC” stands for the individual QD crystal. The spray-deposited QDs reveal an apparent “edge-up” behavior with the 200_{NC} Bragg peak orientation at $\chi_{200NC} = 44.7^\circ$, which means that the (110)_{NC} plane is oriented normal to the substrate. Notably, this orientation distribution is beneficial for a close-packing of QDs in a BCC configuration. In contrast, the 200NC Bragg peak in case of the spin-coated QDs exhibits an orientation at $\chi_{200NC} = 47.5^\circ$, which is due to the superlattice distortion induced facet rotations of the QDs. Nonetheless, from the Gaussian fitting results, the spin-coated QDs have an overall narrower orientation distribution with a standard deviation of $\sigma_{200NC} = 17.5^\circ$, as compared to the spray-deposited QDs with $\sigma_{200NC} = 27.4^\circ$. During the phase transition, the space for the rotation of the individual QDs is more limited in the spray-deposited solid due to the closer inter-dot distance (hard contacting) than that of the spin-coated solid (soft contacting), as illustrated in the schematics in Figure 7.8(c) and Figure 7.8(d). Even though the better-aligned facet orientation of assembled QDs is beneficial for the charge transport, [31, 54] and this would work well between the neighboring QDs or in an ideal QD solid with all well-aligned QDs inside, the practical inhomogeneity of the layout would increase the

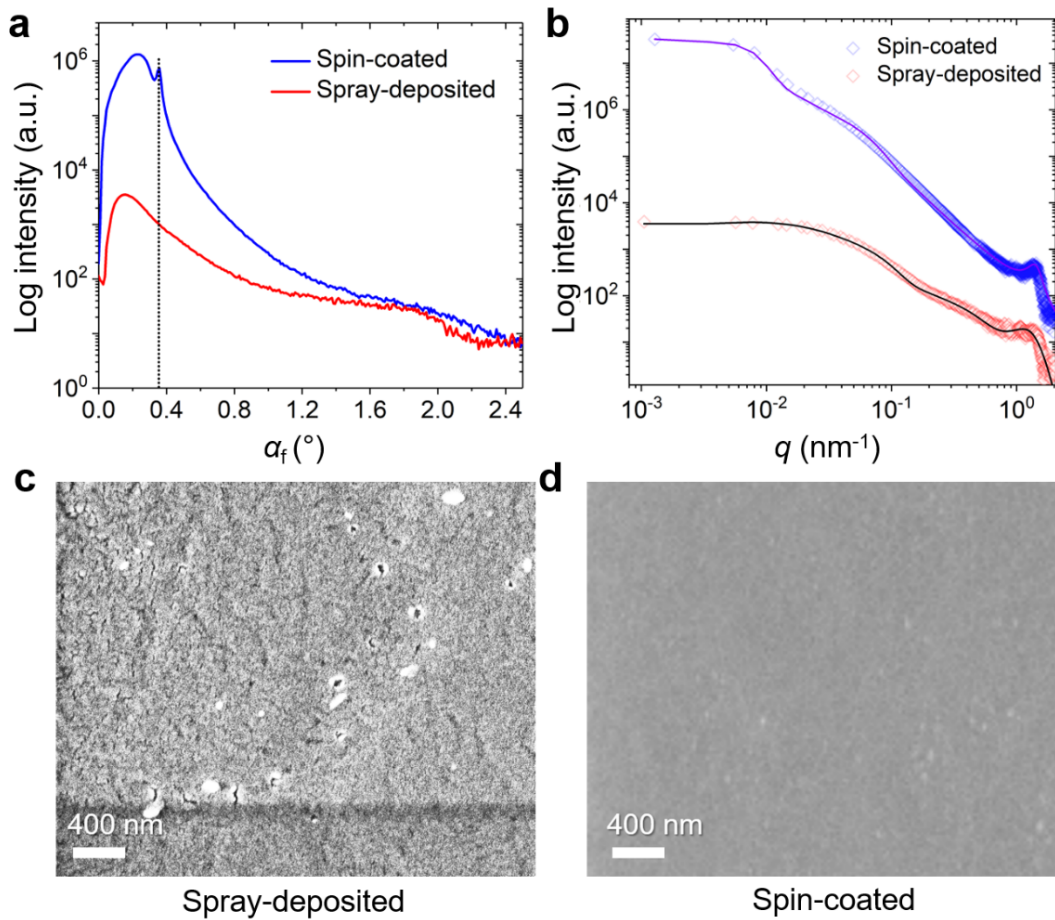


Figure 7.9: (a) Vertical and (b) horizontal line-cuts derived from the 2D GISAXS data for the spin-coated (blue) and spray-deposited (red) QD solids. The horizontal line cuts are analyzed with a model (solid lines) as described in the text with parameters listed in Table 7.1. SEM images for (c) the spray-deposited QD solid and (d) the spin-coated QD solid. Reprinted (adapted) with permission from ref [72]. Copyright (2020) Elsevier Ltd.

energy disorder and depressed the energy transport. [27] The effective carrier dynamics is not only determined by the overall inter-dot distance but also influenced by the stacking homogeneity according to the discussion as below.

7.5 Charge carrier dynamics analysis by TR-PL

To discuss the influence of the inner morphology on the energy disorder in the QD solids prepared by spin-coating and spray deposition, spectral mapping combined TR-PL spectroscopy is used to monitor the charged carrier energy diffusion and the PL lifetime,

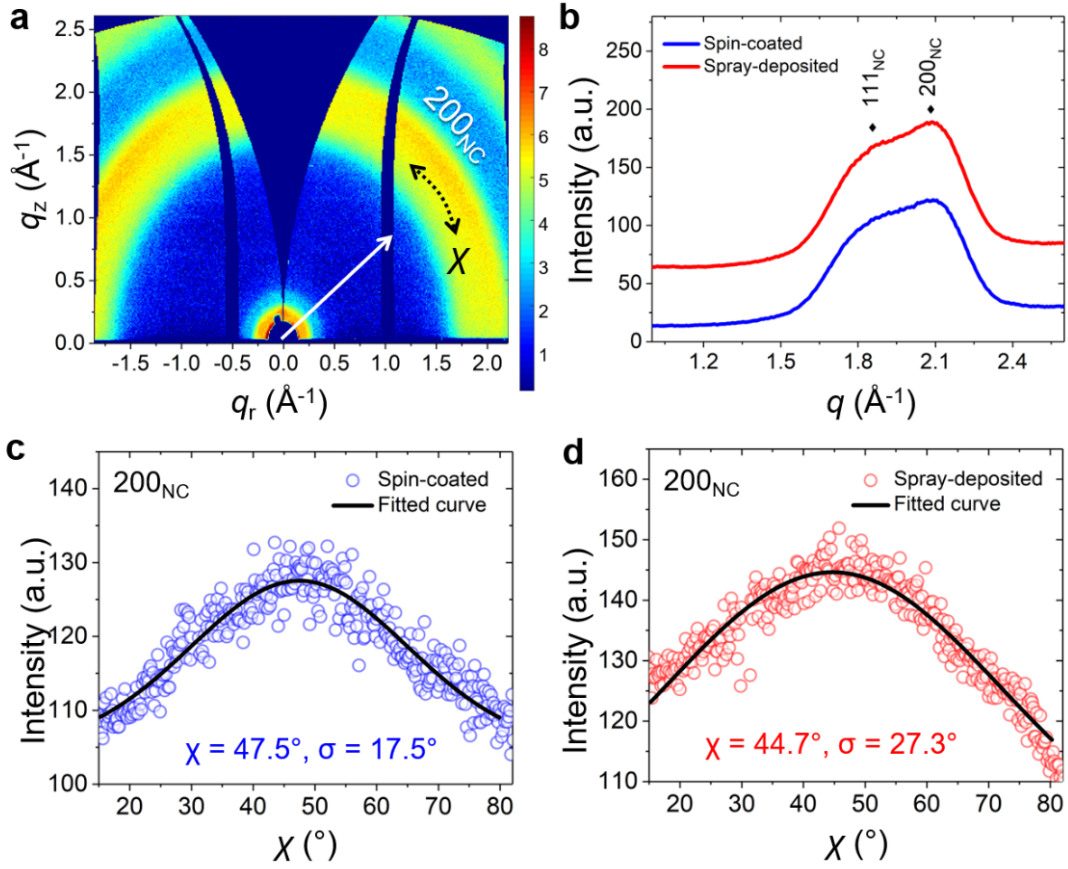


Figure 7.10: (a) 2D GIWAXS data of spin coating QD solid. (b) Azimuthal integration of 2D GIWAXS data of the spin-coated (blue) and spray-deposited (red) QD solid. Tube cuts in the range of $1.97 \text{ \AA}^{-1} < q < 2.17 \text{ \AA}^{-1}$ in 2D GIWAXS patterns for (c) the spin-coated QD solid and (d) the spray-deposited QD solid. Reprinted (adapted) with permission from ref [72]. Copyright (2020) Elsevier Ltd.

with an excitation wavelength of 405 nm. Figure 7.11(a) and Figure 7.11(b) show the 2D TR-PL mapping results for the spin-coated QD solid and the spray-deposited QD solid, respectively. The spin-coated QD solid clearly shows an inhomogeneously broadened emission line-width due to the broad energy states distribution. The charge carriers' diffusion rates are estimated by tracking the time-resolved photon energies of the 1Se-1Sh exciton peak positions, as seen in Figure 7.11(c) for the spin-coated QD solid and in 7.11d for the spray-deposited QD solid. An exponential decay function is used to fit the energy shift as seen in Equation 7.1

$$E(t) = E(0) + \Delta E \exp(-k_{\Delta E} t) \quad (7.1)$$

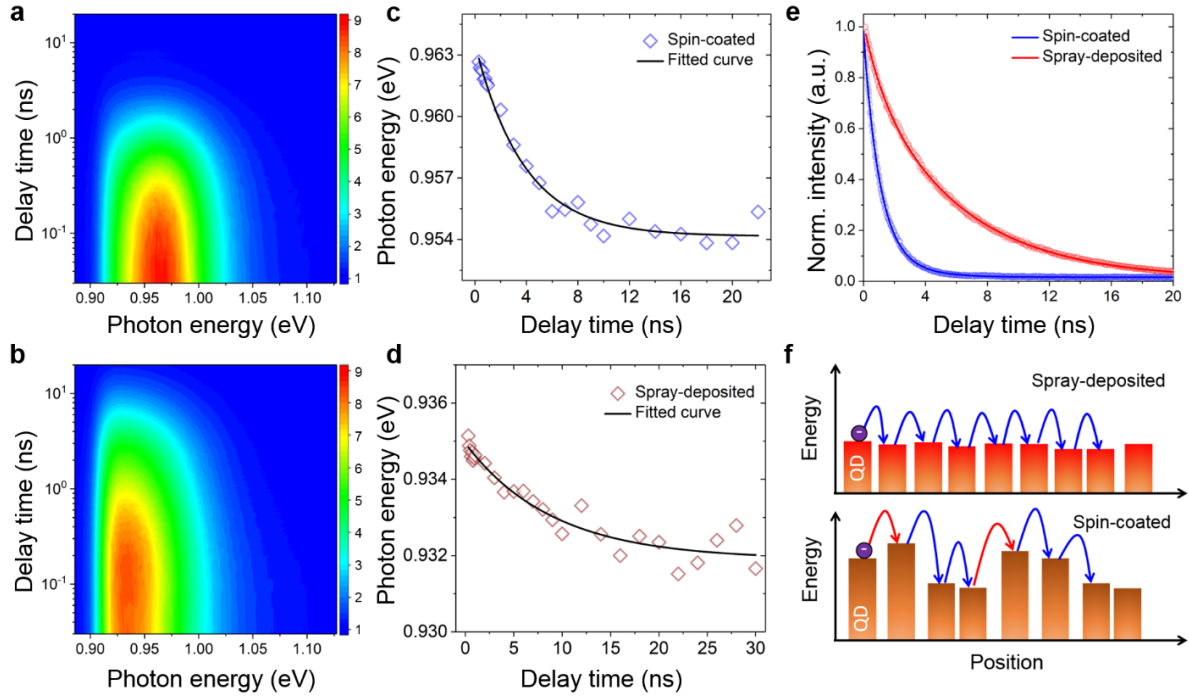


Figure 7.11: Time-resolved spectral mapping data respective to the delay time for (a) spin-coated QD solid and (b) spray-deposited QD solid. Time-resolved photon energy at emission peak positions for (c) spin-coated QD solid and (d) spray-deposited QD solid. PL lifetime at the equilibrium energy state. (e) Normalized TR-PL decays for the QD solids via different depositions. (f) Schematic of the inter-dot distance distribution influences the carrier (for instance: electron) transport, higher efficient carrier transport is supposed in spray-deposited solid than that of the spin-coated solid. Reprinted (adapted) with permission from ref [72]. Copyright (2020) Elsevier Ltd.

in which $E(t)$ represent the real-time peak energy and E_0 stands for the peak energy at equilibrium state. The term $k_{\Delta E}$ in Equation 7.1 is used to describe the charge carriers' diffusion rate from energetically downhill. The transient energy shift is denoted as ΔE and a larger value indicating the larger degree of the energetic disorder. The transient energy shift in the spin-coated QD solid is (9.4 ± 0.25) meV, which is larger than the value for the spray-deposited QD solid (3.0 ± 0.20) meV. The inhomogeneously distributed energy states are caused by the different electronic-coupling behavior in different regions, which originates from the inhomogeneously distributed inter-dot distances of the QDs, in the spin-coated QD solid. According to the fitting results, the rate value for spin-coated QD solid ($k_{\Delta E} = 0.26 \pm 0.02$ ns $^{-1}$) is higher than that of spray-deposited QD solid ($k_{\Delta E} = 0.11 \pm 0.03$ ns $^{-1}$), which is due to the larger energy gap between the non-equilibrium state

Sample	$\tau_1(ns)$	A_1	$\tau_2(ns)$	A_2
Spin	1.02 ± 0.01	0.84 ± 0.01	2.24 ± 0.17	0.12 ± 0.02
Spray	1.19 ± 0.04	0.19 ± 0.01	5.88 ± 0.02	0.82 ± 0.01

Table 7.2: Fitting parameters for the time-resolved photoluminescence decays for spin-coated as well as spray-deposited QD solids. Reprinted (adapted) with permission from ref [72]. Copyright (2020) Elsevier Ltd.

to the equilibrium state of the spin-coated QD solid compared to the spray-deposited one. This red-shifting kinetics is well described by the Miller-Abrahams (M-A) Equation 7.2

$$k_{i \rightarrow j} = \begin{cases} k' \exp\left(-\frac{(\varepsilon_j - \varepsilon_i)/2}{k_B T}\right) & \varepsilon_j > \varepsilon_i \\ k' & \varepsilon_j < \varepsilon_i \end{cases} \quad (7.2)$$

In which the energy states at site i and site j are represented by ε_i and ε_j respectively, k is intrinsic hopping rate between two neighboring QDs, k_B denotes the Boltzmann constant and T is temperature. Consequently, the QD solid with higher in-homogeneously distributed energy states demonstrates a more rapid red-shift rate. The carrier diffusion is thus “effectively hopping” towards lower energy states which is known as “funneling effect”.[55] According to the M-A equation, a large energy shift can indicate a suppressed charge carrier mobility. Specifically, from the upper term of the M-A equation, a slower hopping rate occurs when a carrier transfer from a lower energy site to a higher energy site.

Moreover, the PL lifetimes of the solids are also studied by tracking the PL intensities at their equilibrium peak positions, respectively. The intensity decay curves are fitted by a double exponential decay function as seen in Fig. 4e and the fitting parameters are given in Table 7.2. The PL lifetime of spray-deposited QD solid is much longer than that of the spin-coated QD solid under the same excitation condition for both solids. Overall, as indicated in Figure 7.11(f), compared with the spin-coated QD solid, the spray-deposited QD solid has a more uniform energy state distribution, which benefits the carrier transport by decreasing the energetic disorder. Notably, the spray-deposited QD solid has a larger film thickness (479 ± 35 nm) as compared to the spin-coated QD solid (144 ± 4 nm) although less QD material was needed in the film deposition process. The differences in film thickness can be ignored in the TR-PL results due to the applied “non-quenching” test conditions. [143]

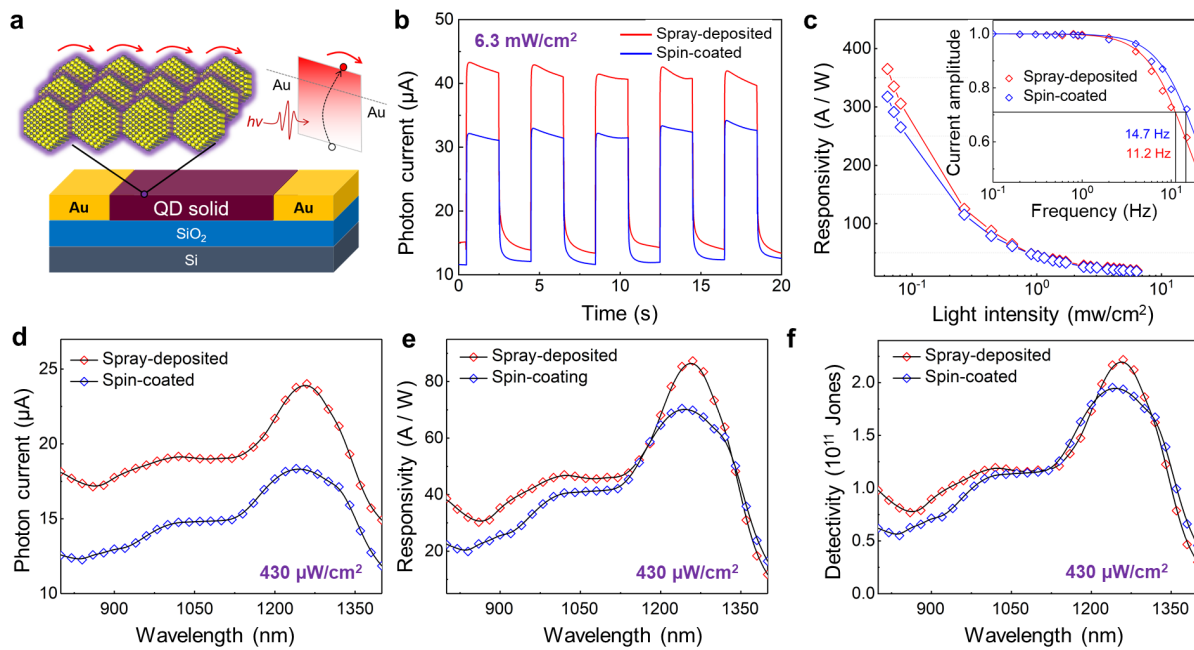


Figure 7.12: (a) Schematic of the photodetector device with the defined total effective area is 0.03 mm^2 . (b) On-off signals derived from the devices with the illumination wavelength of 1250 nm, the intensity of 6.3 mW/cm^2 and applied voltage of 10 V. (c) Responsivity evolutions of the devices with increasing of the illumination light intensity, the illumination wavelength is 1250 nm. inset: Frequency response of the normalized peak-to-peak normalized current amplitude curves fitted by a low pass filter function. Spectra (800-1400 nm) of (d) photon current, (e) responsivity and (f) detectivity of as compared devices, illuminated under $430 \text{ } \mu\text{W/cm}^2$ with the applied voltage of 10 V. Reprinted (adapted) with permission from ref [72]. Copyright (2020) Elsevier Ltd.

7.6 Device performance

The working principle of a photodetector based on QD solids is illustrated in Figure 7.12(a), in which the photon generated charge carriers contribute to the circuit current under a bias voltage. The electronic-coupling between the neighboring QDs and the defects density in the QD solid will influence the device performances. In contrast, the differences in the film thickness will not contribute to the photocurrent and to the conductivity of the QD solids due to the selected device configuration, considering that TBAI treated QD solids have a long carrier diffusion length in the order of 100 nm and a broad width of the carrier generation function. [109, 137, 144] Therefore, the film thickness was optimized in the two different film deposition methods to ensure homogeneous QD solid films. The device based on the spin-coated QD solid is also fabricated for the comparison

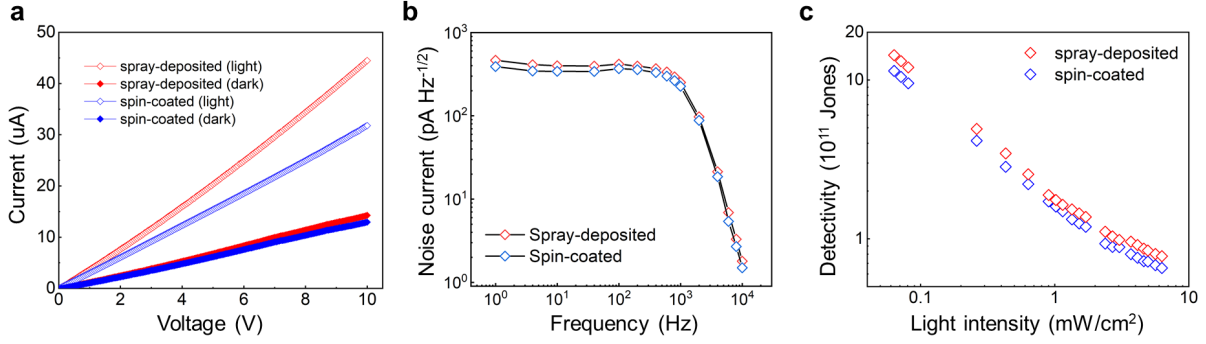


Figure 7.13: (a) IV scanning results of the devices under 1250 nm light illumination with a power density of 6.3 mW/cm². (b) Detectivity evolutions of the devices with the variation of the illumination light intensity, the illumination wavelength is 1250 nm. Devices based on spin-coated QD solids are shown in blue and those out of spray-deposited QD solids in red. Reprinted (adapted) with permission from ref [72]. Copyright (2020) Elsevier Ltd.

with the spray-deposited QD solid device. Figure 7.12(b) illustrates the on-off switching properties of the devices, which indicates their excellent detection repetitions. The photon current in the spray-deposited photodetector is much higher than that of the spin-coated photodetector under the same test conditions, which is due to the lower trap density in the spray-deposited QD solid. Moreover, the photocurrent along with the applied voltage in the spray-deposited device is obviously higher than that of the spin-coated device as seen in Figure 7.13(a). The closer inter-dot distance layout in the spray-deposited QD solid also contributes to the increased photon current, due to the exciton dissociation rate is increased with the decrease of the inter-dot distance. [96] Additionally, a locally higher particle density induced charge carrier density in the spray-deposited QD solid is considered as another factor contributing to the higher photon current in the device circuit. The responsivity (R) and the detectivity (D^*) are calculated based on the previous work as below [8, 9, 24]

$$R = \frac{I_{light} - I_{dark}}{P_{in}} \quad (7.3)$$

$$D^* = \frac{\sqrt{A}}{NEP} = R \sqrt{\frac{A * \Delta f}{\bar{I}_n}} \quad (7.4)$$

I_{light} and I_{dark} represent the currents under illumination and in dark, respectively, and P_{in} denotes the input light power in Equation 7.3. Moreover, in Equation 7.4, the effective area is, represented by A and NEP denotes the noise equivalent power in W/Hz^{1/2}. Δf is the electrical bandwidth (1 Hz). The mean noise current \bar{I}_n (shown in Fig. S8b)) is

also measured for an accurate characterization of detectivity. The responsivities of both devices decrease with increasing the power density of illumination from $63.5 \mu\text{W}/\text{cm}^2$ to $6.3 \text{ mW}/\text{cm}^2$ as seen in Figure 7.12(c), which is due to the saturation of the photon generated charge carriers. [145] Notably, the responsivity of the spray-deposited device reaches up to 365.1 A/W with the illumination power density of $63.5 \mu\text{W}/\text{cm}^2$ with the wavelength of 1250 nm which is higher than that of the spin-coated device, and also higher than that of most devices reported in the literature. [146,147] Figure 7.2 gives an overview about reported devices in comparison to the devices in this work. The frequency-response function for a low pass filter is used to fit the normalized peak-to-peak current amplitude curves as seen in the inset of Figure 7.12(c). The frequency-response function is provided as Equation 7.5 [148–150]

$$H(\omega) = \frac{1}{\sqrt{1 + \alpha\omega^2}} \quad (7.5)$$

Here, H stands for the amplitude as the function of frequency ω with a constant α . The spray-deposited device shows a slightly lower cut-off frequency (3-dB bandwidth, defined as the frequency when the intensity dropped at 70.7% of the initial intensity) of 11.2 Hz than that of the spin-coated device, 14.7 Hz . This is due to the contribution from the shallow-trap states, which are located near the band edges, and could prolong the photogenerated charge carrier lifetime. Fewer shallow traps are in the spin-coated QD solid than in the spray-deposited QD solid as seen by slower response time in the raise/off tests (Figure 7.14). [146] In addition, the detectivity of the spray-deposited device also reaches up to 1.4×10^{12} Jones, which is slightly higher than that of the spin-coated device (1.1×10^{12} Jones), under the illumination power density of $63.5 \mu\text{W}/\text{cm}^2$ with the wavelength of 1250 nm , as seen in Figure 7.13(b). The spectra of photon current, responsivity and detectivity of the devices are shown in Figure 7.12(d) to Figure 7.12f, respectively, which maintain similar tendencies with the absorption spectral features of QDs in solution, specifically around the 1Se-1Sh peak. Thus, the spray-deposited detector shows a better responsivity, as well as detectivity in the NIR ranges. Notably, the spray-deposited device required a significantly lower amount of QDs in the preparation, but achieves a quite competitive device performance compared with the spin-coated QD solid device. These results make the spray deposition of QDs a promising fabrication method for potential large scale spray-deposition based roll-to-roll fabrications, which would decrease costs and moreover could also decrease waste in the fabrication.

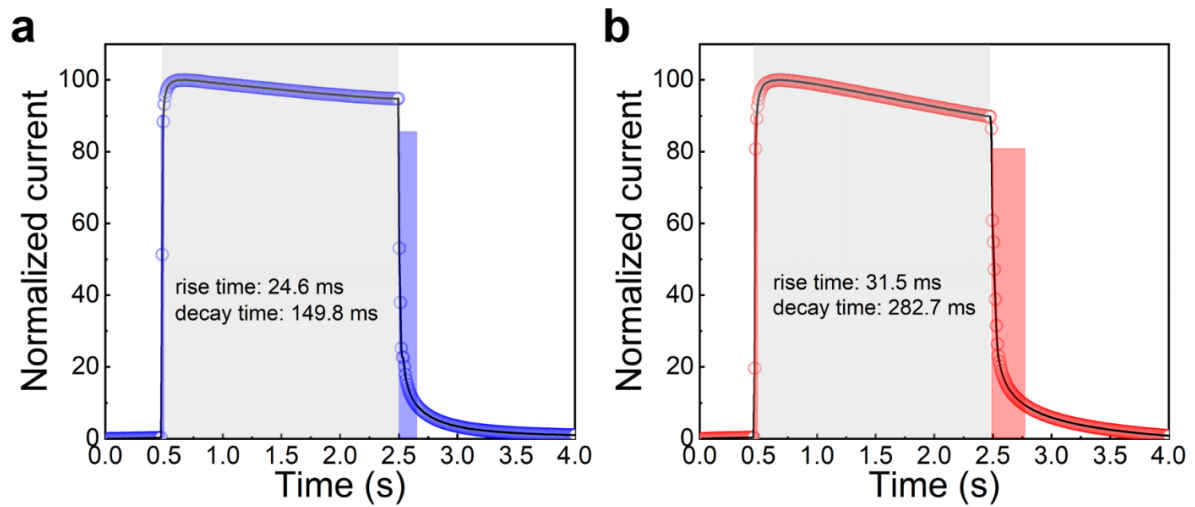


Figure 7.14: Rise (10% to 90% max) and fall (90% to 10% max) times for (a) spin- and (b) spray-deposited QD solid devices. Reprinted (adapted) with permission from ref [72]. Copyright (2020) Elsevier Ltd.

7.7 Conclusions

In conclusion, a spray deposition method of PbS QDs is reported for a potential large-scale fabrication of solution-processed optoelectronic applications. In comparison to the commonly prepared spin-coated QD solids, the spray-deposited QD solids demonstrate a smaller inter-dot distance of neighboring QDs and a narrower distance distribution from the GISAXS azimuthal integration analysis. The superlattice analysis further points out that the spray-deposited QDs reveal a BCC stacking behavior, which is closer to the theoretical stacking behavior than that of the distorted superlattice situation in the spin-coated QD solid. The different deposition methods are considered to be the main factor contributing to these different superlattice stacking behaviors after the ligand exchange treatment. The TR-PL analysis confirms a longer carrier lifetime and better order energy state distribution of the spray-deposited QD solid comparing with the spin-coated solid. The photodetector based on the spray deposition has an improved device performance especially for the responsivity achieving 365.1 A/W and detectivity reaching up to 1.4×10^{12} Jones under the illumination power of $63.5 \mu\text{W}/\text{cm}^2$. These parameters are not only better than those of the spin-coated QD solid detector but also competitive with most reported device performances. The refined but simplified device architecture makes the spray deposition based fabrication large-scalable with low costs and waste.

Year	2006	2017	2018	2019	2020(this work)
Active area (mm ²)	0.015	0.7	0.6	0.22	0.03
Voltage (V)	100	10	40	40	10
Light intensity ($\mu\text{W}/\text{cm}^2$)	0.5	10.6	0.3	12.2	63.5
Spectral range (nm)	400-1300	400-1100	white light	400-900	400-1400
Responsivity (A/W)	2700	0.15	6.32	3.3	365.1
Detectivity (Jones)	2.00×10^{13}	7.50×10^{11}	1.12×10^{13}	5.06×10^{12}	4.40×10^{12}
Bandwidth (Hz)	18	-	-	50	11.2
Reference	[151]	[24]	[9]	[8]	[72]

Table 7.3: The device comparison of PbS QDs based photoconductors from the literature. Reprinted (adapted) with permission from ref [72]. Copyright (2020) Elsevier Ltd.

8 Structural degradation of QD solid in solar cell

Parts of this chapter were prepared in collaborations with Southern University of Science and Technology (SUSTech), Shenzhen, China and Deutsches Elektronen-Synchrotron (DESY), Hamburg, Germany, and are submitted as a **manuscript**: "In Operando Structure Degradation Study of PbS Quantum Dot Solar Cells" (Chen, W.; *et al.*).

8.1 Motivations and main discoveries

PbS quantum dot (QD) solar cells demonstrate great potential in solar energy conversion with a broad and flexible spectral response. Even though long-term storage stabilities of QD solar cells were reported in literature, the operation stability from a more practical aspect, to date, has been not yet investigated. Herein, the structure degradation process of a PbS QD-ink based solar cell during the device operation has been observed. Simultaneously to probing the solar cell parameters, the overall structure evolutions of the QDs in both, active layer and hole transport layer of the solar cell are studied with grazing-incidence small- and wide-angle X-ray scattering (GISAXS/GIWAXS). A spontaneous decrease of the QD inter-dot distance with an increase in the spatial disorder in the active layer (PbX₂-PbS QDs, X = I, and Br) is found during the operation induced degradation. Consequently, the structure disorder-induced broadening of the energy state distribution is responsible for the decrease in open circuit voltage V_{oc} leading the device degradation. These findings elucidate the origin of light-soaking as well as the structure degradation of QD ink-based solar cells and indicate that the stability of the device can be realized by the positional stabilization of the QDs in the QD solid.

8.2 Introduction of in operando experiment

Colloidal PbS quantum dots (QDs) are promising in various solution-processed thin-film optoelectronic devices, including light-emitting diodes, [4, 6] photodetectors, [7, 8] and photovoltaics [10, 46] due to the tunable bandgap of the QDs in a broad spectral range. In PbS QD based solar cell fabrications, the solution-phase ligand-exchange engineering enables to use QDs as ink (QD-ink). This QD-ink can be applied directly to form a solid film *via* just a single-step deposition as the active layer with strong electronic coupling properties. [19, 50] Therefore, the fabrication process is even simpler than the conventional layer-by-layer process. [22] The high efficiency of QD-ink based solar cells is realized by a refined surface engineering and the modifications of the QDs for a high-quality active layer. [45, 74, 152, 153] The modified QDs in the QD-ink are supposed to have an ideal inorganic outer layer, which is normally formed by lead halides, [90] or perovskites. [77] Through the refined ligand engineering, the dangling bonds on the surface of the QDs are eliminated by these inorganic ligands, [78, 108] and the solubility of the QD-ink is also improved by the modifications on the QD facets. [48] Moreover, the lead halide component provides a suitable dielectric matrix to sustain an efficient energy transport configuration between two neighboring QDs according to the carrier hopping theory. [25, 52] By these efforts, the power conversion efficiency (PCE) of QD solar cells, to date, already reached 13.8%. [46]

The QD-ink based solid formation process is described as a self-organization process of the QD particles from a solution state to a dry state. The inter-dot distance-dependent tunneling process of the charge carrier dominates the energy transport of the strongly-coupled QD solid. [17] The carrier transport rate exponentially decays as a function of the surface-to-surface distance of the QDs in a strongly-coupled QD solid. [25] Besides surface treatments before the deposition, the final stacking situation of the QDs, specifically for the inter-dot distance and the distribution, can also determine the charge carrier transport of the QD solid after the deposition. Consequently, an ideal QD-ink based QD solid as active layer is supposed to have a small average QD inter-dot distance as well as a narrow inter-dot distance distribution. To evaluate the inner structure of the thin-film architecture and the corresponding structure parameters, grazing-incidence small-angle X-ray scattering (GISAXS) is a well-established approach to study the QD layout in QD solid films nowadays. [10, 12, 45, 46, 48, 74, 79] Previous studies suggested that different surface treatments and different deposition processes both influenced the stacking configurations of the QDs and the final device performances. [50, 64] Moreover, grazing-incidence wide-angle X-ray scattering (GIWAXS) is a powerful method to probe the crystal structure of the QDs.

As reported in the literature, QD-ink based solar cells showed a good storage stability [50] as well as operation stability over a long time scale. [11, 154] However, a relatively prominent change of the device performance normally happened in an initial short operation time (approximately 20 min), which was described as the “light soaking” effect. [155, 156] Since the electronic coupling of the QDs and their energy transport are sensitive to the QD inter-dot distance, [17] therefore, in an assumption, the device degradation, in the initial burn-in stage, caused by a variation of the stacking configuration of the QD solid.

In this work, an *in operando* GISAXS/GIWAXS study is reported following the initial structure degradation of PbS QD solar cell (performed at synchrotron beamline P03, PETRA III). [126] The *in operando* measurement is designed in a way to rule out influences from ambient conditions, including moisture, oxygen, and temperature, [142, 157] and reducing the impact of the intrinsic degradation of the electron transport layer (ETL) to the device performance. Therefore, in this work, the structure degradation of QD layers is mainly studied in the solar cell, including the hole transport layer as well as the active layer, and findings are correlated to the real-time device performance. Moreover, static studies, including GISAXS and GIWAXS of the independent QD layers are carried out to distinguish the structure degradation from the specific layers. In addition, spectral studies on the QD solids are also introduced to understand the underlying mechanism of the device degradation.

8.3 Experimental details

Materials synthesis: The synthesis method was following previous literature [73] with slight modifications, briefly described as follows: Lead oxide (PbO, 1.1 g) was dissolved into the mixed solvent of oleic acid (OA, $C_{18}H_{34}O_2$, 7 mL) and octadecene (ODE, $C_{18}H_{36}$, 20 mL). After purification by degassing and injecting inert gas (Ar), the mixture was heated up to 150 °C to obtain the lead precursor solvent (Pb(OA)₂). Then the temperature was set to 100 °C and a 6 hours evacuation was applied to further purify the reaction solvent. After that, the flask shifted to the mode of refilling Ar instead of the evacuation. The temperature was maintained at 80 °C. Bis(trimethylsilyl)sulfide [(TMS)₂S, 530 μL] was used as S precursor and rapidly injected into the lead precursor to trigger the nucleation and growth of the PbS nanocrystals. The reaction lasted for 90 s and then was terminated by ice-bath and simultaneous injection 10 mL cool octane. After the purification process, induced by adding with acetone and high-speed centrifugation, the QDs were dispersed in octane with the desired concentration of 50 mg/mL for the deposition and the ink fabrication.

QD ink fabrication: QD-ink fabrication was mainly following previous work by Liu *et al.* [50] Lead iodide (PbI_2 , Sigma (211168), 461 mg), lead bromide (PbBr_2 , Alfa Aesar (35703.03), 75 mg) and ammonium acetate (AA, 35 mg) were dissolved into 20 mL *N,N*-dimethylformamide (DMF) as the ink precursor. 20 mL PbS QDs (10 mg/mL) was added into the ink precursor and then a phase separation was seen after shaking the mixture for 1 min. Thereby, QDs were transferred from the octane phase to the DMF phase. QDs in the DMF were washed 3 times by octane to completely remove the oleic acid and then precipitated by mixing with the same volume of toluene and centrifugation. After vacuum-drying treatment, the QD-ink became pellets and was re-dissolved in *n*-butylamine (BTA) with a concentration of 200 mg/mL.

Device fabrication: The device fabrication was mainly following previous work with modifications. [50] The clean laser-patterned ITO (Lumtec, LT-G001PT) substrates were treated for 10 min with O_2 plasma to improve the wettability of the diluted SnO_2 nanoparticles solution. The SnO_2 nanoparticle, 15% in H_2O colloidal dispersion (Alfa Aesar, 44592.36), was diluted into deionized water with the ratio of 1: 3 ratio and the obtained solution was shaken for over 3 hours. The solvent was deposited on the substrates by spin-coating (3000 rpm for 30 s) and then the layer was annealed at 150 °C for 30 min to form the electron transport layer (ETL). 120 μL QD ink (200 mg/mL) was deposited on the SnO_2 layer to obtain the active layer by spin-coating (2600 rpm for 30 s). 150 μL 50 mg/mL oleic acid capped PbS QDs were spin-coated (3000 rpm for 10 s) on the ink layer. 1,2-Ethanedithiol (EDT) in acetonitrile (0.02 % v:v) was applied afterward to performed the ligand exchange treatment. Then pure acetonitrile was used for rinsing the solid twice and removing the residuals. The deposition of OA capped QDs and the solid-state ligand exchange processes were repeated once to form the final hole transport layer. 80 nm gold layer was deposited *via* thermal evaporation on the EDT-QD layer to finish the cell fabrication. ZnO ETL based solar cells are fabricated following a similar protocol but using the ZnO ink instead of the SnO_2 ink. ZnO ink was purchased from Sigma-Aldrich, and it was used straight forward as received with the same spin-coating parameters with SnO_2 layer.

***In operando* experiment in synchrotron:** The *in operando* experiment was carried out at the MiNaXS beamline P03 of the PETRA III synchrotron (DESY, Hamburg). [126] The X-ray photon energy was set to 11.65 keV, which corresponded to a wavelength of 1.06 Å. The GISAXS detector was a Pilatus 1M (Dectris Inc.) with a pixel size of 172 μm and a frame rate of 10 Hz. The sample-detector distance was 2324 mm. The Pilatus 300K was used as the GIWAXS detector with a sample-detector distance of 168 mm. The micro-focused beam size was about 30 μm \times 20 μm . The solar cell was installed into an evacuated chamber with a pressure of 10^{-2} mbar. The inner temperature was

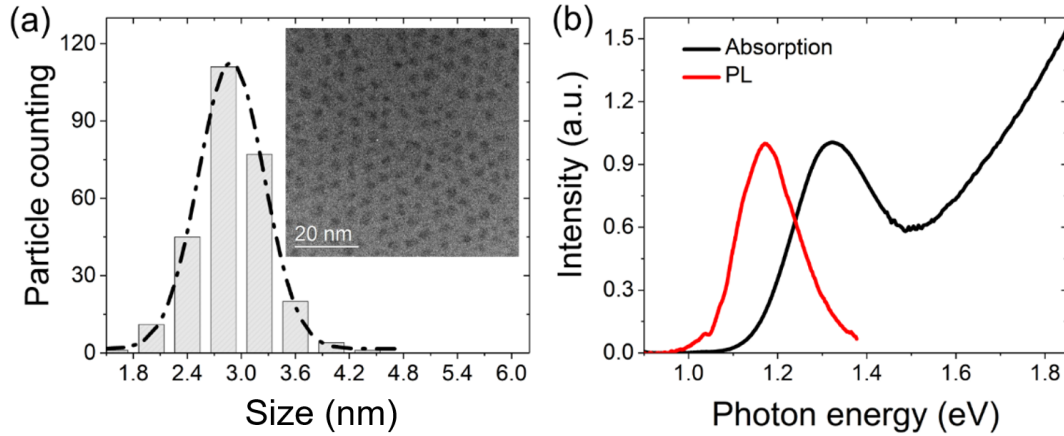


Figure 8.1: (a) Particle size analysis and inset TEM image suggest the average diameter of the QDs is 2.88 ± 0.36 nm. (b) Absorption (black) and emission spectra (red) of the QDs in octane.

stabilized at 15 °C by a water-cooling system to prevent a potential structure change provoked by temperature. The solar simulator was used to provide the illumination (100 mW/cm²). The current-voltage (*IV*) curves as a function of time were recorded by source meter Keithley (2400) with an acquisition frequency of one scanning per 120 s. The whole measurement was performed for 90 min.

In-house GISAXS/GIWAXS measurement: The static GISAXS/GIWAXS measurements were carried out at the Ganesha 300XL SAXS instrument with an 8 keV Cu-K α X-ray source and beam size of 100 $\mu\text{m} \times 100 \mu\text{m}$. The samples were installed in an evacuated chamber (1.2×10^{-3} Pa), and the detector was Pilatus 300 K (Dectris Inc.). The sample-detector distances were 1045 mm for GISAXS and 95.7 mm for GIWAXS measurements, respectively. The degradation conditions for static QD solid samples were the same as in the *in operando* experiment.

8.4 In operando experiment design

PbS QDs are synthesized according to the previous work by Zhang *et al.*, [41,73] and the size and spectral information are shown in Figure 8.1.

The QD-ink and solar cell fabrication mainly follow previous work by Liu *et al.* [50] Detailed information is given in the experimental section. As an indication of the successful ligand exchange of the QDs in the solution phase, QDs transferring automatically from

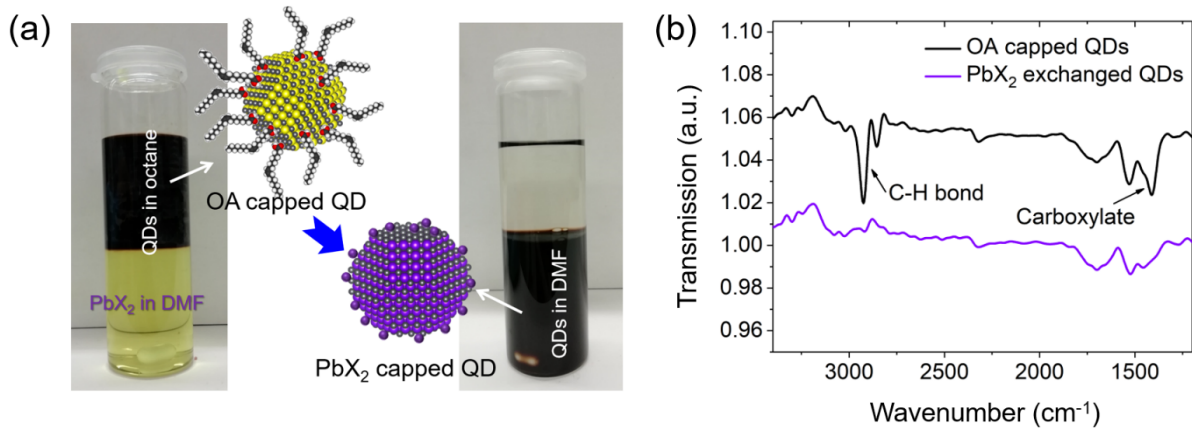


Figure 8.2: (a) Photographs describe the phase transfer of QDs from the octane phase to the DMF phase. (b) FTIR spectra indicate the complete removal of oleic acid ligand on the QDs in the ink phase. The spectra are shifted for clarity.

an octane phase to an *N,N*-dimethylformamide (DMF) phase is recorded by photographs as shown in Figure 8.2.

The Fourier-transform infrared (FTIR) spectra of the QD solids with and without the ligand exchange are also provided. The active layer of the solar cell is made of the QD-ink (PbX₂ capped PbS QDs, X = I, Br), while, the hole transport layer is made of a 1,2-ethanedithiol (EDT) treated QD solid (EDT-QD solid). To reduce the impact of ambient conditions, such as temperature, oxygen, and moisture, the device is installed inside of a vacuum chamber (10⁻² mbar) with a temperature control system to keep the chamber at a constant temperature of 15 °C during the illumination induced burn-in. Moreover, to reduce potential influences from the ETL on the device performance and the structure degradation of the active layer, a tin oxide layer (SnO₂) instead of the conventionally used zinc oxide layer (ZnO) is used as the ETL of the devices for the *in operando* measurement. [158–160] Under a stable illumination (100 mW/cm²), generated by a solar simulator, the device operating parameters and the inner structure of the QD solids are simultaneously recorded by an *IV* analyzer (Keithley Meter source) and the GISAXS detector, respectively. The *in operando* measurement schematic is illustrated in Figure 8.3(a).

The GISAXS detector (Pilatus 1M) is installed at a large sample-detector distance (SDD, 2324 mm) to record the structure variation in the QD superlattice scale. The real photograph of the *in operando* setup can be found in Figure 8.4.

Due to the higher photon energy (11.6 keV), small thickness of the hole transport layer, and selected incidence angle (0.4 °), the X-ray beam can penetrate both QD layers,

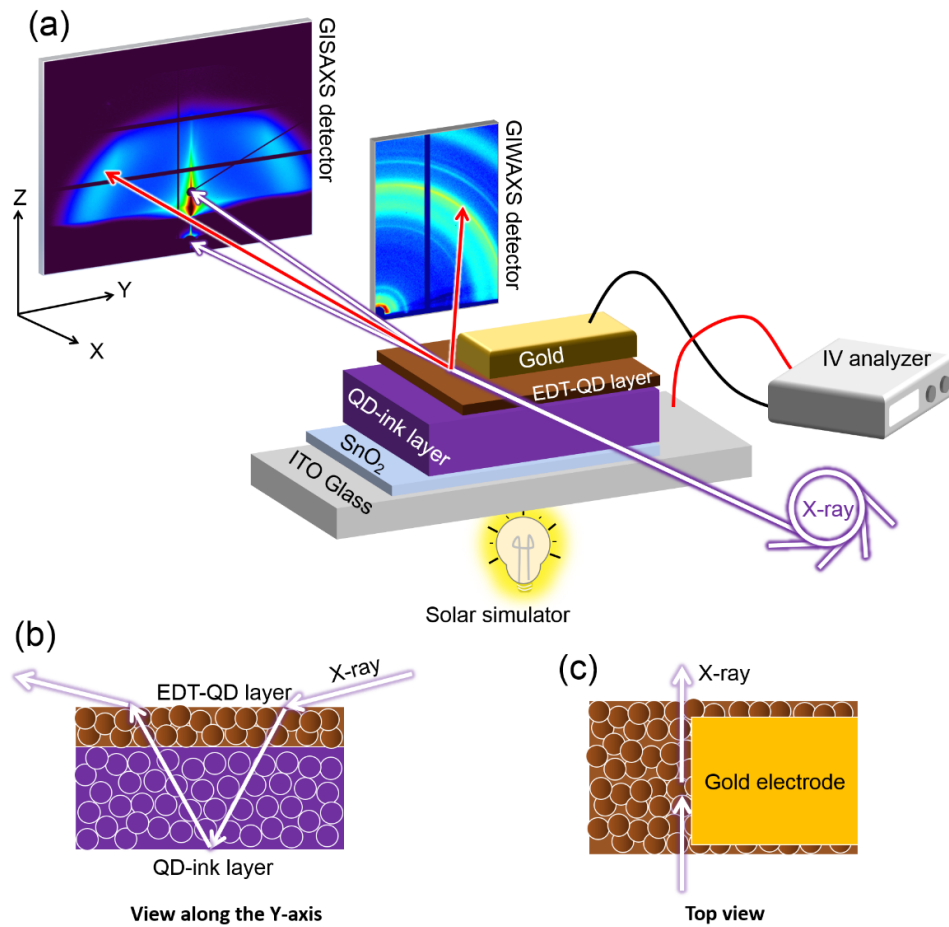


Figure 8.3: (a) Schematic of the *in operando* structure degradation study of QD based solar cells using synchrotron based GISAXS/GIWAXS. The device diagram of QD solar cells and the schematic for X-ray penetration of the QDs are provided as (b) the view from the Y-axis and (c) the top view.

reaching the bottom electrode layer as sketched in side view in Figure 8.3(b). Moreover, as seen from the top view, the X-ray footprint is located extremely close to the top electrode (< 0.1 mm). A GIWAXS detector (Pilatus 300K) is also installed with a short SDD (95.7 mm) to study the structure changes of the crystal lattice. Figure 8.4 provides a real photograph of the measurement setup. In addition, static in-house GISAXS/GIWAXS measurements are also performed to confirm that the overall structure changes mainly originate from the active layer (QD-ink layer) rather than from the hole transport layer (EDT-QD layer), although both layers are made from the same batch of QDs with the same size but different surface treatments. Afterward, the spatial disorder-induced energy states variation of the QD-ink layer before and after the degradation is probed with absorption spectra and findings are in a good agreement with the GISAXS analysis.

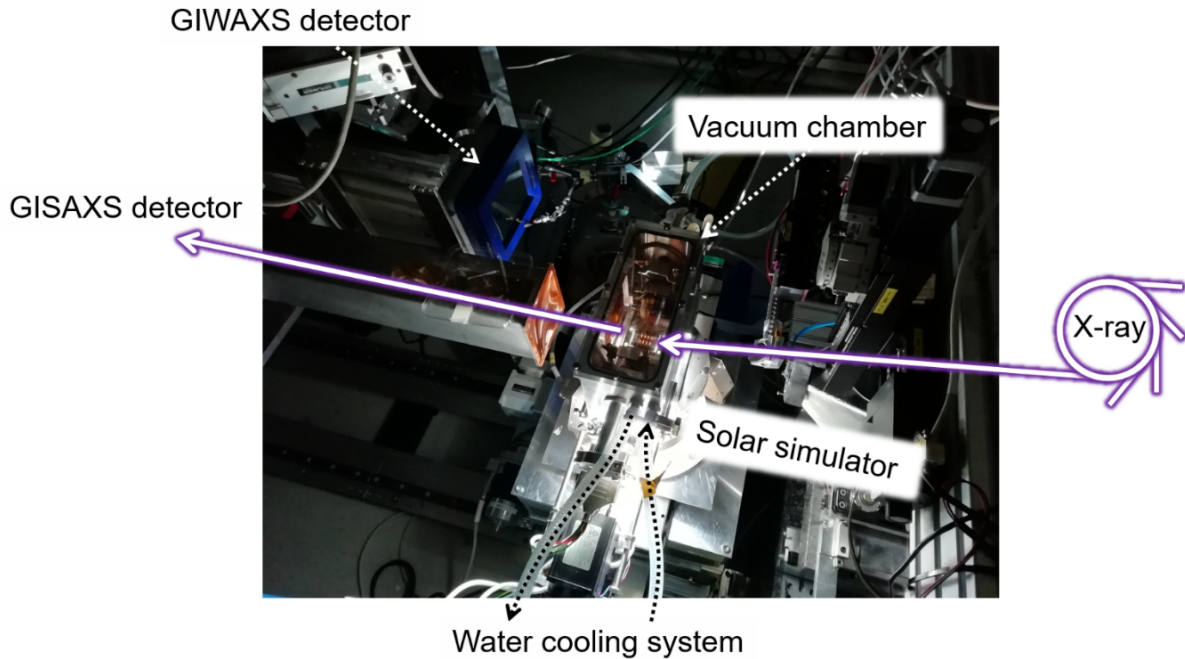


Figure 8.4: Photograph of the *in operando* setup installed at the synchrotron beamline with both GISAXS and GIWAXS detector, a pocket solar simulator, a water-cooling system, a vacuum chamber, an IV analyzer (source meter Keithley).

The device architecture is provided in Figure 8.5(a), in which the thicknesses of the QD layers in the X-ray scattering volume from the top to the bottom are determined to be (45 ± 3) nm for the EDT-layer and (254 ± 10) nm for the QD-ink layer.

8.5 Device performance degradation

The thicknesses are (30 ± 2) nm for the SnO_2 layer or (35 ± 2) nm for the ZnO layer as the transport layer and (140 ± 3) nm for the indium tin oxide (ITO) layer on glass, which is used as the substrate for the solar cells. The thicknesses are estimated by a profilometer and the error values are derived from a set of different measurements. Figure 8.5(b) illustrates the cross-section image of the device architecture in the X-ray scattering volume and is described as EDT-QD layer/QD-ink layer/ SnO_2 /ITO. Figure 8.5(c) demonstrates the device working principle in which the QD-ink layer acts as the active layer generating bound charge carriers (excitons) under illumination. The excitons disassociate immediately into free charge carriers, electrons, and holes, and diffusive randomly inside of the QD solids. The EDT-QD layer acts as the hole transport layer blocking electrons, while the SnO_2 or (ZnO) layer acts as the ETL. The energy diagram is built up according

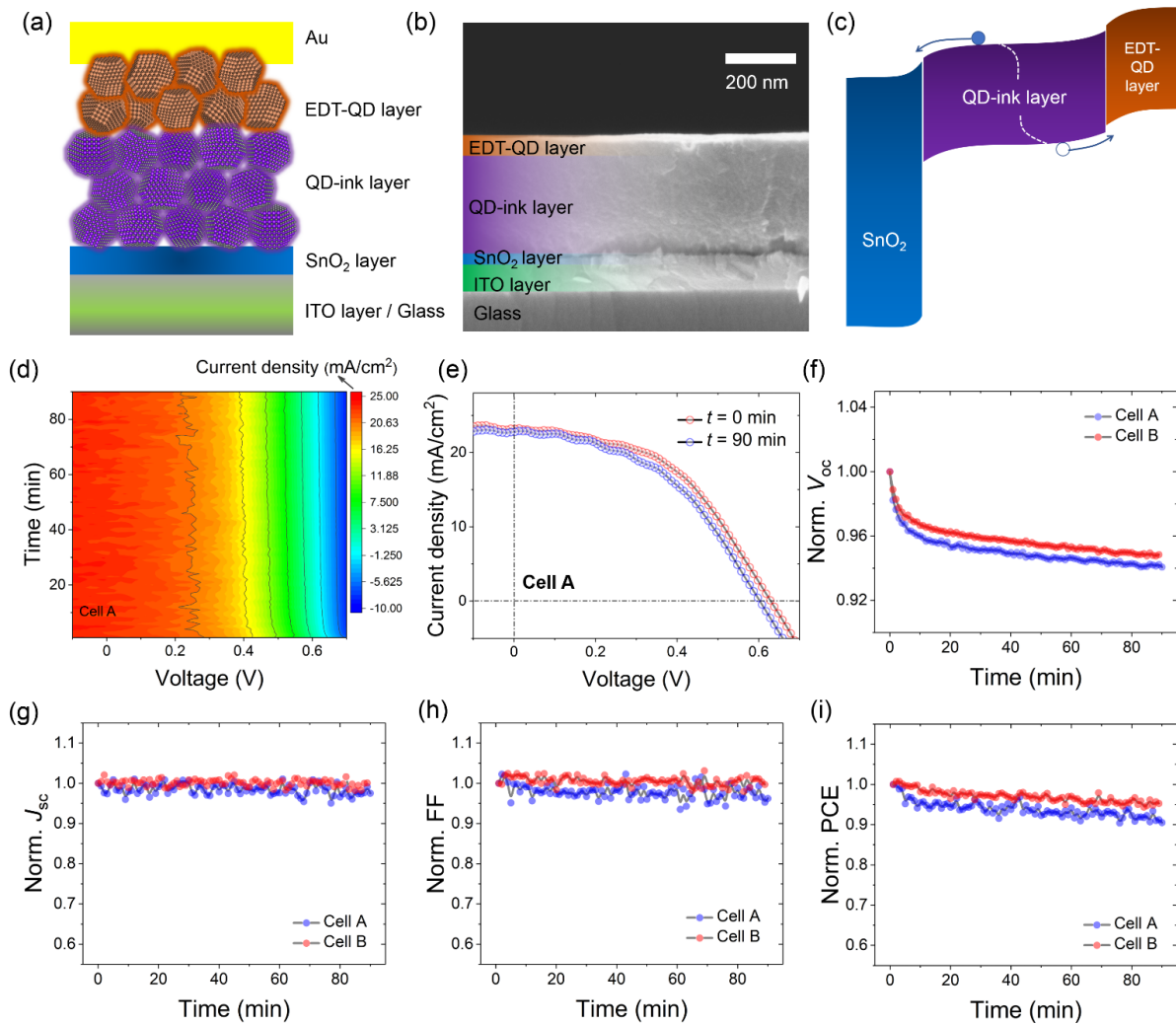


Figure 8.5: (a) Schematic of the QD solar cell with (b) the real cross-section image indicating the individual layers of the functional stack. (c) Energy level diagram of the QD solar cell. (d) 2D mapping of the current density-voltage (JV) curves as a function of operation time. (e) JV curves of the device before (0 min, red) and after the degradation process (90 min, blue). Temporal evolution of normalized device parameters for (f) short circuit current density (J_{sc}), (g) open circuit voltage (V_{oc}), (h) fill factor (FF) and (i) power conversion efficiency (PCE), in which the Cell B is fabricated as a reference sample demonstrating a similar degradation tendency compared to Cell A used in the in operando experiment.

Device	$J_{sc}(mAcm^{-2})$	$V_{oc}(V)$	FF	PCE (%)
SnO ₂ based device	23.2 ± 0.1	0.63 ± 0.01	0.48 ± 0.01	7.0 ± 0.1
ZnO based device	26.5 ± 0.1	0.60 ± 0.01	0.59 ± 0.01	9.4 ± 0.1

Table 8.1: Comparison of device architecture used in the *in operando* experiment (SnO₂) with the ZnO blocking layer device in terms of best achieved device performance.

to references using similar materials and fabrication protocols. [119, 153, 159] The device operation parameters of the target solar cells before the *in operando* experiment are given in 8.1.

Notably, to verify the quality of the QD layers, the device performance of the ZnO based solar is also presented with a thicker QD-ink layer (322 ± 12 nm) resulting in a PCE of 9.4 %. The current densities for both solar cells are in a good agreement with the empirical relation between active layer thicknesses. [45] The lower fill factor (FF) of the SnO₂ based devices is supposed to be due to the higher recombination of the charge carriers, which probably originates from the discrepancy of the intrinsic work functions between the SnO₂ layer and QD active layer. [158] The device performance evolution during the *in operando* experiment of the SnO₂ based device is shown in the current density-voltage (*JV*) mapping over time, as seen in Figure 8.5(d). The open circuit voltage V_{oc} drops dramatically at the initial 10 min burn-in phase and then gradually decreases towards a stable value. Consequently, the PCE of the device gradually decreases from 7.0 % to 6.3 % with the fill factor FF decreasing slightly from 48.7 % to 45.8 %, and a quite stable short circuit current density J_{sc} performance, which decreases from 23.2 mA/cm² to 22.8 mA/cm². As an example, the *JV* curves before and after the *in operando* degradation experiment are shown in Figure 8.5(e). To reproduce the universality of the device degradation, an additional degradation experiment is performed on a reference cell (called cell B) and the normalized degradation parameters as shown in Figure 8.5(f-i). The results indicate that the variations of J_{sc} and FF of the devices (cells A and B), are very limited during the entire 90 min operation induced degradation, which suggests a stable interface configuration for the charge carrier extraction from the active layer as expected. Besides the degradation induced changes of the structure on the electronic relevant length scales (< 10 nm), which are mainly studied with GISAXS/GIWAXS, the microscopic surface morphologies of QD layers are separately studied by with scanning electron microscopy (SEM) before and after the degradation process. The SEM results are presented in Figure 8.6, and they suggest an excellent surface stability of the QD layers.

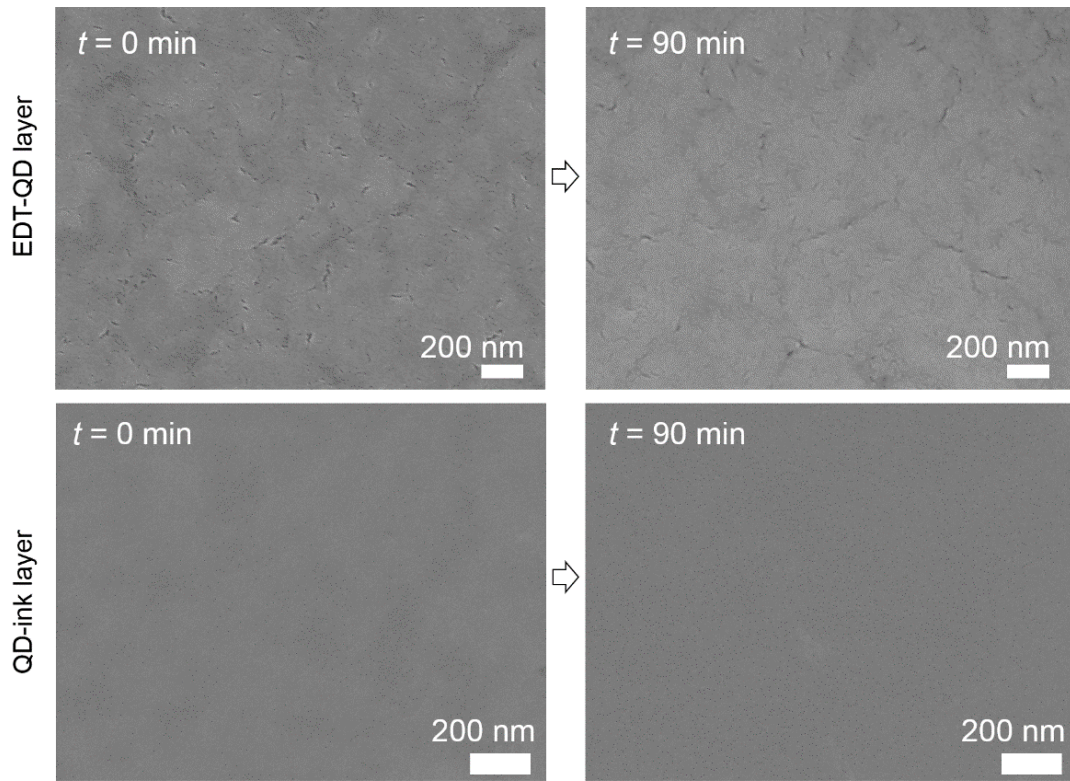


Figure 8.6: Surface morphologies of the (top) QD-ink layer and (bottom) EDT-QD layer on glass substrate (left) before and (right) after degradation (under the same illumination degradation conditions as the *in operando* experiment).

Thus, a major device degradation induced by changes the interface on the microscopic scale can be ruled out. Notably, the slight current fluctuations in the degradation curves are supposed to correlate with the intrinsic properties of the QD solar cell in a fast current-voltage scanning mode (1 cycle/s), as also found in literature. [45,79] For comparison, the ZnO based solar cell burn-in results are also provided (Figure 8.7), which demonstrates a similar degradation process lead by the decrease of the V_{oc} as seen in the SnO₂ based devices.

However, the degradation of J_{sc} , as well as FF, are more prominent than those in the SnO₂ based devices, which is possibly attributed to the intrinsic degradation of ZnO layer or the interface induced degradation between the ZnO layer and the QD-ink layer. To essentially understand the device degradation, *in operando* experiments as well as independent burn-in tests are associated to specific QD solids in order to differentiate the degradation contributions in the QD solar cells.

The real-time 2D GISAXS data of QD layers have been recorded with a data acquisition frequency of $\sim 1 \text{ min}^{-1}$ in the first 5 min, 5 min^{-1} between 5 - 60 min, 10 min^{-1} in range of

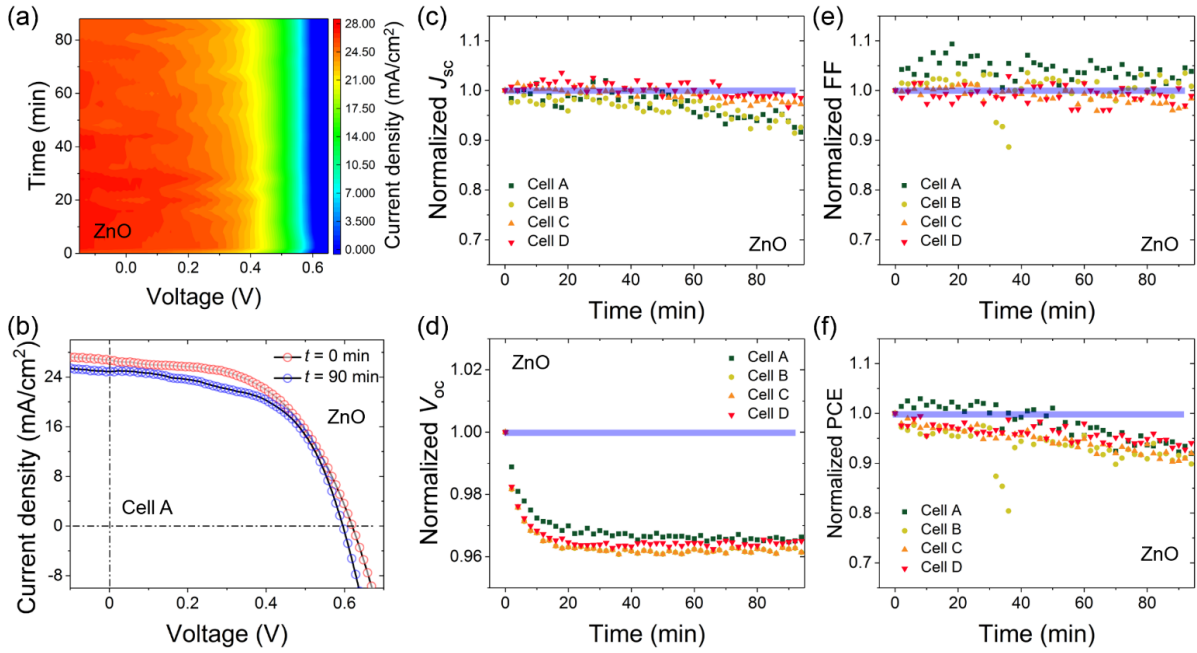


Figure 8.7: (a) 2D JV curve mapping of ZnO based solar cell during the degradation process. (b) The JV curves of the device before (0 min, red) and after (90 min, blue) the degradation. Evolution of normalized device parameters for (c) short circuit current density (J_{sc}), (d) open circuit voltage (V_{oc}), (e) fill factor (FF) and (f) power conversion efficiency (PCE), in which the Cell B, C, D are fabricated as reference samples demonstrating a similar degradation tendency compared to Cell A.

60 - 90 min, to rule out radiation damage (by the intense X-ray beam). X-ray radiation damage tests were performed before the *in operando* experiment to rule out potential structure damage from the X-ray exposure as seen in Figure 8.8.

Figure 8.9.(a-c) presents selected GISAXS data measured at different device operation times ($t = 0, 30, 90$ min), which indicates a stable layout of the QDs in the device without significant changes in the scattering patterns. Azimuthal integrations of the scattering intensity as a function of q are shown in Figure 8.9(d).

8.6 Structural degradation analysis

The overall inter-dot distance and the distance distribution of the QDs are investigated by the corresponding modeling, [103] in which spherical models are used to fit the scattering from the QDs and the intensity as described by the equation 8.1.

$$I(q) \propto P(q)S(q) + Aq^{-n} \quad (8.1)$$

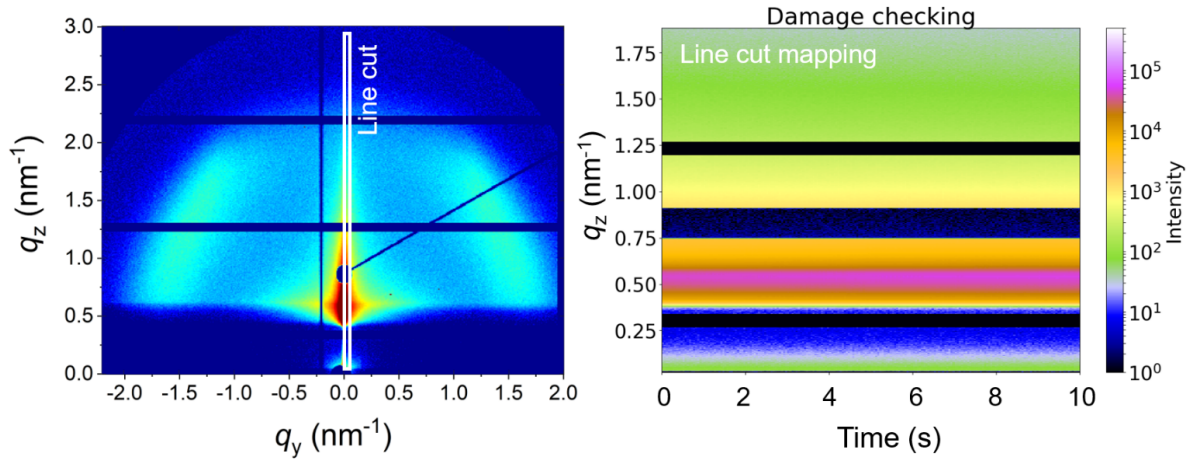


Figure 8.8: Radiation damage test before the *in operando* experiment, in which the X-ray illuminates on a selected position (not the *in operando* position) for $0.1 \text{ s} \times 100$, which is longer than the total exposure time $0.5 \text{ s} \times 19$ chosen for the *in operando* experiment. The line cut is indicated in the 2D GISAXS data (left) and the line-cut mapping (right) records the structure evolution over the operation time. A potential radiation damage from the X-ray exposure is ruled out for all studies performed in this work.

In this equation, $I(q)$ is the intensity distribution, $P(q)$ denotes the form factor (assuming a spherical shape of the QDs) and $S(q)$ denotes the structure factor, which reflects the inter-dot distance of the spheres. The term Aq^{-n} represents a scattering contribution from potential QD aggregates described by a power-law function. Selected modeling curves are shown for the beginning ($t = 0 \text{ min}$) and end ($t = 90 \text{ min}$) of the *in operando* experiment (Figure 8.11) and illustrate the changes in the structure. The modeling parameters are shown in Figure 8.9(e-f). Accordingly, during the burn-in phase, the QD inter-dot distance decreases rapidly from $2.96 \pm 0.01 \text{ nm}$ to $2.92 \pm 0.01 \text{ nm}$ in the initial stage ($t < 10 \text{ min}$) of the device degradation process before the value stabilizes at $2.91 \pm 0.01 \text{ nm}$. The error bars give an estimate of the fit tolerance. The smaller QD inter-dot distance indicates an increased electronic coupling configuration between neighboring QDs during the degradation. [96] However, the distribution width of the inter-dot distance is found to increase simultaneously (Figure 8.9(f)), indicating that the spatial disorder of the QDs increases. Notably, for strongly-coupled QD solids, the increased spatial disorder means that more QDs are potentially touching each other and thereby dimerize, aggregate or facet-align, which can provoke local relaxations the excitons and broaden the overall energetic states. [26,27] Moreover, the peak intensity as derived from the modeling, increases at the beginning ($t < 20 \text{ min}$) due to a uniform structure variation

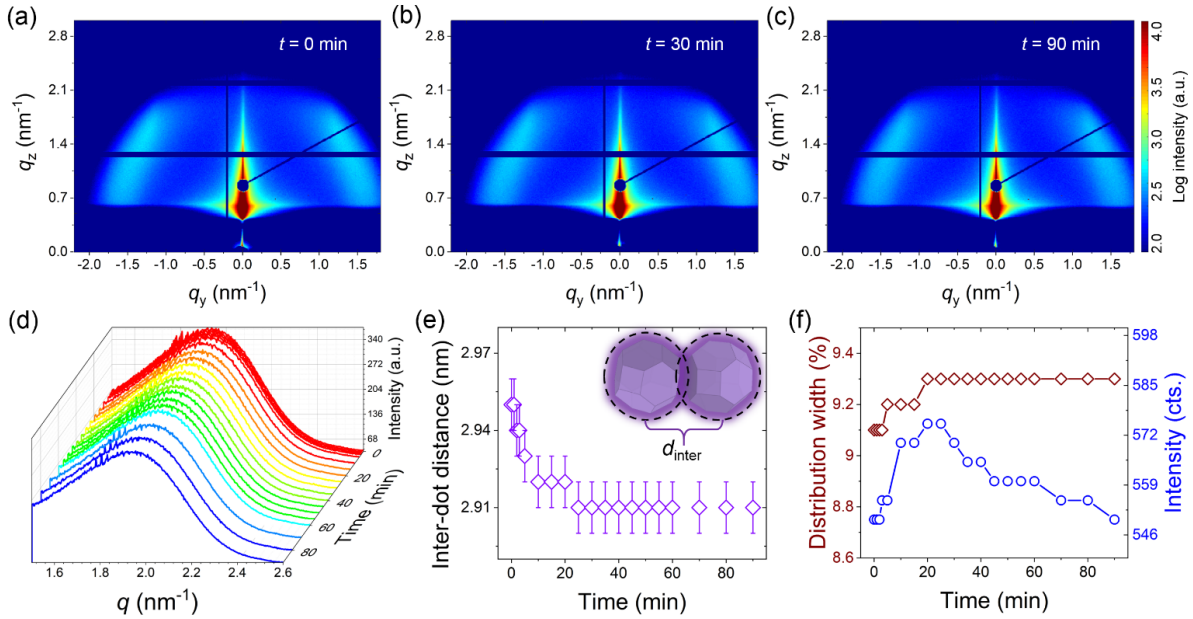


Figure 8.9: 2D GISAXS data from the *in operando* experiment at different times: (a) 0, (b) 30 and (c) 90 min. The scattering patterns contain contributions from both, the EDT-QD layer as well as the QD-ink layer. (d) Temporal evolution of the azimuthal integrated intensity as a function of q . (e) As derived overall QD inter-dot distance of both QD layers based on modeling of the GISAXS data with spheres. The error bars indicate the fit parameter tolerance. (f) Distribution width of the QD inter-dot distance (red) and intensity (blue) as deduced from the fits.

in the scattering volume, before it gradually decreases with further structure variations occurring continuously and slowly.

To study changes of the crystal structure, GIWAXS measurements are selectively carried out at different operation times ($t = 0, 32, 62,$ and 92 min).

The 2D GIWAXS data at the beginning and the end of the degradation are shown in Figure 8.10 (a) and (b), 2D GIWAXS patterns at 32 and 62 min can be found in Figure 8.12 which shows “split peaks” at around $q = 2.1 \text{ \AA}^{-1}$ and $q = 2.4 \text{ \AA}^{-1}$ appearing during the *in operando* experiment.

The corresponding azimuthal integrations are shown in Figure 8.10(c). The peaks at $q = 2.13 \text{ \AA}^{-1}$ and $q = 2.46 \text{ \AA}^{-1}$ are assigned to the Bragg peaks $(222)_{\text{ITO}}$ and $(400)_{\text{ITO}}$ of the ITO layer, which both do not change significantly during the entire degradation process. Besides, the sharp peaks at $q = 2.09 \text{ \AA}^{-1}$ and $q = 2.41 \text{ \AA}^{-1}$ are supposed to originate from the lattice anchoring (or passivation) effect of PbX_2 with a uniform lattice distance on the facets of the PbS QDs. [50, 161]

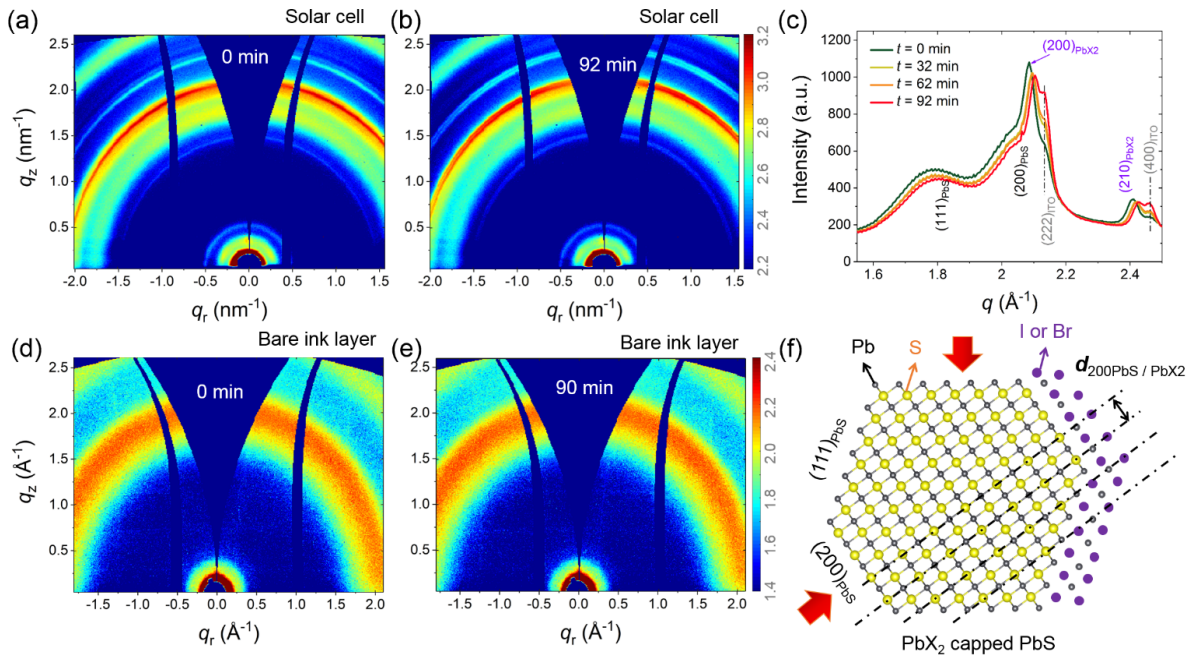


Figure 8.10: Selected 2D GIWAXS data of the QD solids in the solar cell at different operation times: (a) $t = 0$ and (b) $t = 92$ min. (c) Azimuthal integration of the 2D GIWAXS data with marked Bragg peaks. Selected 2D GIWAXS data of the QD-ink (d) before (0 min) and (e) after illumination degradation (90 min). (f) Schematic of a single QD lattice with (200) and (111) facets passivated by lead halides (selected facets in the schematic). The red arrows indicate the QD lattice distances suffering from an overall compression during the *in operando* degradation experiment.

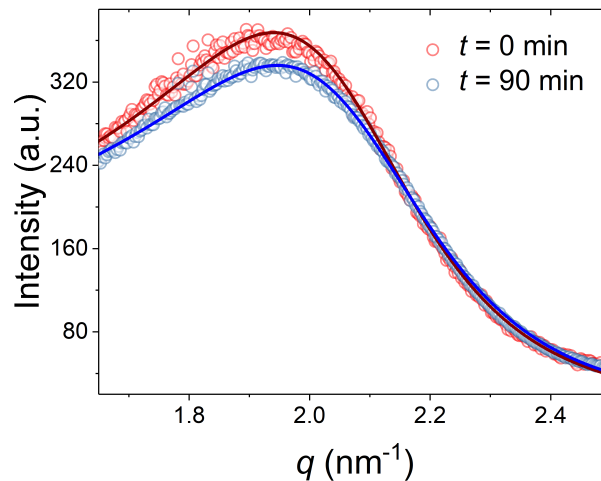


Figure 8.11: Azimuthal integrations of 2D GISAXS data (symbols) of the solar cell before (0 min, red) and after degradation (90 min, blue) are shown with the best model fits (solid lines) using a model as described in the text.

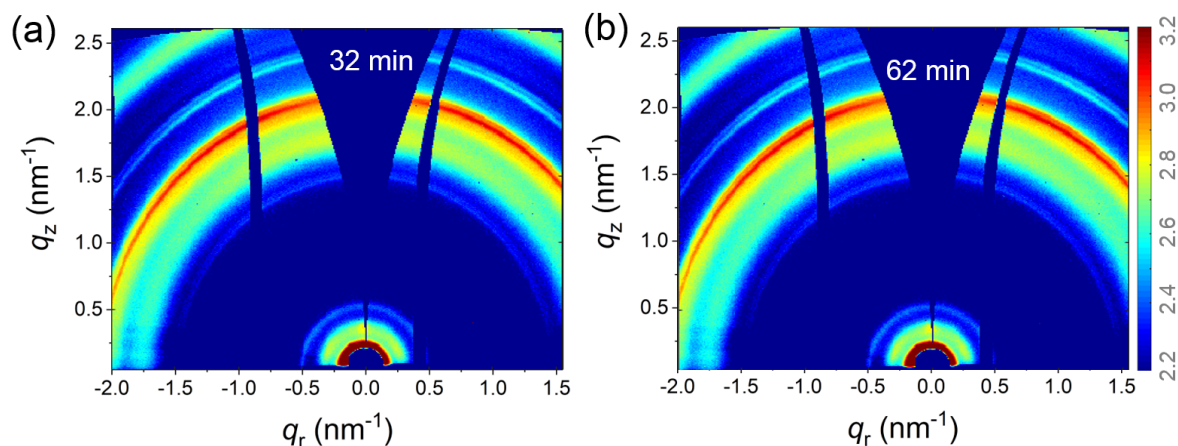


Figure 8.12: 2D GIWAXS data at (a) $t = 32$ min and (b) $t = 62$ min of illumination probed during the in operando experiment.

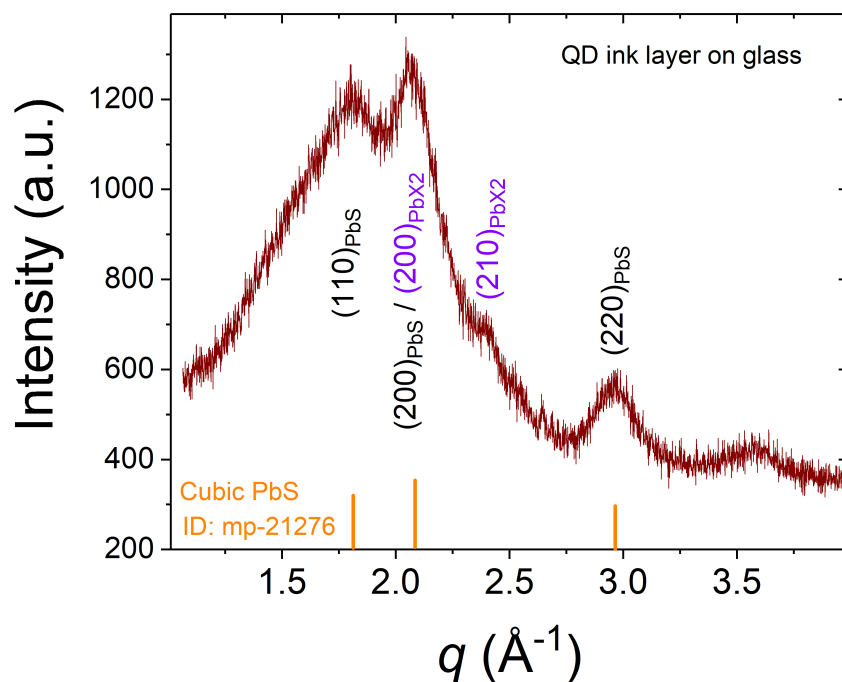


Figure 8.13: XRD data of bare PbS ink layer on glass in which the $(200)_{PbS}$ and $(200)_{PbX_2}$ peaks are merged. The existence of PbX_2 crystallinity can be found from $(210)_{PbX_2}$ at $q = 2.4 \text{ \AA}^{-1}$, which matches well with the in operando GIWAXS data.

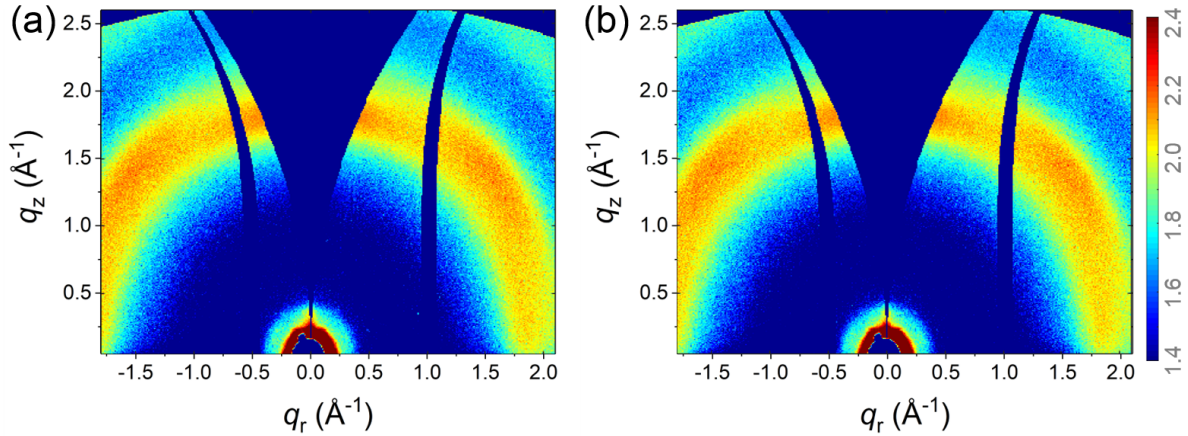


Figure 8.14: Static 2D GIWAXS data of the bare EDT-QD layer (a) before and (b) after degradation.

The X-ray powder diffraction (XRD) pattern of the pure QD-ink layer (Figure 8.13) indicates merged (200) peaks from both, PbS and PbX₂. The anchoring effect can be still recognized from the diffraction pattern of the (210)_{PbX₂} peak. The results match well with the GIWAXS. Moreover, the lattice compression of the QD solid can be seen from the peak shift towards higher q values for both Bragg peaks of the QDs ((111)_{PbS} and (200)_{PbS}) as well as the PbX₂ outer layer of the QDs. The shift in the initial stage ($t < 30$ min) can be attributed to the re-arrangement of the QD stacking as was seen with GISAXS. In the period between $t = 30$ min and $t = 60$ min, the crystal lattice distances are supposed to be stable. Further lattice compression is found at $t = 90$ min. This continuous compression is attributed to the phase transition of PbX₂, from an alpha phase to a delta phase. The overall compression effect is supposed to prevent further device degradation. [162] Static GISAXS/GIWAXS measurements are performed under the same degradation conditions as the *in operando* experiment to separate the contributions of the individual QD layers (EDT-QD layer and QD-ink layer) on glass substrates. The 2D GIWAXS data for the QD-ink layer before and after degradation are seen in Figure 8.10(c) and (d). The 2D GIWAXS patterns for EDT-QD layer before and after the degradation are presented in Figure 8.14.

According to the peak splitting, the lattice compression found in the *in operando* experiment is confirmed to be contributed by the QD-ink layer, as seen in Table 8.2.

The EDT-QD layer demonstrates good lattice stability against illumination in a 90 min burn-in test. The lattice compressions in QDs are from all lattice directions and mainly happen in the QD-ink layer rather than in the EDT-QD layer. This effect is attributed to the presence of the surface passivation layer since the QD-ink layer stoichiometrically

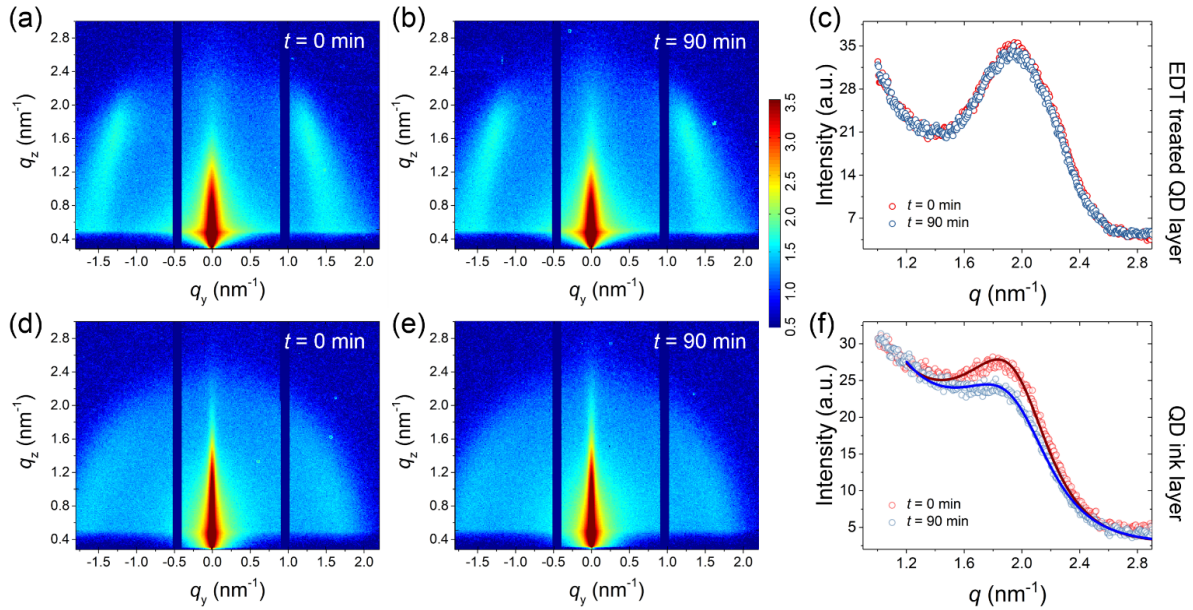


Figure 8.15: 2D GISAXS data of the (a) fresh (0 min) and (b) aged (90 min) EDT-QD layer. (c) Azimuthal integration data show the structure stability of the EDT-QD layer. 2D GISAXS data of the (d) fresh (0 min) and (e) aged (90 min) active layer (QD-ink layer). (f) Azimuthal integration data show the structure variation of the QD-ink layer.

contains a high amount of PbX_2 . [77] The effective compression of PbX_2 capped QDs is supposed to occur due to the surface anchoring effect, as indicated in Figure 8.10(f). The PbX_2 arrangement gradually follows the lattice template of facets of PbS QDs. A further indication is, that the measured lattice distances in the QD-ink layer are all moving towards the lattice distances of the EDT-QDs. Notably, the EDT-QDs have no inorganic passivation layer and the lattice distances of the QDs are closer to that of the intrinsic PbS QDs than the surface inorganically treated QDs in the QD-ink layer.

The static GISAXS results of the individual QD solids are shown in Figure 8.15(a-

Sample	$111_{(EDT-QD)}$ (\AA^{-1})	$200_{(EDT-QD)}$ (\AA^{-1})	$111_{(QD-ink)}$ (\AA^{-1})	$200_{(QD-ink)}$ (\AA^{-1})
Fresh	1.838 ± 0.003	2.117 ± 0.004	1.795 ± 0.011	2.093 ± 0.006
Aged	1.837 ± 0.004	2.118 ± 0.005	1.821 ± 0.013	2.117 ± 0.006
Variation	~ 0.001	~ 0.001	~ 0.026	~ 0.024

Table 8.2: Bragg peak positions of the QDs before and after the aging measurements, derived from the static GIWAXS measurements.

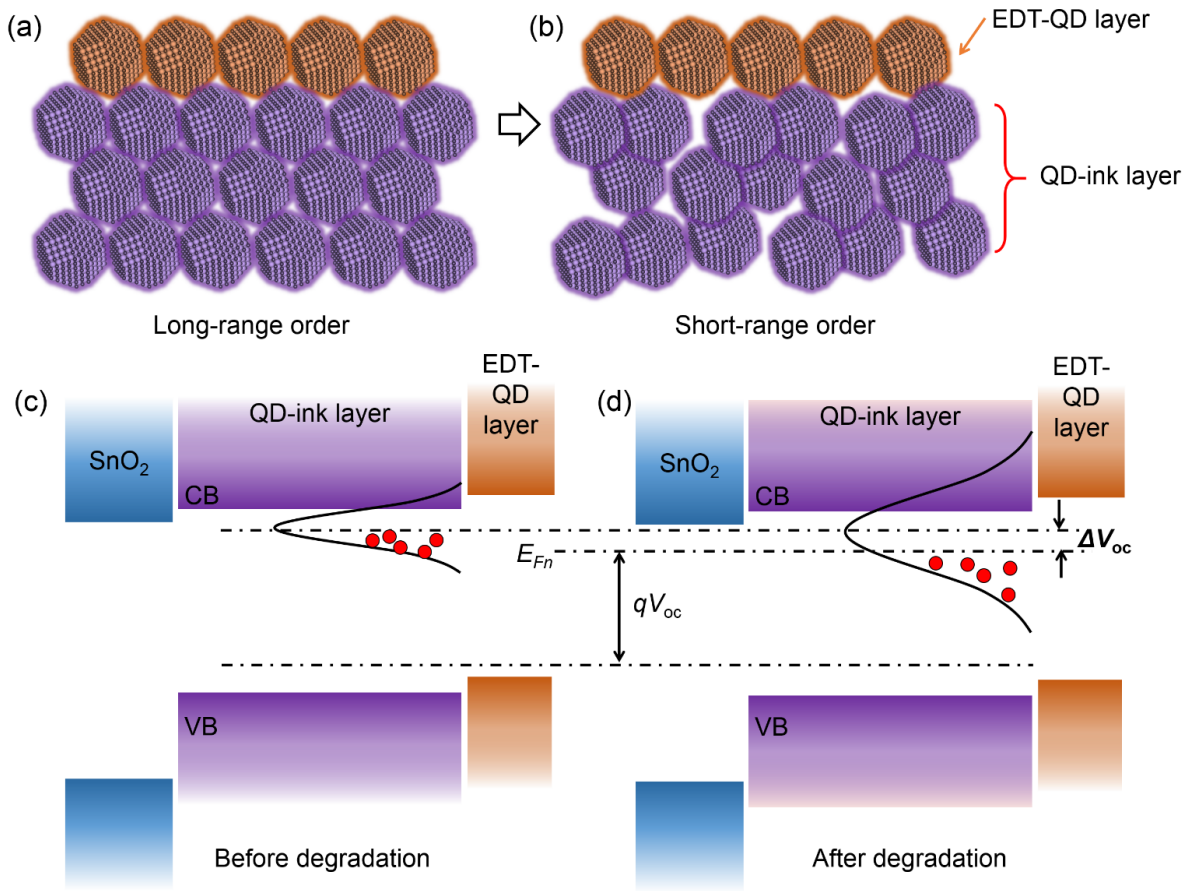


Figure 8.16: (a) Schematic of the structure in the QD layers (a) having long-range order before and (b) short-range order after the degradation. The QD-ink layer is shown in blue and the EDT-QD layer in orange. Energy state distribution in the QD-ink layer (c) before and (d) after degradation.

f). As illustrated in Figure 8.15(c), the azimuthal integrations suggest that the EDT-QD solid also exhibits an excellent structure stability against degradation with a stable inter-dot distance of the QDs of (2.93 ± 0.01) nm as deduced from the modeling. In contrast, a change in the QD inter-dot distance and the distribution width is found in the QD-ink layer during the degradation test as shown in Figure 8.15(f). According to the modeling, the inter-dot distance decreases from (2.95 ± 0.01) nm to (2.91 ± 0.01) nm with an increased distance distribution width, from 10.0 % to 10.9 %. Notably, the slight differences between the scattering data obtained from synchrotron and in-house (Ganesha SAXS machine) GISAXS measurements are attributed to different scattering configurations, including the different resolution function, photon energy, X-ray beam size, footprint length, and penetration depth.

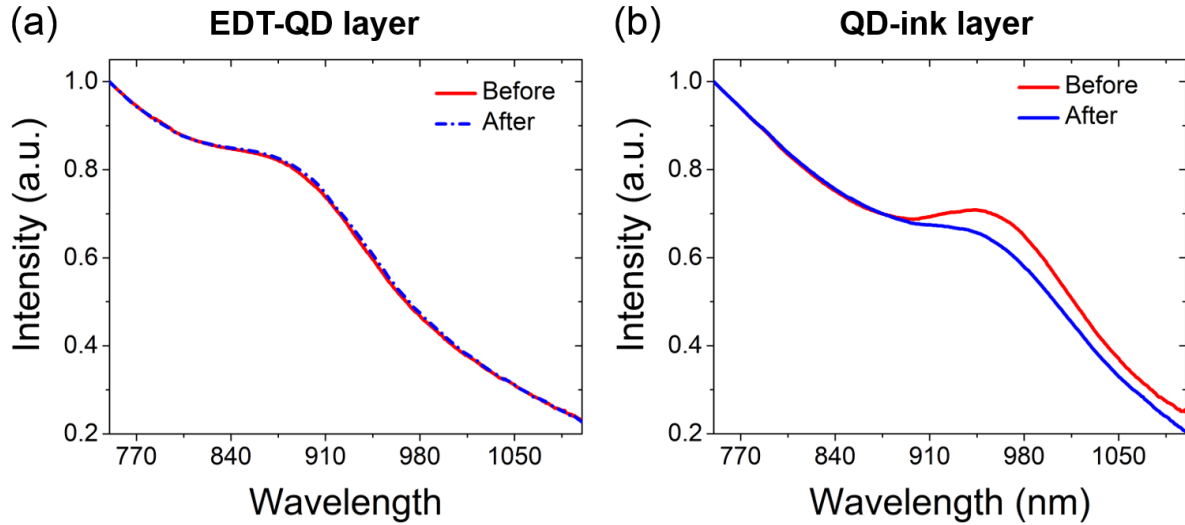


Figure 8.17: Absorption spectra of (a) EDT-QD layer and (b) QD-ink layer on glass substrates before (red) and after (blue) the burn-in experiment.

8.7 Degradation discussion

Based on the structure variations, the increased spatial disorder of the QDs can broaden the energy state distribution in the QD-ink layer, which is further confirmed from the absorption spectra of the QD-ink layer, before and after the degradation, as shown in Figure 8.17. The slightly smeared first exciton peak of the QD-ink layer originates from a disordered coupling. [26,27,163] In contrast, the EDT-QD layer exhibits a stable absorption behavior before and after the degradation test, which is in good agreement with the GISAXS analysis. As a result, the structure evolution of the QDs in the solar cell device is confirmed and the structure degradation is schematically illustrated in Figure 8.16(a) and (b). The QD hole transport layer remains stable during the entire degradation test, which suggests a stable interface for the hole transport and extraction. The observed changes in the scattering are mainly attributed to the QD-ink layer of the device in the *in operando* measurement. To explain the changes, the initial arrangement of the QDs is determined by a single-step spin-coating deposition, which suggests a “fast-freezing” layout formation process. Therefore, a long-ranged ordered QD layout is supposed in the fresh sample, causing a prominent scattering peak. During the initial degradation, the QDs shift to a short-ranged ordered layout, exhibiting more spatial disorder, as seen in the *in operando* experiment. This change in the QD-ink layer is due to maximizing the entropy of the ensemble becoming regionalized, since QDs are not ideally spherical, neither monodisperse in the particle size but polyhedral with facets. [35,60] During the

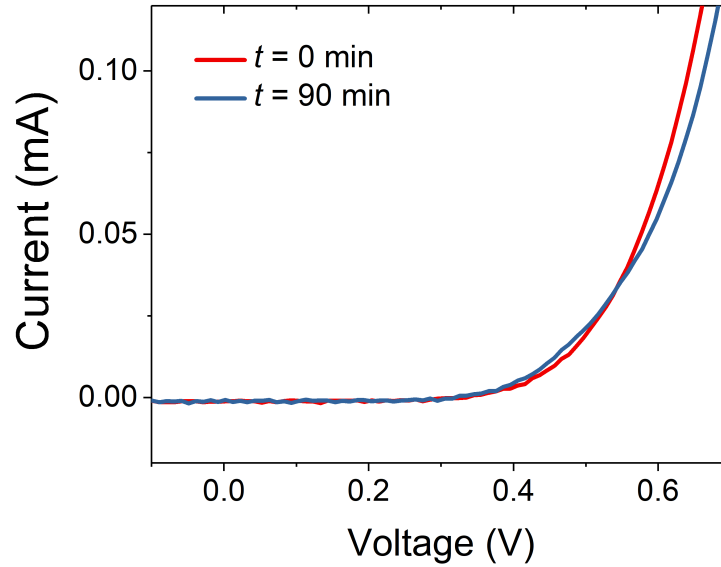


Figure 8.18: Dark IV measurements of cell A (SnO_2 based device) before ($t = 0$ min, red) and after ($t = 90$ min, blue) the in operando experiment.

burn-in test, the structure disorder broadens the energy state distribution of the QD-ink layer, as indicated by the smeared first exciton peak in the absorption spectra. [26] Notably, the broadened energy states can reduce the effective quasi fermi level (E_{Fn}) of electrons, which leads to a reduced V_{oc} of the device. [164–166] Consequently, the energy diagrams of the device before and after degradation are illustrated in Figure 8.16(c) and (d). In the fresh sample, QDs have a narrow energy state distribution (seen from the absorption) due to their uniform coupling configuration to their neighboring QDs. Thus, the effective quasi fermi level of the QD-ink layer can stay at a higher position. After the burn-in test, the inhomogeneous coupling from the QD aggregate analogies broadens the energy state distribution. [26] As a result, the band tails provide more opportunities for the recombination of the charge carriers and the charge carrier lifetime is decreased. The structure variation induced band tails provoke the V_{oc} loss of the device performance found in the initial operation of the solar cell. [167]

8.8 Conclusions

In summary, an *in operando* GISAXS/GIWAXS study of PbS QD solar cells is reported, by which the structure degradation of the QD layers, as well as the device performance degradation, are studied simultaneously. The GISAXS analysis indicates that the solar irradiation provides a condition for spontaneously decreasing the inter-dot distance of QDs in the active layer in combination with increasing the spatial disorder. While

changes in the structure of the QDs in the hole transport layer are ruled out from further static GISAXS studies. Moreover, the GIWAXS measurements confirm the overall lattice compression during the degradation process. Interestingly, it is found that the V_{oc} simultaneously decreases and exhibits a quite similar temporal evolution as that of the QD inter-dot distance in the active layer. The J_{sc} and FF of the devices undergo only minor changes. It is found that the spatial disorder of the QD-ink layer broadens the energy state distribution, which is confirmed from changes in the absorption spectra and in the charge carrier lifetime. It is responsible for the loss of V_{oc} during the burn-in phase. These findings enrich the present understanding of the “light-soaking” effect of QD solar cells by introducing the device structure degradation in the burn-in test. The discussion indicates that the stability of the device can be further improved by a positional stabilization of the QDs in the QD solid.

9 Conclusion and outlook

In high efficient optoelectronic applications, colloidal PbS QDs are used as a strongly-coupled QD solid in which the inter-dot distance of neighboring QDs is extremely small. From a practical fabrication aspect, many factors can influence the electronic properties of the QD solids, such as the surface treatment, the stacking behavior, the facet alignment, the inter-dot distance and the distribution. A thesis has been proposed and established to elucidate the connections between the structural landscape and electronic properties of the QD solids. The inner structure of the QD solid is mainly investigated by GIXS in different scales, such as, GISAXS which has been used to mainly describe the structure on in the superlattice scale (1-20 nm) and GIWAXS reveals the structure information from the crystal lattice scale (< 1 nm). The electronic properties of the QD solids are studied by photo-physics and related device engineering. Different depositions, such as spin-coating, printing, and spray deposition, will intrinsically bring in different inner structural configurations of the QD solids. In the thesis, different fabrication processes have been explored in order to establish the connections between the fabrication and device properties. The main findings, via implementing these projects, are presented as follows:

The phase transition of the conventional solid-state ligand exchange (LBL) is well observed by GISAXS and GIWAXS from a superlattice scale and a crystal lattice scale, respectively. An FCC to BCC transition of the QD superlattice is found when the QD solid film is transferred from a colloidal state to a close-packed state in a strongly-coupled configuration. The intrinsic shape of QDs, a polyhedron (truncated tetrahedron) instead of a sphere, plays an important role in the stacking behavior determination. Thermal annealing at different temperatures is used to adjust the facet alignment of the QDs in the QD solid films in which the 100 °C treated QD solid exhibits the best facet alignment layout from the GIWAXS analysis. By using *fs* level pump-probe TAS, it is found that the charge carrier dynamics are influenced by the overall facet alignment of the QD solids. According to the analysis, a better facet-aligned configuration of the QD solid is beneficial for a higher efficient transport of the charge carriers, from the energy maximum downhill to the minimum.

Moreover, towards a potential large-scale deposition, *in situ* GISAXS is also employed

to monitor the stacking behavior of the QDs during a slot-die printing deposition process. Small-sized QDs (~ 3 nm) are employed to address this application in high efficient photovoltaic devices. Due to the large ratio of the ligand thickness to the QD radius, the ordered arrangement of the QDs is initialized by a hexagonal arrangement of the QDs. Thus, the QDs exhibit spherical behavior with the ligands are fully stretched in a wet phase. With further drying, the ligand collapse leads to transferring the stacking of the QDs transfer from an FCC layout to a BCC layout. However, the transition is not completely performed and the final film exhibits a nested FCC and BCC configuration, which is responsible for the positional disorder of the printed QD solid. The kinetic study explains the role of the ligand thickness to QD radius during a self-organization process, which is different from that in a conventional spin-coated QD film before the ligand exchange process.

Further work introduces the deposition of the QDs via a spray deposition. The solid-state ligand exchange treatment is also integrated into the deposition process to achieve strongly-coupled QD solids for photodetector applications. Large-sized QDs (~ 5 nm) are used for the application in a longer wavelength regime. The stacking configurations of the QDs deposited *via* spin-coating and spray deposition are investigated with static GISAXS and GIWAXS, before and after the solid-state ligand exchange process. The results reveal the origin of different inner structure configurations due to different deposition methods. Due to the self-organization and small ratio of ligand thickness to QD radius, QDs deposited *via* the spray deposition and solid-state ligand exchange treatment exhibit a BCC superlattice configuration, which is an indication of a better ordered QD arrangement. The GISAXS analysis verifies the better arrangement of the QDs with smaller inter-dot distances, and the spectral TR-PL analysis infers a narrow energy state distribution in the spray-deposited QD solid. As a result, the spray-deposited based photodetector demonstrates comparable device performances and a higher ratio of the device performance to the cost than the spin-coated devices.

In addition, *via* the solution-phase ligand exchange process, QD-ink based solar cells are fabricated and investigated with respect to the structure degradation by *in operando* GISAXS and GIWAXS measurements. It is found that the open-circuit voltage (V_{oc}) of the device decreases simultaneously with the decrease of the overall inter-dot distance and the increase of the distance distribution. Static GISAXS of the individual QD solids verifies that the variations are mainly contributed by the PbX_2 -PbS QD-ink layer, and the GIWAXS analysis suggests that the QDs also suffer a continuous compression during the device operation. The spectral analysis indicates that the structure degradation leads to an increased energy state in the QD-ink layer and thus increases the charge carrier recombination, which is responsible for the decrease of the V_{oc} . This finding reveals the

initial structural degradation process of QD-ink based solar cells and suggests a positional anchoring engineering may improve the stability of the QD-ink devices in the future.

In further research projects, facet engineered QDs will be mainly investigated. Since most QDs are conventionally synthesized *via* a hot-injection method and the product is normally capped with oleic acid with the shape described by truncated octahedrons. The structural variation is mostly driven by maximizing the entropy of the QD ensemble. The recent advances from the collaborations suggest that the facet engineered QDs can have a different shape, such as octahedrons, with therefore a different stacking driving force. Consequently, the final stacking configuration of the QDs via a solid-state ligand exchange method can be different from that of conventional QDs. Different energy transport configurations in these QD solids are expected. Therefore, it is interesting to investigate the stacking behavior of these new QDs in large-scalable depositions, such as spray coating or slot-die printing. The energetic state distribution or related device performances will be studied.

Moreover, in the conventional studies, the product from the solution phased ligand exchange process is known as QD ink which is used in a single-step deposition with extremely high solution concentration (> 200 mg/mL). To reduce the waste from the deposition process, such as high-speed spin-coating, it is necessary to improve the deposition method with higher utilization of the valuable QD ink. Consequently, the stacking configuration of the QDs is supposed to be different due to different self-organization processes. In further investigations, the electronic properties of these ink-based solids via improved depositions are studied.

In addition, the reliability of the QD solids will be tested with different harsh conditions, in which the synchrotron light source is supposed to be useful to reveal the degradation mechanism of the QD solids in *in situ* studies. This possibly provides insights to develop devices with not only higher efficiency but also better reliability.

Bibliography

- [1] Efros, A. L. and Nesbitt, D. J. *Nat Nanotechnol* **11**(8), 661–71 (2016).
- [2] Rogach, A. *ACS Nano* **8**(7), 6511–2 (2014).
- [3] Baskoutas, S. and Terzis, A. F. *J Appl Phys* **99**(1), 013708 (2006).
- [4] Gao, L., Quan, L. N., García de Arquer, F. P., Zhao, Y., Munir, R., Proppe, A., Quintero-Bermudez, R., Zou, C., Yang, Z., Saidaminov, M. I., Voznyy, O., Kinge, S., Lu, Z., Kelley, S. O., Amassian, A., Tang, J., and Sargent, E. H. *Nat Photonics* **14**(4), 227–233 (2020).
- [5] Vasilopoulou, M., Kim, H. P., Kim, B. S., Papadakis, M., Ximim Gavim, A. E., Macedo, A. G., Jose da Silva, W., Schneider, F. K., Mat Teridi, M. A., Coutsolelos, A. G., and bin Mohd Yusoff, A. R. *Nat Photonics* **14**(1), 50–56 (2019).
- [6] Pradhan, S., Di Stasio, F., Bi, Y., Gupta, S., Christodoulou, S., Stavrinadis, A., and Konstantatos, G. *Nat Nanotechnol* **14**(1), 72–79 (2019).
- [7] Ramiro, I., Ozdemir, O., Christodoulou, S., Gupta, S., Dalmases, M., Torre, I., and Konstantatos, G. *Nano Lett* **20**(2), 1003–1008 (2020).
- [8] Tang, H., Zhong, J., Chen, W., Shi, K., Mei, G., Zhang, Y., Wen, Z., Müller-Buschbaum, P., Wu, D., Wang, K., and Sun, X. W. *ACS Appl. Nano Mater.* **2**(10), 6135–6143 (2019).
- [9] Wei, Y., Ren, Z., Zhang, A., Mao, P., Li, H., Zhong, X., Li, W., Yang, S., and Wang, J. *Adv Funct Mater* **28**(11), 1706690 (2018).
- [10] Choi, M. J., Garcia de Arquer, F. P., Proppe, A. H., Seifitokaldani, A., Choi, J., Kim, J., Baek, S. W., Liu, M., Sun, B., Biondi, M., Scheffel, B., Walters, G., Nam, D. H., Jo, J. W., Ouellette, O., Voznyy, O., Hoogland, S., Kelley, S. O., Jung, Y. S., and Sargent, E. H. *Nat Commun* **11**(1), 103 (2020).
- [11] Choi, J., Choi, M. J., Kim, J., Dinic, F., Todorovic, P., Sun, B., Wei, M., Baek, S. W., Hoogland, S., Garcia de Arquer, F. P., Voznyy, O., and Sargent, E. H. *Adv Mater* **32**(7), e1906497 (2020).

- [12] Xia, Y., Chen, W., Zhang, P., Liu, S., Wang, K., Yang, X., Tang, H., Lian, L., He, J., Liu, X., Liang, G., Tan, M., Gao, L., Liu, H., Song, H., Zhang, D., Gao, J., Wang, K., Lan, X., Zhang, X., Müller-Buschbaum, P., Tang, J., and Zhang, J. *Adv Funct Mater* **30**(22), 2000594 (2020).
- [13] Xia, Y., Liu, S., Wang, K., Yang, X., Lian, L., Zhang, Z., He, J., Liang, G., Wang, S., Tan, M., Song, H., Zhang, D., Gao, J., Tang, J., Beard, M. C., and Zhang, J. *Adv Funct Mater* **30**(4), 1907379 (2019).
- [14] Ellingson, R. J., Beard, M. C., Johnson, J. C., Yu, P., Micic, O. I., Nozik, A. J., Shabaev, A., and Efros, A. L. *Nano Lett* **5**(5), 865–71 (2005).
- [15] Dohnalová, K., Poddubny, A. N., Prokofiev, A. A., de Boer, W. D. A. M., Umesh, C. P., Paulusse, J. M. J., Zuilhof, H., and Gregorkiewicz, T. *Light Sci Appl* **2**(1), e47–e47 (2013).
- [16] Karani, A., Yang, L., Bai, S., Futscher, M. H., Snaith, H. J., Ehrler, B., Greenham, N. C., and Di, D. *ACS Energy Lett* **3**(4), 869–874 (2018).
- [17] Kagan, C. R. and Murray, C. B. *Nat Nanotechnol* **10**(12), 1013–26 (2015).
- [18] Kholmicheva, N., Moroz, P., Eckard, H., Jensen, G., and Zamkov, M. *ACS Energy Lett* **2**(1), 154–160 (2016).
- [19] Ning, Z., Voznyy, O., Pan, J., Hoogland, S., Adinolfi, V., Xu, J., Li, M., Kirmani, A. R., Sun, J. P., Minor, J., Kemp, K. W., Dong, H., Rollny, L., Labelle, A., Carey, G., Sutherland, B., Hill, I., Amassian, A., Liu, H., Tang, J., Bakr, O. M., and Sargent, E. H. *Nat Mater* **13**(8), 822–8 (2014).
- [20] Voznyy, O., Zhitomirsky, D., Stadler, P., Ning, Z., Hoogland, S., and Sargent, E. H. *ACS Nano* **6**(9), 8448–55 (2012).
- [21] Carey, G. H., Abdelhady, A. L., Ning, Z., Thon, S. M., Bakr, O. M., and Sargent, E. H. *Chem Rev* **115**(23), 12732–63 (2015).
- [22] Chuang, C. H., Brown, P. R., Bulovic, V., and Bawendi, M. G. *Nat Mater* **13**(8), 796–801 (2014).
- [23] Lan, X., Voznyy, O., Garcia de Arquer, F. P., Liu, M., Xu, J., Proppe, A. H., Walters, G., Fan, F., Tan, H., Liu, M., Yang, Z., Hoogland, S., and Sargent, E. H. *Nano Lett* **16**(7), 4630–4 (2016).
- [24] Ren, Z., Sun, J., Li, H., Mao, P., Wei, Y., Zhong, X., Hu, J., Yang, S., and Wang, J. *Adv Mater* **29**(33) (2017).
- [25] Guyot-Sionnest, P. *J Phys Chem Lett* **3**(9), 1169–75 (2012).
- [26] Gilmore, R. H., Liu, Y., Shcherbakov-Wu, W., Dahod, N. S., Lee, E. M. Y., Weidman, M. C., Li, H., Jean, J., Bulović, V., Willard, A. P., Grossman, J. C., and Tisdale, W. A. *Matter* **1**(1), 250–265 (2019).

- [27] Singh, K. and Voznyy, O. *Chem* **5**(7), 1692–1694 (2019).
- [28] Lee, S., Zhitomirsky, D., and Grossman, J. C. *Adv Funct Mater* **26**(10), 1554–1562 (2016).
- [29] Gilmore, R. H., Lee, E. M., Weidman, M. C., Willard, A. P., and Tisdale, W. A. *Nano Lett* **17**(2), 893–901 (2017).
- [30] Walravens, W., Solano, E., Geenen, F., Dendooven, J., Gorobtsov, O., Tadjine, A., Mahmoud, N., Ding, P. P., Ruff, J. P. C., Singer, A., Roelkens, G., Delerue, C., Detavernier, C., and Hens, Z. *ACS Nano* **13**(11), 12774–12786 (2019).
- [31] Chen, W., Zhong, J., Li, J., Saxena, N., Kreuzer, L. P., Liu, H., Song, L., Su, B., Yang, D., Wang, K., Schlipf, J., Körstgens, V., He, T., Wang, K., and Müller-Buschbaum, P. *J Phys Chem Lett* **10**(9), 2058–2065 (2019).
- [32] Ghosh, S. and Manna, L. *Chem Rev* **118**(16), 7804–7864 (2018).
- [33] Bian, K., Choi, J. J., Kaushik, A., Clancy, P., Smilgies, D. M., and Hanrath, T. *ACS Nano* **5**(4), 2815–23 (2011).
- [34] Goodfellow, B. W. and Korgel, B. A. *ACS Nano* **5**(4), 2419–24 (2011).
- [35] Zihlerl, P. and Kamien, R. D. *J Phys Chem B* **105**(42), 10147–10158 (2001).
- [36] Wang, R., Shang, Y., Kanjanaboos, P., Zhou, W., Ning, Z., and Sargent, E. H. *Energy Environ Sci* **9**(4), 1130–1143 (2016).
- [37] Kagan, C. R., Murray, C. B., Nirmal, M., and Bawendi, M. G. *Phys Rev Lett* **76**(9), 1517–1520 (1996).
- [38] Murray, C. B., Kagan, C. R., and Bawendi, M. G. *Annu Rev Mater Sci* **30**(1), 545–610 (2000).
- [39] Schlipf, J. and Müller-Buschbaum, P. *Adv Energy Mater* **7**(16), 1700131 (2017).
- [40] Müller-Buschbaum, P. *Adv Mater* **26**(46), 7692–709 (2014).
- [41] Chen, W., Tang, H., Li, N., Scheel, M. A., Xie, Y., Li, D., Körstgens, V., Schwartzkopf, M., Roth, S. V., Wang, K., Sun, X. W., and Müller-Buschbaum, P. *Nanoscale Horiz* **5**(5), 880–885 (2020).
- [42] Weidman, M. C., Smilgies, D. M., and Tisdale, W. A. *Nat Mater* **15**(7), 775–81 (2016).
- [43] Weidman, M. C., Yager, K. G., and Tisdale, W. A. *Chem Mater* **27**(2), 474–482 (2014).
- [44] Carey, G. H., Chou, K. W., Yan, B., Kirmani, A. R., Amassian, A., and Sargent, E. H. *MRS Commun* **3**(02), 83–90 (2013).

- [45] Sun, B., Vafaie, M., Levina, L., Wei, M., Dong, Y., Gao, Y., Kung, H. T., Biondi, M., Proppe, A. H., Chen, B., Choi, M. J., Sagar, L. K., Voznyy, O., Kelley, S. O., Laquai, F., Lu, Z. H., Hoogland, S., Garcia de Arquer, F. P., and Sargent, E. H. *Nano Lett* **20**(5), 3694–3702 (2020).
- [46] Sun, B., Johnston, A., Xu, C., Wei, M., Huang, Z., Jiang, Z., Zhou, H., Gao, Y., Dong, Y., Ouellette, O., Zheng, X., Liu, J., Choi, M.-J., Gao, Y., Baek, S.-W., Laquai, F., Bakr, O. M., Ban, D., Voznyy, O., García de Arquer, F. P., and Sargent, E. H. *Joule* (2020).
- [47] Biondi, M., Choi, M. J., Ouellette, O., Baek, S. W., Todorovic, P., Sun, B., Lee, S., Wei, M., Li, P., Kirmani, A. R., Sagar, L. K., Richter, L. J., Hoogland, S., Lu, Z. H., Garcia de Arquer, F. P., and Sargent, E. H. *Adv Mater* **32**(17), e1906199 (2020).
- [48] Kim, Y., Che, F., Jo, J. W., Choi, J., Garcia de Arquer, F. P., Voznyy, O., Sun, B., Kim, J., Choi, M. J., Quintero-Bermudez, R., Fan, F., Tan, C. S., Bladt, E., Walters, G., Proppe, A. H., Zou, C., Yuan, H., Bals, S., Hofkens, J., Roeffaers, M. B. J., Hoogland, S., and Sargent, E. H. *Adv Mater* **31**(17), e1805580 (2019).
- [49] Choi, M. J., Kim, Y., Lim, H., Alarousu, E., Adhikari, A., Shaheen, B. S., Kim, Y. H., Mohammed, O. F., Sargent, E. H., Kim, J. Y., and Jung, Y. S. *Adv Mater* **31**(32), e1805886 (2019).
- [50] Liu, M., Voznyy, O., Sabatini, R., Garcia de Arquer, F. P., Munir, R., Balawi, A. H., Lan, X., Fan, F., Walters, G., Kirmani, A. R., Hoogland, S., Laquai, F., Amassian, A., and Sargent, E. H. *Nat Mater* **16**(2), 258–263 (2017).
- [51] Poulidakos, L. V., Prins, F., and Tisdale, W. A. *J Phys Chem C* **118**(15), 7894–7900 (2014).
- [52] Gilmore, R. H., Winslow, S. W., Lee, E. M. Y., Ashner, M. N., Yager, K. G., Willard, A. P., and Tisdale, W. A. *ACS Nano* **12**(8), 7741–7749 (2018).
- [53] Brus, L. *J Phys Chem* **90**(12), 2555–2560 (1986).
- [54] Reich, K. V. and Shklovskii, B. I. *ACS Nano* **10**(11), 10267–10274 (2016).
- [55] Wienhold, K. S., Chen, W., Yin, S., Guo, R., Schwartzkopf, M., Roth, S. V., and Müller-Buschbaum, P. *Solar RRL* (2020).
- [56] Zhitomirsky, D., Voznyy, O., Hoogland, S., and Sargent, E. H. *ACS Nano* **7**(6), 5282–90 (2013).
- [57] Shockley, W. and Queisser, H. J. *J Appl Phys* **32**(3), 510–519 (1961).
- [58] Shrestha, A., Spooner, N. A., Qiao, S. Z., and Dai, S. *Phys Chem Chem Phys* **18**(20), 14055–62 (2016).

- [59] Choi, H., Ko, J. H., Kim, Y. H., and Jeong, S. *J Am Chem Soc* **135**(14), 5278–81 (2013).
- [60] Beygi, H., Sajjadi, S. A., Babakhani, A., Young, J. F., and van Veggel, F. C. J. M. *Appl Surf Sci* **457**, 1–10 (2018).
- [61] Zhang, J., Luo, Z., Quan, Z., Wang, Y., Kumbhar, A., Smilgies, D. M., and Fang, J. *Nano Lett* **11**(7), 2912–8 (2011).
- [62] Zhang, J., Luo, Z., Martens, B., Quan, Z., Kumbhar, A., Porter, N., Wang, Y., Smilgies, D. M., and Fang, J. *J Am Chem Soc* **134**(34), 14043–9 (2012).
- [63] Si, K. J., Chen, Y., Shi, Q., and Cheng, W. *Adv Sci (Weinh)* **5**(1), 1700179 (2018).
- [64] Kramer, I. J., Minor, J. C., Moreno-Bautista, G., Rollny, L., Kanjanaboos, P., Kopilovic, D., Thon, S. M., Carey, G. H., Chou, K. W., Zhitomirsky, D., Amassian, A., and Sargent, E. H. *Adv Mater* **27**(1), 116–21 (2015).
- [65] Geuchies, J. J., van Overbeek, C., Evers, W. H., Goris, B., de Backer, A., Gantapara, A. P., Rabouw, F. T., Hilhorst, J., Peters, J. L., Kononov, O., Petukhov, A. V., Dijkstra, M., Siebbeles, L. D. A., van Aert, S., Bals, S., and Vanmaekelbergh, D. *Nat Mater* **15**(12), 1248–1254 (2016).
- [66] Simon, P., Rosseeva, E., Baburin, I. A., Liebscher, L., Hickey, S. G., Cardoso-Gil, R., Eychmuller, A., Kniep, R., and Carrillo-Cabrera, W. *Angew Chem Int Ed Engl* **51**(43), 10776–81 (2012).
- [67] Tang, J., Liu, H., Zhitomirsky, D., Hoogland, S., Wang, X., Furukawa, M., Levina, L., and Sargent, E. H. *Nano Lett* **12**(9), 4889–94 (2012).
- [68] Yuan, M. J., Liu, M. X., and Sargent, E. H. *Nat Energy* **1**(3), 16016 (2016).
- [69] Hexemer, A. and Müller-Buschbaum, P. *IUCrJ* **2**(Pt 1), 106–25 (2015).
- [70] Proppe, A. H., Xu, J., Sabatini, R. P., Fan, J. Z., Sun, B., Hoogland, S., Kelley, S. O., Voznyy, O., and Sargent, E. H. *Nano Lett* **18**(11), 7052–7059 (2018).
- [71] Fang, Y., Armin, A., Meredith, P., and Huang, J. *Nat Photonics* **13**(1), 1–4 (2018).
- [72] Chen, W., Tang, H., Chen, Y., Heger, J. E., Li, N., Kreuzer, L. P., Xie, Y., Li, D., Anthony, C., Pikramenou, Z., Ng, K. W., Sun, X. W., Wang, K., and Müller-Buschbaum, P. *Nano Energy* , 105254 (2020).
- [73] Zhang, J., Crisp, R. W., Gao, J., Kroupa, D. M., Beard, M. C., and Luther, J. M. *J Phys Chem Lett* **6**(10), 1830–3 (2015).
- [74] Liu, M., Che, F., Sun, B., Voznyy, O., Proppe, A., Munir, R., Wei, M., Quintero-Bermudez, R., Hu, L., Hoogland, S., Mandelis, A., Amassian, A., Kelley, S. O., García de Arquer, F. P., and Sargent, E. H. *ACS Energy Lett* **4**(6), 1225–1230 (2019).

- [75] Brown, P. R., Kim, D., Lunt, R. R., Zhao, N., Bawendi, M. G., Grossman, J. C., and Bulovic, V. *ACS Nano* **8**(6), 5863–72 (2014).
- [76] Ning, Z., Dong, H., Zhang, Q., Voznyy, O., and Sargent, E. H. *ACS Nano* **8**(10), 10321–7 (2014).
- [77] Xu, J., Voznyy, O., Liu, M., Kirmani, A. R., Walters, G., Munir, R., Abdelsamie, M., Proppe, A. H., Sarkar, A., Garcia de Arquer, F. P., Wei, M., Sun, B., Liu, M., Ouellette, O., Quintero-Bermudez, R., Li, J., Fan, J., Quan, L., Todorovic, P., Tan, H., Hoogland, S., Kelley, S. O., Stefik, M., Amassian, A., and Sargent, E. H. *Nat Nanotechnol* **13**(6), 456–462 (2018).
- [78] Jo, J. W., Choi, J., Garcia de Arquer, F. P., Seifitokaldani, A., Sun, B., Kim, Y., Ahn, H., Fan, J., Quintero-Bermudez, R., Kim, J., Choi, M. J., Baek, S. W., Proppe, A. H., Walters, G., Nam, D. H., Kelley, S., Hoogland, S., Voznyy, O., and Sargent, E. H. *Nano Lett* **18**(7), 4417–4423 (2018).
- [79] Liu, M., Chen, Y., Tan, C. S., Quintero-Bermudez, R., Proppe, A. H., Munir, R., Tan, H., Voznyy, O., Scheffel, B., Walters, G., Kam, A. P. T., Sun, B., Choi, M. J., Hoogland, S., Amassian, A., Kelley, S. O., Garcia de Arquer, F. P., and Sargent, E. H. *Nature* **570**(7759), 96–101 (2019).
- [80] Xue, Y., Yang, F., Yuan, J., Zhang, Y., Gu, M., Xu, Y., Ling, X., Wang, Y., Li, F., Zhai, T., Li, J., Cui, C., Chen, Y., and Ma, W. *ACS Energy Lett* **4**(12), 2850–2858 (2019).
- [81] Zhang, Y., Kan, Y., Gao, K., Gu, M., Shi, Y., Zhang, X., Xue, Y., Zhang, X., Liu, Z., Zhang, Y., Yuan, J., Ma, W., and Jen, A. K. Y. *ACS Energy Lett* **5**(7), 2335–2342 (2020).
- [82] Tang, X., Ackerman, M. M., and Guyot-Sionnest, P. *ACS Nano* **12**(7), 7362–7370 (2018).
- [83] Gong, X., Yang, Z., Walters, G., Comin, R., Ning, Z., Beauregard, E., Adinolfi, V., Voznyy, O., and Sargent, E. H. *Nat Photonics* **10**(4), 253–257 (2016).
- [84] Kagan, C. R., Lifshitz, E., Sargent, E. H., and Talapin, D. V. *Science* **353**(6302) (2016).
- [85] Bederak, D., Balazs, D. M., Sukharevska, N. V., Shulga, A. G., Abdu-Aguye, M., Dirin, D. N., Kovalenko, M. V., and Loi, M. A. *ACS Appl Nano Mater* **1**(12), 6882–6889 (2018).
- [86] Liu, Y., Tolentino, J., Gibbs, M., Ihly, R., Perkins, C. L., Liu, Y., Crawford, N., Hemminger, J. C., and Law, M. *Nano Lett* **13**(4), 1578–87 (2013).

- [87] Osedach, T. P., Zhao, N., Andrew, T. L., Brown, P. R., Wanger, D. D., Strasfeld, D. B., Chang, L. Y., Bawendi, M. G., and Bulovic, V. *ACS Nano* **6**(4), 3121–7 (2012).
- [88] Bi, Y., Bertran, A., Gupta, S., Ramiro, I., Pradhan, S., Christodoulou, S., Majji, S. N., Akgul, M. Z., and Konstantatos, G. *Nanoscale* **11**(3), 838–843 (2019).
- [89] Wang, R., Wu, X., Xu, K., Zhou, W., Shang, Y., Tang, H., Chen, H., and Ning, Z. *Adv Mater* **30**(7) (2018).
- [90] Yang, Z., Fan, J. Z., Proppe, A. H., Arquer, F. P. G., Rossouw, D., Voznyy, O., Lan, X., Liu, M., Walters, G., Quintero-Bermudez, R., Sun, B., Hoogland, S., Botton, G. A., Kelley, S. O., and Sargent, E. H. *Nat Commun* **8**(1), 1325 (2017).
- [91] Khan, J., Yang, X., Qiao, K., Deng, H., Zhang, J., Liu, Z., Ahmad, W., Zhang, J., Li, D., Liu, H., Song, H., Cheng, C., and Tang, J. *J Mater Chem A* **5**(33), 17240–17247 (2017).
- [92] Voznyy, O., Sutherland, B. R., Ip, A. H., Zhitomirsky, D., and Sargent, E. H. *Nat Rev Mater* **2**(6), 17026 (2017).
- [93] Whitham, K., Smilgies, D.-M., and Hanrath, T. *Chem Mater* **30**(1), 54–63 (2017).
- [94] Li, R., Bian, K., Hanrath, T., Bassett, W. A., and Wang, Z. *J Am Chem Soc* **136**(34), 12047–55 (2014).
- [95] Corricelli, M., Altamura, D., Curri, M. L., Sibillano, T., Siliqi, D., Mazzone, A., Depalo, N., Fanizza, E., Zanchet, D., Giannini, C., and Striccoli, M. *CrystEngComm* **16**(40), 9482–9492 (2014).
- [96] Choi, J. J., Luria, J., Hyun, B. R., Bartnik, A. C., Sun, L., Lim, Y. F., Marohn, J. A., Wise, F. W., and Hanrath, T. *Nano Lett* **10**(5), 1805–11 (2010).
- [97] Semonin, O. E., Luther, J. M., and Beard, M. C. *Mater Today* **15**(11), 508–515 (2012).
- [98] Liu, Y., Gibbs, M., Puthussery, J., Gaik, S., Ihly, R., Hillhouse, H. W., and Law, M. *Nano Lett* **10**(5), 1960–9 (2010).
- [99] Balazs, D. M., Bijlsma, K. I., Fang, H. H., Dirin, D. N., Dobeli, M., Kovalenko, M. V., and Loi, M. A. *Sci Adv* **3**(9), eaao1558 (2017).
- [100] Li, T., Senesi, A. J., and Lee, B. *Chem Rev* **116**(18), 11128–80 (2016).
- [101] Zarghami, M. H., Liu, Y., Gibbs, M., Gebremichael, E., Webster, C., and Law, M. *ACS Nano* **4**(4), 2475–85 (2010).
- [102] Hines, M. A. and Scholes, G. D. *Advanced Materials* **15**(21), 1844–1849 (2003).
- [103] Renaud, G., Lazzari, R., and Leroy, F. *Surf Sci Rep* **64**(8), 255–380 (2009).

- [104] Micic, O. I., Ahrenkiel, S. P., and Nozik, A. J. *Appl Phys Lett* **78**(25), 4022–4024 (2001).
- [105] Choi, J. J., Bealing, C. R., Bian, K., Hughes, K. J., Zhang, W., Smilgies, D. M., Hennig, R. G., Engstrom, J. R., and Hanrath, T. *J Am Chem Soc* **133**(9), 3131–8 (2011).
- [106] Bian, K., Wang, Z., and Hanrath, T. *J Am Chem Soc* **134**(26), 10787–90 (2012).
- [107] Lu, H., Carroll, G. M., Neale, N. R., and Beard, M. C. *ACS Nano* **13**(2), 939–953 (2019).
- [108] Fan, J. Z., Andersen, N. T., Biondi, M., Todorovic, P., Sun, B., Ouellette, O., Abed, J., Sagar, L. K., Choi, M. J., Hoogland, S., de Arquer, F. P. G., and Sargent, E. H. *Adv Mater* **31**(48), e1904304 (2019).
- [109] Chen, W., Castro, J., Ahn, S., Li, X., and Vazquez-Mena, O. *Adv Mater* **31**(14), e1807894 (2019).
- [110] Lim, H., Kim, D., Choi, M., Sargent, E. H., Jung, Y. S., and Kim, J. Y. *Adv Energy Mater* **9**(48), 1901938 (2019).
- [111] Bae, W. K., Joo, J., Padilha, L. A., Won, J., Lee, D. C., Lin, Q., Koh, W. K., Luo, H., Klimov, V. I., and Pietryga, J. M. *J Am Chem Soc* **134**(49), 20160–8 (2012).
- [112] Gesuele, F., Sfeir, M. Y., Koh, W. K., Murray, C. B., Heinz, T. F., and Wong, C. W. *Nano Lett* **12**(6), 2658–64 (2012).
- [113] Liu, Y., Liu, M., Yin, D., Zhu, D., and Swihart, M. T. *Nanoscale* **11**(1), 136–144 (2018).
- [114] YousefiAmin, A., Killilea, N. A., Sytnyk, M., Maisch, P., Tam, K. C., Egelhaaf, H. J., Langner, S., Stubhan, T., Brabec, C. J., Rejek, T., Halik, M., Poulsen, K., Niehaus, J., Kock, A., and Heiss, W. *ACS Nano* **13**(2), 2389–2397 (2019).
- [115] Zhang, X., Hägglund, C., and Johansson, E. M. J. *Energy Environ Sci* **10**(1), 216–224 (2017).
- [116] Stavrinadis, A., Pradhan, S., Papagiorgis, P., Itskos, G., and Konstantatos, G. *ACS Energy Lett* **2**(4), 739–744 (2017).
- [117] Fan, J. Z., Liu, M., Voznyy, O., Sun, B., Levina, L., Quintero-Bermudez, R., Liu, M., Ouellette, O., Garcia de Arquer, F. P., Hoogland, S., and Sargent, E. H. *ACS Appl Mater Interfaces* **9**(43), 37536–37541 (2017).
- [118] Kim, J., Ouellette, O., Voznyy, O., Wei, M., Choi, J., Choi, M. J., Jo, J. W., Baek, S. W., Fan, J., Saidaminov, M. I., Sun, B., Li, P., Nam, D. H., Hoogland, S., Lu, Z. H., Garcia de Arquer, F. P., and Sargent, E. H. *Adv Mater* **30**(45), e1803830 (2018).

- [119] Gu, M., Wang, Y., Yang, F., Lu, K., Xue, Y., Wu, T., Fang, H., Zhou, S., Zhang, Y., Ling, X., Xu, Y., Li, F., Yuan, J., Loi, M. A., Liu, Z., and Ma, W. *J Mater Chem A* **7**(26), 15951–15959 (2019).
- [120] Sliz, R., Lejay, M., Fan, J. Z., Choi, M. J., Kinge, S., Hoogland, S., Fabritius, T., Garcia de Arquer, F. P., and Sargent, E. H. *ACS Nano* **13**(10), 11988–11995 (2019).
- [121] Kiani, A., Sutherland, B. R., Kim, Y., Ouellette, O., Levina, L., Walters, G., Dinh, C.-T., Liu, M., Voznyy, O., Lan, X., Labelle, A. J., Ip, A. H., Proppe, A., Ahmed, G. H., Mohammed, O. F., Hoogland, S., and Sargent, E. H. *Appl Phys Lett* **109**(18), 183105 (2016).
- [122] Chernomordik, B. D., Marshall, A. R., Pach, G. F., Luther, J. M., and Beard, M. C. *Chem Mater* **29**(1), 189–198 (2016).
- [123] Kufer, D., Nikitskiy, I., Lasanta, T., Navickaite, G., Koppens, F. H., and Konstantatos, G. *Adv Mater* **27**(1), 176–80 (2015).
- [124] Pospelov, G., Van Herck, W., Burle, J., Carmona Loaiza, J. M., Durniak, C., Fisher, J. M., Ganeva, M., Yurov, D., and Wuttke, J. *J Appl Crystallogr* **53**(Pt 1), 262–276 (2020).
- [125] Jiang, Z. *J Appl Crystallogr* **48**(3), 917–926 (2015).
- [126] Buffet, A., Rothkirch, A., Dohrmann, R., Körstgens, V., Abul Kashem, M. M., Perlich, J., Herzog, G., Schwartzkopf, M., Gehrke, R., Müller-Buschbaum, P., and Roth, S. V. *J Synchrotron Radiat* **19**(Pt 4), 647–53 (2012).
- [127] Wienhold, K. S., Körstgens, V., Grott, S., Jiang, X., Schwartzkopf, M., Roth, S. V., and Müller-Buschbaum, P. *ACS Appl Mater Interfaces* **11**(45), 42313–42321 (2019).
- [128] Benecke, G., Wagermaier, W., Li, C., Schwartzkopf, M., Flucke, G., Hoerth, R., Zizak, I., Burghammer, M., Metwalli, E., Müller-Buschbaum, P., Trebbin, M., Forster, S., Paris, O., Roth, S. V., and Fratzl, P. *J Appl Crystallogr* **47**(Pt 5), 1797–1803 (2014).
- [129] Roth, S. V., Herzog, G., Körstgens, V., Buffet, A., Schwartzkopf, M., Perlich, J., Abul Kashem, M. M., Dohrmann, R., Gehrke, R., Rothkirch, A., Stassig, K., Wurth, W., Benecke, G., Li, C., Fratzl, P., Rawolle, M., and Müller-Buschbaum, P. *J Phys Condens Matter* **23**(25), 254208 (2011).
- [130] Santoro, G., Buffet, A., Dohrmann, R., Yu, S., Körstgens, V., Müller-Buschbaum, P., Gedde, U., Hedenqvist, M., and Roth, S. V. *Rev Sci Instrum* **85**(4), 043901 (2014).
- [131] Paul, N., Metwalli, E., Yao, Y., Schwartzkopf, M., Yu, S., Roth, S. V., Müller-Buschbaum, P., and Paul, A. *Nanoscale* **7**(21), 9703–14 (2015).

- [132] Busch, P., Rauscher, M., Smilgies, D. M., Posselt, D., and Papadakis, C. M. *J Appl Crystallogr* **39**(3), 433–442 (2006).
- [133] Hsu, C. P. *Acc Chem Res* **42**(4), 509–18 (2009).
- [134] Bisri, S. Z., Piliago, C., Yarema, M., Heiss, W., and Loi, M. A. *Adv Mater* **25**(31), 4309–14 (2013).
- [135] Huang, Z., Zhai, G., Zhang, Z., Zhang, C., Xia, Y., Lian, L., Fu, X., Zhang, D., and Zhang, J. *CrystEngComm* **19**(6), 946–951 (2017).
- [136] Carey, G. H., Levina, L., Comin, R., Voznyy, O., and Sargent, E. H. *Adv Mater* **27**(21), 3325–30 (2015).
- [137] Rinnerbauer, V., Egelhaaf, H. J., Hingerl, K., Zimmer, P., Werner, S., Warming, T., Hoffmann, A., Kovalenko, M., Heiss, W., Hesser, G., and Schaffler, F. *Phys Rev B* **77**(8) (2008).
- [138] Azzaro, M. S., Dodin, A., Zhang, D. Y., Willard, A. P., and Roberts, S. T. *Nano Lett* **18**(5), 3259–3270 (2018).
- [139] Akselrod, G. M., Prins, F., Poulidakos, L. V., Lee, E. M., Weidman, M. C., Mork, A. J., Willard, A. P., Bulovic, V., and Tisdale, W. A. *Nano Lett* **14**(6), 3556–62 (2014).
- [140] Wang, Y., Liu, Z., Huo, N., Li, F., Gu, M., Ling, X., Zhang, Y., Lu, K., Han, L., Fang, H., Shulga, A. G., Xue, Y., Zhou, S., Yang, F., Tang, X., Zheng, J., Antonietta Loi, M., Konstantatos, G., and Ma, W. *Nat Commun* **10**(1), 5136 (2019).
- [141] Kramer, I. J., Moreno-Bautista, G., Minor, J. C., Kopilovic, D., and Sargent, E. H. *Appl Phys Lett* **105**(16), 163902 (2014).
- [142] Yang, D., Löhrer, F. C., Körstgens, V., Schreiber, A., Bernstorff, S., Buriak, J. M., and Müller-Buschbaum, P. *ACS Energy Lett* **4**(2), 464–470 (2019).
- [143] Lee, E. M. Y. and Tisdale, W. A. *J Phys Chem C* **119**(17), 9005–9015 (2015).
- [144] Chen, W., Ahn, S., Rangel, C., and Vazquez-Mena, O. *Front Mater* **6** (2019).
- [145] Liang, F.-X., Wang, J.-Z., Zhang, Z.-X., Wang, Y.-Y., Gao, Y., and Luo, L.-B. *Adv Opt Mater* **5**(22), 1700654 (2017).
- [146] Saran, R. and Curry, R. J. *Nat Photonics* **10**(2), 81–92 (2016).
- [147] García de Arquer, F. P., Armin, A., Meredith, P., and Sargent, E. H. *Nat Rev Mater* **2**(3) (2017).
- [148] Konstantatos, G., Clifford, J., Levina, L., and Sargent, E. H. *Nat Photonics* **1**(9), 531–534 (2007).
- [149] Konstantatos, G. and Sargent, E. H. *Proc. IEEE* **97**(10), 1666–1683 (2009).

- [150] Xiao, X., Tang, H., Zhang, T., Chen, W., Chen, W., Wu, D., Wang, R., and Wang, K. *Opt Express* **24**(19), 21577–86 (2016).
- [151] Konstantatos, G., Howard, I., Fischer, A., Hoogland, S., Clifford, J., Klem, E., Levina, L., and Sargent, E. H. *Nature* **442**(7099), 180–3 (2006).
- [152] Song, J. H., Kim, T., Park, T., and Jeong, S. *J Mater Chem A* **8**(9), 4844–4849 (2020).
- [153] Yang, X., Yang, J., Khan, J., Deng, H., Yuan, S., Zhang, J., Xia, Y., Deng, F., Zhou, X., Umar, F., Jin, Z., Song, H., Cheng, C., Sabry, M., and Tang, J. *Nano-Micro Lett* **12**(1) (2020).
- [154] Cao, Y., Stavrinadis, A., Lasanta, T., So, D., and Konstantatos, G. *Nat Energy* **1**(4) (2016).
- [155] Bhandari, K. P., Roland, P. J., Gao, J. B., and Ellingson, R. J. *2013 Ieee 39th Photovoltaic Specialists Conference (Pvsc)*, 258–263 (2013).
- [156] Lu, K., Wang, Y., Yuan, J., Cui, Z., Shi, G., Shi, S., Han, L., Chen, S., Zhang, Y., Ling, X., Liu, Z., Chi, L., Fan, J., and Ma, W. *J Mater Chem A* **5**(45), 23960–23966 (2017).
- [157] Wienhold, K. S., Chen, W., Yin, S., Guo, R., Schwartzkopf, M., Roth, S. V., and Müller-Buschbaum, P. *Solar RRL*, 2000251 (2020).
- [158] Jiang, Q., Zhang, X., and You, J. *Small*, e1801154 (2018).
- [159] Jiang, Q., Zhang, L., Wang, H., Yang, X., Meng, J., Liu, H., Yin, Z., Wu, J., Zhang, X., and You, J. *Nat Energy* **2**(1) (2016).
- [160] Schutt, K., Nayak, P. K., Ramadan, A. J., Wenger, B., Lin, Y., and Snaith, H. J. *Adv Funct Mater* **29**(47), 1900466 (2019).
- [161] Jia, D., Chen, J., Zheng, S., Phuyal, D., Yu, M., Tian, L., Liu, J., Karis, O., Rensmo, H., Johansson, E. M. J., and Zhang, X. *Adv Energy Mater* **9**(44), 1902809 (2019).
- [162] Rolston, N., Bennett-Kennett, R., Schelhas, L. T., Luther, J. M., Christians, J. A., Berry, J. J., and Dauskardt, R. H. *Science* **368**(6488) (2020).
- [163] Bederak, D., Balazs, D. M., Sukharevska, N. V., Shulga, A. G., Abdu-Aguye, M., Dirin, D. N., Kovalenko, M. V., and Loi, M. A. *ACS Appl Nano Mater* **1**(12), 6882–6889 (2018).
- [164] Heumueller, T., Burke, T. M., Mateker, W. R., Sachs-Quintana, I. T., Vandewal, K., Brabec, C. J., and McGehee, M. D. *Adv Energy Mater* **5**(14), 1500111 (2015).
- [165] Liu, C., Peng, H., Wang, K., Wei, C., Wang, Z., and Gong, X. *Nano Energy* **30**, 27–35 (2016).

- [166] Shao, Y., Yuan, Y., and Huang, J. *Nat Energy* **1**(1) (2016).
- [167] Du, T., Kim, J., Ngiam, J., Xu, S., Barnes, P. R. F., Durrant, J. R., and McLachlan, M. A. *Adv Funct Mater* **28**(32), 1801808 (2018).

List of publications

Publications related to the dissertation

- Chen, W., Wang, K., Cao, W. Q. and Müller-Buschbaum, P. “Spatial disorder suppresses charge carrier transport in strongly coupled quantum dot solids: direct indication from GISAXS” *in submission* (2020)
- Chen, W., Duan, W., Tang, H., Wang, K., Cao, W. Q., and Müller-Buschbaum, P. “Colloidal PbS Quantum Dot Ink: A New Era of Solution-processed Optoelectronic Devices” *in submission* (2020)
- Chen, W., Guo, R., Wienhold, K. S., Li, N., Jiang, X., Tang, H., Kreuzer, L. P., Schwartzkopf, M., Sun, X. W., Roth, S. V., Wang, K., Müller-Buschbaum, P. “*In Operando* Structure Degradation Study of PbS Quantum Dot Solar Cells” *in submission* (2020)
- Chen, W., Liang, S., Löhrer, F. C., Schaper, S. J. Li, N., Cao, W., Kreuzer, L. P., Liu, H., Tang, T., Körstgens, V., Schwartzkopf, M., Wang, K., Sun, X. W., Roth, S. V., and Müller-Buschbaum, P. “*In situ* Grazing-Incidence Small-Angle X-ray Scattering Observation of Gold Sputter Deposition on a PbS Quantum Dot Solid” *ACS Appl Mater Interfaces* **12**(41), 46942-46952 (2020)
- Chen, W., Tang, H., Li, N., Scheel, M. A., Xie, Y., Li, D., Körstgens, V., Schwartzkopf, M., Roth, S. V., Wang, K., Sun, X. W., Müller-Buschbaum, P. “Spray-deposited PbS Colloidal Quantum Dot Solid for Near-Infrared Photodetectors” *Nano Energy* **78**, 105254 (2020)
- Xia, Y., Chen, W. (Co-first author), Zhang, P., Liu, S., Wang, K., Yang, X., Tang, H., Lian, L., He, J., Liu, X., Liang, G., Tan, M., Gao, L., Liu, H., Song, H., Zhang, D., Gao, J., Wang, K., Lan, X., Zhang, X., and Müller-Buschbaum, P., Tang, J., Zhang, J. “Facet Control for Trap-State Suppression in Colloidal Quantum Dot Solids” *Adv Funct Mater* **30**(22), 2000594 (2020)
- Chen, W., Tang, H., Li, N., Scheel, M. A., Xie, Y., Li, D., Körstgens, V., Schwartzkopf, M., Roth, S. V., Wang, K., Sun, X. W., and Müller-Buschbaum, P. “Colloidal PbS

- quantum dot stacking kinetics during deposition via printing” *Nanoscale Horiz* **5**(5), 880-885 (2020)
- Tang, H., Zhong, J., Chen, W. (Co-first author), Shi, K., Mei, G., Zhang, Y., Wen, Z., Müller-Buschbaum, P., Wu, D., Wang, K., and Sun, X. W. “Lead Sulfide Quantum Dot Photodetector with Enhanced Responsivity through a Two-Step Ligand-Exchange Method” *ACS Appl Nano Mater* **2**(10), 6135-6143 (2019)
 - Chen, W., Zhong, J., Li, J., Saxena, N., Kreuzer, L. P., Liu, H., Song, L., Su, B., Yang, D., Wang, K., Schlipf, J., Körstgens, V., He, T., Wang, K., and Müller-Buschbaum, P. “Structure and Charge Carrier Dynamics in Colloidal PbS Quantum Dot Solids” *J Phys Chem Lett* **10**(9), 2058-2065 (2019)

Further publications

- Liu, P., Chen, W., Decossas, M., Okazaki, Y., Battie, Y., Brocard, L., Pouget, E., Müller-Buschbaum, P., Kauffmann, B., Pathan, S., Sagawa, T., Oda, R. “Optically Active Perovskite CsPbBr₃ Nanocrystals Helically Arranged on Inorganic Silica Nanohelices” *Nano Lett* (2020)
- Wienhold, K. S., Chen, W., Yin, S., Guo, R., Schwartzkopf, M., Roth, S. V., Müller-Buschbaum, P. “Following in Operando the Structure Evolution Induced Degradation in Printed Organic Solar Cells with Nonfullerene Small Molecule Acceptor” *Solar RRL* **4**(9), 2000251 (2020)
- Kluge, R. M., Saxena, N., Chen, W., Körstgens, V., Schwartzkopf, M., Zhong, Q., Roth, S. V., Müller-Buschbaum, P. “Doping Dependent In-Plane and Cross-Plane Thermoelectric Performance of Thin n-Type Polymer P(NDI2OD-T2) Films” *Adv Funct Mater* **30**(28), 2003092 (2020)
- Guo, R., Buyruk, A., Jiang, X., Chen, W., Reb, L. K., Scheel, M. A., Ameri, T., Müller-Buschbaum, P. “Tailoring the orientation of perovskite crystals via adding two-dimensional polymorphs for perovskite solar cells” *J Phys Energy* **2**(3), 034005 (2020)
- Yin, S., Song, L., Xia, S., Cheng, Y., Hohn, N., Chen, W., Wang, K., Cao, W., Hou, S., Müller-Buschbaum, P. “Key Factors for Template-Oriented Porous Titania Synthesis: Solvents and Catalysts” *Small Methods* **4**(3), 1900689 (2020)
- Yang, D., Cao, B., Körstgens, V., Saxena, N., Li, N., Bilko, C., Grott, S., Chen, W., Jiang, X., Heger, J. E., Bernstorff, S., Müller-Buschbaum, P. “Tailoring Morphology Compatibility and Device Stability by Adding PBDTPD-COOH as Third

- Component to Fullerene-Based Polymer Solar Cells” *ACS Appl Energy Mater* **3**(3), 2604-2613 (2020)
- Tang, X., Chen, W. (Co-first author), Wu, D., Gao, A., Li, G., Sun, J., Yi, K., Wang, Z., Pang, G., Yang, H., Guo, R., Liu, H., Zhong, H., Huang, M., Chen, R., Müller-Buschbaum, P., Sun, X. W., Wang, K. “In Situ Growth of All-Inorganic Perovskite Single Crystal Arrays on Electron Transport Layer” *Adv Sci* **7**(11), 1902767 (2020)
 - Fang, F., Liu, M., Chen, W., Yang, H., Liu, Y., Li, X., Hao, J., Xu, B., Wu, D., Cao, K., Lei, W., Müller-Buschbaum, P., Sun, X. W., Chen, R., Wang, K. “Atomic Layer Deposition Assisted Encapsulation of Quantum Dot Luminescent Microspheres toward Display Applications” *Adv Opt Mater* **8**(12), 1902118 (2020)
 - Xia, S., Song, L., Chen, W., Körstgens, V., Opel, M., Schwartzkopf, M., Roth, S. V., Müller-Buschbaum, P. “Printed Thin Diblock Copolymer Films with Dense Magnetic Nanostructure” *ACS Appl Mater Interfaces* **11**(24), 21935-21945 (2019)

Scientific reports

- Chen, W., and Müller-Buschbaum, P. “Quantum dot based novel device architectures”, *Lehrstuhl für Funktionelle Materialien, Annual Report* (2019)
- Chen, W, Wang, K., and Müller-Buschbaum, P. “Inner structure study of quantum dot solids for practical applications”, *Lehrstuhl für Funktionelle Materialien, Annual Report* (2018)
- Chen, W, Wang, K., Yang, D., and Müller-Buschbaum, P. “Inner structure analysis on annealing treated colloidal quantum dots solids”, *Lehrstuhl für Funktionelle Materialien, Annual Report* (2017)
- Chen, W, Yang, D., and Müller-Buschbaum, P. “Nanocrystals and polymer hybrid active layer in bulk heterojunction solar cell”, *Lehrstuhl für Funktionelle Materialien, Annual Report*, (2016)

Conference talks

- Chen W., Guo, R., Wienhold, K. S., Yin, S., Kreuzer, L. P., Körstgens, V., Schwartzkopf, M., Roth, S. V., and Müller-Buschbaum, P. “Structural degradation in quantum dot solar cells”, *DESY Photon Science Users’ Meeting 2020*, Hamburg, 30 – 31 Jan 2020
- Chen, W., and Müller-Buschbaum, P. “Inner structure analysis of quantum dot solids for photo-devices”, *DPG-Fruhjahrstagung*, Regensburg, 31 Mar – 5 Apr 2019

- Chen, W., and Müller-Buschbaum, P. “*In – situ* sputtering deposition of gold on close packed quantum dot solid”, *NanoWorkshop 2019*, Espoo, Finland, 22 – 24 Jul 2019
- Chen, W., Heger, J. E., Brett, C., Ohm, W., Wang, K., Roth, S. V., and Müller-Buschbaum, P. “In-situ observation of quantum dots spray deposition”, *DESY Photon Science Users’ Meeting 2019*, Hamburg, 24 – 25 Jan 2019
- Chen, W., Grott, S., and Pratap, S. “Small angle X-ray and neutron scattering”, *Polymer Physics Summer School Obertauern*, Austria, 12 – 15 Jun 2018
- Chen, W., “Introducing colloidal quantum dots in solar cells”, *3rd Internal Biennial Science Meeting of the MLZ*, Grainau, 19 – 27 Jun 2017

Conference poster presentations

- Chen, W., Guo, R., Wienhold, K. S., Kreuzer, L. P., Körstgens, V., Schwartzkopf, M., Roth, S. V., and Müller-Buschbaum, P. “Structural degradation in quantum dot solar cells”, *DESY Photon Science Users’ Meeting 2020*, Hamburg, 30 – 31 Jan 2020
- Chen, W., and Müller-Buschbaum, P. “Quantum dot solids for photo-devices”, *4th internal biennial science meeting of the MLZ*, Grainau, 24 – 27 Jun 2019
- Chen, W., Heger, J. E., Brett, C., Ohm, W., Wang, K., Roth, S. V., and Müller-Buschbaum, P. “In-situ observation of quantum dots spray deposition”, *DESY Photon Science Users’ Meeting 2019*, Hamburg, 24 – 25 Jan 2019
- Chen, W., and Müller-Buschbaum, P. “Colloidal quantum dot solids for photo-voltaics”, *DPG-Fruhjahrstagung*, Berlin, 11 – 16 Mar 2018
- Chen, W., and Müller-Buschbaum, P. “Colloidal quantum dot solids for photo-voltaics”, *8th Colloquium of the Munich School of Engineering*, Garching, 19 Jul 2018
- Chen, W., and Müller-Buschbaum, P. “Colloidal quantum dot solids for photo-voltaics”, *4th German SNI Conference*, Garching, 17 – 19 Sep 2018
- Chen, W., Yang, D., Wang, K., and Müller-Buschbaum, P. “Polymer and nanocrystals hybrid solar cells”, *DPG-Fruhjahrstagung*, Dresden, 19 – 24 Mar 2017
- Chen, W., and Müller-Buschbaum, P. “Colloidal quantum dots with narrow band gap in solar cells”, *6th SolTech Conference: Solar Technologies go Hybrid*, Munich, 4 – 5 Oct 2017

Acknowledgments

Foremost, I would like to thank the funding support from the China Scholarship Council (CSC) during my Ph.D. study in Germany.

I would like to thank Prof. Peter Müller-Buschbaum, my supervisor, for his guidance and help through each stage of my Ph.D. training. Thanks for his full support to my research project. He's always there willing to answer all my questions, join discussions, and provide suggestions. I am grateful for his careful corrections and modifications to my manuscripts and the final thesis. I've learned a lot from him during the past years, not only about the professional skills, knowledge but also the diligent and rigorous attitude to all research projects and collaborations.

I would like to thank Prof. Kai Wang, my co-supervisor, and the professor at Southern University of Science and Technology (SUSTech), for his support of my research topic. I have worked with him for over 7 years since I was a research assistant in his Lab. I could not build up my research topic without his solid support and encouragement. I have always appreciated it to receive his helpful feedback on my questions and demands. I do admire him, not only for his talent and great achievements as a young scholar but also for his humble and open-mind personality.

Many people in SUSTech need to be acknowledged. Specifically, I would like to thank Prof. Xiao Wei Sun and the group members, Prof. Dan Wu, Junjie Hao, Jing Qin, Dan Wang, Dr. Bing Xu, Jiagen Li, Ziming Zhou, Haodong Tang, Tianqi Zhang, Zuoliang Wen, Xiangtian Xiao, Jialin Zhong, Shang Li, Kanming Shi, Xiaobing Tang, Haochen Liu, Chenhao Li, Yue Xie, and Depeng Li for the great and solid support.

I would like to thank Prof. Wan-Qiang Cao, my former supervisor at Hubei University, and the group members, Peizhao Liu, Fan Fang, Yang Li, and Ming Mei for the discussion and help. My student, Wenyan Duan is acknowledged for her interest in my topic and joining my research. Looking forward to seeing great results of our collaboration.

I would extremely thank my collaborators, Prof. Tingchao He and Junzi Li, at Shenzhen University for the ultrafast spectroscopy measurement.

I would very grateful to my collaborators, Prof. Jianbing Zhang and Dr. Yong Xia, at Huazhong University of Science and Technology for the interesting and fruitful collaboration, which stimulates my interests to keep going the research topic in the future.

Thanks for the great help and important support from the collaborators, Prof. Yu Tong and Dr. He Huang from J. Feldmann group at Ludwig Maximilian University of Munich (LMU). Looking forward to more great collaborations in the future.

All E13 members have deserved a huge acknowledgment from my mind. Without the great atmosphere in the group and all open-mind discussions, it would be extremely hard for me to make a small step in the X-ray scattering field. Specifically, I would like to thank Dr. Volker Körstgens, Dr. Nitin Saxena, Prof. Qi Zhong, Marc Gensch, Sebastian Grott, Renjun Guo, Julian Eliah Heger, Xinyu Jiang, Nian Li, Franziska Carina Löhner, Suzhe Liang, Lennart Reb, Simon Jakob Schaper, Manuel Andree Scheel, Kerstin Sabrina Wienhold, Shanshan Yin, the beamtime members for the experience together and great memories. Moreover, thank the senior members, Dr. Shuai Guo, Prof. Weijia Wang, Prof. Lin Song, Dr. Bo Su, Dr. Johannes Schlipf, Dr. Rui Wang, Prof. Kun Wang, Dr. Nuri Hohn, Dr. Senlin Xia, Dr. Lorenz Bießmann, and Dr. Dan Yang for all great help and suggestions. Thanks for the supports and group organizations by Wei Cao, Christina Geiger, Tianfu Guan, Lucas Philipp Kreuzer, Anna-Lena Oechsle, Shambhavi Pratap, Roy Schaffrinna, Dominik Schwaiger, Ting Tian, Suo Tu, Peixi Wang, Christian Ludwig Weindl, Tobias Widmann, Tianxiao Xiao, and Yuqin Zou.

I am very grateful for the experimental support and inspired discussions from Prof. Stephan V. Roth, Dr. Matthias Schwartzkopf, Dr. Pallavi Pandit, and many other technicians in P03 beamline, DESY.

I would also like to thank Prof. Christine M. Papadakis, and the group members, Dr. Xiaohan Zhang, Dr. Bart-Jan Niebuur, Florian Jung, Jia-Jhen Kang, Chia-Hsin Ko, and Yanan Li for the professional support and a lot of help.

More importantly, I would like to thank Ms. Marion Waletzki, and Ms. Carola Kappauf, for your great contribution to make E13 running smoothly.

For the last, I am truly grateful to my mother and my father, my sister and my brother-in-law, my cousins and all my relatives. Thanks so much for their great contributions to the big family, which relieves me and encourages me when I was feeling alone abroad. I can not make it without their contributions behind.